UNIVERSITY OF LIVERPOOL

High Resolution Size and Structural Characterisation of Nanomedicines by Asymmetric Flow Field Flow Fractionation

Edyta Niezabitowska

September 2019

Thesis submitted in accordance with the requirements of the University of Liverpool for the degree of Doctor in Philosophy

ACKNOWLEDGMENTS

Firstly, I'd like to begin by acknowledging my supervisor Dr Tom McDonald. I am really grateful for his guidance and encouragement during my PhD project. He is excellent supervisor, kind and patient. His help and support improved my skills significantly. I'd like to also thank my second supervisor Prof. Steve Rannard for the intellectual support and equipment access.

I am much indebted to Dr Bassem Sabagh from PostNova Analytics for his guidance and constant support about asymmetric flow field flow fractionation technique. I'd like to also thank Dr Riaz Akhtar for atomic force miscroscopy measurements, Dr Felix W. von Aulock for the thermogravimetric analysis, Dr Sebastian Spain, Marissa Morales and Emma Owens from the University of Sheffield for their help about synthesis of PNIPAM nanogels by RAFT polymerisation and Tiago Entradas for providing the non-spherical gold and silver samples.

I'd like to also acknowledge people with I had privilege to work: Adam Town, Jess Taylor, Jess Smith, Steph Edwards for their amazing support and their enthusiasm I'd also like to thank my research group, and the larger nanomedicine group for all their help and support.

I would like to thank my family for the emotional support during the PhD. Especially to my beloved husband Sylwek, my mum and dad, my sister Lidka, my uncle Jacek. I would like to dedicate this thesis to the memory of my grandmother Marysia and grandfather Stanisław, who always believed in my ability to be successful in the chemistry arena. You are gone but your beliefs in me has made this journey possible.

ABSTRACT

The interest of nanomedicine has grown substantially over the last 30 years. Due to this growth, it has become very important to obtain analytic techniques to provide high resolution characterisation particles with nanoscale sizes. A promising approach is to fractionate nanoparticle distributions through the use of asymmetric field flow fractionation (AF4). This separation method is particularly useful for as allows detailed information to be obtained (such as concentration of particles, size and shape) on all particles within the system. In our research, three different nanomaterials are analysed by AF4, these are nanocomposites made of carbon nanotubes (CNTs) and polycaprolactone (PCL), poly(N-isopropylacrylamide) (PNIPAM) based nanogels and metallic particles with different sizes and shapes.

The high-aspect ratio PCL-CNT nanocomposites were produced by developing a simple oil-in water emulsion solvent evaporation method. The high drug entrapment efficiencies of the nanocomposites offer the potential for these nanocomposites to be used in drug delivery applications. AF4 analysis showed good and reproducible separation of PCL-CNTs nanocomposites.

PNIPAM based nanogels are a well-known temperature responsive type of nanogels that has been shown to present attractive properties for applications in drug delivery. In order to characterise PNIPAM nanogels a novel, versatile AF4 method was developed. The different nanogel samples with mean diameters between 65 and 310 nm were synthesised via free radical dispersion polymerisation by varying the amount of surfactant used during the polymerisation. The AF4 was combined with multi-angle light scattering (MALS) and dynamic light scattering (DLS) detectors to provide detailed size (hydrodynamic radius, R_h) and structural information (radius of gyration, R_g and shape factor, R_g/R_h) on the nanogels. A single AF4 method was then used to fractionate the samples and this revealed differences in the internal structures of the differently sized nanogels.

The PNIPAM nanogels were also synthesized by RAFT polymerization dispersion polymerisation in the presence of a degradable crosslinker. We analysed our nanogel samples by AF4 varying the fractionation conditions (crossflow and detector flow rate). The degradation rate were analysed also by AF4 technique. Our findings reveal interesting behaviour of nanogels under AF4 analysis conditions.

The AF4-MALS-DLS measurements also allowed for the analysis of anisotropic metallic particles with different shape and aspect ratio. Prior to this work, there have been very little research about directly investigating the shape and the size of particles and nanogels characterised by flow field fractionation techniques.

Contents

Abbreviations

AF4 - asymmetrical flow field flow fractionation

AFM – atomic force microscopy

BAC - N,N'bis(acryloyl)cystamine

BIS - *N*,*N*'-methylenebisacrylamide

CHPOA–PEGSH - crosslinked polysaccharide–polyethylene glycol hybrid nanogels

CMC – critical micelle concentration

CNTs – carbon nanotubes

CTA – chain transfer agent

CTA – chain transfer agent

CTAB - cetyl-trimethyl ammonium bromide

DCM – dichloromethane

DCX – docetaxel

DLS – dynamic light scattering

DMHA - N,O-dimethacryloylhydroxylamine

DOX – doxorubicin

DP – degree of polymerisation

DTT – dithiothreitol

ETPN - European Technology Platform on Nanomedicine

FDA – Food and Administration agency

FFF – field flow fractionation

GNRs - gold nanorods

GSH – glutathione

H_D – hydrodynamic diameter

HEMP - 2-(hydroxyethylthiocarbonothioylthio)-2-methylpropanoic acid

HLB - hydrophilic-lipophilic balance

HPLC - High Performance Liquid Chromatography

ICP-MS - inductively coupled plasma mass spectrometry

ISFI – in situ forming implants

KPS, $K_2S_2O_8$ – potassium persulphate

LCST – lower critical solution temperature

MALS - multi angle light scattering detector

M_n - Number average molecular weight

MWNT – multiwalled carbon nanotubes

NMR – nuclear magnetic resonance

PBS - phosphate buffer saline

PCL - poly(Ɛ-caprolactone)

PdI – polydispersity index

PDMA - poly(N,N-dimethylacrylamide)

PGA - poly(glycerol adipate)

PLGA- poly(lactide-co-glycolide)

PNIPAM - poly(N-isopropylacrylamide)

polyHEMA - poly(2-hydroxyethyl methacrylate

PVA - poly(vinyl alcohol)

QELS - quasi-elastic light scattering

RAFT - reversible addition−fragmentation chain transfer polymerisation

R_g - radius of gyration

R_h – hydrodynamic radius

RI – refractive index

SAXS - Small angle X-ray scattering

SDS - sodium dodecyl sulphate

SEC – size exclusion chromatography

SEM – scanning electron microscopy

SI – supporting information

SWNT – single walled carbon nanotubes

TEM - Transmission electron microscopy

T_g - Glass Transition Temperature

TGA - Thermo-gravimetric analysis

UV-VIS - Ultraviolet–visible spectroscopy

VPTT – volume phase transition temperature

ρ – shape factor

Presentation and Publications

Publications included in the thesis:

Niezabitowska, E., Smith, J., Prestly, M. R., Akhtar, R., von Aulock, F. W., Lavallee, Y., Ali-Boucetta H., McDonald, T. O. (2018). Facile production of nanocomposites of carbon nanotubes and polycaprolactone with high aspect ratios with potential applications in drug delivery. RSC ADVANCES, 8(30), 16444-16454. doi:10.1039/c7ra13553j

Publications not included in the thesis:

Town, A., **Niezabitowska, E.,** Kavanagh, J., Barrow, M., Kearns, V. R., Garcia-Tunon, E., & McDonald, T. O. (2019). Understanding the Phase and Morphological Behavior of Dispersions of Synergistic Dual-Stimuli-Responsive Poly(N-isopropylacrylamide) Nanogels. JOURNAL OF PHYSICAL CHEMISTRY B, 123(29), 6303-6313. doi:10.1021/acs.jpcb.9b04051

Town, A. R., Taylor, J., Dawson, K., **Niezabitowska, E.,** Elbaz, N. M., Corker, A., McDonald, T. O. (2019). Tuning HIV drug release from a nanogel-based in situ forming implant by changing nanogel size. JOURNAL OF MATERIALS CHEMISTRY B, 7(3), 373-383. doi:10.1039/c8tb01597j

Oral Presentations:

The Department of Chemistry: Postgraduate Symposium Day; University of Liverpool, 2019

19th International Symposium on Field- and Flow-based Separations (FFF2018); Columbia, USA, 2018.

Poster Presentations:

European Polymer Congress, Crete, 2019

Young Researchers Meeting, Macro Group UK, Edinburgh, 2017

European Nanomedicine Meeting British Society for Nanomedicine, London, 2017

Young Researchers Meeting British Society for Nanomedicine, Swansea, 2016

Chapter 1

Introduction

1.1. Nanomedicine

The interest of nanotechnology has grown over the past 30 years amongst scientists and researchers. Nanotechnology is now showing benefits in everyday life,[1] with new materials being made available that could revolutionize many areas of manufacturing. One example is the advances it has brought to electronic products, procedures and applications.[2] A number of definitions exist related to 'nano' products, the most established is that of IUPAC (International Union of Pure and Applied Chemistry) stating that nanoparticles are particles of any shape with an equivalent diameter from 1 nm and 100 nm.[3] Thus, nanotechnology is connected with the unique physical and chemical properties observed for particles in this size range.[4,5] The key aspects of nanotechnology can be listed as follows: controlling of matter at the atomic range, studying the unique physical and chemical properties of nanomaterials and the synthesis of complex systems with novel properties.[4] These benefits have been explored in medicine field known as nanomedicine. The first clinical example of a nanomedicine, doxorubicin containing liposomes helped to expand the interest of the global market in this field.[6] Interestingly, the definition of nanomedicine is not globally agreed with at least two widely used definitions existing at present. The National Institute of Health has defined nanomedicine as '*an offshoot of nanotechnology, [which] refers to highly specific medical interventions at the molecular scale for curing disease or repairing damaged tissues, such as bone, muscle, or nerve*'.[7,8] Another definition of nanomedicine, that does not directly map onto the IUPAC definition of nanomaterials has been proposed by European Technology Platform on Nanomedicine (ETPN) stating that "*Nanomedicine is the application of nanotechnology to health. It exploits the improved and often novel physical, chemical, and biological properties of materials at the nanometric scale".*[9,10] Nanomedicine may be divided into five main sub-classes: analytical tools, nanoimaging, nanomaterials and nanodevices, novel therapeutics and drug delivery systems; for clinical, regulatory and toxicological issues.[8] The most popular applications of this field of research are a generation of nanoscale materials for drug delivery systems, with particularly successful examples within anticancer

therapeutics,[11,12] disease markers and several other therapeutic systems.[13–15] Therapeutic systems, refer to a process or method that allows for introduction of active pharmaceutical compounds in human or animals and help to achieve therapeutic effect.[16,17] An ideal drug delivery system should deliver the therapy only to the targeted tissue or cell, be biocompatible, cause minimal side effects and reduce toxicity of medicines.[18] To achieve this the drug delivery system should: 1) keep the drug concentration in the therapeutic window, 2) localise the therapeutic to the desired site of action to reduce the side effects, 3) have the ability to degrade or be cleared after administration and 4) improve medical adherence.[19,20] Regulatory considerations are critical in the development of new therapeutic system and it is important to note that the Food and Administration agency (FDA) does not provide definitions of nanomaterial or nanotechnology.[21] During the regulation of nano-products, FDA considers following properties: "(1) whether a material or end product is engineered to have at least one external dimension, or an internal or surface structure, in the nanoscale range (around 1 nm to 100 nm); and (2) whether a material or end product is engineered to exhibit properties or phenomena, including physical or chemical properties or biological effects, that are attributable to its dimension(s), even if these dimensions fall outside the nanoscale range, up to one micrometer (1,000 nm)".[21,22] This thesis will therefore define nanomedicine as the application of materials at the nanometric scale (1-1000 nm) for healthcare applications.

The design of nanomedicines is heavily influenced by the route of administration of which there are two most common route: *parenteral route* (through the skin by injection, avoiding the digestive system) and the *enteral route* (directly at some point of the gastrointestinal tract). Less local way of drug administration can be pulmonary (or respiratory), nasal, ophthalmic or vaginal. [23] Nanoparticles are currently widely investigated as drug delivery systems across all routes of administration and some systems have been approved for clinical use.[24–26] Well-known examples of nanocarriers used as a drug delivery systems are: polymers and polymeric nanoparticles,[13,27] dendrimers, magnetic nanoparticles[28], liposomes[29] and solid lipid nanoparticles[30,31] (see Figure 1.1).[32] Examples of these different nanoparticle drug delivery systems will be discussed in the following sections.

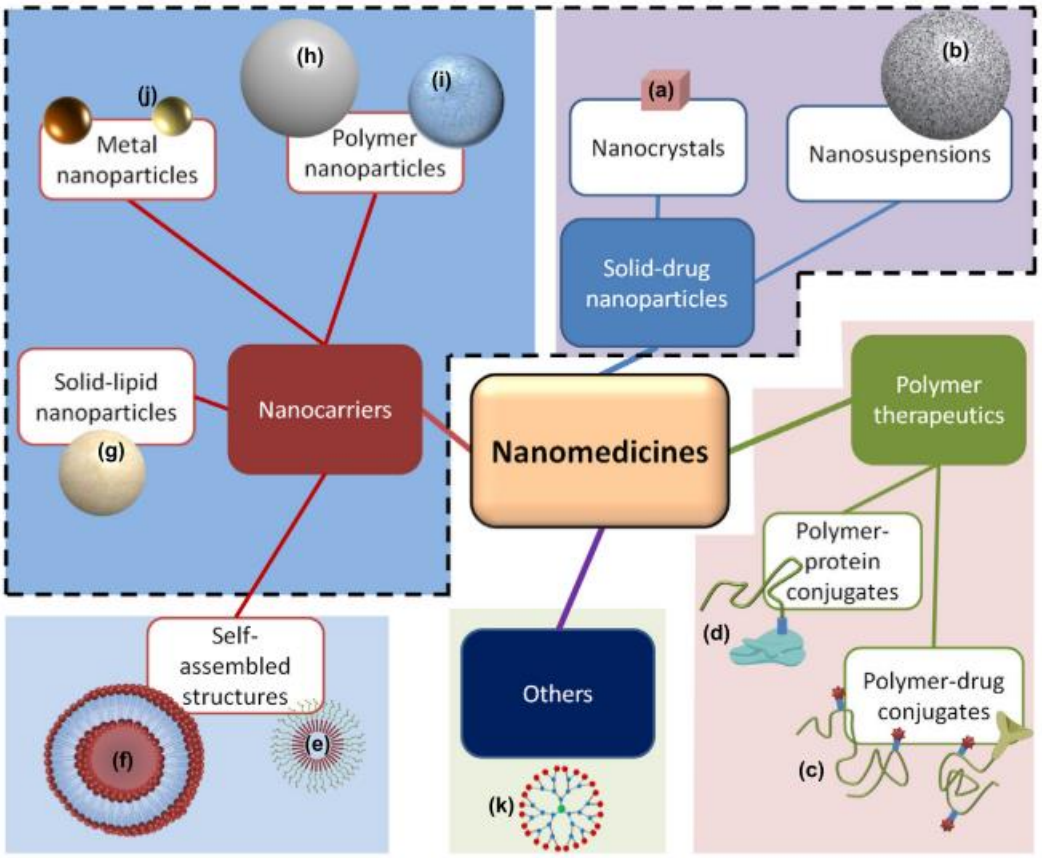

Figure 1.1. Schematic representation of different categories and subcategories of nanomedicines for drug delivery. The structures of the nanomedicines shown are: (a), nanocrystal; (b), nanosuspension; (c), polymer drug conjugate; (d), polymer protein conjugate; (e), polymer micelle; (f), liposome; (g), solid lipid nanoparticle; (h), solid polymer nanoparticle; (i), nanogel; (j), gold nanoparticles; (k), dendrimer.[10]

Reprinted from *Nanoengineering Global approaches to Health and Safety Issues*, 2015, T. O. McDonald, M. Siccardi, D. Moss, N. J. Liptrott, M. Gardiello, S. P. Rannard and A. Owen, The Application of Nanotechnology to Drug Delivery in Medicine, 173-223, Copyright (2015), with permission from Elsevier.

It is also possible to categorise nanoparticles as either 'hard nanoparticles' which keep their original shape and size during different processes and 'soft nanoparticles', made from material which can change size or shape when facing different biological conditions such as pressure, pH or ionic strength.[33] The examples of hard nanoparticles and their application, which can be used in nanomedicine field are: silica nanoparticles (photodynamic therapy for treating cancer breast cells)[34], gold nanoparticles (carrier and adjuvant for vaccines)[35], quantum dots (sensor for the

detection of the CA-125 serum biomarker in patients with ovarian cancer)[36]and magnetic nanoparticles (detecting foodborne pathogens such as Salmonella enterica)[37]. The soft nanoparticles used for drug delivery systems include biodegradable polymers[38], non-biodegradable polymers[39], liposomes[40], micelles[41], lipid nanoparticles[42] or micro and nanogels[43].

The theory of colloidal stabilisation for drug delivery systems are discussed in next subsection 1.2. Colloidal stability.

1.2. Colloidal stability

Understanding colloidal stability is critical to the design of viable nanomedicines. Colloidal systems typically possess both attractive and repulsive interactions. If the attractive forces between particles are greater than the forces dispersing the particles (repulsive) then aggregation can occur. Aggregation can be divided into coagulation (irreversible aggregation of particles), flocculation (weaker, often reversible aggregation) and coalescence (merging of droplets or bubbles). To prevent aggregation, the repulsive forces must be stronger that the attractive interactions. Repulsive interactions arise from steric stabilisation and/or electrostatic repulsion. Steric stabilisation can be obtained by the presence of solvated polymer chains on a particle, which can be either physically adsorbed or covalently bonded solvated polymers. When two particles with surface coating of solvated polymers approach one another eventually the polymer chains on the neighbouring particles will begin in interpenetration. If ΔG_{mix} for polymer chain interpenetration is negative, then there will be the overlap of the adsorbed layers, will result in flocculation or coagulation. Therefore, in order to achieve effective steric stabilisation this polymer mixing should be unfavourable (ΔG_{mix} should be positive). To do this, a number of conditions need to be required: high surface coverage, thick polymer layer, strong adsorption, good solvent for stabilising chain and low free polymer concentration. The second type of repulsive attraction is electrostatic repulsion. Particles often have a surface charge, derived from surface functional groups or adsorbed ionic surfactant molecules, which lead to repel each other. Electrostatic repulsion occurs as a result

of an electric double layer (see Figure 1.2) consisting a surface charge compensated by an unequal distribution of counter- and co-ions.[44]

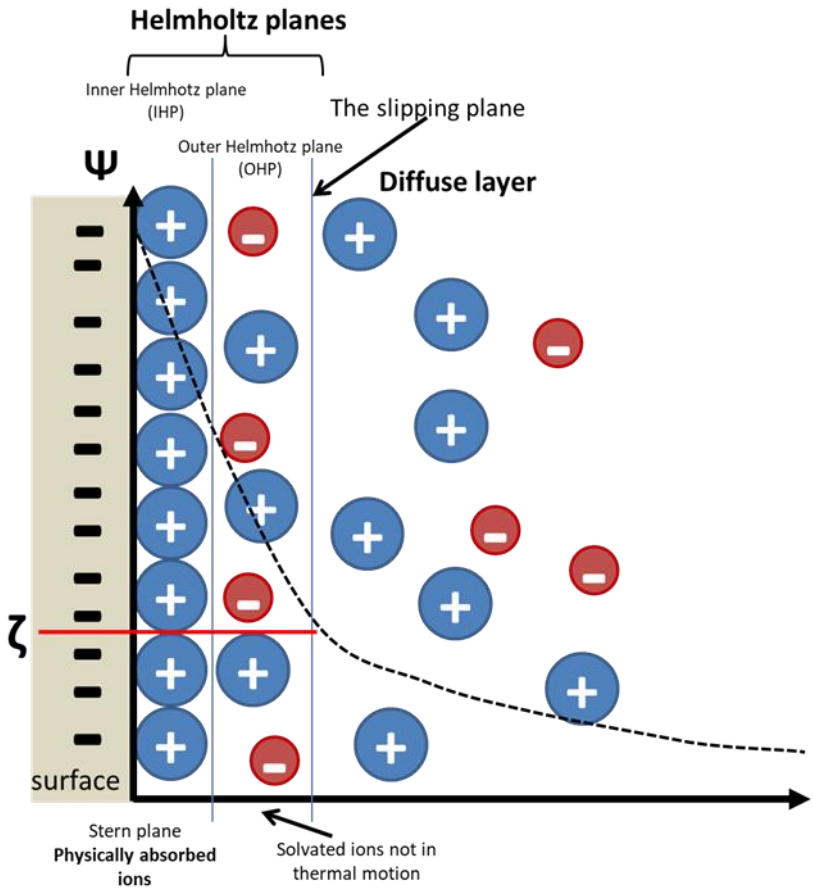

Figure 1.2. Stern-Grahame Model of the double Layer.

An important measure of the surface charge and thus an indicator of electrostatic stability is the zeta potential, (ζ) which is difference in the potential between the bulk and the stationary layer around the particle. Zeta potential is typically measured in mV. A higher zeta potential will mean that there is stronger electrostatic repulsion between the particles. Provides a higher energy barrier for aggregation to occur. The opportunities to further improve the drug delivery and colloids for potential of nanomedicines has led to further research into the effect of shape on biological behaviour and the use of responsive systems. The following two sections will discuss the literature on these topics.

1.3 Non-spherical carriers for therapeutic compounds

The majority of drug delivery systems are spherical, due to the sphere being energetically favoured due to its lowest surface area to volume ratio for a volume. Spherical drug delivery systems have established clinical benefits. For example, liposomes have been used clinically since 1995 and have been shown to provide improved bioavailability, limited toxicity and control over pharmacokinetics.[45] Polymer nanoparticles such as those made of poly(lactide-co-glycolide) (PLGA) or solid lipid nanoparticles have been used as drug delivery systems in chemotherapy of tuberculosis have shown benefits in the reduction of the dosing frequency of drug, feasibility of the versatile routes of drug administration and high stability of nanoparticles.[46] However, in recent research, there is growing understanding that a shape plays a key role in the biological behaviour of nanomedicines and control of shape might allow further benefits.[47–50] For example, it has been shown that size and shape of particles influence the therapeutic effect, with the shape influencing the physical properties of the nanomedicine such as drug loading efficiency, drug release rate.[51,52]. For example, Cai *et al.* showed that polyethylene glycol-polycaprolactone worm-like micelles could be loaded with two-fold higher anticancer drug paclitaxel compared to spherical ones.[53] Yang *et al.* presented a study where a cross-linked worm-like vesicle had a slower drug release rate than a non-cross-linked one. [54] The size and shape have also been shown to influence biological behaviour such as targeting efficiency.[55] Some of this behaviour may be linked to the understanding that shape and size of nanoparticles plays a crucial role in phagocytosis,[56] the process by which a cell absorbs solid particle and in the process forms an internal component known as a phagosome.[57] Studies have shown that particles with very high aspect ratio of size have decreased phagocytosis.[56,58] From therapeutic perspective, reducing phagocytosis can increase time for drug release. Moreover, there is a hypothesis that the rate of phagocytosis for a particle of desired geometry can be organ dependent, with different organs taking up shapes in different ways.[59] Ellipsoidal particles has been found to show better adhesion to aortae than spherical micro or nanoparticles when tested *in vivo*.[50,60] Geng *et al*. have shown that the shape of particles has effect on biodistribution.[61] Elongated polymer

micelle assemblies described as filomicelles with a diameter 18 μm showed half-lives ~5 days, which was 3 days longer compared with stealth spherical liposomes.[61] Muro *et al.* have shown that the elliptical disks with high surface-area-to-volume ratio obtained higher targeting specify for endothelial cells compared with spheres due to improved interaction.[62] In a separate study, it was reported that rods targeted to ovalbumin, with two times more specific binding interactions than ovalbumin targeted spheres.[63]

There are two approaches to synthesise nanomaterials, including non-spherical particles: "top-down" and "bottom-up". The most popular top down method for preparation of ellipsoidal particles is film stretching. Ho *et al.* prepared ellipsoidal polystyrene particles by embedding the particles in polyvinyl alcohol film.[64] This matrix was then stretched using different forces at 200 °C. This temperature was chosen as it was above the T_g of polystyrene. The particles were then recovered by dissolving the film and were found to have ellipsoidal shapes with different aspect ratios from 1.5 to 2.6.[64] The advantage of this method is the simplicity and speed to producing particles. An example of non-spherical polystyrene nanoparticles synthesised by stretching method was shown in Figure 1.3**.** [65]

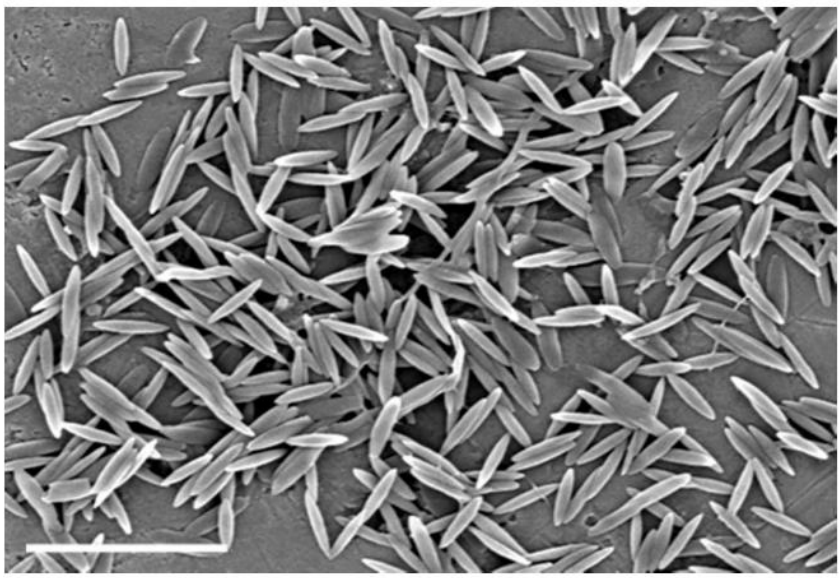

Figure 1.3. Polystyrene non-spherical particles obtained by stretching method. Scale bar 2 μm.[65] Copyright (2007) National Academy of Sciences, U.S.A.

Another example of bottom-up synthesis of non-spherical particles is seed-meditated growth method, which is the most popular way of preparing gold nanorods (GNRs).[66] This synthetic method was first introduced by Jana *et al*. in 2001.[67] Firstly, a seed solution was prepared by the reduction of gold salt $HAuCl_4$ with $NaBH_4$ in the presence of sodium citrate. The resulting citrate-capped gold nanoseeds with diameter 3-4 nm were then added to a growth solution of $HAuCl_4$, cetyl-trimethyl ammonium bromide (CTAB, as the template), $AgNO_3$ (for shape induction) and ascorbic acid (as the reducing agent). This strategy allowed for production of GNRs, different aspect ratios were synthesised by changing the volumes of seed solution in the sample. An advantage of gold nanorods over spherical gold nanoparticles was demonstrated in the application of photothermal-triggered therapy. The photothermal absorption efficiency for the gold nanorod particles increased by tenfold compared with spherical gold nanoparticles which led to improvement of therapeutic efficiency.[59,68]

1.3.1. Carbon nanotubes

Carbon nanotubes (CNTs) are a type of high aspect ratio nanomaterial that possess a range of interesting properties including their fibre structure, large surface area and high mechanical stiffness. These properties have led to CNTs being investigated as drug delivery systems. CNTs have shown benefits in DNA delivery[69], use as cancer theranostics[70], small molecule drug delivery[71] and regenerative medicine.[72] CNTs can be classified by their structure into: single-walled (SWNT) and multi-walled (MWNT) carbon nanotubes (see Figure 1.4).

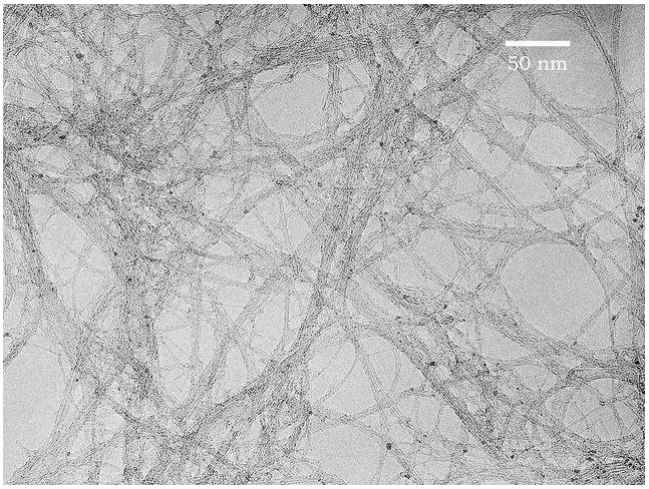

Figure 1.4. TEM images of single walled carbon nanotubes and multiwalled carbon nanotubes.[73] Reproduced with permission of the Wiley.

CNTs can be covalently modified with drug molecules, or they can physically adsorb aromatic drugs via the strong π-π and hydrophobic interactions between the drug and the aromatic surface of the CNT.[71] Such physical adsorption of drugs has been exploited for loading anthracyclines, a class of anticancer drug.[71] However, in spite of their drug loading potential, the inherently hydrophobic nature of CNTs can limit their application in aqueous environments. As such, surface modification and coating is often utilised to improve the colloidal stability of CNTs.[74] Polymers are typically used for surface modification and these have been grafted to the surfaces of CNTs by amidation, radical coupling, esterification and other reactions.[75] Alternatively, grafting from the surface of CNTs by anionic/cationic polymerizations or atom transfer radical polymerization has also been used.[76,77] Khoee *et al*.[78] demonstrated the ability to carry out surface modification of carbon nanotubes by using thermo and reduction-responsive polymers as poly(N-isopropylacrylamide) (PNIPAM) and poly(2-hydroxyethyl methacrylate) (polyHEMA) with the degradable crosslinking agent N,N'-bis(methacryloyl)-L-cystine (SS). The nanoparticles of poly(NIPAM-HEMA-SS)/MWCNT were used as carriers for doxorubicin (DOX), which is commonly used as an anticancer therapeutic. The research showed that the greater release of DOX occurred in the presence of dithiothreitol (DTT) at higher temperature than at physiological temperature (37 ˚C) within the absence of DTT. The *in vitro* cytotoxicity

studies showed that the poly(NIPAM-HEMA-SS)/MN-MWCNTs were biocompatible with blood and no toxicity was seen in the liver or kidneys of mice.

Complexes of CNTs/DOX showed increased cell death for human cancer breast cells (MCF7) treated with the compared to application of DOX alone.[79] Moreover, many tests *in vitro* and *in vivo* showed that functionalized CNTs are compatible with biological media.[79–81] The cytotoxicity and biocompatibility of CNTs has been shown to be dependent on many factors such as the route of administration, the size and type of the CNTs (MWNT or SWNT) and presence of any surface modification;[82,83] generally higher surface functionalisation of CNTs reduced cytotoxicity.[84]

The other example of material which possess interesting properties and it showed potential as drug delivery systems are poly(N-isopropylacrylamide) polymers and nanogels.[85,86] In next subsection (1.3), there is more information about poly(N-isopropylacrylamide) nanocarriers.

1.3. Poly(N-isopropylacrylamide) nanogels

In addition to shape, the ability to respond to an external stimulus or multiple stimuli provides the opportunity to achieve highly targeted drug release. Thermoresponsive behaviour is an example of this and it provides the opportunity to use temperature changes as a stimulus to trigger drug release. Thermoresponsive polymers exhibit either a lower critical solubility temperature (LCST) and an upper critical solubility temperature (UCST) in aqueous medium.[87] The LCST is the temperature when the polymer is soluble below a critical temperature, and insoluble above. For UCST polymer, it is the opposite – polymer is soluble above a critical temperature. The LCST/UCST temperature of the solution provides information if a polymer chains interact more with another polymer chain or with the surrounding solvent. In the case where polymer-polymer interactions prevail, the polymer chains tend to associate together and eventually phase separate out from the solution, thus leading to a turbid suspension. [88] For UCST polymers, the polymer chains are well solubilised above the UCST. They maintain a high affinity with the surrounding medium and the

solution is transparent.[89] An example of phase diagram for thermoresponsive polymers is presented on Figure 1.5.

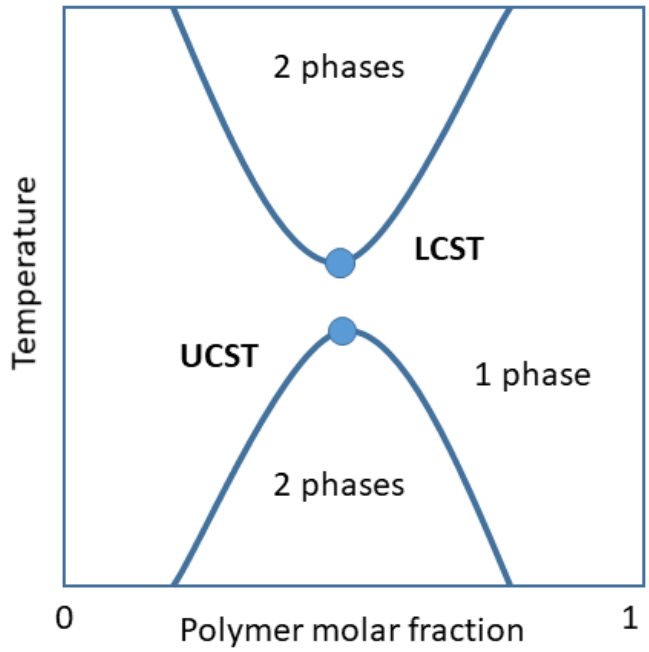

Figure 1.5 Simplified phase diagrams of thermoresponsive polymers. Outside the region delimited by the binodal curve, there is a homogeneous solution of solubilized polymer in aqueous solution (1 phase). Inside the region, the solution is not stable anymore and the polymer phases out (2 phases).

A common type of thermoresponsive nanoparticle is nanogels. Nanogels are nanoscale, three-dimensional hydrogel particles, made of cross linked polymer chains that swell in a good solvent such as water.[90] Hydrogels or nanogels can be prepared by physical or chemical crosslinking and are used widely in biomedical applications. The interactions in physically crosslinked nanogels are intermolecular reversible interactions such as electrostatic,[91] hydrophobic/hydrophilic,[92,93] crystallisation/stereocomplex formation,[94] metal coordination,[95] π–π stacking[96] and hydrogen bonding between polymer chains.[97–100] The network gel prepared by physical crosslinking is usually reversible and is attractive is cases where crosslinking is undertaken within biological systems (such as cell scaffolds or *in situ* gelling systems). The absence of chemical crosslinking agents avoid potential cytotoxicity from unreacted chemical crosslinkers.[100,101] Up to now, some chemical crosslinking methods were reported such as free radical polymerization induced crosslink,[102]

enzymatic induced crosslink,[95] Diels–Alder "click" reaction,[44] Schiff base formation,[103] oxime formation,[104] Michael type-addition[105] and photopolymerisation.[106] Chemically cross-linked hydrogels allows absorption of water and/or bioactive compounds without dissolution and permits drug release by diffusion[98,107] and it also shows high stability under physiological conditions.[100]

A popular example of a thermoresponsive nanogel, based on a chemically crosslinked network is made from poly(N-isopropylacrylamide) (PNIPAM) (see structure in Figure 1.6).

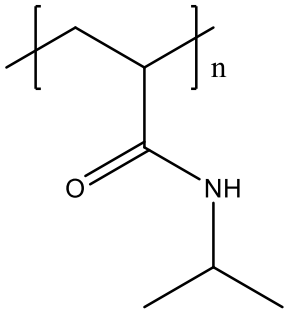

Figure 1.6. Chemical structure of poly(N-isopropylacrylamide) (PNIPAM)

PNIPAM nanogels have shown potential as drug carriers, biosensors and for applications in enzyme encapsulation.[108,109] PNIPAM nanogels are sensitive to the temperature, showing de-swell response for volume phase transition temperature (VPTT).[110] The VPTT can be explained as briefly as a temperature at which the behaviour of the nanogel is altered as a result of its intramolecular interactions. Below the VPTT, the nanogels are hydrophilic due to the favourable hydrogen bonding between the amide group and water. Above the VPTT, the particles de-swell, expel solvent and decrease size as a result of the polymer-polymer hydrogen bonding becoming more favourable (see Figure 1.7). The VPTT for PNIPAM nanogels is around 34°C, depending on factors such as the crosslinker structure and crosslinking density. Leobandung *et al.*[111] synthesised PNIPAM nanogels with the presence of poly(ethylene glycol) 1000 methacrylate as the comonomer and poly(ethylene glycol) 400 dimethacrylate as crosslinker. Insulin was encapsulated into microgels and

stability of insulin was studied. The *in vitro* data showed that drug delivery system can protect insulin from denaturation, which makes them good carrier for insulin.

PNIPAM nanogels can also display dual responsive behaviour in which they undergo a different transition in the presence of two stimuli simultaneously (see Figure 1.7). Typically, the PNIPAM nanogels possess steric and electrostatic stabilisation. The electrostatic repulsion between nanogels provides colloidal stability even above the VPTT. However, in the presence of the salt like PBS, the charges are screened and flocculation occurs.[112] This transition behaviour can be used as an advantage for forming *in situ* implants upon injection into the body, where the nanogels are at body temperature (above the VPTT) and in the presence of salt.[112]

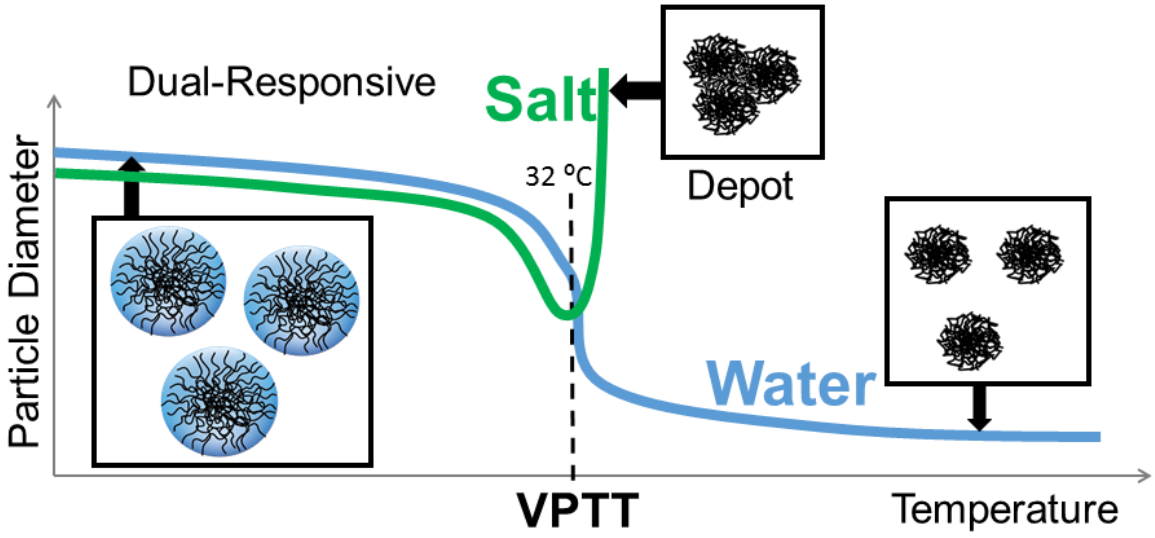

Figure 1.7. Dual responsive behaviour of PNIPAM nanogels. [113] **The nanogels in the water medium near the VPTT deswell and the diameter of nanogels decrease. In the presence of salt, PNIPAM nanogels form a depot near the VPTT.**

A disadvantage of PNIPAM nanogels in drug delivery applications is their non-degradable nature. PNIPAM nanogels are typically crosslinked using *N*,*N*'-methylenebisacrylamide (BIS) which provides no opportunity for degradation. One approach investigated to address this is by using N,N'bis(acryloyl)cystamine (BAC) as the crosslinker. This crosslinker introduces disulphide bonds between polymer chains which are degradable in the presence of reductant dithiothreitol (DTT) – a molecule that mimicks the role of glutathione (GSH) in the body.[114] The

mechanism of DTT in the cleavage of disulphide crosslinkers is given in Figure 1.8. This means that nanogels might be slowly degraded in an extracellular environment, to generate low molecular weight of polymers which can be easily removed from the body.

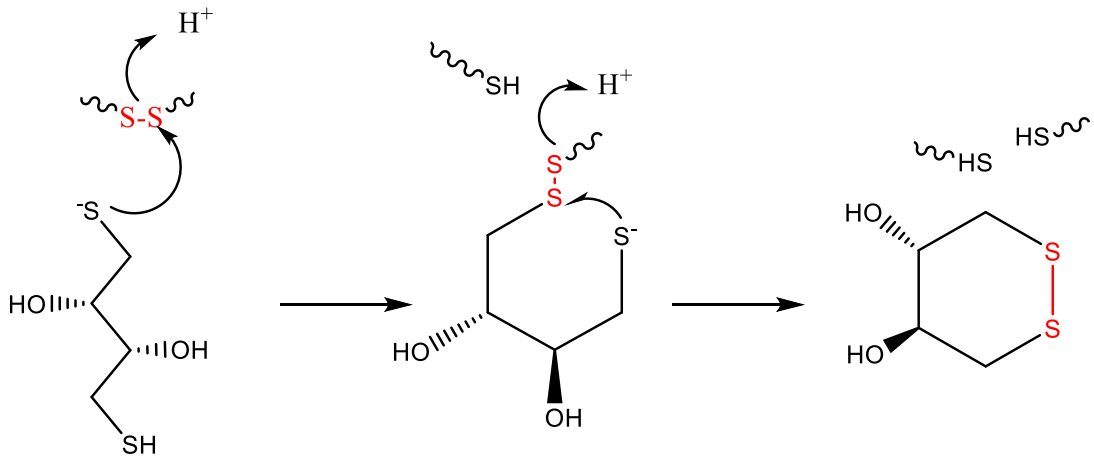

Figure 1.8. Disulphide Cleavage Mechanism by dithiothreitol (DTT)

PNIPAM nanogels are typically prepared using either precipitation or dispersion polymerisation.[115] These polymerisations can be by free radical polymerisations,[116] radiation induced[117] and reversible addition−fragmentation chain transfer (RAFT) polymerisation.[118] Precipitation/dispersion polymerisation and RAFT polymerisation were used to prepared PNIPAM nanogels during this research. Information about those types of polymerisation is covered in the following subsections.

1.4.1. Precipitation and dispersion polymerisation of NIPAM

Heterogeneous free-radical polymerisations are typically used to obtain PNIPAM cross-linked, non-soluble nanogels in water from water-soluble NIPAM monomers.[119] The most common types of heterogeneous free-radical polymerisations used for PNIPAM nanogels are precipitation or dispersion.[116] Precipitation polymerisation is a process where insoluble polymer is synthesised from a monomer that is soluble in the reaction medium (usually water). For this method an ionic initiator is commonly

used and at the start of the reaction all the compounds are soluble in the reaction solvent. However, the solvent is a poor solvent for the polymer. Upon initiation, the polymer chains grown in the medium and the hydrophilic initiator-containing chain ends concentrate at the surface of the particles, increasing surface charge density. The particle grows until the colloidal stability is achieved, thus creating polymeric particles. A scheme of precipitation polymerisation of PNIPAM is shown in Figure 1.9a.[120]

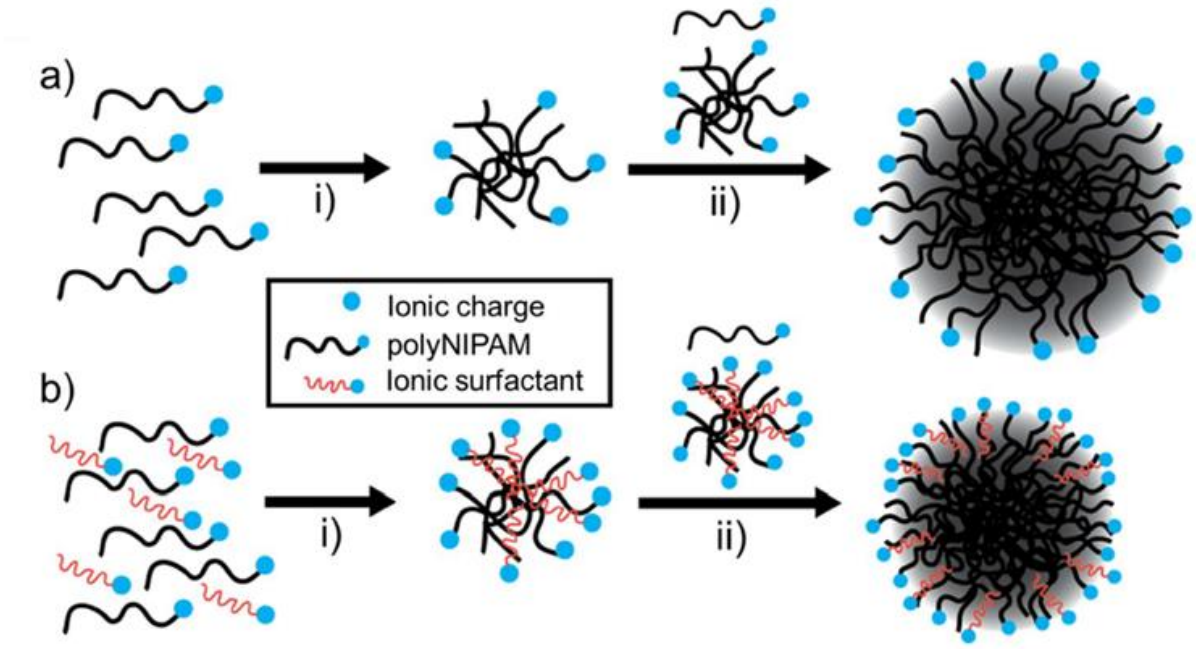

Figure 1.9. Schematic representation of a) precipitation and b) dispersion polymerisation to produce PNIPAM nanogels, i) formation of precursor particle and ii) coagulation of precursor particles and oligomers to colloidally stable particles.[113,121]

The crosslinker plays a crucial role for synthesis of homogeneous nanogels. For example, the concentration of crosslinker can control morphology, polydispersity or even gel properties like the equilibrium swelling of nanogel particles.[119,122] Senff *et al.*[123] showed that if the concentration of crosslinker was increased in the synthesis of PNIPAM nanogels then the polymerisation produced smaller diameter nanogels with the typical diameters of particles synthesised by precipitation polymerisation is in the range of 130 nm to 2.4 µm.[124] Dispersion polymerisation can be classified as a

sub-type of precipitation polymerisation that gives sub-micron monodisperse gels and particles. Dispersion polymerisation differs from precipitation in that it also uses a surfactant in the reaction media. This surfactant can be either provide stabilisation by steric and/or electrostatic means. A polymeric stabilizer may act as a steric stabilizer, forming barrier on the surface of polymer, leading the colloidal stability and the particle size. A common example of steric stabiliser used in dispersion polymerisation is poly(vinyl alcohol).[125] Electrostatic stabilisation can be obtained further the use of an ionic stabiliser. Pelton *et al*. showed that higher concentrations of the electrostatic stabiliser, sodium dodecyl sulphate (SDS) decreased the size of PNIPAM nanogels.[126] These two types of colloidal stability play a key role in dispersion polymerisation by reducing the amount of precursor particles that must coagulate to reach a colloidal stable particles (Figure 1.9b).[127] The typical diameters of particles are in range 100 nm to 15 µm.[119,128] Many polymeric nanogel systems are fabricated by precipitation and dispersion polymerisation. [43,128–134]

1.5. Reversible addition-fragmentation chain transfer polymerisation (RAFT) of crosslinked particles and nanogels

A type of living polymerisation that has been gaining popularity in recent years is reversible addition−fragmentation chain transfer (RAFT) polymerisation.[135] RAFT polymerisation is based on a conventional radical polymerization which is mediated by a RAFT agent which is essentially a chain transfer agent (CTA) that fragments in presence of free radical from initiator. The general structure of RAFT agent is shown in Figure 1.10. The typical RAFT agent is a thiocarbonylthio compound [RSC(Z)=S]. They consist of an R group, a radical leaving group which is able to reinitiate polymerisation, a reactive C=S bond and a Z group which control C=S reactivity.

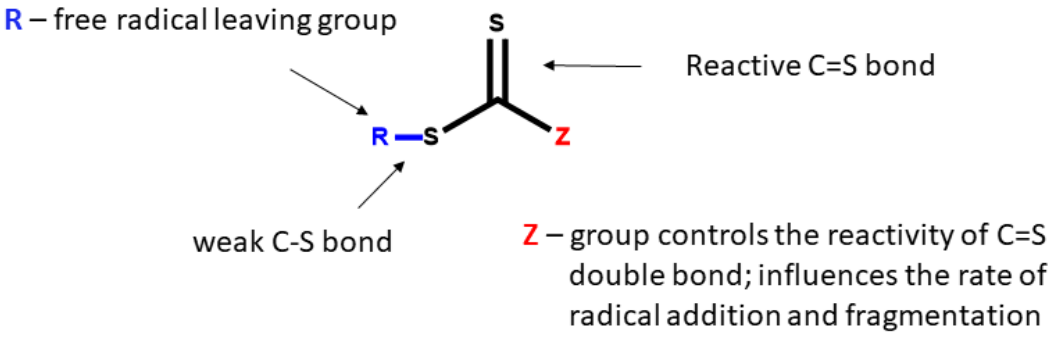

Figure 1.10. General structure of a RAFT agent.

There are several steps in a RAFT polymerization: initiation, pre-equilibrium, re-initiation, main equilibrium, propagation and termination. The mechanism of RAFT polymerisation is presented on Figure 1.11. The initiation step begins with the creation of radicals (I•), which react with a single monomer molecule to yield a propagating (i.e. growing) polymeric radical, denoted as P_n•. Further monomer molecules, M, are added to the radical molecules P_n• to form longer propagating radicals. In next step P_n• reacts with the RAFT agent to achieve equilibrium between active and dormant species. The addition of a propagating radical (P_n•) to the thiocarbonylthio compound [RSC(Z)=S (**4**)] leads to fragmentation of the intermediate radical. This may undergo a reversible fragmentation in which the intermediate RAFT adduct radical is capable of losing either the R group (R•) or the polymeric species (P_n•) (**1-3**). If a polymeric thiocarbonylthio compound [P_nSC(Z)=S (**6**)] and a new radical R• are formed, the reaction of this radical (R•) with the monomer induces a new propagating radical (P_m•). The quick equilibrium between the active propagating radicals (P_n• and P_m•) and the dormant polymeric thiocarbonylthio compounds (**6**) assure equal probability for narrow polydisperse polymers. The resulting polymers have well-defined length, molecular weight and low polydispersity (PdI < 1.15).[136,137] After the finishing of polymerisation, the majority of chains retains the thiocarbonylthio end group and can be isolated as stable materials.[135,136]

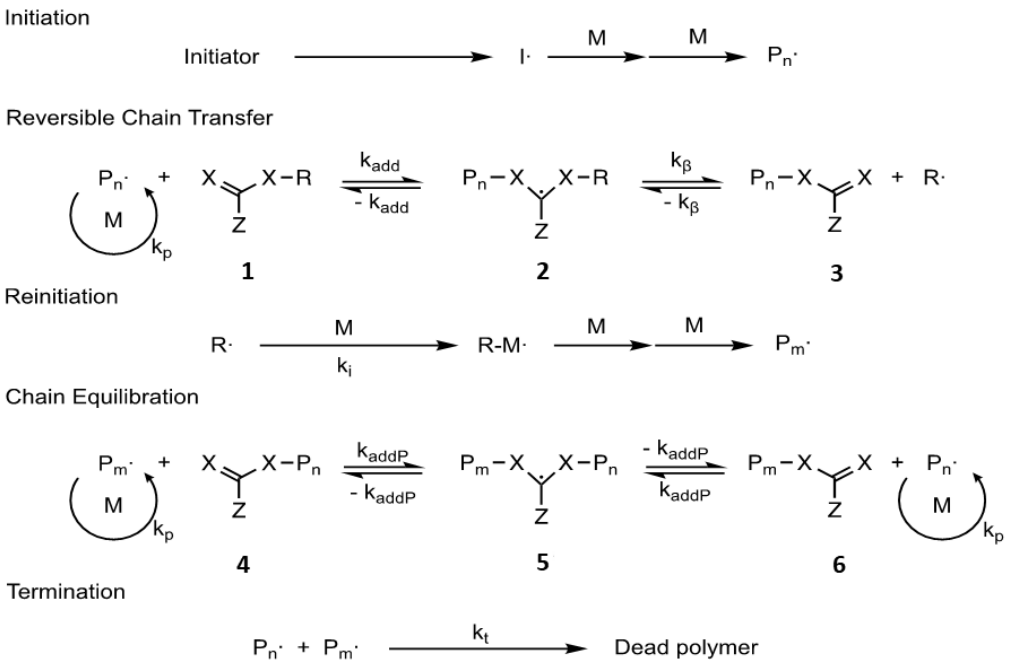

Figure 1.11. The mechanism of RAFT polymerisation.[135]

A RAFT agent needs to meet the following criteria to allow for achievement for an efficient, controlled polymerisation; it needs to have a reactive C=S double bond (high k_{add}) and a weak S-R bond for rapid fragmentation (high $k_{ß}$). The R group should be characterised as a good leaving group ($k_{ß} \geq k_{-add}$) and should re-initiate polymerisation. RAFT polymerisation can be performed in a range of solvents (organic and aqueous) and in the absence of metals. RAFT polymerisation has been used to synthesise different polymer architectures such as blocks, gradients, statistical, combs, brushes, stars, hyperbranched, and network copolymers.[138] It has shown also potential for synthesis of smart materials and biological application.[139]

To date, there are few articles on the synthesis of PNIPAM hydrogels by RAFT polymerisation. This was the main motivation to conduct the research which is described in Chapter 4 (The synthesis of degradable poly(N-isopropylacrylamide) nanogels by RAFT polymerisation).

Lu *et al*. demonstrated the synthesis of bulk PNIPAM hydrogels by RAFT polymerisation in the presence of crosslinker N,N-methylenebisacylamide (BIS), 4-cyanopentanoic acid dithiobenzoate as chain transfer agent (CTA) and 1,4-dioxane as solvent. The swelling property of PNIPAM hydrogels was tested showed that the presence of CTA may cause the acceleration of shrinking kinetics of PNIPAM hydrogels produced by RAFT polymerisation compared with PNIPAM hydrogels prepared by free radical polymerisation.[140] Xu *et al*. have shown the synthesis of PNIPAM nanogels by RAFT dispersion polymerization in cononsolvents water–ethanol (75 : 25, v:v) solution.[86] The RAFT dispersion polymerisation was conducted in the presence of poly(N,N-dimethylacrylamide) (PDMA) as the macro-molecular CTA, showing good control of molecular weight and polydispersity. The approach of polymerisation of NIPAM in the presence of N,N'-methylenebis(acrylamide) (BIS) was presented and PDMA-b-P(NIPAM-co-BIS) nanogels were successfully synthesised. Two macro RAFT agents with different DPs (PDMA64 and PDMA35) were used during the RAFT synthesis. The results showed that the length or molecular weight of macro-CTA had effect on the diameter and colloidal stability of nanogels.[141–143] Generally, it was shown that higher DPs of the PNIPAM block, higher molar ratios of [BIS]:[MacroCTA], and higher solid contents led to synthesis of defined nanogels using PDMA64 compared with PDMA35. The size of nanogels became smaller with increasing degree of polymerisation (DP). [141]

The study of copolymerisation of NIPAM and N,N'-bis(acryloyl)cystamine (BAC) by RAFT polymerisation was carried out by Sumerlin *et al.* [144] Their research showed that redox and thermoresponsive hyperbranched copolymers can be used to prepare core-crosslinked star copolymers by chain extension in N,N-dimethylacrylamide. The self-assembly of thermoresponsive copolymers was determined by DLS and turbidity measurements. Degradation studies were conducted in the presence of DTT in water at 25 °C and 45 °C for 5 h. To determine the degradation behaviour, the hydrodynamic diameter and the number average molecular weight (M_n) were analysed by DLS and SEC, respectively showing decreasing in size from 52 nm to 23 nm at 25 °C and 24 nm at 45 °C and M_n SEC decreased from 1 372 000 to 34 400 g/mol.

The approach of using RAFT polymerisation showed well controlled M_n of polymers, nanogel size and colloidal stability and it has potential to be used in the field of nanomedicine.

The effects of nanoscale drug delivery systems in living systems are complex, and in order to design successful nanomedicines it is crucial to understand the biological behaviour of a nanocarrier and the drug it is delivering. Therefore, the development within the field of nanomedicine also requires the improvement of the analytical tools for characterising nanoparticles in complex environments. For example, methods are required for separating and analysing single components from complex biological samples.[145–147] It is also critical to understand the chemical and physical properties of potential drug delivery systems.

1.6. Principles of asymmetric flow field flow fractionation (AF4)

In the field of nanoscience, it has become very important to obtain analytic techniques to provide high resolution characterisation of particles with nanoscale sizes. A promising approach is to fractionate nanoparticle distributions using field flow fractionation (FFF), a technique that allows the separation of molecules and colloids based on their diameter. Field flow fractionation was invented in 1966 by J. Calvin Giddings, but the first commercial use took place in 1987.[148] FFF techniques were classified as belonging to chromatography category where separation is based on hydrodynamic principles.[149] The most widely used is asymmetrical field flow field fractionation (AF4). The advantages of AF4 compared with other chromatographic techniques like size exclusion chromatography (SEC) can be for example: absence of stationary phase and minimisation of shearing forces,[150–152] no need for filtration in sample preparation,[149] the ability to undertake analysis of in complex mixtures, the ability to analysis sensitive and soft particles like proteins,[153] and the high resolution characterisation that the method provides. The separation of particles by AF4 take place in a narrow, ribbon and trapezoid channel. The typical dimension of channel are 50 cm in length, 2 cm in width and the channel height can

be between 50 and 500 µm. The scheme for separation of particles in the AF4 channel is presented in Figure 1.12.

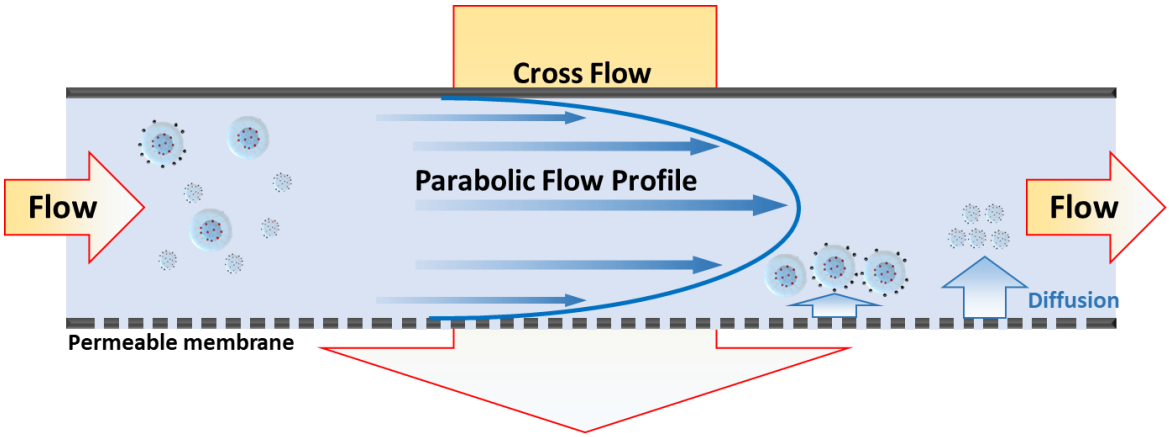

Figure 1.12. Schematic structure of AF4 channel illustrating the principle of hydrodynamic separation.

In the channel, there is a membrane acting as an accumulation wall which is supported by a porous plate. A spacer is used to determine the channel height and it is clamped between porous frit and the (typically transparent) impermeable wall. The simple construction of the channel and transparent wall allow for visual controlling of separation especially for colourful samples. Typically, molecules with sizes between 1 nm and 100 µm can be separated by AF4.[154] However, the lower size limit is determined by the size cut-off of the used membrane (typical 10 kDa) and the upper size limit is determined by the channel thickness.[148] The typical fractionation of injected sample in AF4 is as follows: an eluent is pumped from the inlet through the channel, creating a parabolic laminar Newtonian flow profile, moving the molecules towards the outlet.[145,149] The second, perpendicular flow of mobile phase called cross-flow is applied in order to fractionate and retain particles according to their different diffusion coefficients which is associated with the size of particles. In this way, components are split by their hydrodynamic volume, size, density and surface properties which are visible at different retention times.[155,156] The eluents shall be chosen to give the same electrical polarity between sample and the membrane. The repulsion between analyte and accumulation wall of membrane must be sufficient. Appropriate selection of the cross-flow is important, the cross-flow should be sufficient to fractionate particles but it also should not be too high

due to the possibility of accumulation of particles in the membrane wall. The combination of retention theory and Stokes−Einstein equation allow to define the hydrodynamic radius from AF4 theory and is shown in equation (1).[157]

$$R_h = \frac{t_R k_B T}{\pi \eta \omega^2 (F_x/F_{c)}} \qquad (1)$$

where k_B is the Boltzmann constant, t_R is retention time, T is the absolute temperature, η is the dynamic viscosity of the solvent, ω is the channel thickness, and F_x/F_c is the ratio of the cross-flow rate F_x to the channel flow rate F_c.

1.6.1. Different detector types for AF4

Early systems used the retention time to calculate the particle sizes. However nowadays, AF4 systems are typically coupled to a range of different detectors so the retention time is now rarely used to determine sample diameter. Commonly used detectors include multi angle light scattering detector (MALS), dynamic light scattering (DLS), refractive index (RI) detectors, UV-VIS detectors, inductively coupled plasma mass spectrometry (ICP-MS) etc. to obtain the desired information about molecules. [158]

MALS is one of the most widely used with the AF4 technique. MALS is based on static light scattering and determines the scattered light intensity as a function of the scattering angle. By using photo-detectors around the flow-cell in a multi-angle geometry, measurements can be performed over a broad range of angles, the schematic of MALS detector is shown in Figure 1.13. MALS measures the scattered light intensity at many angles then extrapolates back to 0˚, giving molecular weight and radius of gyration (R_g) for all sizes of molecules.

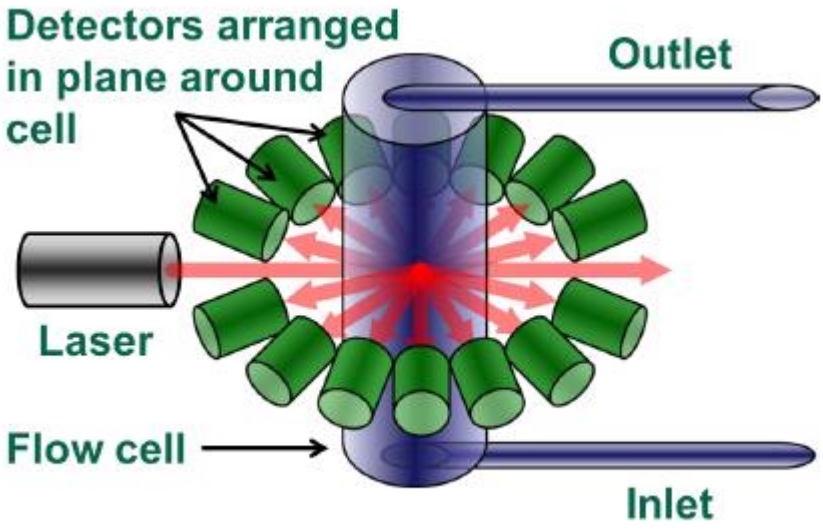

Figure 1.13. Schematic of MALS detector.[159] The figure shows inlet and outlet, flow cell, laser and detectors located around the flow cell.

The R_g is defined as is the distance from the centre of mass of an object at which the whole mass could be concentrated without changing its moment of rotational inertia about an axis through the centre of mass.[160] To understand more about R_g, some more information about light scattering theory will now be discussed. The relationship between the intensity of scattered light by sample and its molar weight and size was described in Rayleigh theory in 1948:

$$\frac{KC}{R_\theta} = \left(\frac{1}{M_W} + 2A_2C\right)\frac{1}{P_\theta}$$

Where: C the sample concentration, Θ the measurement angle, R_θ the Rayleigh ratio (the ratio of scattered light intensity to incident light intensity) at the measurement angle Θ, M_W molecular weight, A_2 the second virial coefficient.

K is a constant and along with P_θ (the particle scattering factor) are more complex terms and there are defined as:

$$K = \frac{4\pi^2}{N_A \lambda_0^4} (n_0 \frac{dn}{dc})^2$$

Where : λ_0 the wavelength of laser in vacuum; N_A Avogadro's number, n_0 is the refractive index of the solvent, dn/dc which is a measure of the difference in refractive index between sample and the solvent.

$$\frac{1}{P_\theta} = 1 + \frac{16\pi^2 n_0 R_g^2}{3\lambda_0^2} sin^2(\frac{\theta}{2})$$

Where: n_0 the refractive index of the solvent, R_g the sample's radius of gyration, λ_0^2 the wavelength of the laser in a vacuum, Θ measured angle

When an object is small compared to the wavelength of light (size less than <1/20th of laser wavelength) as in Figure 1.14A, the light is scattered with even intensively all directions. Such objects are therefore isotropic scatterers. The second type of scatterer is called anisotropic and it refers larger molecules, i.e. size of particles is more than >1/20th of the laser wavelength. In large molecules, the light is scattered by different mass cores within the molecule.

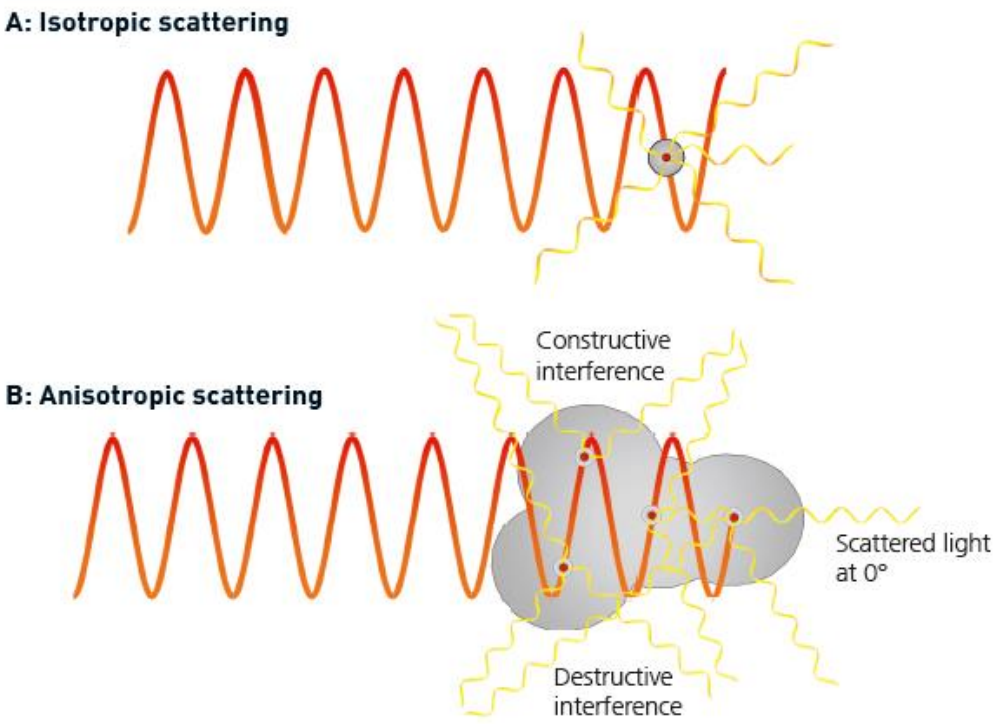

Figure 1.14. A. An isotropic scatterer is small relative to the wavelength of the light and scatters light evenly in all directions. B. An anisotropic scatterer has significant size compared with the wavelength of the incident light and scatters light in different directions with different intensities. [159]

By plotting $\frac{Kc}{R_\theta}$ as a function of $sin^2(\frac{\theta}{2})$ for larger molecules, the change in scattering intensity with angle can be visible and $1/M_w$ can be calculated from $\frac{Kc}{R_\theta}$ at the intercept (see Figure 1.15).[161,162] From the initial slope of the line, the R_g can also be calculated. Unfortunately, at small molecular sizes (<1/20th of the laser wavelength; <10-15 nm radius), the slope will be very small and the noise may hide the data. The most important factor for making measurements using MALS is the form of the extrapolation. It is extremely important that a MALS instrument should have as many low angles as possible as this will provide the most accurate extrapolation back to 0°. Generally, in order to maximise the accuracy of the extrapolation, having more angles is beneficial. The intercept of the line is $1/M_w$ and the initial slope of the line is related to R_g as shown in Figure 1.15.

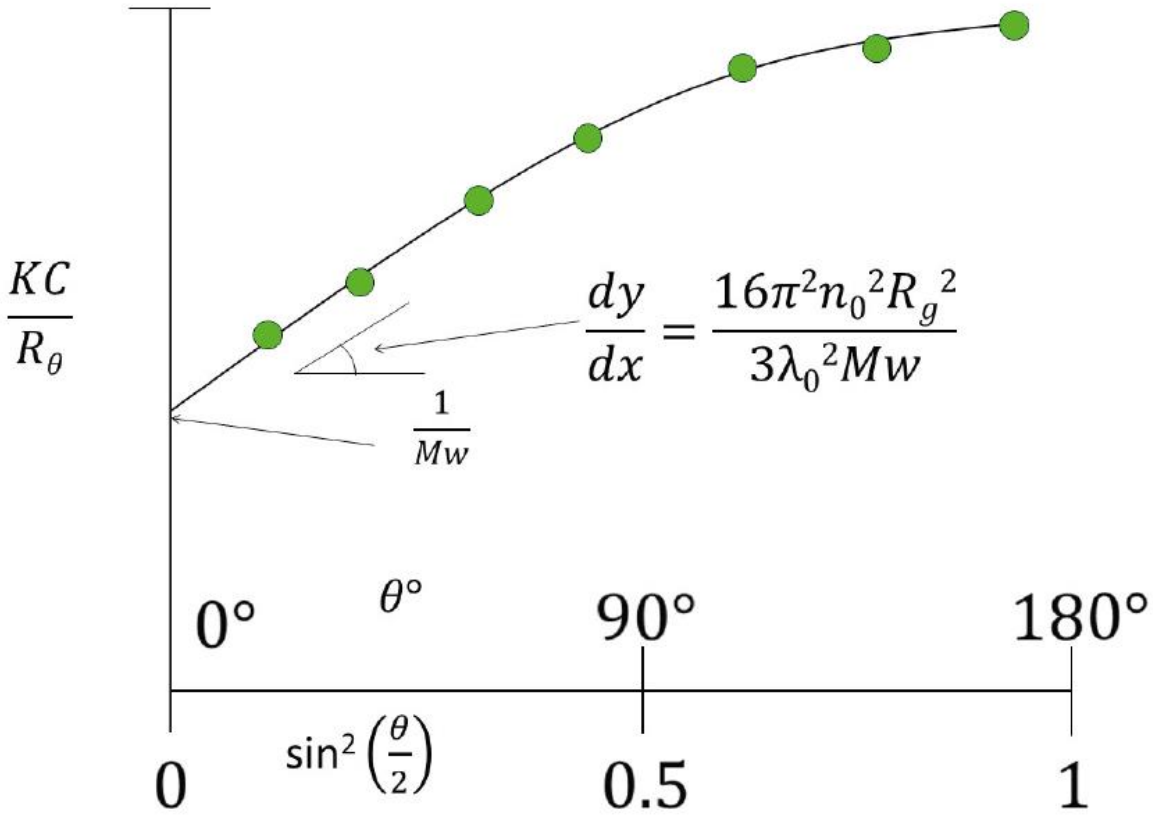

Figure 1.15. A Guinnier plot shows KC/R_Θ as a function of $\sin^2(\Theta/2)$. The intercept of the line is $1/M_w$ and the initial slope of the line is related to R_g.[159]

The measurement at multiple angles can increase the confidence in the data for MALS measurements. MALS offers insights into the angular dependence of the scattered light for large molecules (>10-15 nm radius) enabling the highest quality and most accurate measurement of R_g, characterising structure for these large molecules. MALS detectors can measure the molecular weight of molecules from small (R_g > 10 nm) to large (R_g <~ 500 nm) since any angular dependence in the light scattering is always accounted for. A second type of detector that is commonly coupled to AF4 system is dynamic light scattering (DLS), also called as quasi-elastic light scattering (QELS) equipment. In DLS, a laser is directed into the dispersion of the particles and the scattered light is collected at one angle over time. The random movement of the particles due to Brownian motion leads to random variations of the intensity of the scattered light. From these fluctuations an autocorrelation function is derived, which is converted for assessment of particle diffusion coefficient and size,

in case that the analytes are spherical. The correlation signal G depends on the diffusion of the particles being measured.

$$G = \int_0^\infty I(t)I(t+\tau) = B + Ae^{-2q^2D\tau}$$

Where: B = is the baseline, A is the amplitude, D is the translational diffusion coefficient and q is scattering vector.

The scattering vector (q) is defines as:

$$q = \frac{4\pi n}{\lambda_0} \sin(\frac{\Theta}{2})$$

where: n is solvent refractive index, λ_0 is the vacuum wavelength of the laser, and Θ is the scattering angle.

The hydrodynamic radius can be converted from diffusion coefficient D using Stock-Einstein equation:

$$R_h = \frac{kT}{6\pi\eta D}$$

Where: k is Boltzmann's constant, T is the absolute temperature, η coefficient of viscosity and D is the diffusion coefficient. [163] The DLS measurements can be obtained in batch or in flow mode.[164] Nowadays, DLS can measure the size for spherical particles in diameter from a few nm to 1 µm.[159] It was shown before that R_g/R_h, defined as shape factor (ρ), can give information about shape of particles and internal structure.[165,166] The examples of different material shape and values of ρ are placed in the table below.

Table 1.1. The examples of shape particles with values of shape factor (ρ)

Shape of particles	ρ = Rg/Rh
Homogeneous hard sphere	0.778[167]
Stiff rod	2.36[167]
Oblate ellipsoids	0.875 to 0.987[168]
Prolate ellipsoids	1.36 to 2.24[168]
Core-shell particles	<0.7[169]

The application of AF4 for fractionation and analysis of different molecules using MALS and DLS instruments are discussed in next subsections. In subsections 1.6.2. AF4 the state of art technique, the areas where AF4 has been used and showed a promise. In subsection 1.6.3. the application of AF4 on nanogels were discussed. In subsection 1.6.4. the potential of AF4 on analysis non-spherical particles were mentioned.

1.6.2. AF4 – state of art technique

The AF4 showed a promise in the range of different fields as: biotechnology (viruses,[170] aggregates,[171] cell organelles,[172] bioparticles[173]), pharmacy (proteins,[174] antibodies,[174] liposomes,[175] drug delivery,[176] micelles[177]), environment (humic and fulvic acid,[178] environmental colloids,[179] clay particles[180]), material science (latex beads,[181] nanoparticle[182]) and polymers (biopolymers,[183] starches,[184] polyelectrolytes[185]). There is also increasing interest in AF4 as a state of art technique in nanomedicine application.[186] One application of AF4 have been used to understand the formation of the protein corona on nanoparticles. When a nanomedicine is exposed to physiological fluid the proteins in the liquid absorb on the surface of the particle. It has been suggested that there two types of protein coronas exist: strongly bound proteins (hard corona) or loosely bound proteins (soft

corona). Weber *et al*.[187] showed that it was possible to use AF4 to separate the soft protein corona from hard corona. AF4 has also been used to separate biological material. Hawe *et al*. showed that they could separate immunoglobulin G and its aggregates.[188] Another interesting example of AF4 an application in nanomedicine field was published by Engel *et al*.[189] In their work, the release of poly(D,L-lactide-co-glycolide) (PLGA) nanoparticles from tablets were studied by AF4. This research provided information on the particle size and indicated that AF4 is a useful technique for analysis of for drug release from different nanocarriers. In next subsections, the application of AF4 on nanogels and the potential of AF4 on analysis non-spherical particles are discussed.

1.6.3. AF4 and nanogels

Thus far, there is relatively a small body of literature that is concerned with analysing nanogels by asymmetric flow field flow fractionation. AF4 coupled with different detectors like MALS, DLS, RI can give information about size, shape molecular weight and distribution of particles. Shimoda *et al.*[190] have prepared crosslinked polysaccharide–PEG hybrid nanogels (CHPOA–PEGSH) and analysed these particles by dynamic light scattering (DLS), AF4-UV-VIS-MALS to determine the particle size and degradation kinetics. The AF4 and DLS measurements showed good separation with a regenerative cellulose membrane in eluent phosphate buffered saline (PBS) buffer at pH 7.4. The different diameters of CHPOA-PEGSH hybrid nanogels were obtained i.e. from 78 to 108 nm, depending on the ratio of the reagents. Hartlieb *et al.*[191] prepared of poly(2-oxazoline)-based block copolymers consisting of a cationic (PAmOx) block and hydrophilic segments (PEtOx) and studied their self-assembly in different organic solvents. A schematic of the synthesis is shown in Figure 1.16. AF4 was used to investigate the M_n of polymers and R_g, R_h and shape factor for crosslinked nanostructures. The value of shape factor was different for two solvents dependent upon its nature used for assembly, showing results for ρ less than 0.8 for $CHCl_3$ which they suggested indicated compact micellar structure, and around 1.0 for isopropanol which was assigned to a soft structure with the architecture of a vesicle.

Authors showed a limitation for MALS detector as the particles with R_g of less than approximately were 15 nm not detected.[147,191] Unfortunately, the chosen membrane cut-off was 10 kDa and seems to be too high for a polymer with M_n between 9200 and 13600 due to low recovery (around 75%).

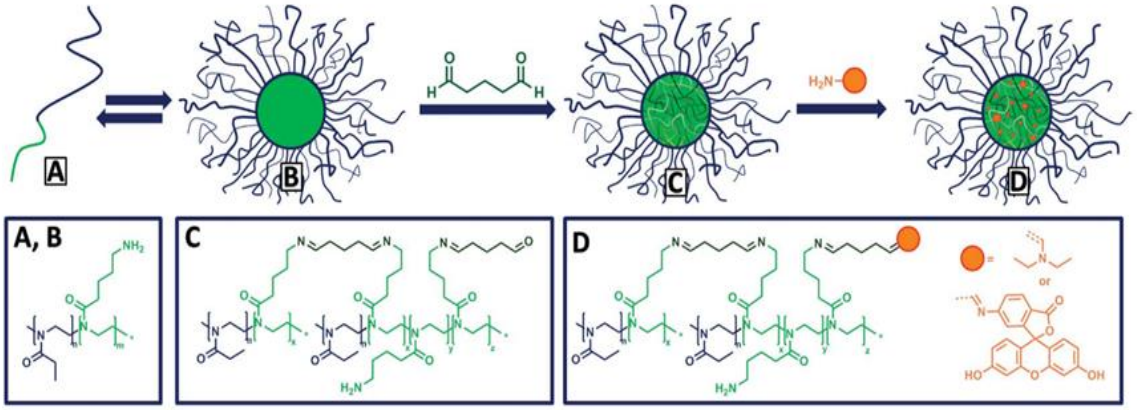

Figure 1.16. Schematic representation of the self-assembly of P(EtOx-b-AmOx) followed by cross-linking and quenching/loading. Reproduced from M. Hartlieb, D. Pretzel, M. Wagner, S. Hoeppener, P. Bellstedt, M. Görlach, C. Englert, K. Kempe and U. S. Schubert, *J. Mater. Chem. B*, 2015, 3, 1748–1759 with permission from The Royal Society of Chemistry.

The group of L. Andrew Lyon have contributed a few research articles regarding the analysis of PNIPAM nanogels by AF4. Their articles are discussed below. Their paper by Blackburn *et al*. studied core/shell nanogels made of PNIPAM crosslinked with BIS and copolymerised with acrylic acid.[132] The size of particles was controlled by changing the concentration of initiator and surfactant providing samples from 100 nm to 280 nm in diameter. The analysis of the samples by AF4-MALS showed that the nanogels had monomodal and narrow distributions. Unfortunately, the paper provides limited details about separation conditions like eluent or cross-flow for method. In another paper from the same group by Smith *et al*.[192] they synthesised PNIPAM nanogels by precipitation copolymerisation with degradable crosslinker N,O-dimethacryloylhydroxylamine (DMHA). The degradation of particles was tested under different pH and temperature conditions and then characterised using AF4-

MALS-DLS. The authors also determined the shape factor for the particles. They showed that values of ρ for PNIPAM nanogels of ~1.4 for non-crosslinked chains below the volume phase transition temperature (VPTT) and between 0.54 to 0.85 in the swollen state. The ρ values for PNIPAM-DMHA was 0.6 at 20 °C which indicated that particles have denser core and less dense shell. The degradation studies showed a decrease in the normalized scattering intensity for AF4-MALS measurements for PNIPAM-DMHA nanogels incubated at 37 °C and pH values higher than 7, which indicated that particles degraded faster at higher pHs. By measuring a MALS90º signal before and after degradation they found changes in intensity thus demonstrating how much of nanogels were degraded. The most degradable nanogels showed that around 20% of nanogels left in pH 8.4. However, these results were limited to measurements of R_g and R_h and are therefore not representative of molecular weight of degradable products. Molecular weight analysis of degradation products would have been valuable in an attempt to solve issue with mechanism of nanogels erosion.

In a follow up study, Lyon *et al.*[114] demonstrated the ability to synthesis PNIPAM nanogels with disulphide based crosslinker N,N'-bis(acryloyl)cystamine (BAC) by aqueous, redox-initiated precipitation polymerization approach. To improve the control over disulfide incorporation a non-degradable cross-linker N,N-methylenebis(acrylamide) (BIS) was used to synthesise thiol-bearing microgels. These microgels were characterised by using AF4-MALS and batch DLS techniques. The degradation of particles was triggered by dithiothreitol (DTT) and measured by AF4-MALS in phosphate buffer at pH 7. The molecular mass of nanogels was found to decrease in the presence of DTT, indicating that swelling was accompanied by mass loss. This change in the nanogels caused the decrease in light scattering intensity in MALS (see Figure 1.17.). The erosion was also found in the presence of cysteine, although in slower mode. The AF4-MALS-DLS measurement showed potential in analysis of degradation for PNIPAM nanogels and it was much powerful than DLS batch analysis due to fractionation of particles and presentation of range sizes in samples.

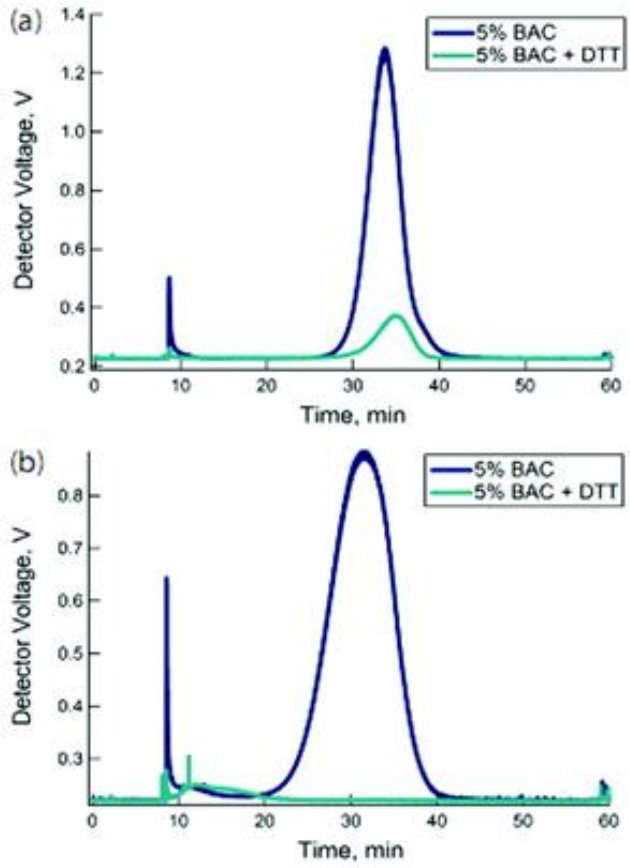

Figure 1.17. A4F-MALS separation of pNIPMAm-BAC (5%) microgels formed by the (a) thermal and (b) redox initiation methods. Incubating the particles with DTT increased retention of the thermally initiated particles yet led to degradation of the redox-initiated. Reprinted with permission from L. A. Lyon, Macromolecules, 2012, 45, 39–45. Copyright (2012) American Chemical Society.

1.6.4. AF4 and non-spherical particles

A growing body of literature is concerned with fractionation of non-spherical and particles with different shapes by AF4 measurements. By far, the most comprehensive article of separation gold nanorods by flow field flow fractionation technique is the work of Gigault *et al.*[193] Their work investigated the influence of composition of eluent and flow ratios on the separation of positively charged non-spherical gold nanoparticles. The different molar ratios of ammonium nitrate (NH_4NO_3) and cetyl trimethyl ammonium bromide (CTAB) were used as the eluent in the system. Gigault *et al*. showed that mobile phases consisting of 30 % CTAB and

70 % of NH_4NO_3 gave the best reproducibility and recovery. The samples used in their research were gold nanorods with range of aspect ratio obtained from SEM/TEM (from 1.4 to 4.4). The chosen cross-flow for separation of gold nanorods was fixed at 0.5 mL/min as optimised due to the size of particles and recovery. The elution time was found to be shorter for longer rods. The experimental data obtained from AF4 measurements were compared with the values from theoretically calculated Brownian model. The results suggested that the fractionation of non-spherical particles was made by a combination of diffusion coefficient and aspect ratio due to the steric-entropy contribution associated with their orientation. A possible explanation is that the longer rods have a concentration profile further removed from the accumulation wall compared to the shorter rods, and consequently elution is faster.

Weiss *et al.* [194] showed the acylation of biodegradable poly(glycerol adipate) (PGA) with different fatty acids (laurate, stearate and behenate) to create range of different polymer structures. The polymers were characterised by AF4-MALS and also with the range of different techniques including: DLS and zeta potential measurement. The AF4 measurements showed a range of shape factors and it agreed with aspect ratio obtained from SEM images. For spherical particles, shape factor values were between 0.7 and 0.8, while for more non-spherical particles the values increased to around 0.99. This article showed potential for AF4 technique to obtain shape factor as information about structure and shape of nanomaterials.

Mathaes *et al.*[167] gives some reliable methods and techniques to characterise polystyrene non-spherical particles. In this research, non-spherical poly(1-phenylethene-1,2-diyl (polystyrene) particles over a wide size range (40 nm, 2 µm and 10 µm) were successfully synthesised by a film stretching method. The authors used 350 spacer and a 30 kD a cut-off regenerated cellulose membrane. Focusing period was 7 min with an applied focus flow of 2 mL/min. For the analysis of particles, the mobile phase consisted of 0.5% SDS in water was used. The critical micelle concentration (CMC) of SDS is 8.2 mM at 25°C,[195] therefore, the concentration of SDS used in their research resulted in the formation of micelles which might have influenced the results as micelles are easy detected by AF4-MALS-DLS

measurements. Nevertheless, the shape factor for non-spherical particles was around 0.99, indicating more rod structure in agreement with SEM images. Mathaes *et al.* gave sufficient detail on the method for separation of particles which would allow the data to be reproduced. This is noteworthy as often articles in AF4 literature do not give sufficient information on the methods to allow reproduction. Typical missing details can be values and changes of cross-flow, temperature or type of membrane. Another typical issue, which can be seen in the literature for AF4 measurements, is lack of information about fit used for calculation R_g.

A comprehensive article about analysis of biohybrid structures of avidin and biotinylated glycodendrimers based on poly(propyleneimine) (GD-B) was published by Boye *et el.*[157] AF4 coupled with DLS and MALS detectors was used to characterise biohybrid structures consist of single components (avidin, differently valent GD-B) and nanostructures (see Figure 1.18.). It was shown that the differences in shape factors, R_g and R_h revealed the molecular shape of biohybrid structures was changed from rod-like to spherical. The R_h was obtained by two different strategies by online DLS and by calculation from retention theory. Both methods provided comparable results for single components. Authors put attention on weakness of online DLS measurements suggesting that for high molar masses, DLS measurements underestimated R_h.

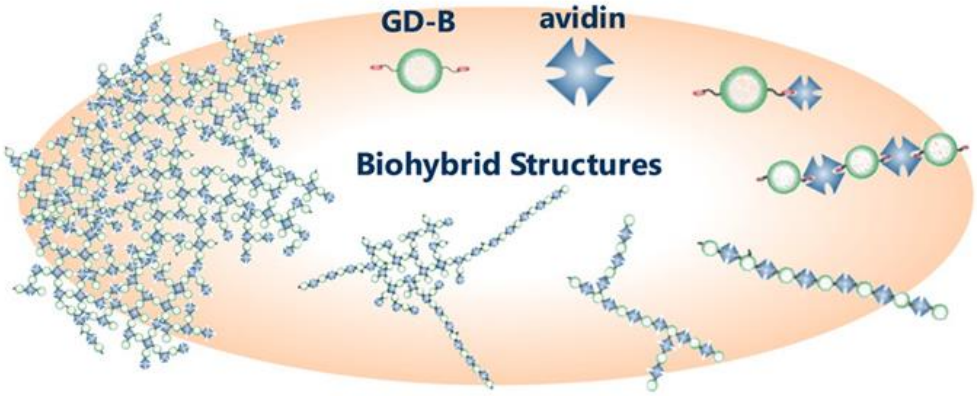

Figure 1.18. A structures of biohybrid analysed by AF4. Reprinted with permission from S. Boye, F. Ennen, L. Scharfenberg, D. Appelhans, L. Nilsson and A. Lederer, Macromolecules, 2015, 48, 4607–4619. Copyright (2015) American Chemical Society.

The issue of underestimation of R_h by DLS was also published previously by Sitar *et al.*[196] The size and shape of soft particles of various size and type: polystyrene nanoparticle size standards, lipid droplets (LDs), and large unilamellar vesicles (LUVs) were analysed by AF4-MALS-DLS. Three different detector flow rates were used in this study, (0.2, 0.5, and 1 mL/min) and were shown to have no significant influence on the shape factor and R_g of spherical nanoparticles. On the other hand, the expected R_h was obtained experimentally only for the lowest flow rate at the detector (0.2 mL/min). The difference in the expected and measured R_h was largest for the larger particles (diameter 200 nm). These finding suggest that the detector flow should be used in relatively low values to obtain realistic values from online DLS measurements. It should be noted that this finding, the inaccuracy of R_h measurement for larger colloids has been contested by one of the AF4 manufacturers (PostNova Analytics Ltd.), however, to date there have not been any publications that refute the findings of Sitar *et al.*[196]

Few attempts were also made to characterise carbon nanotubes by asymmetric flow field flow fractionation.[197–199] Gigault *et al*. [199] studied multi-walled carbon nanotube (MWCNT) length dispersion state in aqueous medium by AF4-UV-MALS technique. Fractionation key parameters like mobile phase composition, spacer thickness, range of cross-flows were studied to obtain a robust method for evaluation of nanomaterials. Cross-flows between 1.8 and 2.5 mL/min were tested, obtaining lengths of MWCNTs from 200 to 1100 nm. The MWCNTs were dispersed in SDS aqueous solution to give more a hydrophilic character to the samples. Two different mobile phases with different concentrations were tested in this work (NH_4NO_3 and SDS). Various ionic strengths were also tested to obtain the best reproducibility, size fractionation and detection. The most appropriate results in terms of reproducibility was obtained in 1.10^{-5} mol/L NH_4NO_3 mobile phase and 250 µm thickness of spacer due to the highest recovery of particles (>90%). The recovery (<70%) and reproducibility in SDS were poor. The results are visible in Figure 1.19. The article showed the ability of powerful analytical technique to evaluate MWCNT aqueous dispersion giving information about the number and size of different populations, as well as size distributions.

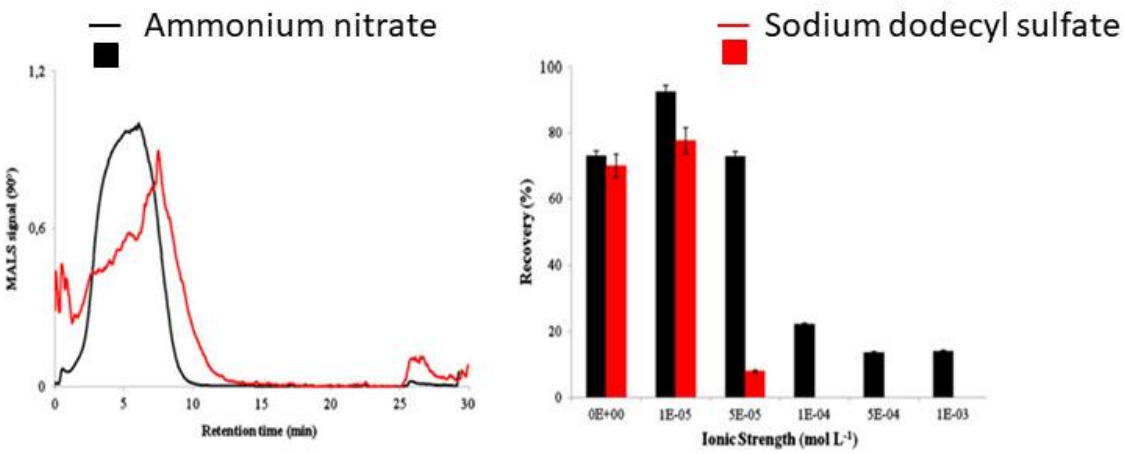

Figure 1.19. a) Typical fractograms of MWCNT obtained for two different mobile phase natures with an ionic strength of 1.10^{-5} mol/L b) MWCNT recoveries R (%) for different ionic strengths and two salt natures. Reprinted by permission from Springer, J. Gigault, B. Grassl and G. Lespes, Anal. Bioanal. Chem., 2011, 401, 3345–3353. Copyright 2011.

1.7. Research objectives and thesis overview

The shape and structure of nanomedicines have a considerable impact on their biological behaviour.[200] Therefore, it is a challenge in the field of nanomedicine to develop new methods for synthesising and characterising nanomaterials with non-spherical and controlled internal structures. This challenge is the motivating factor for the research presented in this thesis. The aim of the work described in this thesis is to synthesise nanoparticles, nanocomposites and nanogels with different sizes and morphologies that might have potential applications in nanomedicine. These nanomaterials will then be analysed by AF4 to provide insight into their size, shape and degradation behaviour that could not be provided by alternative characterisation techniques. This analysis using AF4 will also provide new methods to those in the growing field of AF4 and a better understanding of the fractionation behaviour of complex (core-shell structures and non-spherical) nanomaterials. This thesis contains four results chapters:

In Chapter 2, nanocomposites of multiwalled carbon nanotubes/ polycaprolactone particles were synthesised by a facile oil-in-water emulsion solvent evaporation route. These nanocomposites were then loaded with the anti-cancer drug docetaxel. The nanocomposite composition and novel morphology of the particles were characterised by DLS, SEM, AFM and AF4. This work provides a novel method for preparing non-spherical nanocomposites. The AF4 measurements showed analysis for different shapes and morphology of nanoparticles. This was a motivation to continue of development of AF4 methods for analysis of different materials like PNIPAM nanogels.

In Chapter 3, the research about the development of a versatile AF4 method to characterize PNIPAM nanogel sample with mean diameters from 65 to 310 nm were presented. This approach would also provide insight into the internal structures of samples. Therefore, the evaluation of separation conditions using different mobile phases and crossflows with inline MALS and DLS detectors for analysis were tested.

The aim of Chapter 4 was to produce degradable PNIPAM nanogels by RAFT polymerisation with well-defined length of polymer chains. The nanogels were characterised by DLS, nuclear magnetic resonance (NMR) and AF4. The degradation studies were conducted in the presence of DTT by AF4-MALS and DLS.

Chapter 5 is focussed on the analysis of a range of nanoparticles made of different materials with different sizes and shapes, with the aim of establishing methods that can be used to provide size and shape information on different types of metal nanoparticles. The particles were fractionated by AF4-MALS-DLS, with the aim of better understanding the relationship between particle size, shape and separation behaviour. The samples analysed were gold nanoparticles, gold nanorods, silver nanoparticles and silver nanoprisms.

1.8. References

1 https://www.nano.gov/you/nanotechnology-benefits.

2 https://www.weforum.org/agenda/2016/06/the-computer-revolution-how-its-changed-our-world-over-60-years.

3 S. Slomkowski, J. V. Alemán, R. G. Gilbert, M. Hess, K. Horie, R. G. Jones, P. Kubisa, I. Meisel, W. Mormann, S. Penczek and R. F. T. Stepto, *Pure Appl. Chem.*, 2011, **83**, 2229–2259.

4 K. Riehemann, S. W. Schneider, T. A. Luger, B. Godin, M. Ferrari and H. Fuchs, *Angew. Chemie - Int. Ed.*, 2009, **48**, 872–897.

5 R. Singh and L. J. W., *Exp. Mol .Pathol.*, 2009, **86**, 215–223.

6 S. Svenson, *Curr. Opin. Solid State Mater. Sci.*, 2012, **16**, 287–294.

7 Robert A. Freitas Jr, *Nanomedicine, Volume I: Basic Capabilities*, 1999.

8 N. Moran, *Nanomedicine lacks recognition in Europe*, 2006, vol. 24.

9 No Title, https://etp-nanomedicine.eu/about-nanomedicine/what-is-nanomedicine/.

10 T. O. McDonald, M. Siccardi, D. Moss, N. J. Liptrott, M. Gardiello, S. P. Rannard and A. Owen, *Nanoengineering Global approaches to Health and Safety Issues*, 2015.

11 M. L. Etheridge, S. A. Campbell, A. G. Erdman, C. L. Haynes, S. M. Wolf and J. McCullough, *Nanomedicine Nanotechnology, Biol. Med.*, 2013, **9**, 1–14.

12 J. I. Hare, T. Lammers, M. B. Ashford, S. Puri, G. Storm and S. T. Barry, *Adv. Drug Deliv. Rev.*, 2017, **108**, 25–38.

13 K. S. Soppimath, T. M. Aminabhavi and A. R. Kulkarni, *Control. release*, 2001, **70**, 1–20.

14 X. Zhang, L. Meng, Q. Lu, Z. Fei and P. J. Dyson, *Biomaterials*, 2009, **30**, 6041–6047.

15 T. L. Doane and C. Burda, *Chem. Soc. Rev.*, 2012, **41**, 2885–911.

16 G. Tiwari, R. Tiwari, B. Sriwastawa, L. Bhati, S. Pandey, P. Pandey and S. K. Bannerjee, *Int J Pharm Investig*, 2012, **2**, 2–11.

17 J. De Andres, J. M. Asensio-Samper and G. Fabregat-Cid, *Intrathecal delivery of analgesics*, 2014, vol. 1141.

18 W. H. De Jong and P. J. a Borm, *Int. J. Nanomedicine*, 2008, **3**, 133–149.

19 M. W. Tibbitt, J. E. Dahlman and R. Langer, *J. Am. Chem. Soc.*, 2016, **138**, 704–717.

20 A. S. H. Makhlouf, *1 – Historical development of drug delivery systems: From*

conventional macroscale to controlled, targeted, and responsive nanoscale systems, Elsevier Ltd., 2018.

21 https://www.fda.gov/regulatory-information/search-fda-guidance-documents/considering-whether-fda-regulated-product-involves-application-nanotechnology.

22 https://www.fda.gov/regulatory-information/search-fda-guidance-documents/guidance-industry-safety-nanomaterials-cosmetic-products.

23 T. Kerz, G. Paret and H. Herff, *Routes of drug administration*, 2007.

24 S. R. D'Mello, C. N. Cruz, M. L. Chen, M. Kapoor, S. L. Lee and K. M. Tyner, *Nat. Nanotechnol.*, 2017, **12**, 523–529.

25 K. M. Tyner, N. Zheng, S. Choi, X. Xu, P. Zou, W. Jiang, C. Guo and C. N. Cruz, *AAPS J.*, 2017, **19**, 1071–1083.

26 C. N. Cruz, K. M. Tyner, L. Velazquez, K. C. Hyams, A. Jacobs, A. B. Shaw, W. Jiang, R. Lionberger, P. Hinderling, Y. Kong, P. C. Brown, T. Ghosh, C. Strasinger, S. Suarez-Sharp, D. Henry, M. Van Uitert, N. Sadrieh and E. Morefield, *AAPS J.*, 2013, **15**, 623–628.

27 S. Freiberg and X. X. Zhu, *Int. J. Pharm.*, 2004, **282**, 1–18.

28 U. Sakulkhu, M. Mahmoudi, L. Maurizi, J. Salaklang and H. Hofmann, *Sci. Rep.*, 2014, **4**, 5020.

29 M. Park, *Biochimica et Biophysica Acta*,1991, **1066**, 29–36.

30 K. Jores, W. Mehnert, M. Drechsler, H. Bunjes, C. Johann and K. Mäder, *J. Control. Release*, 2004, **95**, 217–227.

31 R. Dal Magro, F. Ornaghi, I. Cambianica, S. Beretta, F. Re, C. Musicanti, R. Rigolio, E. Donzelli, A. Canta, E. Ballarini, G. Cavaletti, P. Gasco and G. Sancini, *J. Control. Release*, 2017, **249**, 103–110.

32 A. Z. Wilczewska, K. Niemirowicz, K. H. Markiewicz and H. Car, *Pharmacol. Reports*, 2012, **64**, 1020–1037.

33 A. Díaz-Moscoso, *Int. J. Med. Biomed. Res.*, 2012, **1**, 12–23.

34 D. Brevet, M. Gary-Bobo, L. Raehm, S. Richeter, O. Hocine, K. Amro, B. Loock, P. Couleaud, C. Frochot, A. Morère, P. Maillard, M. Garcia and J. O. Durand, *Chem. Commun.*, 2009, 1475–1477.

35 S. A. C. Carabineiro, *Molecules*, **2017**, *22*, 857.

36 W. C. W. Chan and S. Nie, *Science*, 1998, **281**, 2016–2018.

37 S. Wang, Y. Zhang, W. An, Y. Wei, N. Liu, Y. Chen and S. Shuang, *Food Control*, 2015, **55**, 43–48.

38 C. Lynch, P. P. D. Kondiah, Y. E. Choonara, L. C. du Toit, N. Ally and V. Pillay, *Polymers (Basel).*, **2019**, *11*(8), 1371.

39 S. Imazato, H. Kitagawa, R. Tsuboi, R. Kitagawa, P. Thongthai and J. ichi Sasaki, *Dent. Mater. J.*, 2017, **36**, 524–532.

40 L. Sercombe, T. Veerati, F. Moheimani, S. Y. Wu, A. K. Sood and S. Hua, *Front. Pharmacol.*, 2015, **6**, 1–13.

41 W. Xu, P. Ling and T. Zhang, *J. Drug Deliv.*, 2013, **2013**, 1–15.

42 A. Puri, K. Loomis, B. Smith, J. H. Lee, A. Yavlovich, E. Heldman and R. Blumenthal, *Crit. Rev. Ther. Drug Carrier Syst.*, 2009, **26**, 523–580.

43 A. R. Town, M. Giardiello, R. Gurjar, M. Siccardi, M. E. Briggs, R. Akhtar and T. O. McDonald, *Nanoscale*, 2017, **9**, 6302–6314.

44 F. Yu, X. Cao, J. Du, G. Wang and X. Chen, *ACS Appl. Mater. Interfaces*, 2015, **7**, 24023–24031.

45 U. Bulbake, S. Doppalapudi, N. Kommineni and W. Khan, *Pharmaceutics*, 2017, **9**, 1–33.

46 S. Gelperina, K. Kisich, M. D. Iseman and L. Heifets, *Am. J. Respir. Crit. Care Med.*, 2005, **172**, 1487–1490.

47 M. H. Lai, J. H. Jeong, R. J. Devolder, C. Brockman, C. Schroeder and H. Kong, *Adv. Funct. Mater.*, 2012, **22**, 3239–3246.

48 B. T. Liu and J. P. Hsu, *Chem. Eng. Sci.*, 2006, **61**, 1748–1752.

49 X. C. Luu and A. Striolo, *J. Phys. Chem. B*, 2014, **118**, 13737–13743.

50 K. Namdee, A. J. Thompson, A. Golinski, S. Mocherla, D. Bouis and O. Eniola-Adefeso, *Atherosclerosis*, 2014, **237**, 279–286.

51 R. A. Petros and J. M. Desimone, *Nat. Rev. Drug Discov.*, 2010, **9**, 615–627.

52 S. Barua and S. Mitragotri, *Nano Today*, 2014, **9**, 223–243.

53 S. Cai, K. Vijayan, D. Cheng, E. M. Lima and D. E. Discher, *Pharm. Res.*, 2007, **24**, 2099–2109.

54 X. Yang, J. J. Grailer, I. J. Rowland, A. Javadi, S. A. Hurley, D. A. Steeber and S. Gong, *Biomaterials*, 2010, **31**, 9065–9073.

55 J. Chen, N. E. Clay, N. Park and H. Kong, *Chem. Eng. Sci.*, 2015, **125**, 20–24.

56 J. A. Champion and S. Mitragotri, *Proc. Natl. Acad. Sci.*, 2006, **103**, 4930–4934.

57 C. T. Ambrose, *Cell. Immunol.*, 2006, **240**, 1–4.

58 J. A. Champion and S. Mitragotri, *Pharm. Res.*, 2009, **26**, 244–249.

59 R. Toy, P. M. Peiris, K. B. Ghaghada and E. Karathanasis, *Nanomedicine (Lond)*, 2014, **9**, 121–134.

60 S. Cai, K. Vijayan, D. Cheng, E. M. Lima and D. E. Discher, *Pharm. Res.*, 2007, **24**, 2099–2109.

61 Y. Geng, P. Dalhaimer, S. Cai, R. Tsai, M. Tewari, T. Minko and D. E. Discher, *Nat. Nanotechnol.*, 2007, **2**, 249–255.

62 S. Muro, C. Garnacho, J. A. Champion, J. Leferovich, C. Gajewski, E. H. Schuchman, S. Mitragotri and V. R. Muzykantov, *Mol. Ther.*, 2008, **16**, 1450–1458.

63 P. Kolhar, A. C. Anselmo, V. Gupta, K. Pant, B. Prabhakarpandian, E. Ruoslahti and S. Mitragotri, *Proc. Natl. Acad. Sci.*, 2013, **110**, 10753–10758.

64 C. C. Ho, A. Keller, J. A. Odell and R. H. Ottewill, *Colloid Polym. Sci.*, 1993, **271**, 469–479.

65 J. A. Champion, Y. K. Katare and S. Mitragotri, *Proc. Natl. Acad. Sci.*, 2007, **104**, 11901–11904.

66 J. Cao, T. Sun and K. T. V. Grattan, *Sensors Actuators, B Chem.*, 2014, **195**, 332–351.

67 N. R. Jana, L. Gearheart and C. J. Murphy, *Adv. Mater.*, 2002, **13**, 1389–1393.

68 P. K. Jain, K. S. Lee, I. H. El-Sayed and M. A. El-Sayed, *J. Phys. Chem. B*, 2006, **110**, 7238–7248.

69 D. Pantarotto, R. Singh, D. McCarthy, M. Erhardt, J. P. Briand, M. Prato, K. Kostarelos and A. Bianco, *Angew. Chemie - Int. Ed.*, 2004, **43**, 5242–5246.

70 A. Sanginario, B. Miccoli and D. Demarchi, *Biosensors*, 2017, **7**, 1–23.

71 B. S. Wong, S. L. Yoong, A. Jagusiak, T. Panczyk, H. K. Ho, W. H. Ang and G. Pastorin, *Adv. Drug Deliv. Rev.*, 2013, **65**, 1964–2015.

72 P. A. Tran, L. Zhang and T. J. Webster, *Adv. Drug Deliv. Rev.*, 2009, **61**, 1097–1114.

73 N. B. Singh and S. Agrawal, *JSM Chem.*, 2013, **1**, 1–8.

74 N. K. Mehra and S. Palakurthi, *Drug Discov. Today*, 2016, **21**, 585–597.

75 Y. P. Sun, K. F. Fu, Y. Lin and W. J. Huang, *Acc. Chem. Res.*, 2002, **35**, 1096–1104.

76 H. Kong, C. Gao and D. Yan, *J. Am. Chem. Soc.*, 2004, **126**, 412–413.

77 H. Zeng, C. Gao and D. Yan, *Adv. Funct. Mater.*, 2006, **16**, 812–818.

78 R. Bafkary and S. Khoee, *RSC Adv.*, 2016, **6**, 82553–82565.

79 H. Ali-Boucetta, K. T. Al-Jamal, D. McCarthy, M. Prato, A. Bianco and K. Kostarelos, *Chem. Commun.*, 2008, 459–461.

80 L. Lacerda, A. Bianco, M. Prato and K. Kostarelos, *Adv. Drug Deliv. Rev.*, 2006, **58**, 1460–1470.

81 S. Marchesan, K. Kostarelos, A. Bianco and M. Prato, *Mater. Today*, 2015, **18**, 12–19.

82 S. K. Smart, A. I. Cassady, G. Q. Lu and D. J. Martin, *Carbon N. Y.*, 2006, **44**, 1034–1047.

83 A. Bianco, K. Kostarelos and M. Prato, *Chem. Commun.*, 2011, **47**, 10182.

84 C. M. Sayes, F. Liang, J. L. Hudson, J. Mendez, W. Guo, J. M. Beach, V. C. Moore, C. D. Doyle, J. L. West, W. E. Billups, K. D. Ausman and V. L. Colvin, *Toxicol. Lett.*, 2006, **161**, 135–142.

85 M. Patenaude and T. Hoare, *ACS Macro Lett.*, 2012, **1**, 409–413.

86 Y. Xu, Y. Li, X. Cao, Q. Chen and Z. An, *Polym. Chem.*, 2014, **5**, 6244–6255.

87 E. A. Clark and J. E. G. Lipson, *Polymer (Guildf).*, 2012, **53**, 536–545.

88 A. Gandhi, A. Paul, S. O. Sen and K. K. Sen, *Asian J. Pharm. Sci.*, 2015, **10**, 99–107.

89 J. Niskanen and H. Tenhu, *Polym. Chem.*, 2017, **8**, 220–232.

90 S. Pant, M. Sharma, K. Patel, S. Caplan, C. M. Carr and B. D. Grant, 2009, **5**, 1–8.

91 B. Ye, S. Zhang, R. Li, L. Li, L. Lu and C. Zhou, *Compos. Sci. Technol.*, 2018, **156**, 238–246.

92 W. Fu and B. Zhao, *Polym. Chem.*, 2016, **7**, 6980–6991.

93 J. J. Escobar-Chávez, M. López-Cervantes, A. Naïk, Y. N. Kalia, D. Quintanar-Guerrero and A. Ganem-Quintanar, *J. Pharm. Pharm. Sci.*, 2006, **9**, 339–358.

94 X. Jiang, N. Xiang, H. Zhang, Y. Sun, Z. Lin and L. Hou, *Carbohydr. Polym.*, 2018, **186**, 377–383.

95 J. J. Sperinde and L. G. Griffith, *Macromolecules*, 1997, **30**, 5255–5264.

96 F. Li, Y. Zhu, B. You, D. Zhao, Q. Ruan, Y. Zeng and C. Ding, *Adv. Funct. Mater.*, 2010, **20**, 669–676.

97 J. Berger, M. Reist, J. M. Mayer, O. Felt and R. Gurny, *Eur. J. Pharm. Biopharm.*, 2004, **57**, 35–52.

98 R. Parhi, *Adv. Pharm. Bull.*, 2017, **7**, 515–530.

99 N. Boucard, C. Viton and A. Domard, *Biomacromolecules*, 2005, **6**, 3227–3237.

100 W. Hu, Z. Wang, Y. Xiao, S. Zhang and J. Wang, *Biomater. Sci.*, 2019, **7**, 843–855.

101 J. Berger, M. Reist, J. M. Mayer, O. Felt, N. A. Peppas and R. Gurny, *Eur. J. Pharm. Biopharm.*, 2004, **57**, 19–34.

102 M. R. Yoon Yeo, Wenliang Geng, Taichi Ito, Daniel S. Kohane, Jason A. Burdick, *J. Biomed. Mater. Res. B. Appl. Biomater.*, 2007, **81**, 312–322.

103 Y. Zhang, L. Tao, S. Li and Y. Wei, *Biomacromolecules*, 2011, **12**, 2894–2901.

104 S. Mukherjee, M. R. Hill and B. S. Sumerlin, *Soft Matter*, 2015, **11**, 6152–6161.

105 Y. Wen, F. Li, C. Li, Y. Yin and J. Li, *J. Mater. Chem. B*, 2017, **5**, 961–971.

106 Y. D. Park, N. Tirelli and J. A. Hubbell, *Biomater. Silver Jubil. Compend.*, 2002, **24**, 203–210.

107 N. Bhattarai, J. Gunn and M. Zhang, *Adv. Drug Deliv. Rev.*, 2010, **62**, 83–99.

108 N. Welsch, A. Wittemann and M. Ballauff, *J. Phys. Chem. B*, 2009, **113**, 16039–16045.

109 K. Ogawa, B. Wang and E. Kokufuta, *Langmuir*, 2001, **17**, 4704–4707.

110 R. Pelton, *Adv. Colloid Interface Sci.*, 2000, **85**, 1–33.

111 W. Leobandung, H. Ichikawa, Y. Fukumori and N. A. Peppas, *J. Control. Release*, 2002, **80**, 357–363.

112 M. Rasmusson, A. Routh and B. Vincent, *Langmuir*, 2004, **20**, 3536–3542.

113 A. Town, DUAL-STIMULI RESPONSIVE NANOGELS FOR INJECTABLE DRUG DELIVERY IMPLANTS, PhD thesis, University of Liverpool, 2018.

114 L. A. Lyon, *Macromolecules*, 2012, **45**, 39–45.

115 J. Ramos, A. Imaz and J. Forcada, *Polym. Chem.*, 2012, **3**, 852–856.

116 G. Odian, *Principles of Polymerization*, New York, 4th Editio., 2004.

117 C. Dispenza, G. Spadaro and M. Jonsson, *Top. Curr. Chem.*, 2016, **374**, 95–120.

118 F. Kiraç and O. Güven, *Radiat. Phys. Chem.*, 2015, **112**, 76–82.

119 P. Sahu, D. Das, V. Kashaw, A. K. Iyer and S. K. Kashaw, *Nanogels: A New Dawn in Antimicrobial Chemotherapy*, 2017.

120 R. Pelton, *Adv. Colloid Interface Sci.*, 2000, **85**, 1–33.

121 Zermina Rashid, *Intech*, 2016, **i**, 13.

122 Y. Yoshizawa, Y. Kono, K. I. Ogawara, T. Kimura and K. Higaki, *Int. J. Pharm.*, 2011, **412**, 132–141.

123 H. Senff and W. Richtering, *Colloid Polym. Sci.*, 2000, **278**, 830–840.

124 S. Pardeshi and S. K. Singh, *RSC Adv.*, 2016, **6**, 23525–23536.

125 A. Lee, H. Y. Tsai and M. Z. Yates, *Langmuir*, 2010, **26**, 18055–18060.

126 W. McPhee, K. C. Tam and R. Pelton, *J. Colloid Interface Sci.*, 1993, 156, 24–30.

127 Y. Chen, N. Ballard, O. D. Coleman, I. J. Hands-Portman and S. A. F. Bon, *J. Polym. Sci. Part A Polym. Chem.*, 2014, **52**, 1745–1754.

128 S. Kawaguchi and K. Ito, *Adv. Polym. Sci.*, 2005, **175**, 299–328.

129 J. C. Gaulding, M. H. Smith, J. S. Hyatt, A. Fernandez-Nieves and L. A. Lyon, *Macromolecules*, 2012, **45**, 39–45.

130 M. Andersson and S. L. Maunu, *J. Polym. Sci. Part B Polym. Phys.*, 2006, **44**, 3305–3314.

131 X. Zhang, S. Lü, C. Gao, C. Chen, X. Zhang and M. Liu, *Nanoscale*, 2013, **5**, 6498–506.

132 W. H. Blackburn and L. A. Lyon, *Colloid Polym. Sci.*, 2008, **286**, 563–569.

133 J. Faucheu, C. Gauthier, L. Chazeau, J. Y. Cavaillè, V. Mellon and E. B. Lami, *Polymer (Guildf).*, 2010, **51**, 6–17.

134 R. Arshady, *Colloid Polym. Sci.*, 1992, **270**, 717–732.

135 G. Moad, E. Rizzardo and S. H. Thang, *Polymer (Guildf).*, 2008, **49**, 1079–1131.

136 S. Perrier, *Macromolecules*, 2017, **50**, 7433–7447.

137 D. J. Keddie, *Chem. Soc. Rev.*, 2014, **43**, 496–505.

138 S. Perrier and P. Takolpuckdee, *J. Polym. Sci. Part A Polym. Chem.*, 2005, **43**, 5347–5393.

139 E. Rizzardo, *Macromol. Symp.*, 2001, **174**, 209–212.

140 Q. Liu, P. Zhang, A. Qing, Y. Lan and M. Lu, *Polymer (Guildf).*, 2006, **47**, 2330–2336.

141 W. Shen, Y. Chang, G. Liu, H. Wang, A. Cao and Z. An, *Macromolecules*, 2011, **44**, 2524–2530.

142 Z. An, Q. Shi, W. Tang, C. K. Tsung, C. J. Hawker and G. D. Stucky, *J. Am. Chem. Soc.*, 2007, **129**, 14493–14499.

143 J. Rieger, C. Grazon, B. Charleux, D. Alaimo and C. Jerome, *J. Polym. Sci. Part A Polym. Chem.*, 2009, **47**, 2373–2390.

144 S. Pal, M. R. Hill and B. S. Sumerlin, *Polym. Chem.*, 2015, **6**, 7871–7880.

145 W. Fraunhofer and G. Winter, *Eur. J. Pharm. Biopharm.*, 2004, **58**, 369–383.

146 M. Gaborieau and P. Castignolles, *Anal. Bioanal. Chem.*, 2011, **399**, 1413–1423.

147 M. Wagner, S. Holzschuh, A. Traeger, A. Fahr and U. S. Schubert, *Anal. Chem.*, 2014, **86**, 5201–5210.

148 M. I. Malik and H. Pasch, *Prog. Polym. Sci.*, 2016, **63**, 42–85.

149 M. E. Schimpf, K. Caldwell and J. C. Giddings, *Field-Flow Fractionation Handbook*, John Wiley & Sons, Inc., 2000.

150 M. A. Benincasa and J. C. Giddings, *Anal. Chem.*, 1992, **64**, 790–798.

151 S. K. R. Williams, J. R. Runyon and A. A. Ashames, *Anal. Chem.*, 2011, **83**, 634–642.

152 M. E. Schimpf, K. Caldwell and J. C. Giddings, *Field-Flow Fractionation Handbook*, John Wiley & Sons, Inc., 2000.

153 P. Reschiglian, A. Zattoni, B. Roda, E. Michelini and A. Roda, *Trends Biotechnol.*, 2005, **23**, 475–483.

154 http://www.postnova.com/.

155 J. Gigault, J. M. Pettibone, C. Schmitt and V. A. Hackley, *Anal. Chim. Acta*, 2014, **809**, 9–24.

156 B. Roda, A. Zattoni, P. Reschiglian, M. H. Moon, M. Mirasoli, E. Michelini and A. Roda, *Anal. Chim. Acta*, 2009, **635**, 132–143.

157 S. Boye, F. Ennen, L. Scharfenberg, D. Appelhans, L. Nilsson and A. Lederer, *Macromolecules*, 2015, **48**, 4607–4619.

158 A. C. Makan, R. P. Williams and H. Pasch, *Macromol. Chem. Phys.*, 2016, **217**, 2027–2040.

159 https://www.malvernpanalytical.com/en/.

160 A. Rudin, *Elem. Polym. Sci. Eng.*, 2007, **3**, 73–120.

161 S. Podzimek, Light Scattering, Size Exclusion Chromatography and Asymmetric Flow Field Flow Fractionation: Powerful Tools for the Characterization of Polymers, Proteins and Nanoparticles, John Wiley & Sons, Inc., 2011, 353–354.

162 C. Wu and S. Zhou, *J. Macromol. Sci. B*, 1997, **36**, 345–355.

163 M. Kaszuba, D. McKnight, M. T. Connah, F. K. McNeil-Watson and U. Nobbmann, *J. Nanoparticle Res.*, 2008, **10**, 823–829.

164 H. Hagendorfer, R. Kaegi and M. Parlinska, *Anal.Chem*, 2012, **84**, 2678–2685.

165 B. Plazzotta, J. S. Diget, K. Zhu, B. Nyström and J. S. Pedersen, *J. Polym. Sci. Part B Polym. Phys.*, 2016, **54**, 1913–1917.

166 P. Jurney, R. Agarwal, V. Singh, D. Choi, K. Roy, S. V. Sreenivasan and L. Shi, *J. Control. Release*, 2017, **245**, 170–176.

167 R. Mathaes, G. Winter, J. Engert and A. Besheer, *Int. J. Pharm.*, 2013, **453**, 620–629.

168 J. Loscalzo, H. Slayter, R. I. Handin and D. Farber, *Biophys. J.*, 1986, **49**, 49–50.

169 G. R. Deen, T. Alsted, W. Richtering and J. S. Pedersen, *Phys. Chem. Chem. Phys.*, 2011, **13**, 3108–3114.

170 P. Reschiglian, A. Zattoni, B. Roda, S. Casolari, M. H. Moon, J. Lee, J. Jung, K. Rodmalm and G. Cenacchi, *Anal. Chem.*, 2002, **74**, 4895–4904.

171 J. R. Runyon, L. Nilsson, J. Alftrén and B. Bergenståhl, *Anal. Bioanal. Chem.*, 2013, **405**, 6649–6655.

172 C. Arfvidsson and K. G. Wahlund, *Anal. Biochem.*, 2003, **313**, 76–85.

173 G. Yohannes, M. Jussila, K. Hartonen and M. L. Riekkola, *J. Chromatogr. A*, 2011, **1218**, 4104–4116.

174 M. Leeman, J. Choi, S. Hansson, M. U. Storm and L. Nilsson, *Anal. Bioanal. Chem.*, 2018, **410**, 4867–4873.

175 S. Hupfeld, D. Ausbacher and M. Brandl, *J. Sep. Sci.*, 2009, **32**, 1465–1470.

176 S. Huclier-Markai, A. Grivaud-Le Du, E. N'tsiba, G. Montavon, M. Mougin-Degraef and J. Barbet, *J. Chromatogr. A*, 2018, **1573**, 107–114.

177 T. Miller, R. Rachel, A. Besheer, S. Uezguen, M. Weigandt and A. Goepferich, *Pharm. Res.*, 2012, **29**, 448–459.

178 R. Backett, Z. Jue and J. C. Giddings, *Environ. Sci. Technol.*, 1987, **21**, 289–295.

179 M. Baalousha, B. Stolpe and J. R. Lead, *J. Chromatogr. A*, 2011, **1218**, 4078–4103.

180 I. C. Regelink, G. F. Koopmans, C. van der Salm, L. Weng and W. H. van Riemsdijk, *J. Environ. Qual.*, 2013, **42**, 464–473.

181 H. Kato, A. Nakamura, K. Takahashi and S. Kinugasa, *Nanomaterials*, 2012, **2**, 15–30.

182 J. Gigault, E. Mignard, H. El Hadri and B. Grassl, *Chromatographia*, 2017, **80**, 287–294.

183 U. B. Kavurt, M. Marioli, W. T. Kok and D. Stamatialis, *J. Chem. Technol. Biotechnol.*, 2015, **90**, 11–18.

184 S. Juna and A. Huber, *J. Chromatogr. A*, 2012, **1219**, 161–172.

185 M. Wagner, C. Pietsch, L. Tauhardt, A. Schallon and U. S. Schubert, *J. Chromatogr. A*, 2014, **1325**, 195–203.

186 M. Wagner, S. Holzschuh, A. Traeger, A. Fahr and U. S. Schubert, *Anal. Chem.*, 2014, **86**, 5201–5210.

187 C. Weber, J. Simon, V. Mailänder, S. Morsbach and K. Landfester, *Acta Biomater.*, 2018, **76**, 217–224.

188 A. Hawe, W. Friess, M. Sutter and W. Jiskoot, *Anal. Biochem.*, 2008, **378**, 115–122.

189 A. Engel, M. Plöger, D. Mulac and K. Langer, *Int. J. Pharm.*, 2014, **461**, 137–144.

190 A. Shimoda, S. ichi Sawada, A. Kano, A. Maruyama, A. Moquin, F. M. Winnik and K. Akiyoshi, *Colloids Surfaces B Biointerfaces*, 2012, **99**, 38–44.

191 M. Hartlieb, D. Pretzel, M. Wagner, S. Hoeppener, P. Bellstedt, M. Görlach, C. Englert, K. Kempe and U. S. Schubert, *J. Mater. Chem. B*, 2015, **3**, 1748–1759.

192 M. H. Smith, A. B. South, J. C. Gaulding and L. A. Lyon, *Anal. Chem.*, 2010, **82**, 523–530.

193 J. Gigault, T. J. Cho, R. I. MacCuspie and V. A. Hackley, *Anal. Bioanal. Chem.*, 2013, **405**, 1191–1202.

194 V. M. Weiss, T. Naolou, G. Hause, J. Kuntsche, J. Kressler and K. Mäder, *J. Control. Release*, 2012, **158**, 156–164.

195 K. L. Mukerjee, P. Mysels, *Critical Micelle Concentration of Aqueous Surfactant Systems*, Washington DC, US Governm., 1971.

196 S. Sitar, V. Vezočnik, P. Maček, K. Kogej, D. Pahovnik and E. Žagar, *Anal. Chem.*, 2017, acs.analchem.7b03251.

197 A. Gogos, R. Kaegi, R. Zenobi and T. D. Bucheli, *Environ. Sci. Nano*, 2014, **1**, 584–594.

198 E. Niezabitowska, J. Smith, M. R. Prestly, R. Akhtar, F. W. Von Aulock, Y. Lavallée, H. Ali-Boucetta and T. O. Mcdonald, *RSC Adv.*, 2018, **8**, 16444–16454.

199 J. Gigault, B. Grassl and G. Lespes, *Anal. Bioanal. Chem.*, 2011, **401**, 3345–3353.

200 A. Albanese, P. S. Tang and W. C. W. Chan, *Annu. Rev. Biomed. Eng.*, 2012, **14**, 1–16.

Chapter 2

Facile Production of Nanocomposites of Carbon Nanotubes and Polycaprolactone with High Aspect Ratios with Potential Applications in Drug Delivery

This chapter is based on publication:

E. Niezabitowska, J. Smith, M. R. Prestly, R. Akhtar, F. W. Von Aulock, Y. Lavallée, H. Ali-Boucetta and T. O. Mcdonald, Facile Production of Nanocomposites of Carbon Nanotubes and Polycaprolactone with High Aspect Ratios with Potential Applications in Drug Delivery, *RSC Adv.*, 2018, 8, 16444–16454.

I would like to thank: Jessica Smith for contribution as Master Student, Dr Mark Prestly for SEM images, Dr Riaz Akhtar for AFM analysis, Dr Felix Wendelin Von Aulock and Prof. Yan Lavallée for TGA analysis, Dr Hanene Ali-Boucetta for providing multiwalled carbon nanotubes.

2.1. Introduction

The use of nanomaterials for applications in drug delivery has been shown to offer a wide range of potential benefits such as encapsulating both hydrophilic and hydrophobic substances, improving the stability of drugs and providing targeted delivery.[1] These benefits have been particularly well demonstrated in the treatment of cancer where a large number of therapies are now used clinically.[2,3] However, effectively maximising the dose of the drug at the target site versus systemic distribution still remains to be a considerable challenge for any therapy. Recently, there has been growing interest in the influence of the geometry and stiffness of nanomaterials on their interaction with cells and tissues.[4–11] A wide range of geometries and structures are synthetically possible such as nanoparticles,[12–14] nanotubes,[15–17] nanodisks,[18] nanoshells[19,20] and nanowires.[21] The size, shape, stiffness and surface chemistry of nanomaterials has been shown to influence cytotoxicity,[22] drug release,[23] targeting and imaging contrast efficiency.[24] Generally, high aspect ratio (length/diameter) nanomaterials can provide improved drug delivery potential in comparison to spherical nanoparticles.[4,5]

Carbon nanotubes (CNTs) are a type of high aspect ratio nanomaterial and they possess a range of interesting properties including their nanoscale size, unique fibre structure, large surface area and high mechanical stiffness.[15] These properties have led to CNTs being investigated as drug delivery systems.[16,25] CNTs have shown benefits in DNA delivery,[26] use as cancer theranostics,[27,28] small molecule drug delivery[16] and regenerative medicine.[29] CNTs can both be covalently modified with drug molecules, or they can physically adsorb aromatic drugs via the strong π-π and hydrophobic interactions between the drug and the aromatic surface of the CNT. Such physical adsorption of drugs has been exploited for loading anthracyclines, a class of anticancer drug.[16] However, in spite of their drug loading potential, the inherently hydrophobic nature of CNTs can limit their application in aqueous environments. As such, surface modification and coating is often utilised to improve the colloidal stability of CNTs and to minimise their inherent toxicity.[30] Polymers are typically used for this purpose, with the polymers usually introduced onto CNTs by

covalent approaches consisting of either “grafting to” or “grafting from” the surface of the CNT. The former approach involves binding polymers to CNT surfaces by amidation, radical coupling, esterification and other rections.[31] While the latter, “grafting from”, applies in-situ polymerizations of immobile monomers on the CNTs surfaces by anionic/cationic polymerizations or atom transfer radical polymerization (ATRP).[32] For example, Gao *et al.* used “grafting from” to modify the surface of multiwalled carbon nanotubes (MWNTs) with poly(Ɛ-caprolactone) (PCL).[33] An alternative approach is to modify the CNTs by a non-covalent functionalisation. This approach is particularly attractive due to the relative simplicity of process, additionally it has also been shown to introduce fewer defects to the graphitic structure of the CNTs.[34] A few examples of this approach have been shown, these include coating the CNTs with poly(ethylene glycol)-phospholipid conjugates,[35] forming a biopolymer coating using layer-by-layer assembly,[36] or stabilising the surface with Pluronic F-127, a commercially available surfactant.[37] However, one issue with non-covalent modification is that the forces between the coating and the CNT are typically weak and desorption may occur.[38] A useful coating for CNTs would be PCL, a polymer that has been widely investigated for drug delivery[12] and is currently used as a component of clinically approved devices.[39] PCL nanoparticles can be prepared by the oil-in-water emulsion solvent evaporation method. In this process the polymer solution is emulsified and particles are formed upon evaporation of the solvent for the polymer.[40] Using this oil-in-water emulsion solvent evaporation method with CNTs would potentially provide a solid PCL coating that would not be easily desorbed. Additionally, PCL nanoparticles can provide entrapment efficiencies exceeding 80% and drug loadings of up to 20%.[41] The potential for combining CNTs with their high modulus and drug loading with PCL, a polymer with proven medical usage and drug delivery potential may provide a unique nanomaterial for applications in medicine.

In this study, we demonstrate a facile approach to produce high-aspect ratio nanocomposites comprising of CNTs and PCL, with the aim of combining the benefits of both materials and encapsulating the anti-cancer drug docetaxel. We investigate the formation of nanocomposites by an oil-in-water emulsion solvent evaporation

route (Figure 2.1) and examine how to control the size and morphology of the particles. The nanocomposite composition and novel morphology of the particles are characterised by DLS, SEM, AFM and AF4. Finally, we investigate the potential for loading the nanocomposites with docetaxel and monitor the *in vitro* drug release.

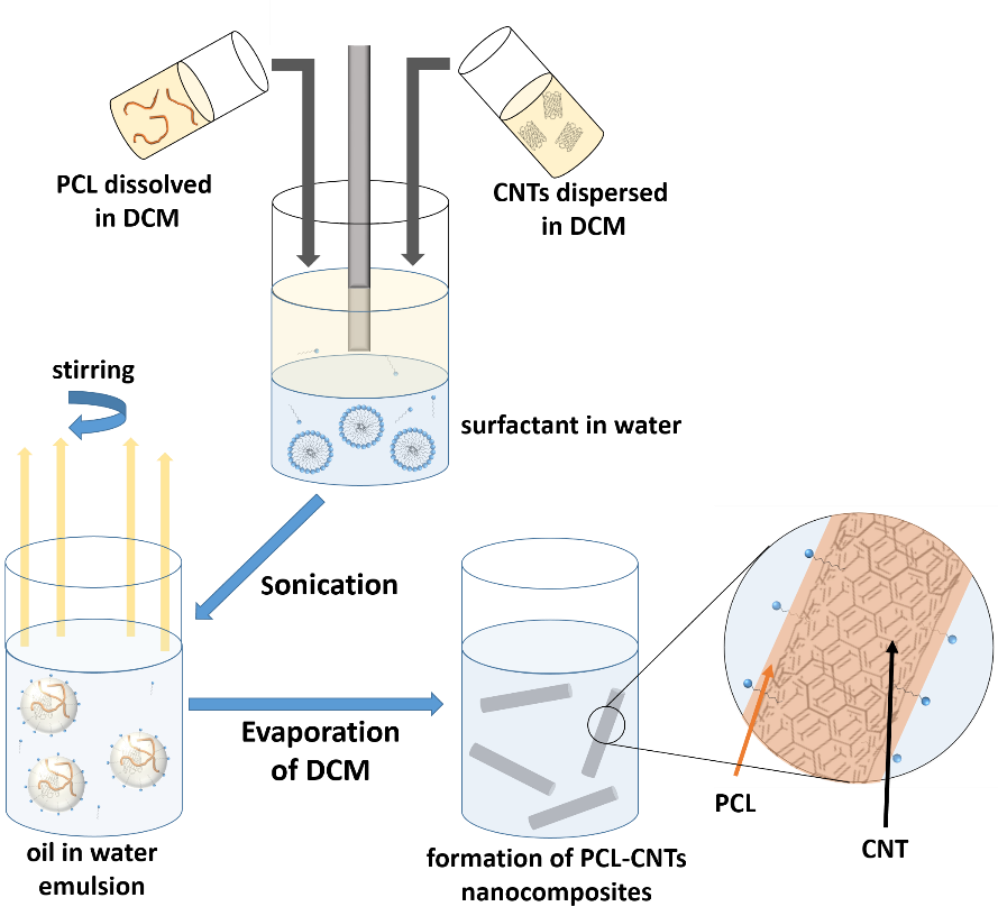

Figure 2.1. Scheme for the preparation of PCL-CNTs nanocomposites by an oil-in water emulsion solvent evaporation method. The solution of PCL and dispersion of CNTs (both in DCM) was emulsified in an aqueous surfactant solution. The resulting emulsion was kept stirring until the DCM had evaporated resulting in PCL-CNTs nanocomposites.

2.2. Experimental

2.2.1. Materials

Polycaprolactone (PCL, molecular weight 14,000 g/mol), sodium dodecyl sulphate (SDS), ammonium nitrate were purchased from Sigma-Aldrich. Non-functionalised multiwalled carbon nanotubes (MWCNTs) were purchased from Nanostructured & Amorphous Materials Inc. (Houston, USA) at 95% purity (Stock no. 1237YJS). According to the manufacturer, MWCNTs have an outside diameter 20-30 nm and length ranging between 0.5 and 2µm. Docetaxel was purchased from Chemleader Biomedical. Dichloromethane (DCM) (analytical reagent grade), acetone, acetonitrile (HPLC grade) were purchased from AgraNova. Milli-Q water obtained from a water purification system had a resistivity of > 18 MΩ cm^{-1} (PURELAB option R, Veolia). 10 kDa dialysis membrane was purchased from Spectrum Labs.

2.2.2. Synthesis of PCL-CNTs

Nanocomposites of PCL and CNTs were prepared by an oil-in-water emulsion solvent evaporation method. CNTs were dispersed in DCM (1 mL) to form a dispersion with a concentration of 0.5 mg/mL. The dispersion of CNTs was sonicated for 30 s using a Hielscher UP400s ultrasonic processor (400 Watts, 24 kHz, 45% of amplitude, 1 cycle). Next, the specific amount of PCL was dissolved in DCM (total volume 1 mL) to form the organic phase. The aqueous phase was prepared by dissolution of SDS in 4 mL of distilled water. The two organic phases were transferred into 14 mL glass vials containing the aqueous phase, dropwise through a needle (21G). In the next step, the immiscible phases were homogenised for 30 s using a Hielscher UP400s ultrasonic processor (400 Watts, 24 kHz, 45% of amplitude, 1 cycle) to obtain an emulsion. The nanodispersion was mixed by magnetic stirring (500 rpm, hotplate model: Stuart US152D) overnight (~16 h) to allow evaporation of DCM.

2.2.3. Synthesis of PCL NPs

Nanoparticles of PCL were prepared by an oil-in-water emulsion solvent evaporation method. The specific amount of PCL was dissolved in DCM (total volume 1 mL) to form the organic phase. The aqueous phase was prepared by dissolution of SDS in 4 mL of distilled water. The two organic phases were transferred into 14 mL glass vials containing the aqueous phase, dropwise through a needle (21G). In the next step, the immiscible phases were homogenised for 30 s using a Hielscher UP400s ultrasonic processor (400 Watts, 24 kHz, 45% of amplitude, 1 cycle) to obtain an emulsion. The nanodispersion was mixed by magnetic stirring (500 rpm, hotplate model: Stuart US152D) overnight (~16 h) to allow evaporation of DCM. Next, samples were purified by centrifugation for 50 min at 8,500 rpm and 20 °C in distilled water. This procedure was repeated 3 times.

2.2.4. Encapsulation of docetaxel into PCL-CNTs nanocomposites

PCL-CNTs nanocomposites with encapsulated docetaxel were prepared by an oil-in-water emulsion solvent evaporation method as previously described in the synthesis of PCL-CNTs method. CNTs were dispersed in 1 mL of DCM to form a dispersion with a concentration of 0.5 mg/mL. Next, the specific amount of PCL was dissolved in DCM (total volume 1 mL) to form the organic phase. Docetaxel (DCX) (see structure Figure 2.2) was dissolved in 1 mL of acetone. The aqueous phase was prepared by dissolving SDS in 4 mL of distilled water. The three organic phases were transferred into 14 mL glass vials containing the water phase, dropwise through a needle (21G). In the next step, the immiscible solution was homogenised for 30 s using a Hielscher UP400s ultrasonic processor (45% of amplitude, 1 cycle) to obtain an emulsion. The nanosuspension was mixed by magnetic stirring (500 rpm) overnight ~16 h to allow the DCM to evaporate. The same method was used to obtain PCL and CNTs alone.

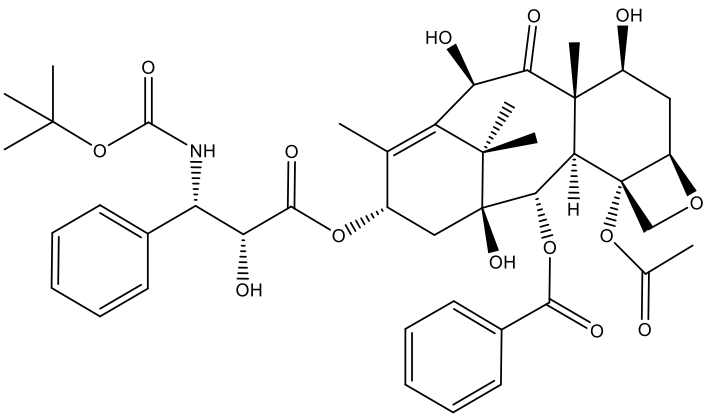

Figure 2.2. The structure of docetaxel – anticancer drug.

2.2.5. Characterisation

A Hitachi S-4800 cold Field emission (FE-SEM) scanning electron microscope (SEM) was used to image PCL NPs and PCL-CNTs. The samples to be analysed were centrifuged at 9000 rpm for 1 hours and washed with deionised water three times prior to addition (concentration 1 mg/mL) to glass coverslips stuck onto an aluminium stubs using carbon double-sided sticky tabs from Agar Scientific, Essex, UK and left to evaporate overnight. The prepared samples were coated with gold for 2.5 minutes at 20 mA using an EMITECH K550X Sputter Coater.

Asymmetric flow field flow fractionation experiments were performed on an MT2000 with RI and UV-Vis detectors from Postnova Analytics, Landsberg/Germany. The sizes of the samples were obtained by dynamic light scattering (DLS) using a Malvern Zetasizer Nano ZS (running Malvern Zetasizer software V7.11) (Malvern Instruments, Malvern, UK) with 633 nm He–Ne laser and the detector positioned at 173°, coupled online to the MT2000. A 350 µm spacer and 10 kDa regenerated cellulose (RC) membrane were installed in the separation channel. The conditions used for the separations was based on a method existing in the literature.[42] Briefly, the eluent was 1 x 10^{-5} mol/L NH_4NO_3 in Milli-Q H_2O. Type I distilled water was obtained from a water purification system had a resistivity of > 18 MΩ cm^{-1} (PURELAB option R,

Veolia). The injected volume was 30 µL of 1 mg/mL sample. The injection/focussing time was 5 min using a cross flow of 2 mL min^{-1}. The cross-flow rate was 2 mL min^{-1} for the first 15 min (t_0-t_{15}) in constant manner, and thereafter, the cross flow was linearly decreased from its initial value to 0 over a period of 5 min. Following the complete reduction in cross flow, the tip-flow continued for an additional 35 min. The UV-Vis detector measured wavelength were monitored for 300 nm. The z-average diameter and count rate were measured by an inline Malvern Zetasizer ZS DLS at 3 second intervals. DLS calculates the z-average size of particles using the Stokes-Einstein equation.

AFM measurements of the samples were performed with the samples deposited on glass coverslips which were adhered to mica substrates. The samples were prepared on the glass coverslip stuck onto mica substrates. A few microliters of suspended sample (concentration ~ 1 mg/mL) were pipetted onto the mica surface and left to dry by exposing to air overnight (~16 h). AFM imaging was conducted using a Bruker Multimode 8 instrument (Bruker, Santa Barbara, USA), operated in ambient conditions with a Bruker RTESPA-525 probe using the Peakforce Quantitative Nanomechanical Mapping (PFQNM) method.[43,44] The RTESPA-525 probe has a nominal spring constant of 200 N/m and a tip radius of 8 nm. All scans were conducted at a scan rate of 0.576 Hz with a scan size of 2.00 µm.[43]

Thermo-gravimetric analyses (TGA) were performed in a simultaneous thermal analyser (STA) 449F1 Jupiter (Netzsch GmbH), which includes a thermo-gravimetric analyser. Samples of unprocessed CNTs, PCL nanoparticles and the PCL-CNT nanocomposites (5-15 mg) were added to platinum pan. In the case of the PCL nanoparticles and the PCL-CNT nanocomposites, these dispersions were prepared using the usual method and were then freeze-dried prior to addition of the dry powder to the analysis pans. The atmosphere of the samples, the pan and the sample holder were evacuated and purged with argon three times to remove the air before analysis. The samples were then analysed by heating at a heating rate of 10˚C/min to 700˚C in an atmosphere of argon flowing at 20 mL/min, whilst monitoring weight changes at a resolution of ±25 ng.

2.2.6. Quantification of docetaxel by HPLC

HPLC measurements were performed with the use of a PerkinElmer Series 200 instrument. The chromatographic conditions were used as previously described in the literature.[45] The chromatograph column used was an Agilent Zorbax Eclipse Plus C18. Solvent A contained HPLC grade water and solvent B consisted of HPLC grade acetonitrile. The flow rate of the mobile phase was 1.0 mL/min. The HPLC gradient was kept as T/%B (T is time and B is a percentage of acetonitrile solvent): 0/35, 15/65, 25/75, 30/95, 35/100, 39/100 and 40/35 with a post run time of 5 min. The column was maintained at 25 °C. The detection wavelength was 230 nm. The injection volume was 10 µL. The diluent used was a 1:1 mixture of water and acetonitrile.

A calibration curve was prepared for docetaxel from 14 standard solutions. Samples were prepared by dissolving the appropriate amount of docetaxel in 1:1 mixture water and acetonitrile. A linear calibration plot for the above method was obtained over 3.9 µg/mL to 250 µg/mL. The correlation coefficient was 0.99.

In order to calculate the encapsulation efficiency of the samples the amount of 'free' docetaxel (i.e. not encapsulated in the nanoparticles) was measured. Firstly, the samples loaded with docetaxel were freeze dried for 24 h to remove the water. After that, the freeze-dried samples were dispersed in 2 mL of HPLC methanol for 15 min. The methanol was then transferred to a spin filter tube (cut off 3.5 kDa) and centrifuged at 6,000 g for 1h at 20 °C. The filtered solution was then analysed by HPLC using the same method and column as for the drug release study.

2.2.7. In vitro drug release

Briefly, 4 mL of PCL, CNTs and PCL-CNTs–PLGA nanoparticles solution (1 mg/mL) were introduced into dialysis membrane bag (12-14 kDa, Spectrum Laboratories Inc.) The end-sealed dialysis bag was incubated into 500 mL of distilled water in the 25˚C. Every 24 h, 250 mL of water was taken and freeze dried to remove water. After that, the freeze-dried samples were dispersed in 2mL of 1:1 mixture water and acetonitrile. Solution was analysed by HPLC, using the same method as described in HPLC method section. The release media was changed every 24h.

2.3. Results and Discussion

2.3.1. Factors controlling the diameter of PCL NPs

This section is divided into 2 subsections. In the first section, the impact of the concentration of PCL on the diameter of nanoparticles is discussed. Secondly, the effects of the concentrations of different types of surfactants were investigated. The method used in this research is fast, simple and can be used to preparation polymer nanoparticles from solution of polymers dissolved in non-water-miscible organic solvents. Formation of nanoparticles occurred when the organic solvent with dissolving the polymer evaporated at the water/air interface resulting in solid polymer nanoparticles.

2.3.1.1. Effect of varying the concentration of PCL on the nanoparticle properties

Firstly, the effect of varying the concentration of PCL on the nanoparticle properties was investigated. The composition for these samples was as follows: the amount of PCL changed from 1 mg/mL to 10 mg/mL dissolved in DCM, and the amount of surfactant (SDS) was fixed 0.75 mg/mL in distilled water. The particles were then analysed by DLS to provide the mean particle diameter and polydispersity index (PdI) (see Figure 2.3).

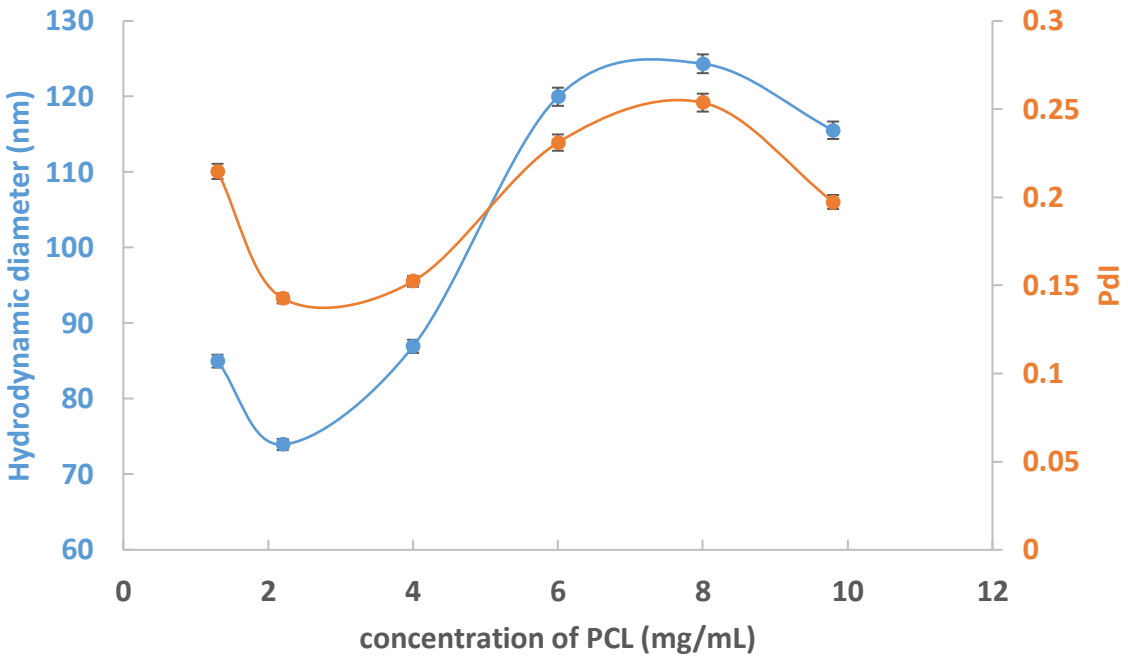

Figure 2.3. The relationship between the concentration of PCL in the organic phase and the resulting nanoparticle size and PdI.

With increasing concentration of PCL, the diameter of particles was increased. This trend was likely caused by increasing of viscosity in the polymer solution.[46] The PdI of the nanoparticles was found to be independent of the polymer concentration and varied from 0.15 to 0.25, the highest value for PdI was obtained for 8 mg/mL of polymer. The mean particle size of samples prepared by miniemulsion has been shown to be dependent on the size of the droplets produced during sonication,[47] it appears that varying the polymer concentration did not influence the broadness of the droplets formed or the colloidal stability of the droplets or nanoparticles.

2.3.1.2. The effect of surfactant types and concentration on the diameter and polydispersity of PCL nanoparticles

The effect of varying the concentration and type of surfactant were then tested. For this research surfactants with different hydrophilic-lipophilic balances (HLBs) were checked. HLB value is a measure of the degree to which non-ionic surfactants are hydrophilic or lipophilic, determined by calculating values for the different regions of the molecule.

$$HLB = 20\ \frac{MW_h}{MW}$$

Where MW_h is the molecular weight of the hydrophilic component and MW is the molecular weight of the complete surfactant. For oil in water methods, the best theoretical value for a surfactant should be between 8-16.[48] The HLB values of surfactants and types used for this research are included in Table 2.1.

Table 2.1. Name, structure and HLB value for used surfactants.

Commercial name	Chemical name	Structure	HLB value
Brij S10	Polyethylene glycol octadecyl ether	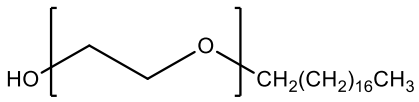	12[49]
Brij 30	Polyoxyethylene(4) lauryl ether.	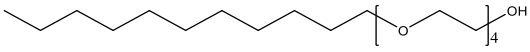	9.7[50]
Pluronic F-68	Polyoxyethylene-Polyoxypropylene Block Copolymer	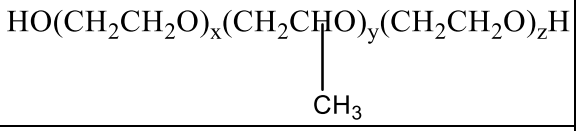	29[51]
SDS	Sodium dodecyl sulphate	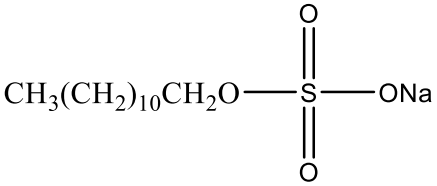	N/A
PVA	Polyvinyl alcohol	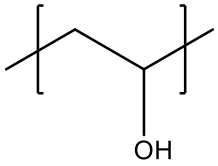	18[52]

Figure 2.4A shows influence of surfactant concentration on the diameter of PCL particles for each of the particular surfactants and Figure 2.4B shows the relationship for the PdI of the different samples. Particles obtained by using SDS are characterised by the lowest diameter (~ 100 nm) and the lowest PdI (< 0.2). It suggests that during the formation of the emulsion, droplets created by added SDS have the lowest size. This evidence exists in the literature.[53] DLS data also revealed that increasing the concentration of surfactants tended to give a very slight decrease in the diameter of the nanoparticles likely as a result of lower surface tension.[54] The difference in size and polydispersity between the surfactants may be due to the higher surface tensions for the some of the surfactants.[55] Samples with higher PdIs indicate poorer colloidal stability as the droplets or particles have coalesced or aggregated. Given the low diameter and PDIs obtained for nanoparticles using SDS, this was selected as the surfactant for further experiments.

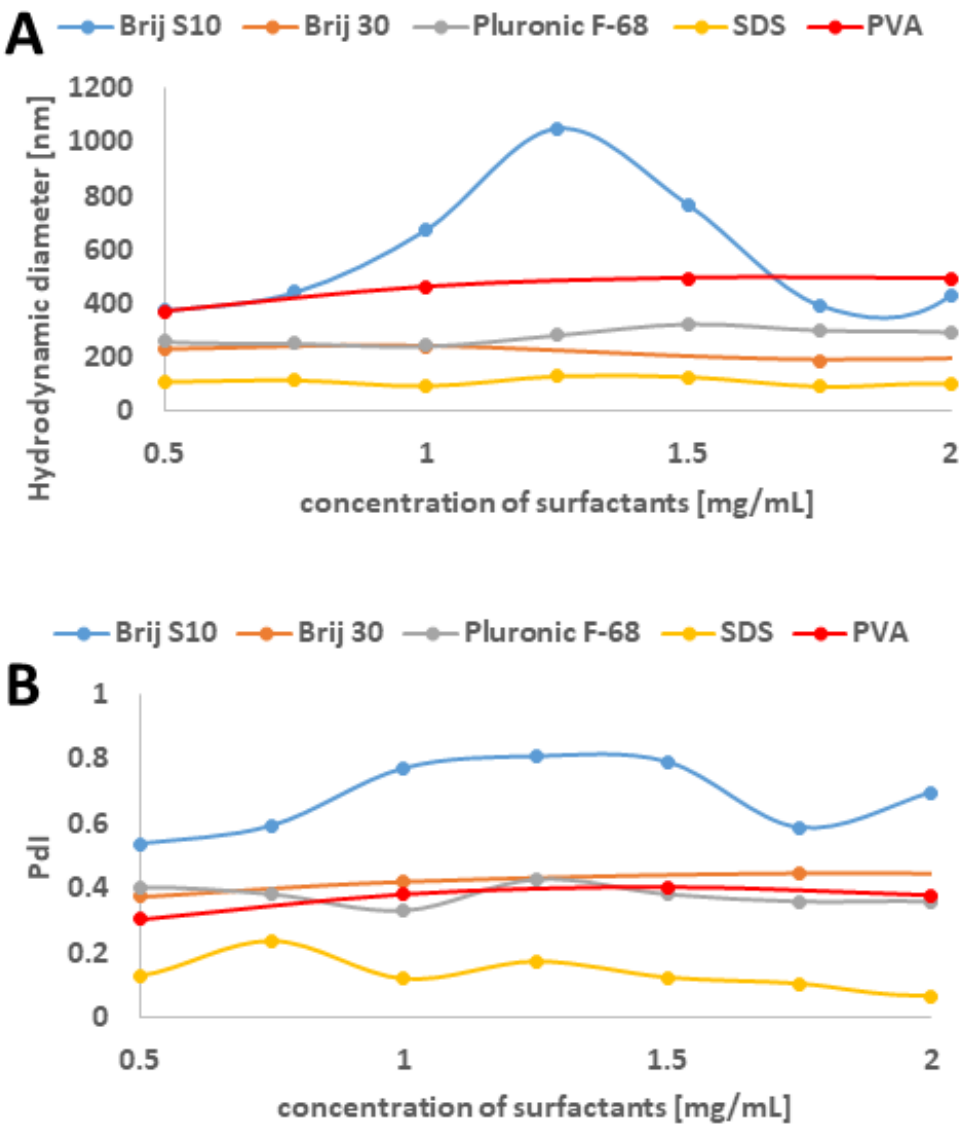

Figure 2.4. A) The effect of concentration of different surfactants on the diameter of PCL nanoparticles with 2 mg/mL of PCL B) The effect of concentration of different surfactants on the PdI of PCL nanoparticles with 2 mg/mL of PCL.

2.3.2. Influence of the concentration of SDS, CNTs and PCL on particle size and morphology of composites

The synthesis of PCL-CNTs nanocomposites was attempted by an oil-in water emulsion solvent evaporation method (see Figure 2.5), PCL and CNTs were contained in DCM which was then emulsified by sonication with an aqueous phase of the surfactant sodium dodecyl sulphate (SDS). The DCM was then left to evaporate under

ambient conditions. Two variables were initially investigated: the concentration of SDS in the aqueous phase and the concentration of CNTs in the oil phase, with the concentration of PCL kept constant at 6 mg/mL.

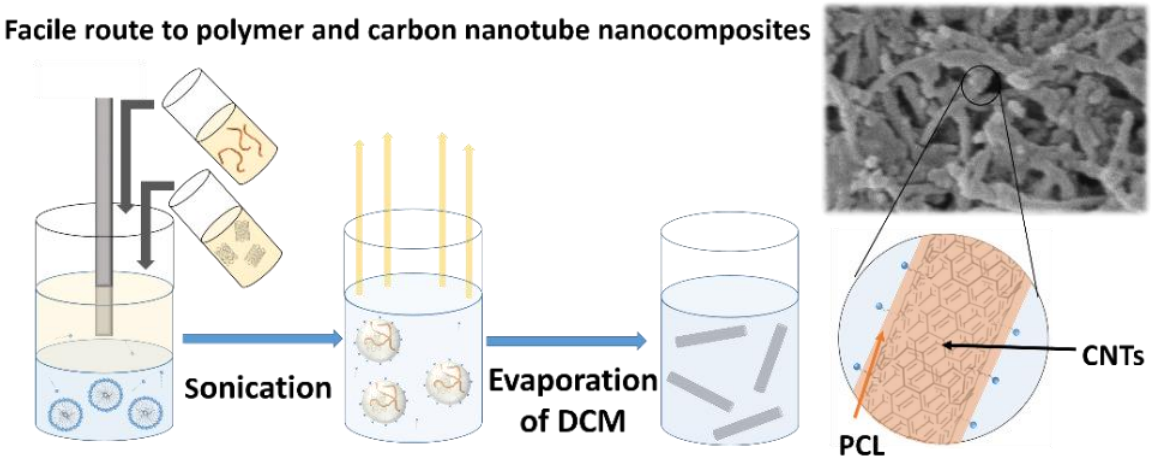

Figure 2.5. Scheme for the preparation of PCL-CNTs nanocomposites by an oil-in water emulsion solvent evaporation method. The solution of PCL and dispersion of CNTs (both in DCM) was emulsified in an aqueous surfactant solution. The resulting emulsion was kept stirring until the DCM had evaporated resulting in PCL-CNTs nanocomposites.

We observed that samples containing higher concentrations of CNTs produced a turbid emulsion which was a darker grey-black in colour. The samples were then purified by centrifugation to remove any excess surfactant before being analysed by DLS. The analysis of the samples by DLS provided the mean hydrodynamic diameters of the particles and a measure of the broadness of the particle size distribution, quantified by the polydispersity index (PdI) (see Figure 2.6).

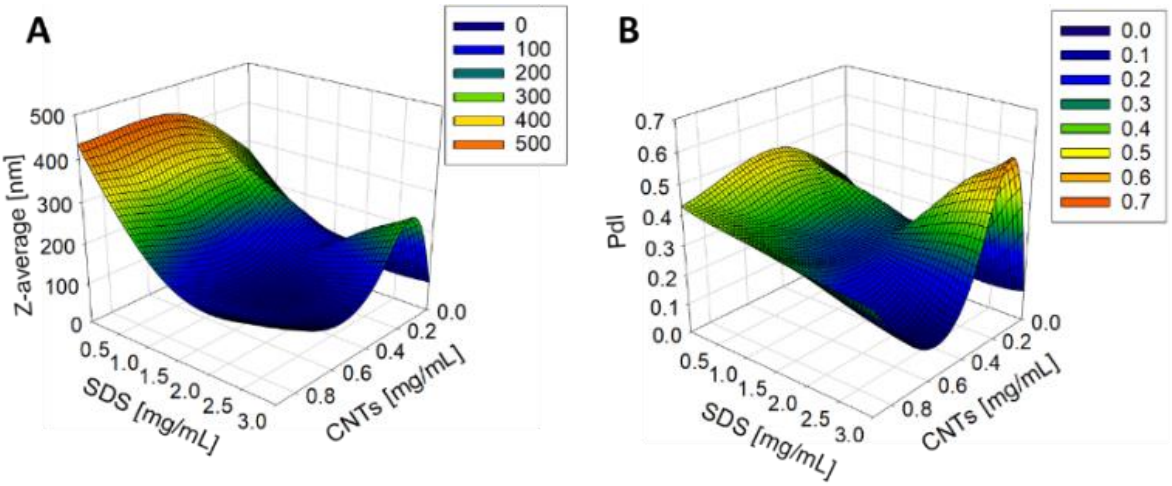

Figure 2.6. The effect of changing the concentration of CNTs and SDS on the Z-average diameter (A) and the PdI (B) of the resulting nanoparticles as measured by DLS. The concentration of PCL was 6 mg/mL.

It was found that particles without SDS had the largest diameters and that there was a further increase in the size as the CNT concentration increased from 0.03 mg/ml to 0.9 mg/ml of CNTs, with a diameter ranging from 289 to 434 nm respectively (Figure 2.6A). The same effect was visible for PdI results; the absence of surfactant resulted in the highest PdI values (Figure 2.6B). The data from DLS measurements in presented in SI, Table 2.3. Without SDS, the high interfacial tension between water and DCM would result in an emulsion with low stability, this will have led to droplet coalescence upon evaporation of the DCM, giving a higher mean particle diameter and broad particle size distribution. An SDS concentration of 1.5 mg/mL produced the smallest particles and the lowest PdIs for all of the three CNT concentrations. Concentrations above 1.5 mg/mL of SDS did not reduce particle size further suggesting 1.5 mg/mL was sufficient concentration of surfactant to minimise droplet coalescence, further increases in concentration generally increased the mean diameter or polydispersity index (Figure 2.6). At the lowest concentration of SDS tested (below 0.5 mg/mL) and a high concentration of CNTs (above 0.6 mg/mL) particles were obtained with larger mean diameters. The presence of the CNTs which had a mean length of 425 nm (Figure 2.7) in the DCM may have resulted in non-spherical droplets with a larger apparent hydrodynamic diameter. DLS analysis generally showed monomodal distributions for the samples (Figure 2.7) with the PdI

ranging between 0.169 (6 mg/mL PCL 0.03 mg/mL CNTs and 1.5 mg/mL SDS) and 0.428, a multimodal distribution (6 mg/mL PCL, 0.9 mg/mL CNTs and 0 mg/mL SDS). The concentration of SDS significantly impacted the results. When there was no SDS, broad size distributions were obtained, whereas present when the SDS concentration was above 1.5 mg/ml smaller particles and a narrower distribution was obtained.

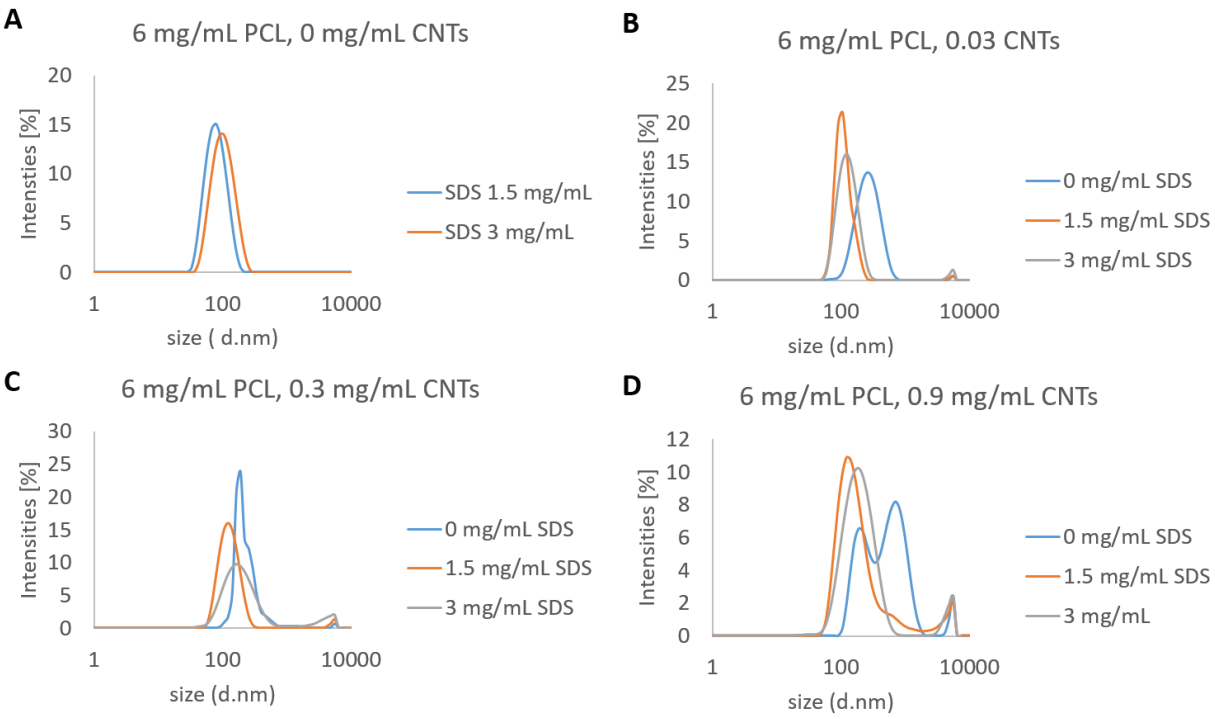

Figure 2.7. Intensity size distribution by DLS for samples of varying composition. A) Samples consisting of: 6mg/mL PCL, 0 mg/mL CNTs and either 1.5 or 3 mg/mL of SDS. B) Samples consisting of: 6 mg/mL PCL, 0.03 mg/mL CNTs and either 0, 1.5 or 3 mg/mL of SDS. C) Samples consisting of: 6 mg/mL PCL, 0.3 mg/mL CNTs and either 0, 1.5 or 3 mg/mL of SDS. D) Samples consisting of: 6 mg/mL PCL, 0.9 mg/mL CNTs and either 0, 1.5 or 3 mg/mL of SDS.

Selected samples were then further characterised by scanning electron microscopy (SEM) to provide information on the morphology and particle size in the dried state, as shown in Figure 2.8. In order to minimise charging during imaging the samples were sputter-coated with gold. All the samples appeared to have agglomerated upon drying. The length and width of the particles was then determined from the SEM images. When no SDS was used large spherical particles (392-659 nm depending on CNTs concentration) were obtained with diameters approximately matching those

determined by DLS. As previously mentioned, it is likely that in the absence of surfactant the interfacial tension between the water and DCM resulted in droplet coalescence. When the concentration of the CNTs was increased it resulted in particles with more irregular, less spherical morphology. At higher concentrations of SDS (1.5 mg/mL and 3 mg/mL) and with CNTs present, rod-like morphologies were observed for all samples, these structures closely resemble those previously reported in the literature for PCL-CNT nanocomposites prepared by a covalent modification with either a "grafting from" approach[56] or click chemistry method.[57] This behaviour was likely due to the SDS lowering the interfacial tension between the DCM and the aqueous continuous phase resulting in smaller emulsion drops. The CNTs will preferentially be wetted by DCM rather than water due to the hydrophobic nature of CNTs.[58] As the diameter of a DCM droplet approaches the length of the CNT dispersed within the droplet there is the potential for the CNT to be exposed to the surrounding aqueous continuous phase as the DCM evaporates. Minimisation of the interfacial energy of the system will lead to the DCM-water interface growing rather than create new CNT-water interface. This behaviour would likely result in a non-spherical droplet being formed. It can then be expected that as the DCM continued to evaporate the PCL would be deposited onto the surface of the CNT. These experiments suggest that the presence of the surfactant would have allowed smaller droplets of DCM containing the PCL and CNTs to form, upon evaporation of the DCM non-spherical nanomaterials were then formed (see Figure 2.9 for a visual representation of this hypothesis).

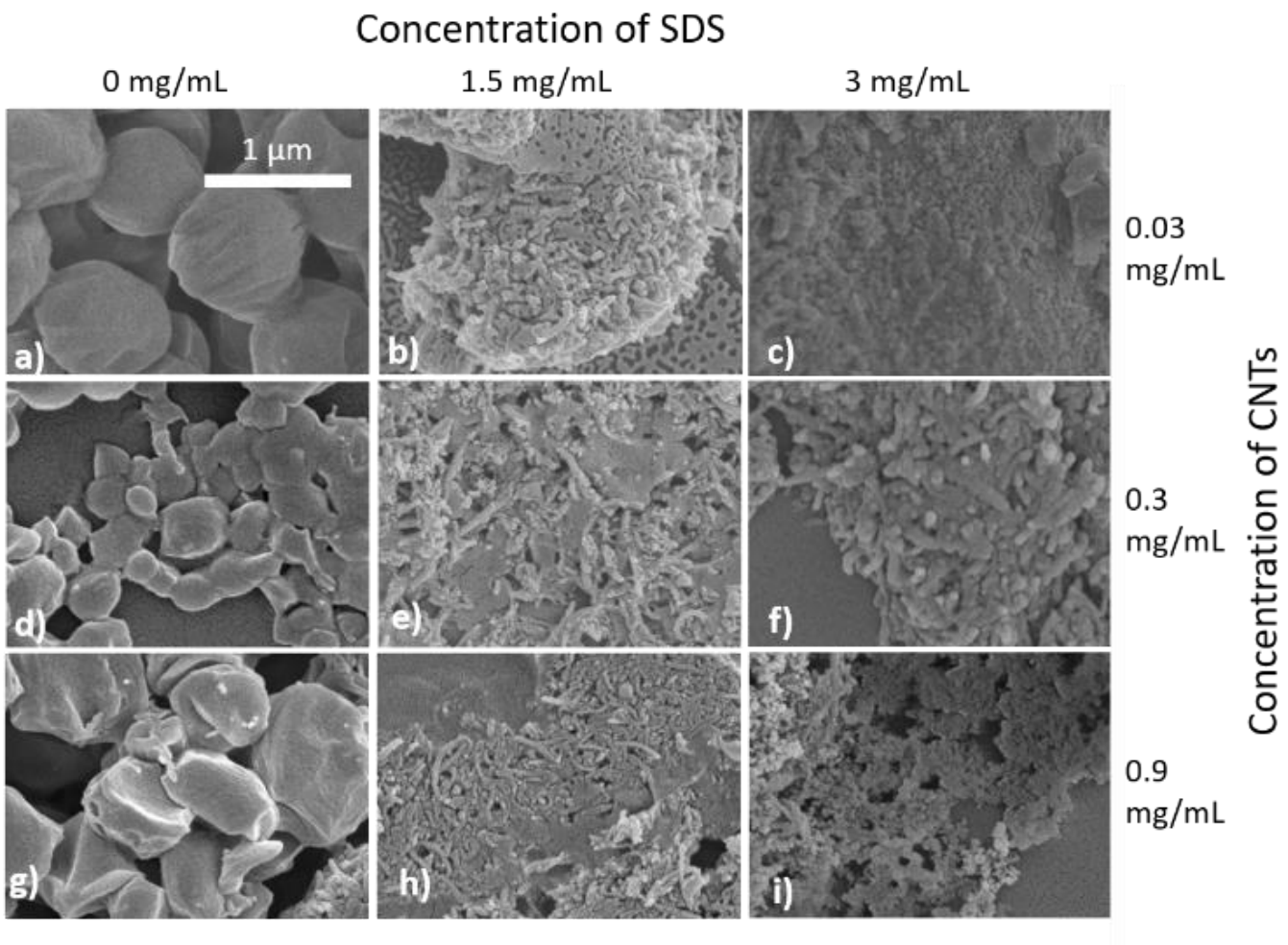

Figure 2.8. SEM images of the nanomaterials showing the influence of SDS and CNT concentration on the different sizes and morphologies of the nanocomposites of PCL/ CNTs. a) 6 mg/mL of PCL, 0.03 mg/mL of CNTs and 0 mg/mL SDS b) 6 mg/mL of PCL, 0.03 mg/mL of CNTs and 1.5 mg/mL of SDS c) 6 mg/mL of PCL, 0.03 mg/mL of CNTs and 3 mg/mL of SDS d) 6 mg/mL of PCL, 0.3 mg/mL of CNTs and 0 mg/mL of SDS e) 6mg/mL of PCL, 0.3 mg/mL of CNTs and 1.5 mg/mL of SDS f) 6 mg/mL of PCL, 0.3 mg/mL CNTs and 3 mg/mL of SDS g) 6 mg/mL of PCL, 0.9 mg/mL of CNTs and 0 mg/mL of SDS h) 6 mg/mL of PCL, 0.9 mg/mL of CNTs and 1.5 mg/mL of SDS i) 6 mg/mL of PCL, 0.9 mg/mL of CNTs and 3 mg/mL of SDS. All samples were dispersed in 4 mL of distilled water. Scale bar applies to all images.

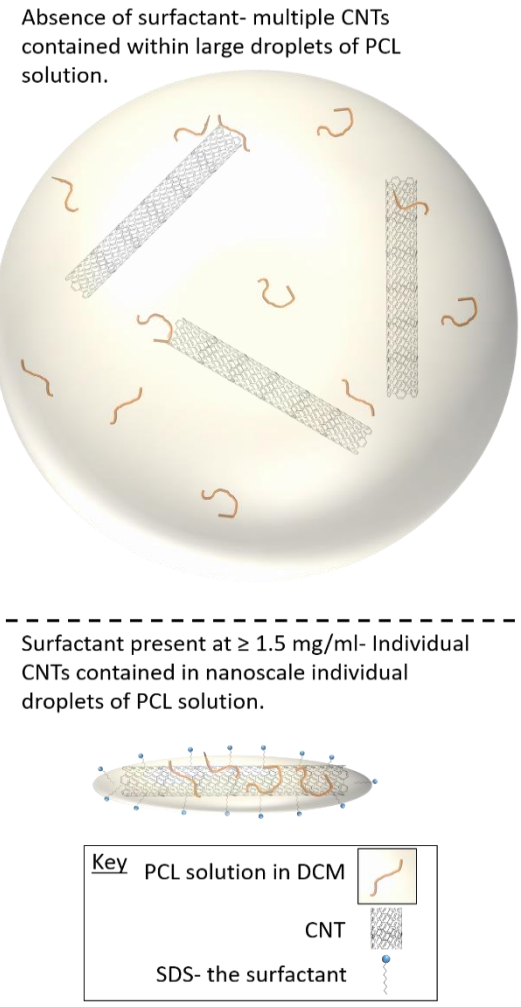

Figure 2.9. Cartoon representation of how the surfactant concentration during the emulsification process influences the morphology of the nanocomposites.

The PCL-CNT nanocomposites displayed colloidal stability in water for at least 5 days with very little change in the mean diameter and polydispersity over that time period (Figure 2.10. Graph shows hydrodynamic diameters (nm) and polydispersity (PdI) versus time (h) obtained from DLS for samples in distilled water at 37 ˚C.). Graphs shows hydrodynamic diameter (nm) and polydispersity index (PdI) versus time (h) obtained from DLS for samples in distilled water at 37 ºC. In phosphate buffered saline, a common mimic for physiological fluids, the nanocomposites showed colloidal instability as the ions in the salt screened out the electrostatic stabilisation of the particles (Figure 2.11).

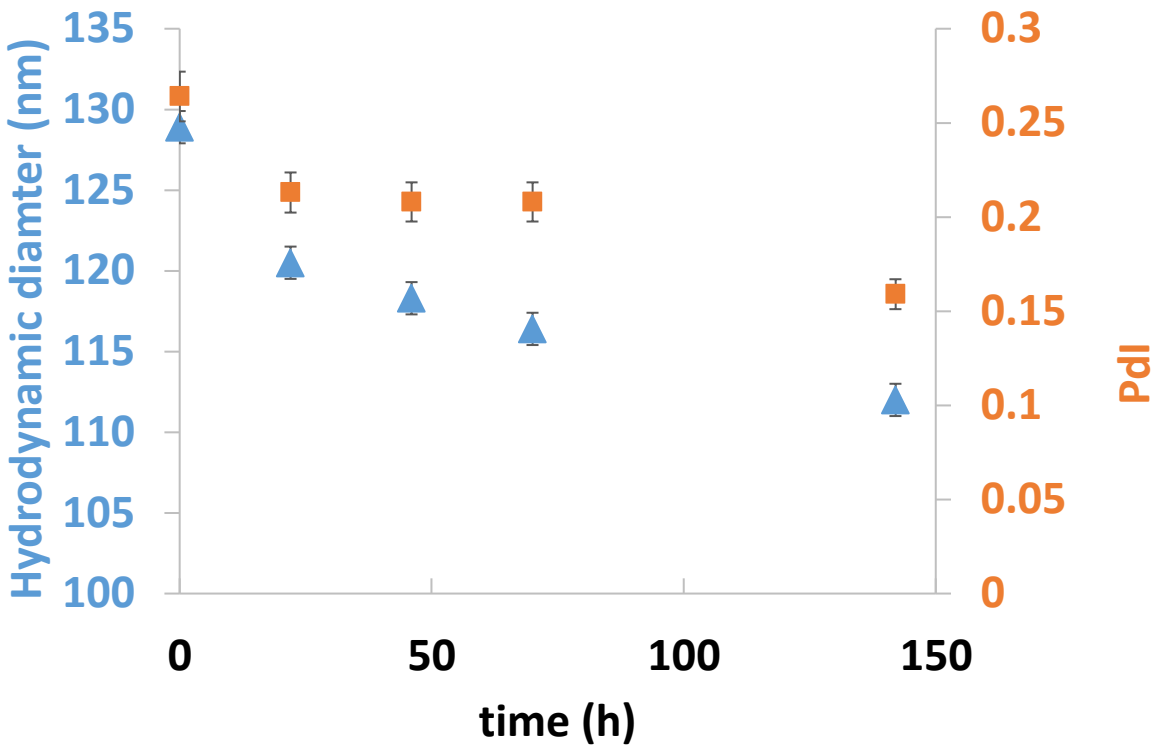

Figure 2.10. Graph shows hydrodynamic diameters (nm) and polydispersity (PdI) versus time (h) obtained from DLS for samples in distilled water at 37 ˚C.

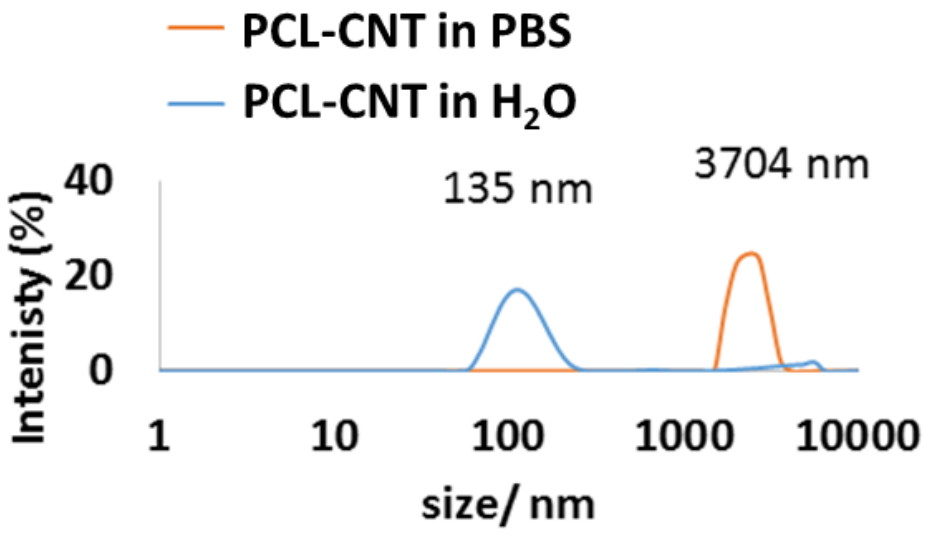

Figure 2.11. Graph shows size i.e. hydrodynamic diameters [nm] versus intensities [%] obtained from DLS for samples in distilled water and Phosphate buffer saline (PBS) incubated for 15 min.

It is likely that this issue with aggregation in PBS could be addressed in the future by the use of a polymer stabiliser that will provide steric stabilisation to the nanocomposites. The reproducibility of synthesis of the PCL-CNT samples was also tested, three selected samples were reproduced, in these the concentration of PCL used 3 mg/mL and with differing concentrations of CNTs (0.01-0.3 mg/mL) and SDS (0-1 mg/mL). In each case the standard deviations (σ) of the replicates were found to be less than 10% of the mean diameter of the sample (Figure 2.12).

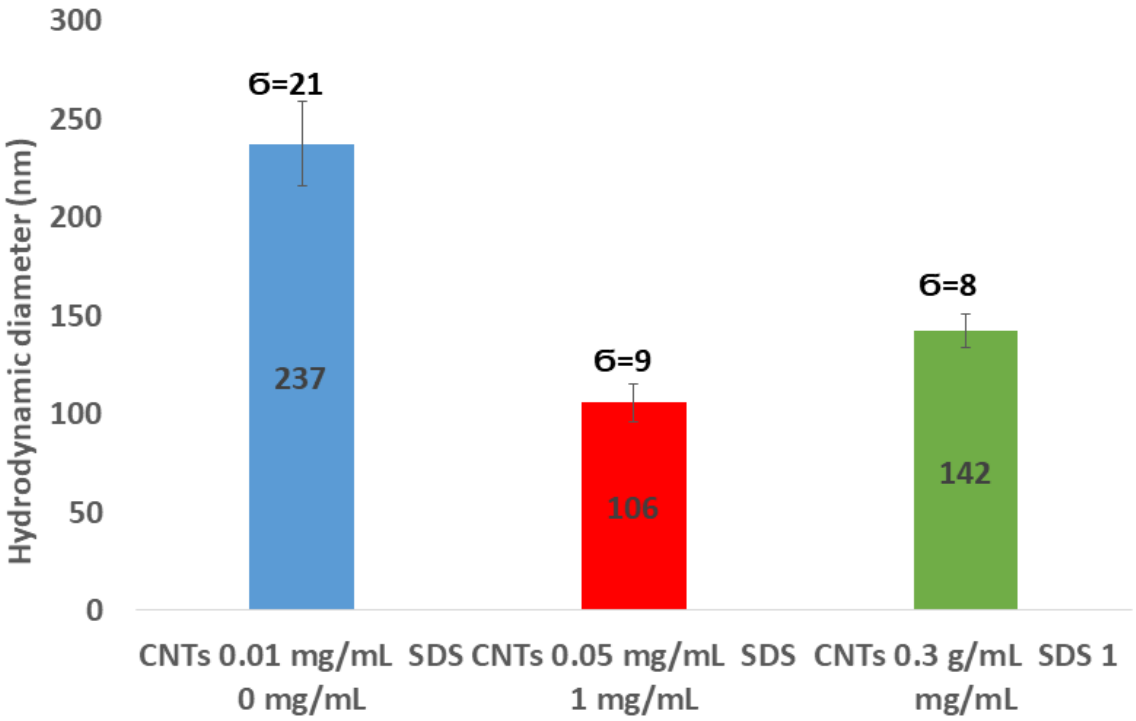

Figure 2.12. Example of results for reproducibility for samples obtained with 3 mg/mL of PCL. The synthesis was repeated 3 times.

This consistent reproducibility showed that the oil-in water emulsion solvent evaporation method is a robust and reliable process for obtaining non-spherical nanomaterials. From the range of concentrations that were tested, a single formulation was selected for each type of nanodispersion: PCL alone nanoparticles, a CNT alone dispersion and a PCL-CNT nanocomposite (see Table 2.2). These samples were then prepared for further analysis and comparison between the properties of the different nanostructures.

Table 2.2. Summary of the concentrations and compositions of the samples of PCL nanoparticles, CNT dispersion and PCL-CNT nanocomposites prepared for further investigation.

Sample	Concentrations used in sample preparation (mg/mL)			Composition (%)	
	PCL	CNTs	SDS	PCL	CNTs
PCL	10	0	1.5	100	0
CNTs	0	0.9	1.5	0	100
PCL-CNTs	10	0.9	1.5	93	7

2.3.3. The morphology and properties of the sample as studied by AFM, SEM and TGA

SEM and AFM characterisation were then conducted to further investigate the surface, morphology and mechanical properties of the PCL-CNT nanocomposite; this was compared to PCL nanoparticles and CNTs alone (Figure 2.13). The same regions of each sample was imaged by both SEM and AFM, however, it was not possible to image precisely the same location with both techniques. In the preparation of these samples no gold coating was used for the SEM as this would invalidate the mechanical characterisation of the sample by AFM analysis. Therefore, in order to prevent surface charging the SEM was operated in deceleration mode, which led to a slight reduction of the image quality. As before, the sample of PCL alone consisted of spherical particles with a mean diameter of 382 nm and appeared to agglomerate upon drying (Figure 2.13A).

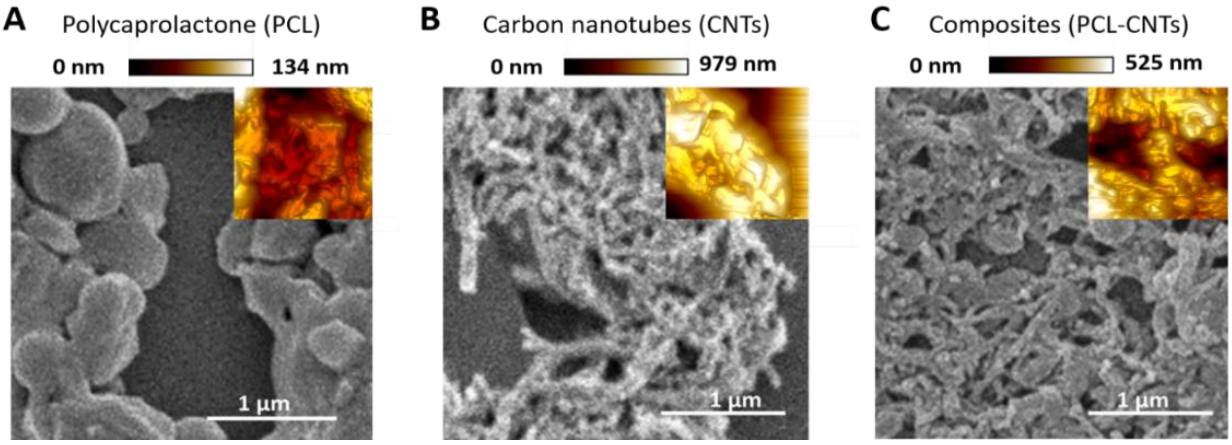

Figure 2.13. Analysis of the PCL, CNT and PCL-CNT (93% PCL, 7% CNTs by mass) nanocomposites by SEM and AFM (inset): A) PCL alone, B) CNTs and C) PCL-CNTs composites. The AFM images are based on the peak force error measurements. The AFM images were not obtained from the same region shown in the SEM image, but have been inset so as to assist direct comparison with the morphologies revealed both techniques at the same scale. The scale bar applies to both the SEM images and inset AFM images

Analysis of the sample of CNTs alone revealed fibres with varying lengths (200-795 nm with a mean length 324 nm and width 53 nm) (Figure 2.13B), a similar morphology was observed for the nanocomposite sample containing both PCL and CNT (Figure 2.13C) where the sample consisted of high aspect ratio fibres with a mean width of 55 nm and mean length of 172 nm (see SI, Figure 2.20- Figure 2.22). Due to the agglomeration upon drying, the length measurements should be interpreted with caution because it was often unclear where one non-spherical nanoparticle ended, however, the larger widths of the PCL-CNTs nanocomposites compared to the CNTs alone suggested that the PCL has deposited on the surface of the CNTs. The SEM characterisation data provides an evidence that the process of combining the PCL and CNTs in the same phase during the oil-in water emulsion solvent evaporation method results in nanocomposite rods that consist of CNTs coated in PCL.

In order to provide more evidence for the preparation of PCL/CNT nanocomposites AFM was utilised to characterise the samples and measure the elastic modulus of all three samples (AFM images are shown as insets in Figure 2.13). Literature values for the elastic modulus of PCL and CNT are 600 MPa[59] and 1 TPa[60] respectively. AFM nanomechanical analysis measures the properties associated with 2 nm depth surface of material,[44] therefore a modulus for

approximately 600 MPa was expected in the event of successful PCL-CNT nanocomposites. The Peakforce quantitative nanoscale mechanical method relies on the selection of an appropriate stiffness cantilever depending on the expected elastic modulus of the sample. However, no probe of an appropriate stiffness was available for the CNTs. Hence, we conducted all the AFM experiments using the same probe. The probe used in this experiment (TAP525) is recommended by the manufacturer (Bruker) for samples with elastic modulus values in the range 1-20 GPa. Therefore, it was not possible to obtain reliable modulus values for the CNTs alone. However, analysis of the DMT[61] modulus for both the PCL and PCL-CNT nanocomposite provide comparatively similar values of 770 and 560 MPa respectively, indicating that all the CNTs have been coated with at least 2 nm of PCL. The moduli of both samples were consistent across the surfaces, and no regions of very high modulus were observed in the nanocomposite sample which would have indicated uncoated CNTs (see Figure 2.14).

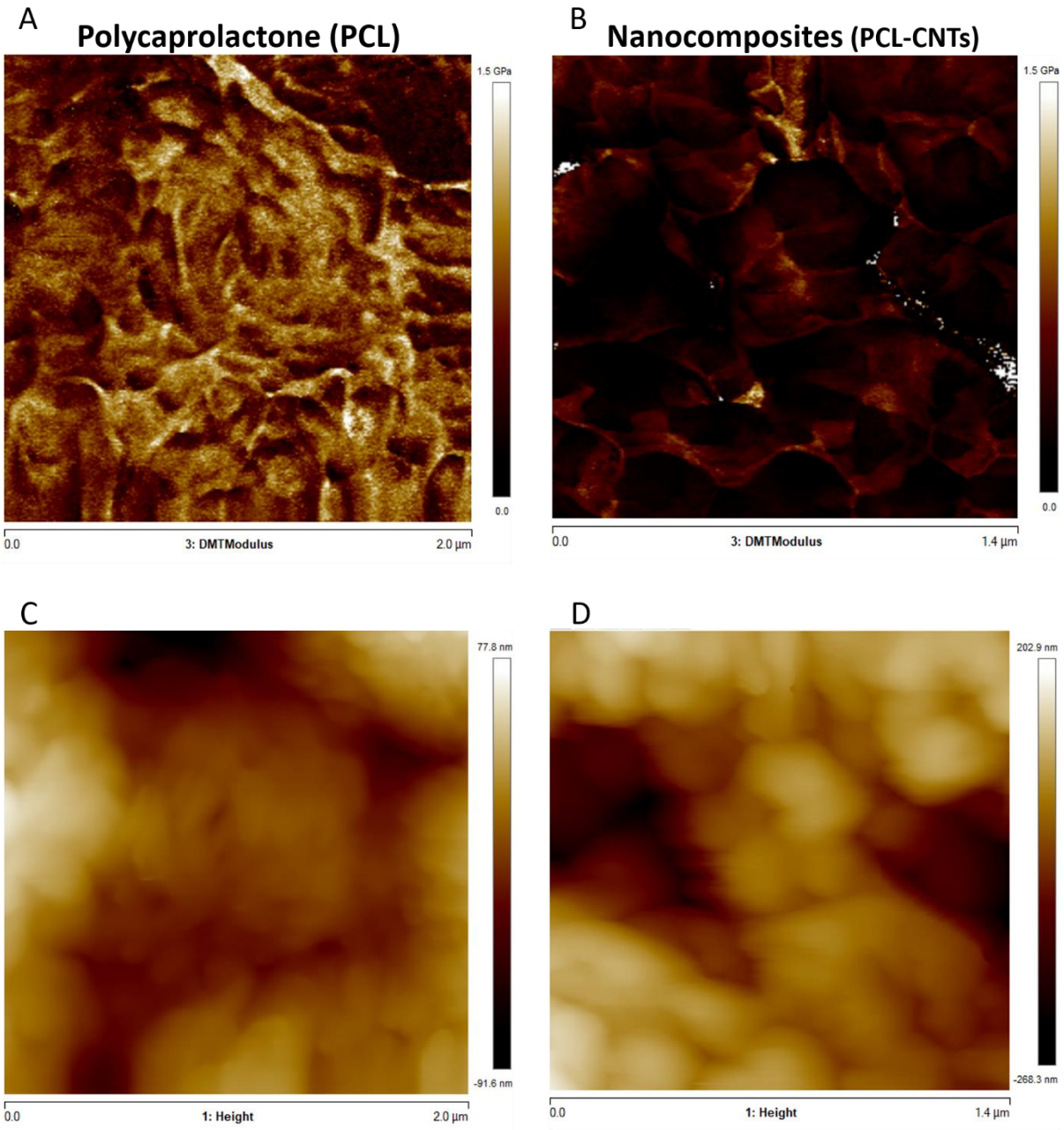

Figure 2.14. Analysis of the PCL and PCL-CNT nanocomposites by AFM to provide the DMT modulus and surface height. (A and B) show the DMT modulus for PCL and PCL-CNT nanocomposites. (C and D) show the heights for PCL and PCL-CNT nanocomposites.

While the nanocomposites showed a similar surface modulus to that of PCL, it is likely that high modulus of the CNT would mean that the bulk modulus of the nanocomposites would be comparable, this could be of particular interest for drug delivery applications as it has previously been shown that materials with higher moduli display greater cellular uptake.[62] The fibrous morphology observed for the PCL-CNT sample by SEM and the stiffness as

determined by AFM further supports the concept that the CNTs have been coated with PCL to give high aspect ratio nanocomposites. Thermo-gravimetric analysis (TGA) was also used to provide information on the thermal stability and CNT content of the PCL-CNT nanocomposites.[56,63,64] The decomposition behaviour of the CNTs and PCL nanoparticles and PCL-CNT nanocomposites are shown in Figure 2.15. The CNTs were found to show thermal stability over the temperature range tested, in agreement with the literature.[65] Literature data on SDS alone has previously shown to display a mass loss commencing at 200°C until 300°C at which 73% of the mass of the compound has been lost,[65] while PCL has been shown to degrade when heated above 360°C under inert atmosphere with no residue mass remaining at 500°C.[66] In the context of this information, the start of degradation for the sample of PCL nanoparticles stabilised by SDS began at approximately 210°C which was likely due to the degradation of the SDS up to approximately 300°C where the data exhibits a shoulder. This TGA curve steepens abruptly at ca. 345°C that is likely associated with the start of the degradation of the PCL. Above 400°C very little further mass loss was noted and the residue mass of 19.6% at 600°C was due to the SDS. For the PCL-CNT nanocomposite sample, the onset of the mass loss was approximately 220°C which also corresponded to the degradation SDS within the nanocomposite. The increase in the degradation temperature of the SDS could potentially suggest that the formation of the nanocomposite structure has increased the thermal stability of the SDS in the nanocomposite. A slight shallowing of the TGA curve was observed at 290°C which may be associated with completion of the SDS degradation. The curves steepen again around 345°C, which may be associated with the PCL beginning to degrade. This effect was less pronounced in the PCL-CNT nanocomposite compared to the PCL nanoparticles which may be due to the presence of the CNT in the nanocomposite altering the degradation behaviour of the PCL.[57] Above 400°C no further mass loss was seen for the nanocomposite and the residue mass at 600°C was 29.2%. The PCL-CNT nanocomposite showed a higher residue mass compared to the PCL alone nanoparticles. This 9.6% of the mass can be attributed to the CNTs present within PCL-CNT nanocomposites, which matches a literature value of 10% for PCL grafted CNTs.[57] This mass is higher than expected (the theoretical composition of the sample was 93% PCL, 7% CNTs by mass) and may be attributed to a slight increase in the concentration of the CNT dispersion due to some evaporative loss of DCM during sonication prior to the emulsification.

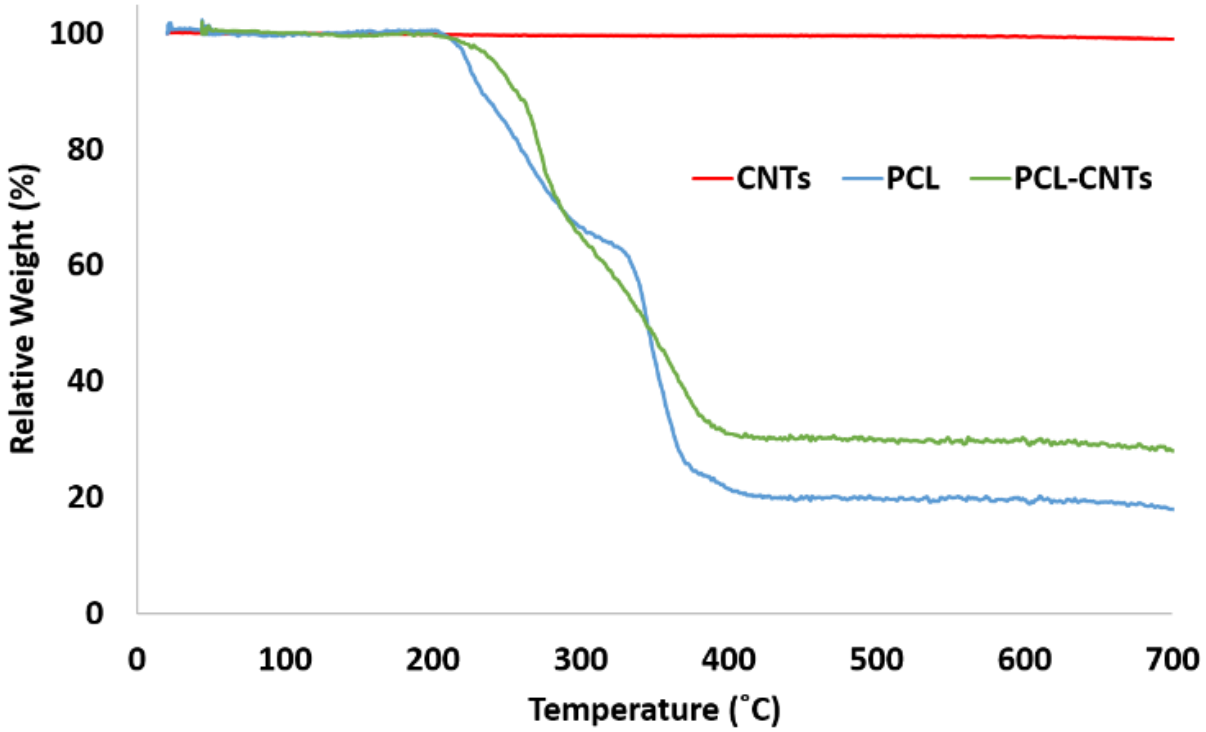

Figure 2.15. Analysis of the PCL-CNT (93% PCL, 7% CNTs by mass) nanocomposite and its constituents by TGA. The concentrations used during preparation were 10 mg/mL of PCL and 1.5 mg/mL SDS for PCL; 10 mg/mL of PCL, 1.5 mg/mL SDS and 0.9 mg/mL CNTs for PCL-CNTs. CNTs consists of 0.9 mg/mL CNTs alone

2.3.4. Fractionation of the particles by asymmetric flow field flow fractionation and measurements of hydrodynamic diameters

Next, the PCL alone and the PCL-CNT nanocomposite samples were further analysed by asymmetric flow field flow fractionation with the aim of obtaining high resolution sizing of the nanoparticles in the dispersed state. High resolution sizing would make it possible to determine if the PCL/CNT nanocomposites consisted of a single population of particle rather than resulted in two separate populations of PCL or CNTs alone. Asymmetric flow field flow fractionation separates samples based on hydrodynamic diameter[67] with smaller particles eluting before larger particles, the fractionated sample then passes through inline detectors to determine the diameter of the particles. The separation conditions were chosen from previous studies of CNTs.[42] Figure 2.16 shows the data for the asymmetric flow field flow fractionation analysis of the samples combining the absorbance from UV-VIS detector and

Z-average diameter as measured by inline DLS. The UV-Vis detector was set to a wavelength of 300 nm, chosen based on absorbance spectra of PCL and CNTs, and thus provides information on the concentration of the particles. The samples showed good separation and the absence of a void peak revealed that aggregation has not occurred in the system. The sample that consisted of PCL alone was found to consist of a higher dynamic diameter distribution between 11 nm and 115 nm, with the mode of the UV-Vis measurement equating to a diameter of 93 nm. The size range of PCL-CNTs sample was between 11 nm and 350 nm with the mode of the UV-Vis measurement equating to a diameter of 138 nm. A sample of CNT alone was also analysed but is not directly comparable to the PCL and nanocomposites, the uncoated CNT surface will likely have a different interaction with the membrane in the AF4 compared to the other samples with the PCL coating which may have resulted in different elution behaviour. The CNTs alone consisted of a distribution of 16 to 187 nm (see Figure 2.17).

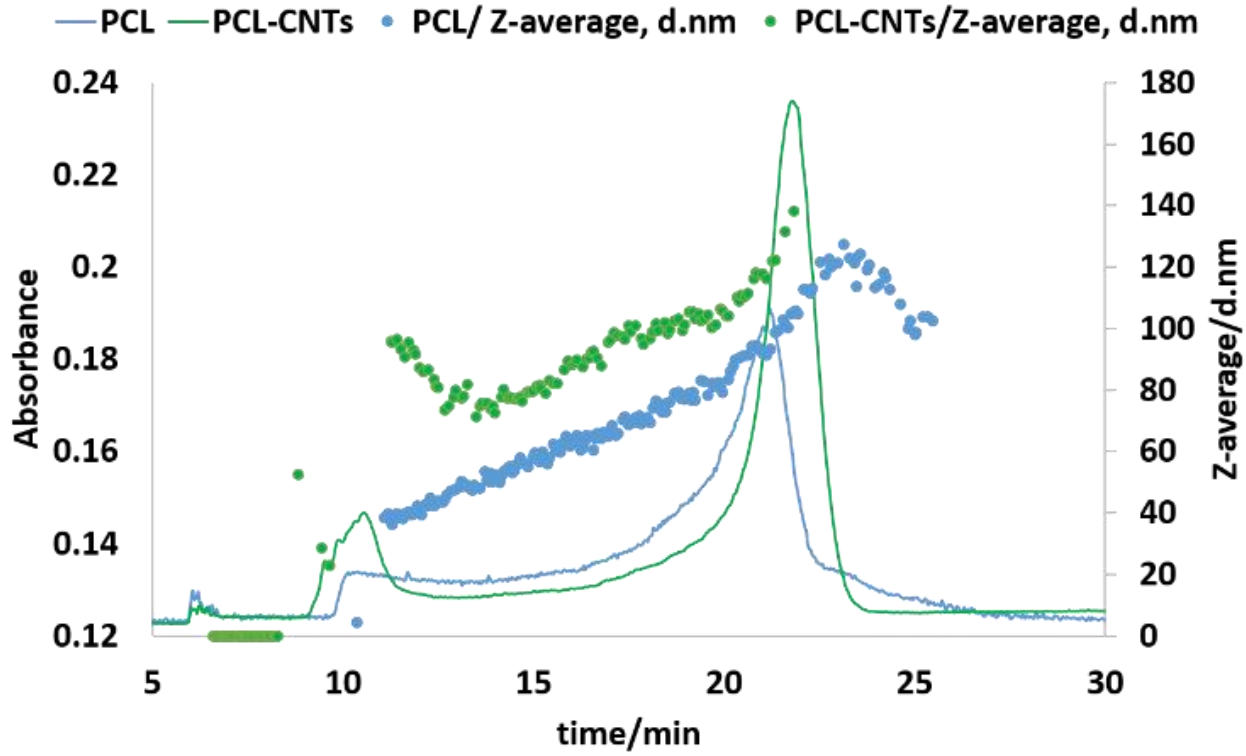

Figure 2.16. Fractogram of PCL and PCL-CNTs (93% PCL, 7% CNTs by mass) obtained from asymmetric flow field flow fractionation coupled online with UV-VIS detector. Hydrodynamic diameters were obtained from DLS coupled online.

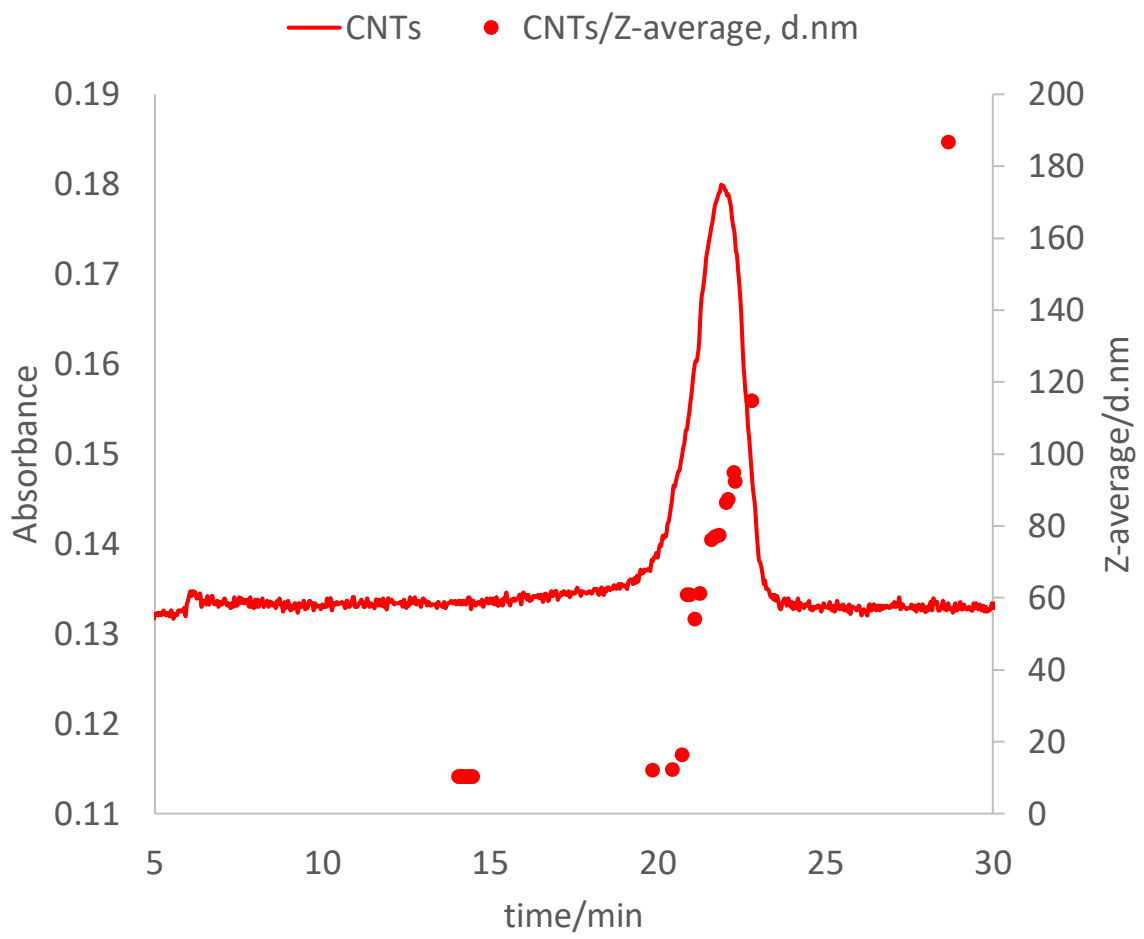

Figure 2.17. Fractogram of CNTs obtained from asymmetric flow field flow fractionation coupled online with UV-VIS detector. Hydrodynamic diameters were obtained from DLS coupled online.

The PCL-CNT nanocomposites were found to have larger hydrodynamic diameters compared with pristine CNTs and PCL alone. The measurements obtained from the detector coupled online with asymmetric flow field flow fractionator showed higher intensity for PCL-CNTs compared to the PCL and CNT, which was due to the higher concentration of PCL-CNTs composites in the sample than PCL and CNT alone.

As previously stated, asymmetric flow field flow fractionation separates a sample based on the hydrodynamic diameter; particles of the same diameter should elute at the same time. However, as shown in Figure 2.16, PCL or PCL-CNT nanocomposite particles with the same hydrodynamic diameter eluted at considerably different times. The PCL-CNT nanocomposites tended to elute before the PCL alone particles. Similar behaviour for non-spherical particles

has been published by Gigault *et al*. in which they showed that longer gold nanorods (GNRs) with the same diameters eluted earlier than shorter GNRs.[68] It has been suggested that elution of non-spherical particles depends on an aspect ratio and steric-entropy contribution associated with their orientation. Gigault *et al*. suggested that GNRs located higher in the channel elute faster than associated closer to the membrane. We believe that the earlier elution of the PCL-CNT nanocomposites compared to the spherical PCL alone nanoparticles was due to their higher aspect ratio of the nanocomposites.

2.3.5. Drug loading and release

Finally, the drug loading and release from PCL, CNTs and PCL-CNTs nanocomposites was investigated. In this work docetaxel, an effective anticancer drug[69–71] was used. Docetaxel (DCX) has some clinical limitations associated with its poor water solubility.[72] The anticancer drug was encapsulated in the nanocomposite carriers, while PCL alone and CNTs alone were also tested as controls. Drug encapsulation was achieved by including DCX into the oil phase for the particle preparation. The resulting DCX loaded samples were analysed by DLS (as an unfractionated sample) to provide a mean diameter, PdI and distribution plot. Table 2 shows the DLS results for PCL, CNT and PCL-CNTs. The nanocomposites showed larger mean diameters compared with PCL and pristine CNT. The DLS distribution graph for the PCL alone sample was monomodal (see Figure 2.18).

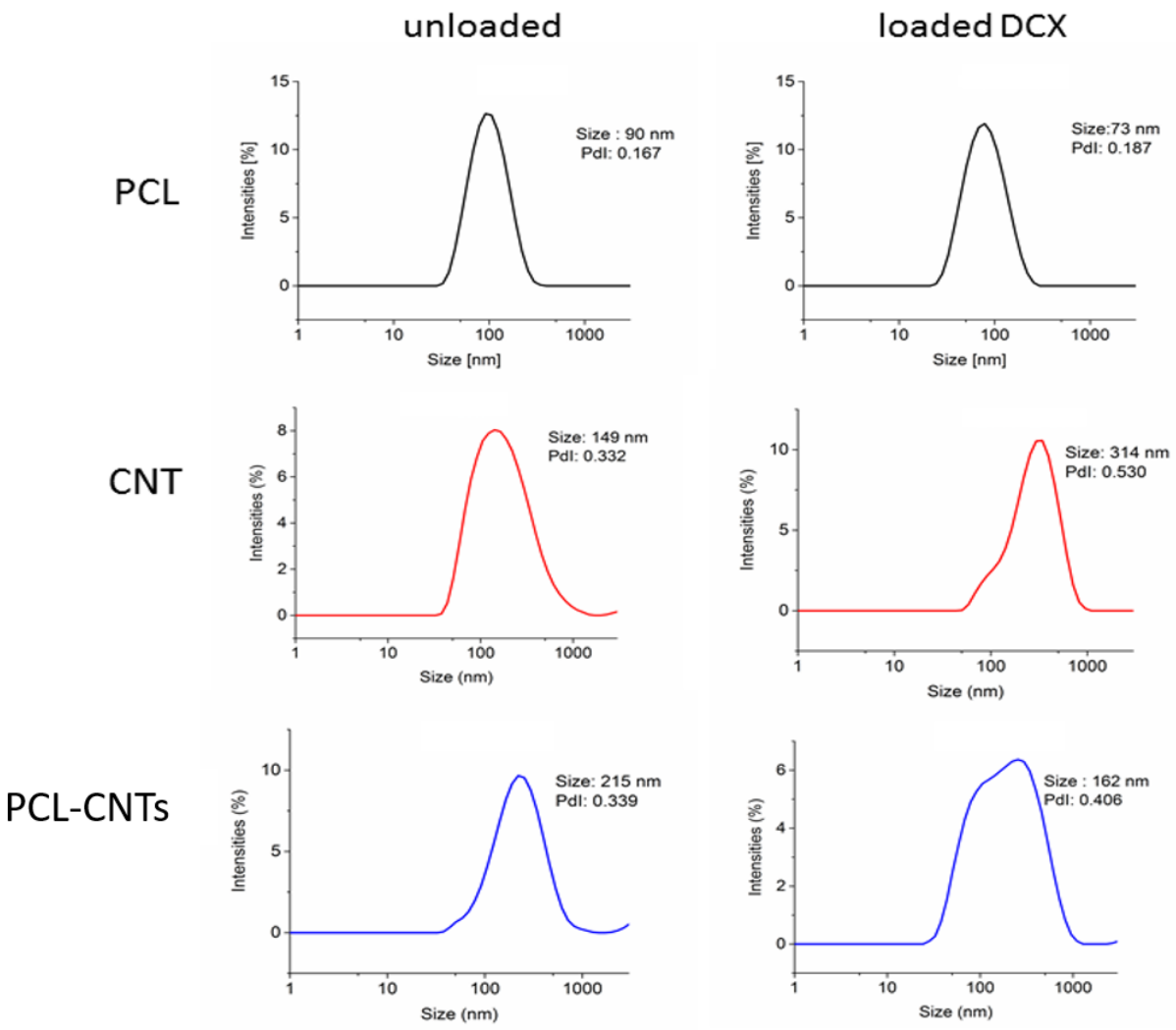

Figure 2.18. Graph shows size i.e. hydrodynamic diameters (nm) versus intensities (%) obtained from DLS for unloaded and loaded with DCX particles of PCL, CNTs and composites.

The CNTs and PCL-CNTs have a PdI of 0.33 which means that the distribution is broader than the PCL alone particles, this is likely due to the polydisperse nature of the CNTs themselves which gave a PdI value of 0.33. Hydrodynamic diameter and PdI of the three samples were also measured after encapsulation of DCX. The size and PdI of CNTs alone were higher compared with unloaded CNTs alone. These results potentially indicate that molecules of anti-cancer drug adsorbed to the surface of the CNTs may have possibly resulted in some aggregation of the CNTs. The properties of CNTs have previously shown that loading via π- π stacking is possible for DCX.[73] It was found that after encapsulation, PCL and PCL-CNTs showed a lower diameter and PdI. In this case it is possible another type of interaction between the

PCL/CNTs and DCX may have altered the size of the PCL - DCX nanoparticles and PCL-CNTs - DCX nanocomposites. The entrapment efficiency (EE) was also analysed by HPLC (EE_{CNT} = 95%, EE_{PCL}= 81% and $EE_{PCL-CNT}$ = 89%).

Table 2.3. Summary of the diameter and PdI for samples without and with encapsulated DCX obtained from DLS

	unloaded		loaded DCX	
	Z-average/diameter nm	PdI	Z-average/diameter nm	PdI
PCL	90±1	0.160± 0.008	73±6	0.180± 0.009
CNTs	149±7	0.330± 0.007	314±10	0.530± 0.034
PCL-CNTs	215±8	0.330± 0.013	162±5	0.400± 0.019

In vitro release experiments were then conducted to observe the drug release behaviour of the nanocomposites. The drug released over time is presented in Figure 2.19.

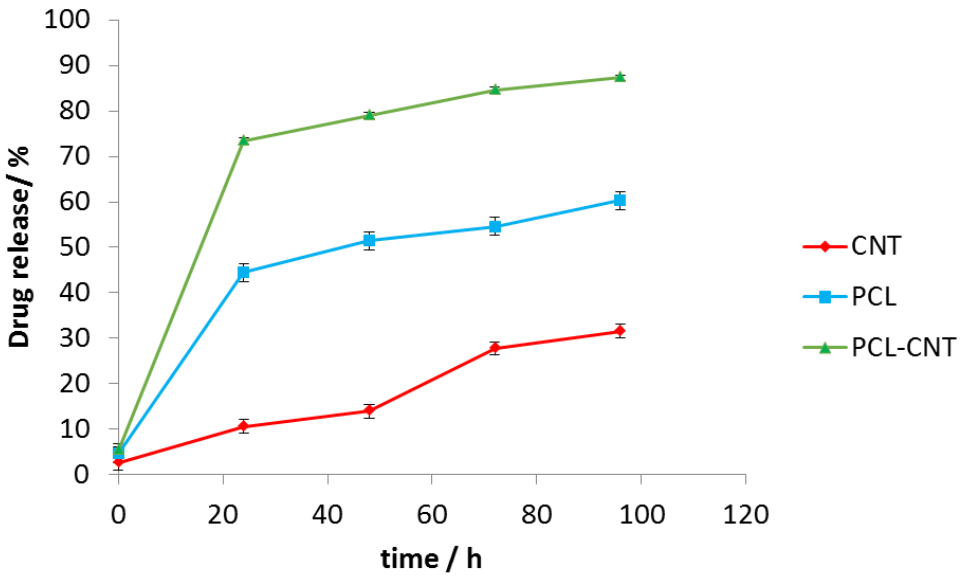

Figure 2.19. The graph presents docetaxel releasing study (% of drug released vs. time) for CNTs, PCL and PCL-CNTs (93% PCL, 7% CNTs by mass) obtained from HPLC analysis. The data showed three different profiles for releasing anti-cancer drug

The nanocomposites and CNT alone encapsulated more anti-cancer drug compared with PCL alone. The release of DCX from different systems has been studied previously.[74,75] In those studies, the authors showed that pH, temperature, solvent and type of carrier have an effect on drug release. Our release data showed that DCX is released most rapidly from the PCL-CNTs. The slowest profile was found with the CNTs alone with 31% of the drug released in 96 hours matching the DCX release behaviour from CNTs previously shown in the literature.[76,77] The difference in the release profiles between the CNTs and the PCL-CNT nanocomposites may be due to the different structures of the nanocarriers. In the case of the PCL-CNT nanocomposites, the PCL coating the surface may have disrupted the ability for the DCX to adsorb onto the CNT. This is supported by the literature in which it is stated that drug release behaviours from CNTs are altered when different polymer surface functionalisations are present.[76] No degradation of the drug was detected after the drug release from all of the samples (examples of the chromatograms obtained from HPLC analysis are shown in the SI, Figures 2.23-Figure 2.26). These findings show that not only can the PCL-CNT successfully encapsulate DCX but also has the ability to release it. More interestingly, the difference in the release behaviour of DCX from the different samples suggests that there is a potential to tune the release profile by varying the composition of the nanocomposites.

2.4. Conclusions

In this chapter, PCL nanoparticles were prepared by oil-in-water emulsion solvent evaporation method. The different concentration of PCL and concentration of different surfactant have been checked whether they have influence on hydrodynamic diameter and PdI of nanoparticles. The presence of surfactant SDS in the synthesis showed the ability to create the smallest size and PdI (<0.2) for PCL nanoparticles. PCL-CNT nanocomposites were prepared by a facile oil-in water emulsion solvent evaporation method. This approach produced rod-like, non-spherical nanoparticles. Different sizes and morphologies of nanoparticles were produced depending on the concentration of SDS, CNTs and PCL. The samples with rod-like morphologies and the lowest diameter and PDI were synthesised using 1.5 mg/mL of SDS, 0.9 mg/mL of CNTs and 10 mg/mL PCL. The AFM analysis revealed that the

incorporation of the CNTs in the nanocomposites did not increase the modulus of the particles, including the successful surface coverage of the CNTs with PCL. In addition, TGA analysis of the PCL-CNT nanocomposite also showed that they contained 9.6% CNTs by mass. Asymmetric flow field flow fractionation measurements showed good separation of particles and the PCL-CNTs had higher hydrodynamic diameters than PCL and CNTs alone. DCX loading in PCL, CNTs and PCL-CNTs were determined by HPLC and showed high entrapment efficiencies (CNT = 95%, PCL= 81% and PCL-CNT = 89%). Moreover, faster release of DCX from PCL-CNTs was observed with about 90% of the drug released from the nanocarriers after approximately 100 h.

To the best of our knowledge this is the first example of producing high-aspect ratio PCL-CNT nanocomposites using a simple oil-in water emulsion solvent evaporation method. The high entrapment efficiencies of the nanocomposites offer the potential for these nanocomposites to be used in drug delivery applications. We hypothesise that the needle-like morphology and high modulus of the nanocomposites will enhance the cellular uptake of anticancer drugs and the coating with PCL will potentially reduce any cytotoxicity associated with the pristine CNTs.

2.5. References

1 S. Gelperina, K. Kisich, M. D. Iseman and L. Heifets, *Am. J. Respir. Crit. Care Med.*, 2005, **172**, 1487–1490.

2 I. Brigger, C. Dubernet and P. Couvreur, *Adv. Drug Deliv. Rev.*, 2002, **54**, 631–651.

3 A. C. Anselmo and S. Mitragotri, *Bioeng. Transl. Med.*, 2016, **1**, 10–29.

4 A. Banerjee, J. Qi, R. Gogoi, J. Wong and S. Mitragotri, *J. Control. Release*, 2016, **238**, 176–185.

5 R. Toy, P. M. Peiris, K. B. Ghaghada and E. Karathanasis, *Nanomedicine (Lond)*, 2014, **9**, 121–134.

6 A. Sen Gupta, *Wiley Interdiscip. Rev. Nanomedicine Nanobiotechnology*, 2016, **8**, 255–270.

7 H. Meng, S. Yang, Z. Li, T. Xia, J. Chen, Z. Ji, H. Zhang, X. Wang, S. Lin, C. Huang, Z. H. Zhou, J. I. Zink and A. E. Nel, *ACS Nano*, 2011, **5**, 4434–4447.

8 P. P. Wibroe, A. C. Anselmo, P. H. Nilsson, A. Sarode, V. Gupta, R. Urbanics, J. Szebeni,

A. C. Hunter, S. Mitragotri, T. E. Mollnes and S. M. Moghimi, *Nat. Nanotechnol.*, 2017, **12**, 589–594.

9 S. Kumar, A. C. Anselmo, A. Banerjee, M. Zakrewsky and S. Mitragotri, *J. Control. Release*, 2015, **220**, 141–148.

10 A. C. Anselmo, S. Kumar, V. Gupta, A. M. Pearce, A. Ragusa, V. Muzykantov and S. Mitragotri, *Biomaterials*, 2015, **68**, 1–8.

11 J. P. Best, Y. Yan and F. Caruso, *Adv. Healthc. Mater.*, 2012, **1**, 35–47.

12 A. Kumari, S. K. Yadav and S. C. Yadav, *Colloids Surfaces B Biointerfaces*, 2010, **75**, 1–18.

13 G. Bao, S. Mitragotri and S. Tong, *Annu. Rev. Biomed. Eng.*, 2013, **15**, 253–82.

14 K. S. Soppimath, T. M. Aminabhavi and A. R. Kulkarni, *Control. release*, 2001, **70**, 1–20.

15 W. Cheung, F. Pontoriero, O. Taratula, A. M. Chen, H. He, L. Lacerda, A. Bianco, M. Prato and K. Kostarelos, *Adv. Drug Deliv. Rev.*, 2006, **58**, 633–649.

16 B. S. Wong, S. L. Yoong, A. Jagusiak, T. Panczyk, H. K. Ho, W. H. Ang and G. Pastorin, *Adv. Drug Deliv. Rev.*, 2013, **65**, 1964–2015.

17 Z. Liu, S. Tabakman, K. Welsher and H. Dai, *Nano Res.*, 2009, **2**, 85–120.

18 I. G. Denisov and S. G. Sligar, *Nat. Struct. Mol. Biol.*, 2016, **23**, 481–486.

19 S. R. Sershen, S. L. Westcott, N. J. Halas and J. L. West, *J. Biomed. Mater. Res.*, 2000, **51**, 293–298.

20 S. Lal, S. E. Clare and N. J. Halas, *Acc. Chem. Res.*, 2008, **41**, 1842–1851.

21 J. Wang, *ChemPhysChem*, 2009, **10**, 1748–1755.

22 N. Lewinski, V. Colvin and R. Drezek, *Small*, 2008, **4**, 26–49.

23 J. A. Champion, Y. K. Katare and S. Mitragotri, *J. Control. Release*, 2007, **121**, 3–9.

24 J. Chen, N. E. Clay, N. Park and H. Kong, *Chem. Eng. Sci.*, 2015, **125**, 20–24.

25 L. Lacerda, A. Bianco, M. Prato and K. Kostarelos, *Adv. Drug Deliv. Rev.*, 2006, **58**, 1460–1470.

26 D. Pantarotto, R. Singh, D. McCarthy, M. Erhardt, J. P. Briand, M. Prato, K. Kostarelos and A. Bianco, *Angew. Chemie - Int. Ed.*, 2004, **43**, 5242–5246.

27 A. De la Zerda, C. Zavaleta, S. Keren, S. Vaithilingam, S. Bodapati, Z. Liu, J. Levi, B. R. Smith, T. J. Ma, O. Oralkan, Z. Cheng, X. Chen, H. Dai, B. T. Khuri-Yakub and S. S. Gambhir, *Nat Nanotechnol*, 2008, **3**, 557–562.

28 Z. Tosun and P. S. McFetridge, *J. Neural Eng.*, 2010, **7**, 066002.

29 P. A. Tran, L. Zhang and T. J. Webster, *Adv. Drug Deliv. Rev.*, 2009, **61**, 1097–1114.

30 N. K. Mehra and S. Palakurthi, *Drug Discov. Today*, 2016, **21**, 585–597.

31 Y. P. Sun, K. F. Fu, Y. Lin and W. J. Huang, *Acc. Chem. Res.*, 2002, **35**, 1096–1104.

32 H. Kong, C. Gao and D. Yan, *J. Am. Chem. Soc.*, 2004, **126**, 412–413.

33 H. Zeng, C. Gao and D. Yan, *Adv. Funct. Mater.*, 2006, **16**, 812–818.

34 L. Meng, C. Fu and Q. Lu, *Prog. Nat. Sci.*, 2009, **19**, 801–810.

35 Z. Liu, X. Sun, N. Nakayama-Ratchford and H. Dai, *ACS Nano*, 2007, **1**, 50–56.

36 X. Zhang, L. Meng, Q. Lu, Z. Fei and P. J. Dyson, *Biomaterials*, 2009, **30**, 6041–6047.

37 H. Ali-Boucetta, K. T. Al-Jamal, D. McCarthy, M. Prato, A. Bianco and K. Kostarelos, *Chem. Commun.*, 2008, 459–461.

38 S. Mallakpour and S. Soltanian, *RSC Adv.*, 2016, **6**, 109916–109935.

39 M. A. Woodruff and D. W. Hutmacher, *Prog. Polym. Sci.*, 2010, **35**, 1217–1256.

40 C. Pinto Reis, R. J. Neufeld, A. J. Ribeiro and F. Veiga, *Nanomedicine Nanotechnology, Biol. Med.*, 2006, **2**, 8–21.

41 T. K. Dash and V. B. Konkimalla, *J. Control. Release*, 2012, **158**, 15–33.

42 J. Gigault, B. Grassl and G. Lespes, *Anal. Bioanal. Chem.*, 2011, **401**, 3345–3353.

43 M. Papi, P. Paoletti, B. Geraghty and R. Akhtar, *Appl. Phys. Lett.*,2014, 104, 103703.

44 T. J. Young, M. A. Monclus, T. L. Burnett, W. R. Broughton, S. L. Ogin and P. A. Smith, *Meas. Sci. Technol.*, 2011, **22**, 125703.

45 B. M. Rao, A. Chakraborty, M. K. Srinivasu, M. L. Devi, P. R. Kumar, K. B. Chandrasekhar, A. K. Srinivasan, A. S. Prasad and J. Ramanatham, *J. Pharm. Biomed. Anal.*, 2006, **41**, 676–681.

46 F. V Leimann, L. C. Filho and C. Sayer, *Brazilian J. Chem. Eng.*, 2013, **30**, 369–377.

47 J. Faucheu, C. Gauthier, L. Chazeau, J. Y. Cavaillé, V. Mellon and E. B. Lami, *Polymer (Guildf).*, 2010, 51, 6–17.

48 A. S. Peshkovsky, S. L. Peshkovsky and S. Bystryak, *Chem. Eng. Process. Process Intensif.*, 2013, **69**, 77–82.

49 A. Y. L. Tang, C. H. Lee, Y. M. Wang and C. W. Kan, 2018, **19**, 894–904.

50 A. Manosroi and J. Manosroi, 2003, **30**, 129–138.

51 P. Koteswari, S. R. Krishna, V. Prabhakar and R. Lakshmi, 2011, **4**, 4–5.

52 Q. Xu, A. Crossley and J. A. N. Czernuszka, 2009, **98**, 2377–2390.

53 X. Xin, H. Zhang, G. Xu, Y. Tan, J. Zhang and X. Lv, *Colloids Surfaces A Physicochem. Eng. Asp.*, 2013, **418**, 60–67.

54 L. L. Hecht, C. Wagner, K. Landfester and H. P. Schuchmann, *Langmuir*, 2011, **27**, 2279–2285.

55 K. Landfester and K. Landfester, *Top. Curr. Chem.*, 2003, **227**, 75–123.

56 H. Zeng, C. Gao and D. Yan, *Adv. Funct. Mater.*, 2006, **16**, 812–818.

57 D.-S. Park, C.-H. Oh, J.-S. Yoon, J. M. Kim, J.-H. Lim and K.-M. Kim, *Compos. Interfaces*, 2015, **22**, 193–201.

58 J. Debgupta, B. a Kakade and V. K. Pillai, *Phys. Chem. Chem. Phys.*, 2011, **13**, 14668–74.

59 O. Loh, X. Wei, K. Nandy and H. D. Espinosa, *Exp. Mech.*, 2011, **2**, 81–82.

60 K. T. Kashyap, P. G. Koppad, K. B. Puneeth, H. R. Aniruddha Ram and H. M. Mallikarjuna, *Comput. Mater. Sci.*, 2011, **50**, 2493–2495.

61 B. V Derjaguin, V. M. Muller and Y. U. P. Toporov, *J. Colloid Interface Sci.*, 1975, **52**, 105–108.

62 A. C. Anselmo and S. Mitragotri, *Adv. Drug Deliv. Rev.*, 2017, **108**, 51–67.

63 K. Saeed, S. Y. Park, H. J. Lee, J. B. Baek and W. S. Huh, *Polymer (Guildf).*, 2006, **47**, 8019–8025.

64 S. Y. Kim, J. Y. Hwang, J. W. Seo and U. S. Shin, *J. Colloid Interface Sci.*, 2015, **442**, 147–153.

65 H. K. F. Cheng, Y. Pan, N. G. Sahoo, K. Chong, L. Li, S. H. Chan and J. Zhao, *J. Appl. Polym. Sci.*, 2012, **124**, 1117–1127.

66 C. Vogel and H. W. Siesler, *Macromol. Symp.*, 2008, **265**, 183–194.

67 T. J. Cho and V. A. Hackley, *Anal. Bioanal. Chem.*, 2010, **398**, 2003–2018.

68 J. Gigault, T. J. Cho, R. I. MacCuspie and V. A. Hackley, *Anal. Bioanal. Chem.*, 2013, **405**, 1191–1202.

69 M. N. Koopaei, R. Dinarvand, M. Amini, H. Rabbani, S. Emami, S. N. Ostad and F. Atyabi, *Int. J. Nanomedicine*, 2011, **6**, 1903–1912.

70 T. Musumeci, C. A. Ventura, I. Giannone, B. Ruozi, L. Montenegro, R. Pignatello and G. Puglisi, *Int. J. Pharm.*, 2006, **325**, 172–179.

71 H. Rosing, V. Lustig, F. P. Koopman, W. W. ten Bokkel Huinink and J. H. Beijnen, *J. Chromatogr. B. Biomed. Sci. Appl.*, 1997, **696**, 89–98.

72 L. Zhang, L. Tan, L. Chen, X. Chen, C. Long, J. Peng and Z. Qian, *Sci. Rep.*, 2016, **6**, 36957.

73 K. Raza, D. Kumar, C. Kiran, M. Kumar, S. K. Guru, P. Kumar, S. Arora, G. Sharma, S. Bhushan and O. P. Katare, *Mol. Pharm.*, 2016, **13**, 2423–2432.

74 P. Jeyamohan, T. Hasumura, Y. Nagaoka, Y. Yoshida, T. Maekawa and D. Sakthi Kumar, *Int. J. Nanomedicine*, 2013, **8**, 2653–2667.

75 J. Dou, H. Zhang, X. Liu, M. Zhang and G. Zhai, *Colloids Surfaces B Biointerfaces*, 2014, **114**, 20–27.

76 R. P. Singh, G. Sharma, Sonali, S. Singh, M. Kumar, B. L. Pandey, B. Koch and M. S. Muthu, *Colloids Surfaces B Biointerfaces*, 2016, **141**, 429–442.

77 S. R. Datir, M. Das, R. P. Singh and S. Jain, *Bioconjug. Chem.*, 2012, **23**, 2201–2213.

78 L. Bokobza and J. Zhang, *Express Polym. Lett.*, 2012, **6**, 601–608.

79 M. A. Ermeydan, E. Cabane, P. Hass, J. Koetz and I. Burgert, *Green Chem.*, 2014, **16**, 3313.

Supporting information

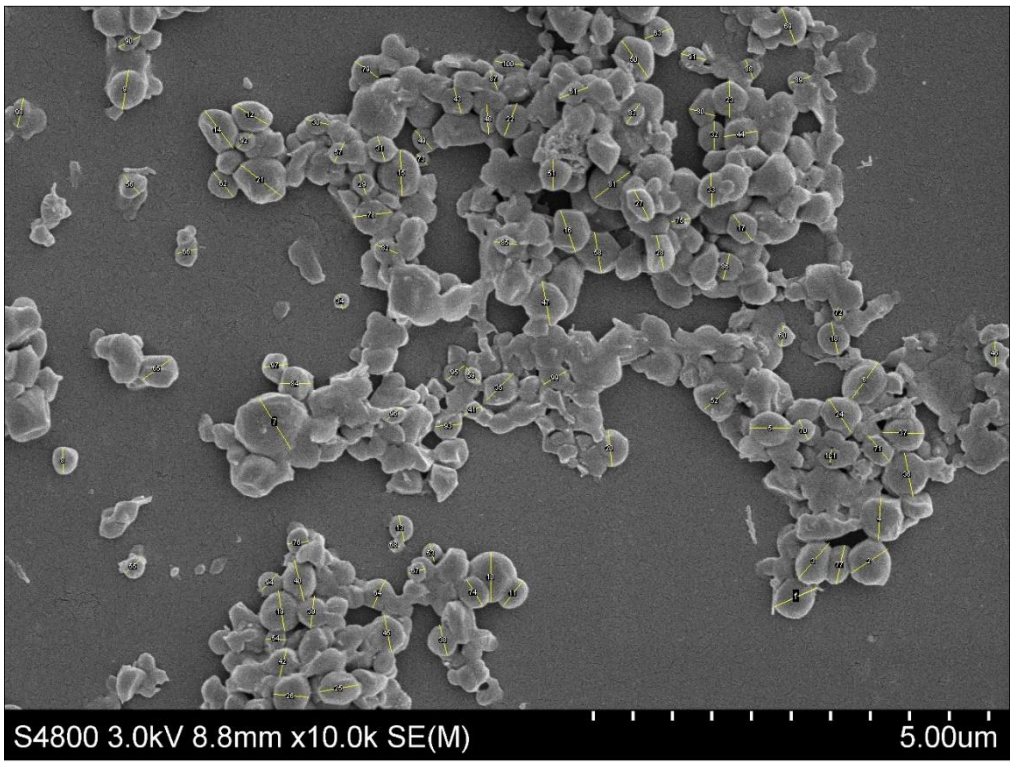

Figure 2.20. The picture presents the measurements of diameter for PCL particles obtained by ImageJ

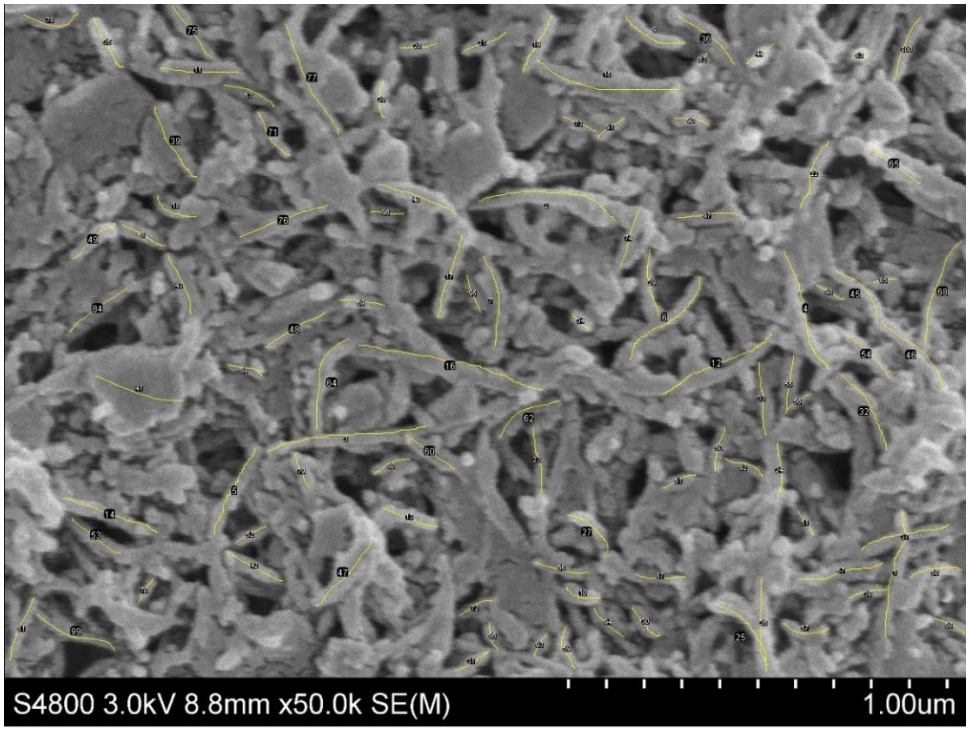

Figure 2.21. The picture presents the measurements of length PCL-CNTs particles obtained by ImageJ.

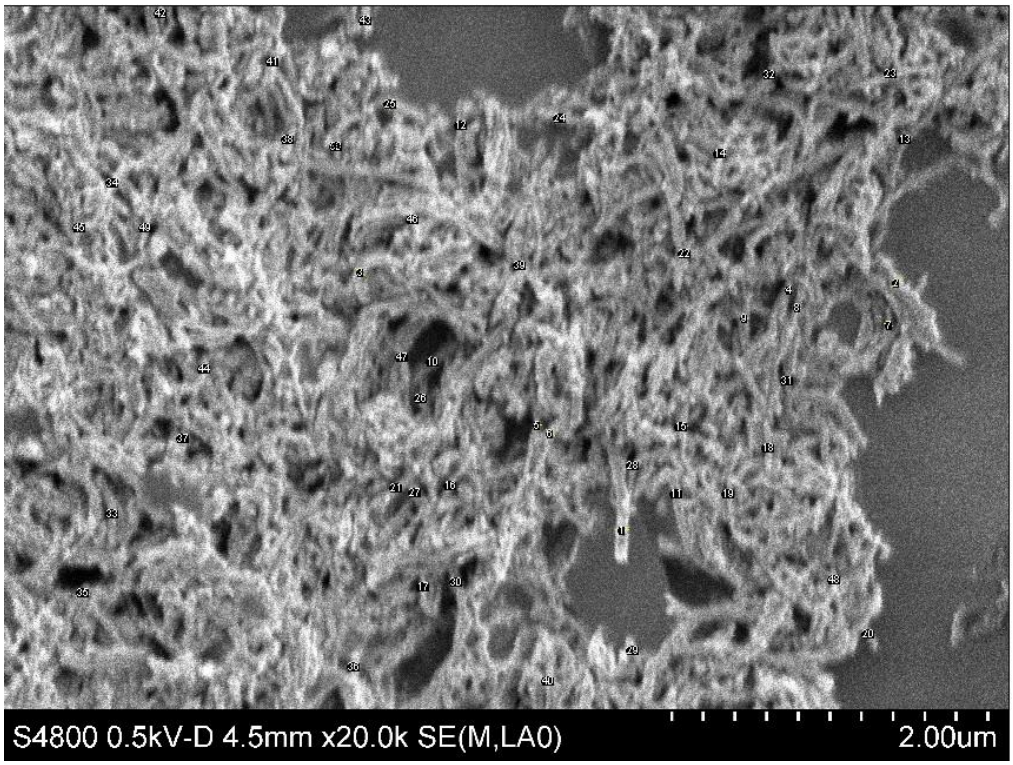

Figure 2.22. The picture presents the measurement of width for CNTs particles obtained by ImageJ.

Table 2.3. The data for effect of changing concentration of CNTs and SDS on Z-average diameter and PdI of the resulting nanoparticles as measured by DLS.

Sample	PCL [mg/mL]	CNTs [mg/mL]	SDS [mg/mL]	Z-ave [nm]	PdI
CNTs042	6	0.03	0	288.6	0.326
CNTs043	6	0.03	1.5	122.03	0.169
CNTs044	6	0.03	3	143.43	0.279
CNTs045	6	0.3	0	403.5	0.475
CNTs046	6	0.3	1.5	134.77	0.278
CNTs047	6	0.3	3	186.57	0.347
CNTs048	6	0.9	0	434.07	0.428
CNTs049	6	0.9	1.5	166.77	0.375
CNTs50	6	0.9	3	184.93	0.334

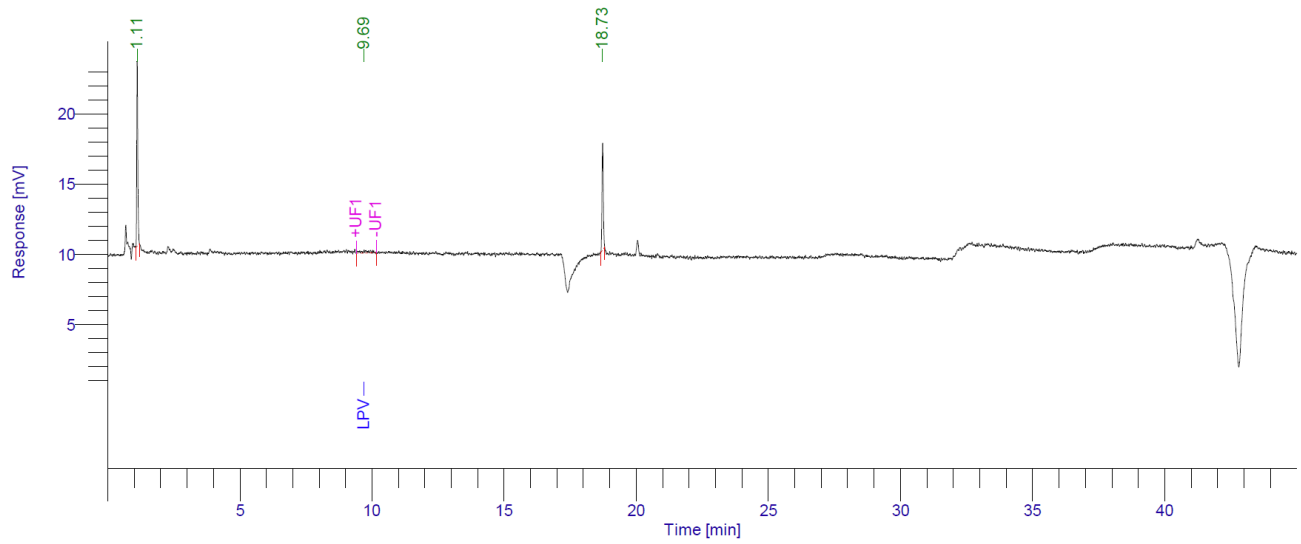

Figure 2.23. HPLC chromatogram of the released docetaxel from CNTs after 15 min.

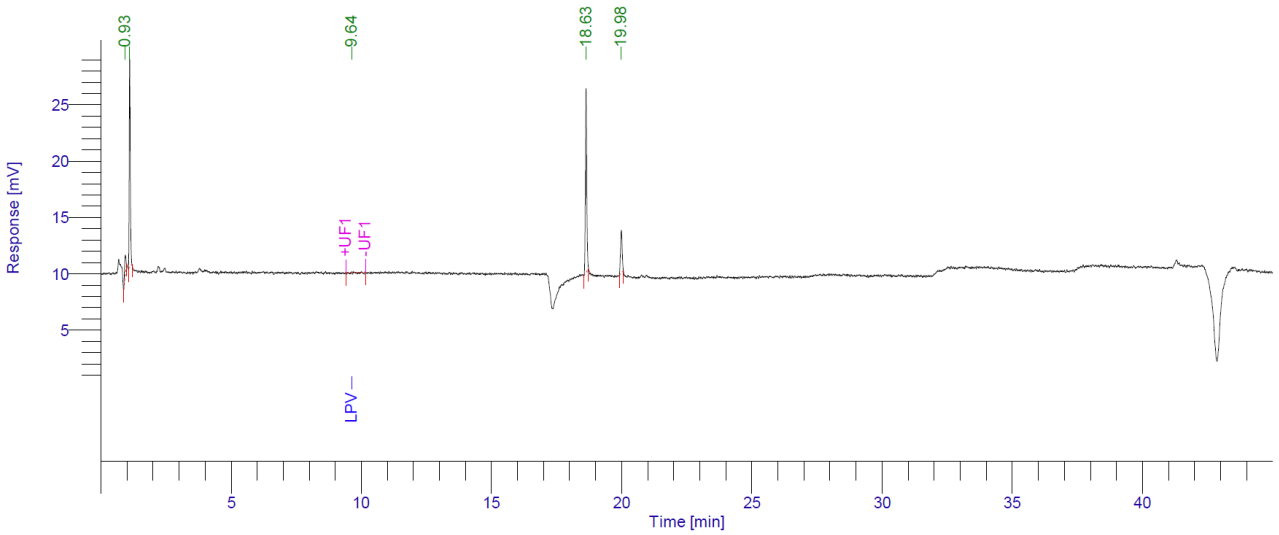

Figure 2.24. HPLC chromatogram of the released docetaxel from PCL-CNTs after 15 min.

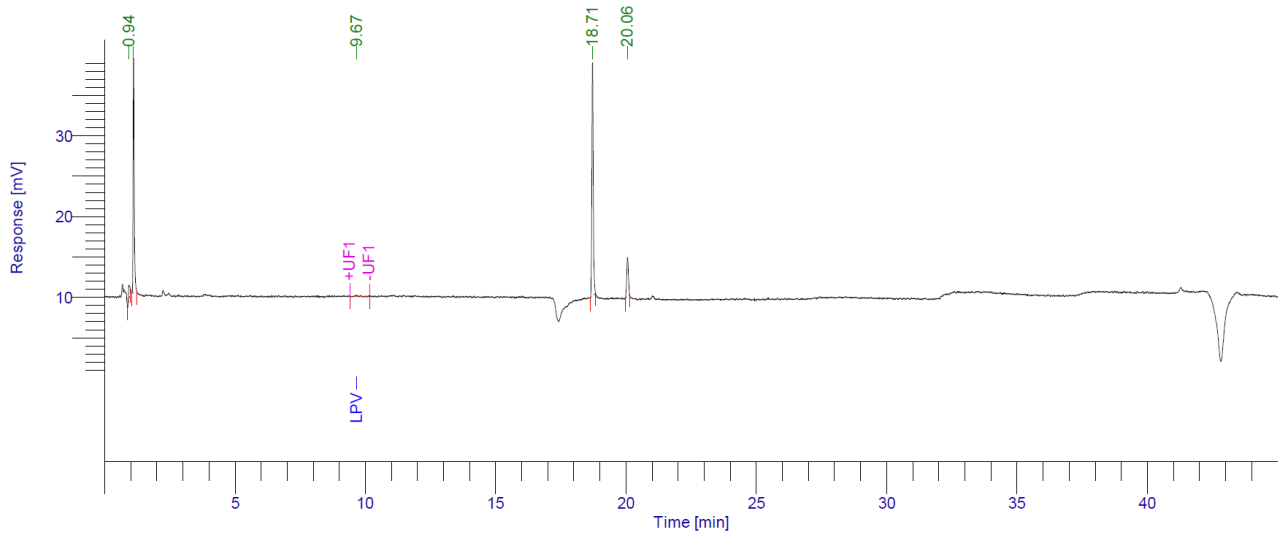

Figure 2.25. HPLC chromatogram of the released docetaxel from PCL after 15 min.

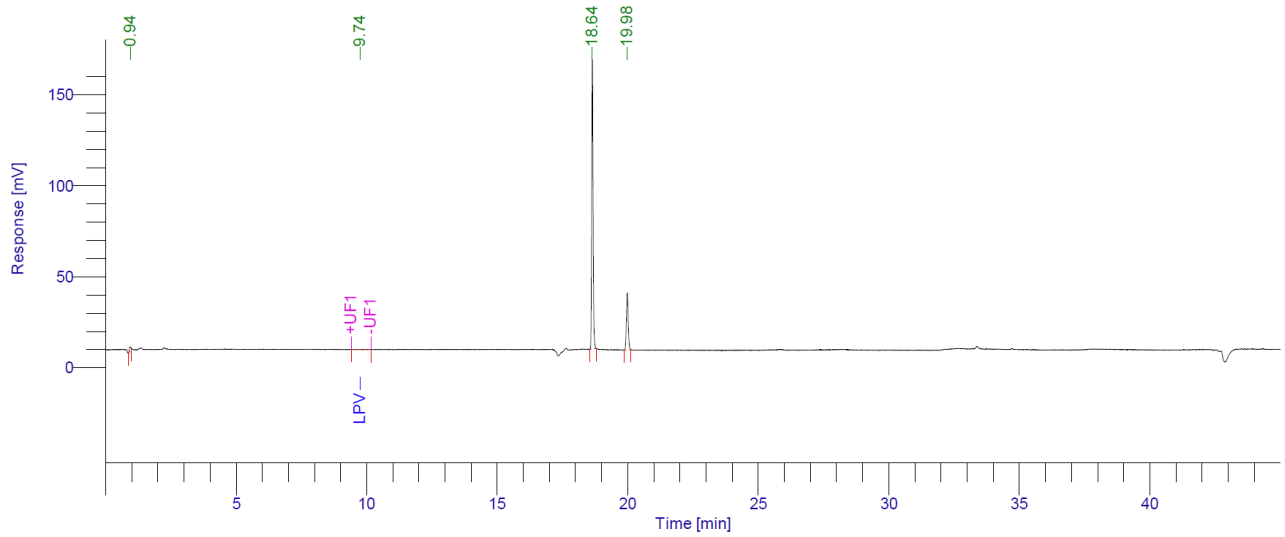

Figure 2.26. HPLC chromatogram of the standard docetaxel with the concentration 60 µg/mL.

Chapter 3

Insights into the Internal Structures of Nanogels Using a Versatile Asymmetric-Flow Field-Flow Fractionation Method

This chapter is based on publication:

E. Niezabitowska, A. Town, B. Sabagh, V. Kearns, S. Rannard and T. O. Mcdonald, Insights into the Internal Structures of Nanogels Using a Versatile Asymmetric-Flow Field-Flow Fractionation Method (under the review)

I would like to thank: Dr Adam Town for synthesis of PNIPAM nanogels, Dr Bassem Sabagh for data consultation and providing MALS detector, Prof. Steve Rannard for possibility of using AF4 equipment.

3.1. Introduction

Nanogels and microgels are colloidal particles consisting of solvated, crosslinked polymeric networks. The terms nanogel and microgel are typically used interchangeably and we will use nanogel from this point onwards. Nanogels composed of hydrophilic polymers have shown promise in a wide range of biomedical applications,[1] but also in other applications such as enhanced oil recovery and sensing.[2] Poly(N-isopropylacrylamide) (PNIPAM) based nanogels are a particularly well-known thermoresponsive nanogel. These particles undergo a deswelling transition upon heating to their volume phase transition temperature (VPTT) which is typically around 32°C. The proximity of this temperature to human body temperature has been exploited for applications in drug delivery.[3] For example, PNIPAM nanogels have been shown to provide triggered release of macromolecules[4] and can produce long acting drug delivery implants upon injection into physiological environments.[5,6] It has been shown that the internal structure of nanogels may be determined by their environment during formation; in particular, the formation of nanogels with core-shell type structures is highly dependent on synthesis conditions.[7] Differences in the internal structure of nanogels may have a considerable impact on their properties,[8] particularly in their use in *in situ* forming implants.[5,6]

In the field of nanoscience, it is important to obtain high resolution characterization of particle sizes and information about internal structure. A promising approach to achieve this is to fractionate samples through the use of asymmetric field flow fractionation (AF4). AF4 offers reduced shear forces, avoids the need for stationary phases and can provide separations over a wide size range within the colloidal domain.[9] These advantages have led to considerable growth in interest of field flow fractionation in fields such as nanomedicine.[10–15] AF4 systems can be easily coupled to different detectors such as dynamic light scattering (DLS), multi-angle light scattering (MALS), UV-Vis spectrophotometry and inductively coupled plasma mass spectrometry (ICP-MS). These hyphenated approaches provide detailed information on a sample such as concentration of particles, size, molecular weight and shape for all particles within the sample.[16]

The use of AF4 for the analysis of aqueous nanodispersions is reasonably well established.[17] However, despite the extensive amount of research undertaken on PNIPAM nanogels there are surprisingly few papers that have studied these materials by AF4. Smith *et al.* used AF4 to characterize the degradation of PNIPAM based nanogels with a hydrodynamic diameter of 132 nm.[18] They used 3 mM NaN_3 as the eluent with a two-step separation process. Firstly, a cross-flow of 1.0 mL/min was used which retained the nanogels while eluting degradation products. The nanogels were subsequently eluted in the second stage using a reduced cross-flow of 0.25 mL/ min. MALS was used for online characterization with batch measurement of the hydrodynamic radius by DLS.[18] Gaulding *et al.* used a 10 mM ionic strength aqueous buffer (containing $NaNO_3$ and NaN_3), and a variable cross-flow method from 1.0 mL/min to 0.1 mL/min to separate nanogels with hydrodynamic diameters of 96-146 nm from degraded polymer chains.[19] In a later paper, Gaulding and coworkers used a 15 mM ionic strength pH 3.3 formate buffer to fractionate core-shell nanogels with hydrodynamic diameters of ~ 260 nm. They achieved particle separation using a constant cross-flow of 0.25 mL/min.[20] It is clear from these methods that there is considerable differences between existing published separation conditions, this makes it difficult for researchers to select appropriate conditions for their PNIPAM nanogel samples.

AF4 also offers the opportunity to obtain information on the internal structure or the polymer architecture of a colloidal system.[21,22] This understanding of size and morphology of particles is extremely valuable. Of particular interest for obtaining insight into the internal structure of samples is the combination of DLS and MALS.[21,23] These techniques provide the hydrodynamic radius (R_h) and the radius of gyration (R_g) respectively. Information about the shape and conformation of particles can then be determined from the ratio $\rho = R_g/R_h$. This is a dimensionless value sometimes referred to as the shape factor.[24] For particles, a shape factor of 0.78 indicates a hard sphere, while values ~1 can indicate soft spheres and ~ 2 reveals that the particles are potentially stiff rods.[25,26] Alternatively, soluble polymers in a random coil confirmation tend to give shape factor values in the range of 1.50-1.78.[27] Thereby,

determination of shape factor may give useful information about internal structure of nanogels. The shape factor of PNIPAM nanogels has previously been determined by using a combination of online and offline (batch) techniques. Static light scattering and DLS measurements below the VPTT have been used on nanogels with hydrodynamic diameters of 100-310 nm. This research has shown that increasing the crosslinking density causes a reduction in the shape factor from ~ 0.9 to 0.6,[28,29] while another article has shown that the crosslinking density had little impact on shape factor values 0.55-0.6.[27] Small angle X-ray scattering (SAXS) has also been used to provide R_g measurement in the place of static light scattering.[7] SAXS has also been used to investigate how the dispersion polymerization synthesis conditions of PNIPAM influence the internal structure, showing that the larger nanogels tended to have more heterogeneous structures than smaller nanogels.[30] It has been suggested that this heterogeneity is due to the different rates of monomer and crosslinker incorporation into the particles.[31] The application of AF4 to the analysis of the internal structure of nanogels provides a number of potential benefits over the use of batch SAXS and SLS. Firstly, it provides high resolution fractionation of the particles which provides insight into the size distribution of a samples. Secondly, the use of the DLS and MALS detectors online gives a shape factor value for a sample much faster than a SAXS measurement.

In this work, we sought to develop a versatile AF4 method to characterize PNIPAM nanogel sample with Z-average hydrodynamic diameters from 65 to 310 nm that would also provide insight into the internal structures of samples. Therefore, we evaluated separation conditions using different eluents and cross-flows with online MALS and DLS detectors for analysis. We demonstrate a method that can effectively fractionate different nanogel samples. Additionally, this approach provides a clear insight into the internal structure of the nanogels.

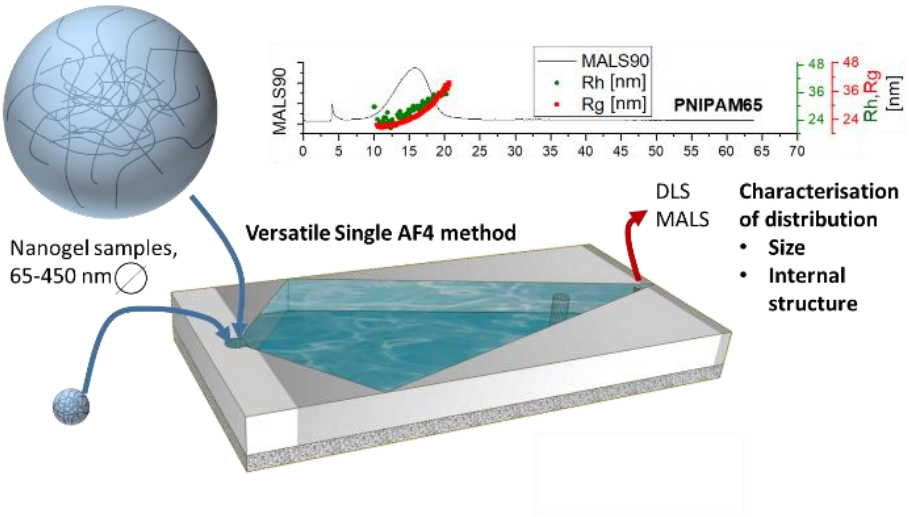

Figure 3.1. Characterizing poly(N-isopropylacrylamide) nanogels by asymmetric flow field flow fractionation, A: Fractionation and analysis of nanogels using asymmetric flow field flow fractionation. B: The internal structure of the differently sized nanogels as revealed by determination of the shape factor.

3.2. Experimental

3.2.1. Materials

N-isopropylacrylamide (NIPAM, ≥99%), N,N-methylenebis(acrylamide) (BIS, 99%), potassium persulfate (KPS, ≥99%), sodium chloride (NaCl, ≥99.5%), sodium nitrate (NaNO3, ≥ 99, sodium dodecyl sulfate (SDS, ≥99%) were purchased from Sigma-Aldrich Company Ltd, Gillingham (Dorset) UK, a subsidiary of Merck KGaA, Darmstadt, Germany. Phosphate buffered saline tablets (PBS) were purchased from Fischer Scientific. Milli-Q water obtained from a water purification system had a resistivity of > 18 MΩ cm^{-1} (PURELAB option R, Veolia). Spectra/por 2 (MWCO = 12-14 kDa) and spectra/por 3 (MWCO = 3.5 kDa) dialysis tubing was purchased from Spectrum Europe B.V., Breda, The Netherlands. Corning bottle top vacuum filter system with cellulose acetate membrane (pore size 0.22 µm) was purchased from Sigma-Aldrich Company Ltd, Gillingham (Dorset) UK, a subsidiary of Merck KGaA, Darmstadt, Germany.

3.2.2. Synthesis of PNIPAM nanogels

The PNIPAM nanogels samples with four different mean diameters were synthesized by dispersion polymerization. The compositions used in the synthesis of each nanogel can be found in Table 3.1. The NIPAM monomer (7000 mg, 61.9 mmol), BIS crosslinker (700 mg, 4.5 mmol) and SDS surfactant (PNIPAM310 = 78.8 mg, PNIPAM160 = 260.2 mg, PNIPAM100 =701.6 mg, PNIPAM65 = 939.1 mg) were dissolved in distilled water (470 mL) in a 1 L two-neck round bottom flask equipped with a stir bar and reflux condenser. This was then sealed and nitrogen was bubbled through the aqueous solution for 1 hour whilst stirring (400 rpm) to remove dissolved oxygen. The solution was then heated to 70 °C. Separately KPS initiator (280 mg) was dissolved in distilled water (30 mL) and degassed with N_2 for 1 hour before being transferred to the flask containing the monomers. The reaction was maintained under a N_2 atmosphere for 4 hours at 70 °C before being cooled down to room temperature. The solution was then filtered through glass wool. To remove unreacted impurities, the nanogel suspension was dialyzed for 5 days using regenerated cellulose dialysis tubing (12-14 kDa MWCO for PNIPAM310 and PNIPAM160 and 3.5 kDa MWCO for PNIPAM100 and PNIPAM65), (Spectrum Labs), replacing the distilled water every 12 hours. The purified suspension was then lyophilized (Virtis Benchtop K with ultra-low temperature condenser) and stored in a desiccator.

Table 3.1 The composition used in nanogel synthesis.

Sample	NIPAM (mg)	SDS (mg ml^{-1})	BIS (mg)	KPS[a] (mg)	Water[b] (ml)
PNIPAM65	7000	1.88	700	280	500
PNIPAM100	7000	1.40	700	280	500
PNIPAM160	7000	0.52	700	280	500
PNIPAM310	7000	0.16	700	280	500

[a] KPS dissolved at 9.3 mg ml^{-1} in distilled water.

[b]Total volume of water, including addition of KPS dissolved in water.

3.2.3. Characterisation of PNIPAM nanogels by AF4

Asymmetric flow field flow fractionation (AF4) experiments were performed on an MT2000 with RI and UV-Vis detectors from Postnova Analytics, Landsberg/Germany. A multi-angle light scattering detector (MALS) PN3621 from with a detector with 21 angles (from 7° to 164 °) operating at 532 nm power wavelength was coupled online to AF4. An autosampler (PN5300) was used with the system. The hydrodynamic radius of the samples were obtained by dynamic light scattering (DLS) using a Malvern Zetasizer Nano ZS (running Malvern Zetasizer software V7.12) (Malvern Instruments, Malvern, UK) with 633 nm He–Ne laser and the detector positioned at 173°. The DLS measurements have been obtained using flow cell ZEN0023 with flow rate 0.5 mL/min at 28°C, coupled online to the MT2000. A 350 µm spacer and 10 kDa regenerative cellulose membrane were installed in the separation channel. The conditions used for the separations was based on a method existing in the literature.[19,32] Briefly, the mobile phase was 0.1 M $NaNO_3$ or 1 x PBS (phosphate buffer saline) in Milli-Q H_2O. Type I distilled water was obtained from a water purification system had a resistivity of > 18 MΩ cm^{-1} (PURELAB option R, Veolia). The solutions were filtered using Corning bottle top vacuum filter system with cellulose acetate membrane with pore size 0.22 µm. The injected volume was 20 µL of a 4 mg/mL sample by autosampler. Each samples was analysed three times to check the reproducibility. A blank was measured between injections of new sample

to ensure that system was clean. The UV-Vis detector measured two wavelengths 250 and 300 nm. The conditions used for the separations was as follows: The injection/focusing time was 3 min using a cross flow from 2 to 0.5 mL min^{-1}. The chosen cross flow rate (initial values of 2 mL/min to 0.5 mL/min were tested) was kept constant for the first 0.2 minutes (t_0-$t_{0.2}$), and thereafter, the cross flow was decreased in a power manner (exponent 0.2) from its initial value to 0.1 over a period of 40 minutes. Following the complete reduction in cross flow, the tip-flow 0.1 mL/min continued for an additional 40 minutes. The optimized method for fractionation conditions of the nanogels is shown in Figure 3.2.

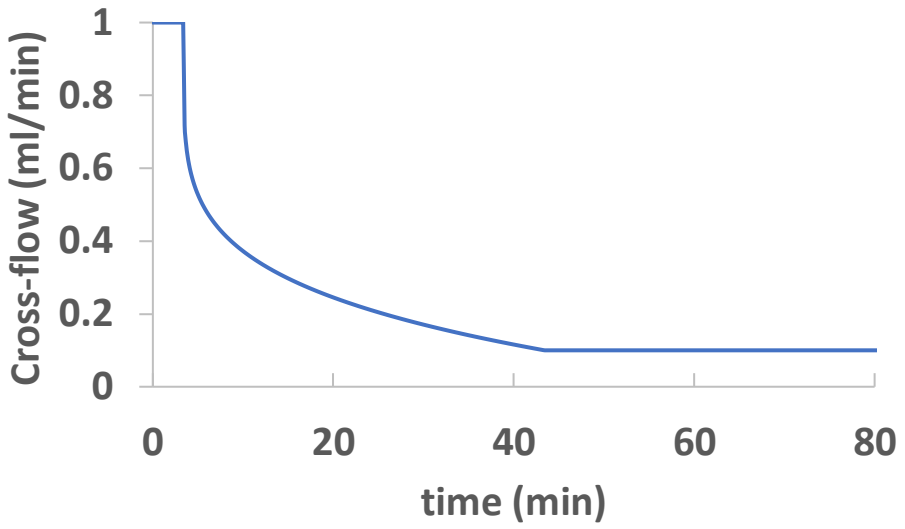

Figure 3.2. The method chosen for separation of samples. The graph present a change of cross-flow with time.

The recovery for PNIPAM samples was calculated using following equation:

$$R = \frac{A}{A^*} * 100\%$$

Where A is the peak area of the nanoparticles with cross flow, A* is the peak area without cross flow obtained from UV-VIS detector. [33]

3.2.4. Dynamic Light Scattering in Batch

Characterization of the nanogels was carried out using dynamic light scattering (DLS) and laser Doppler electrophoresis (LDE). DLS and LDE were performed using a Malvern Zetasizer Nano ZS (running Malvern Zetasizer software V7.12) with 633 nm He-Ne laser and the detector positioned at 173°. Dialyzed samples were diluted to 1 mg mL^{-1}. The Z-average diameter was recorded in the range (15-55 °C) using a thermal equilibration time of 600 seconds in 1 cm path length disposable polystyrene cuvettes. Measurements were repeated in triplicate to give a mean Z-average diameter and polydispersity index (PdI). Zeta potential measurements were performed using DTS1070 folded capillary cells (Malvern, UK). Capillary cells were flushed with ethanol and water prior to usage. The zeta potential measurement was made with a minimum of 10 and maximum of 40 runs, with a voltage of 150 V at 25°C. The Smoluchowski approximation was used to calculate zeta potential. The measurements were conducted in 0.01 M NaCl.

3.3. Results

3.3.1. Synthesis of PNIPAM nanogels

The PNIPAM nanogels were synthesized by dispersion polymerization in the presence of varying concentration of sodium dodecyl sulfate (SDS, 0.16-1.88 mg/mL) as surfactant. This method of synthesis nanogels was first reported by Pelton *et al*.[34] and as reported in the literature, increasing the concentration of SDS reduced the size of particles. The resulting four different samples were analysed by batch dynamic light scattering (DLS) to obtain the hydrodynamic diameter in water at 25 °C. All nanogels had a narrow distribution according to data obtained from DLS. The four samples were named corresponding to their mean approximate diameter at 25 °C. The hydrodynamic diameter and polydispersity index of the samples are shown in Table 3.2.

Table 3.2. The four PNIPAM nanogel samples as measured by batch DLS at 25 °C.

Sample	Hydrodynamic diameter (nm)	Polydispersity index
PNIPAM65	63 ± 1.2	0.13 ± 0.008
PNIPAM100	95 ± 0.8	0.14 ± 0.010
PNIPAM160	165 ± 1.2	0.02 ± 0.012
PNIPAM310	314 ± 4.0	0.01 ± 0.016

Thermoresponsive PNIPAM nanogels presents a characteristic behaviour where particles de-swell during the heating above their volume phase transition temperature (VPTT)[35] (see SI, Figure 3.8). VPTT is similar feature to the lower critical solution temperature (LCST) of linear PNIPAM. Moreover, PNIPAM nanogels can also demonstrate dual-stimuli responsive behaviour where the combination of two stimuli such as temperature and ionic strength results in the nanogels losing colloidal stability and cause aggregation into a gel matrix material.[5,36] However, aggregation must be avoided during analysis by field flow fractionation. Therefore, the change in hydrodynamic diameter of these nanogels in response to a rise in temperature when dispersed in solution of 0.1 M $NaNO_3$ in water was measured by DLS. Nanogels showed volume phase transition temperature around 34 °C (see Figure 3.3). The temperature of separation was chosen for 28 °C to avoid an aggregation and to ensure that the multi-angle light scattering detector maintains a constant temperature (it only can regulate temperature by heating rather than cooling therefore the temperature inside of the system should be higher than a temperature room).

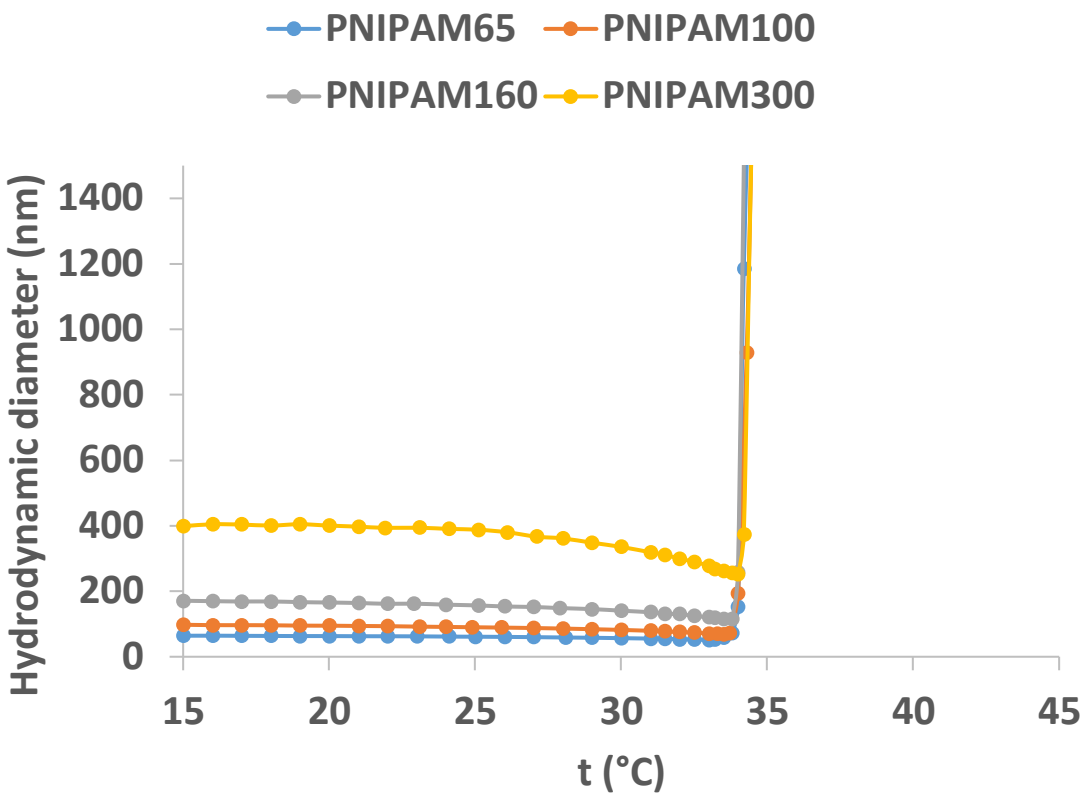

Figure 3.3. Hydrodynamic diameter of nanogels in 0.1 M $NaNO_3$ measured using DLS at 1 mg ml^{-1} with respect to the nanogel concentration. The sample of the nanogels aggregated at 34 °C and produced particles sizes that could not be accurately measured by DLS.

3.3.2. Effect of mobile phase

In order to evaluate the influence of different mobile phases previously used in the literature both PBS[37,38] and 0.1 M $NaNO_3$[19,39] were tested for fractionating a nanogel sample. The reproducibility between three repeat injections in each mobile phase was checked (Figure 3.4.). This showed considerably more variability between repeat injections for PBS compared to $NaNO_3$. This difference may be attributed to increased interaction of the nanogels with the surface of membrane when dispersed in PBS. All the other nanogel samples also displayed highly reproducible separations in $NaNO_3$ (see supporting information (SI), Figure 3.9). Therefore $NaNO_3$ was selected as the mobile phase for further experiments. The thermoresponsive behaviour of PNIPAM means that the nanogels display a characteristic de-swelling upon heating above

their volume phase transition temperature.[35] Moreover, PNIPAM nanogels can also demonstrate dual-stimuli responsive behaviour where the combination of two stimuli such as temperature and ionic strength results in the nanogels losing colloidal stability and aggregating.[40] The consideration of this behaviour is critical as aggregation must be avoided during AF4 analysis. Therefore, the colloidal stability of the nanogel samples was assessed by using batch DLS to monitor the change in hydrodynamic diameter in response to increasing temperature when dispersed in solution of 0.1 M $NaNO_3$. All the nanogel samples showed a dramatic increase in the diameter at 34 °C, the volume phase transition temperature, which revealed that the particles were aggregating. Therefore 28 °C was chosen as the temperature of separation for use in the AF4. This avoided the potential for aggregation and ensured that the multi-angle light scattering detector (which can only can regulate temperature by heating) maintained a constant temperature. The choice of $NaNO_3$ as the mobile phase and 28 °C produced highly reproducible measurements and avoided potential issues caused by the temperature responsive properties of the nanogels.

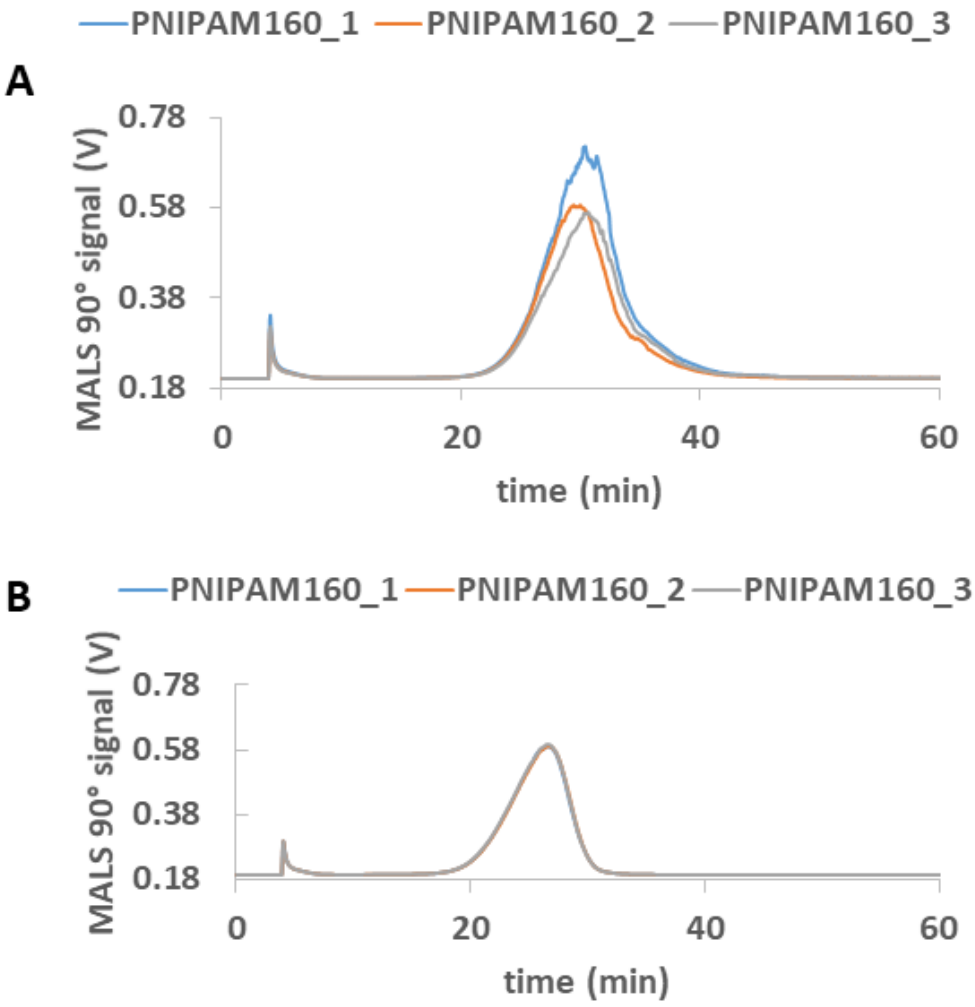

Figure 3.4. Comparison of the reproducibility using PBS (A) or $NaNO_3$ (B) as the mobile phase for characterizing PNIPAM160 with a crossflow of 1.0 ml/min. The different data series are repeat runs of the same sample.

3.3.3. Effect of cross-flow rate

The cross-flow is main factor controlling retention time of particles and their effective separation in the AF4.[41] Appropriate selection of this parameter needs to consider effect separation while also not causing adsorption of particles onto the membrane.[33] Additionally, PNIPAM nanogels are soft materials[42] and might be susceptible to damage. As such, a range of cross-flows from between 0.5 mL/min to 2 mL/min were tested for all five samples. Figure 3.5 shows the separation behaviour of PNIPAM65 at the different crossflows as an example. Being the smallest in diameter, this sample would need the strongest separation force in order to

fractionate the sample. The fractograms for the other nanogels are shown in SI Figure 3.10. In the case of all samples, with increasing crossflow the retention time was increased. Additionally, increasing the crossflow reduced the concentration of particles that were eluting in the void peak (seen at ~5 minutes). Both of these behaviours were due to the increased separation force that is obtained by increasing the crossflow.

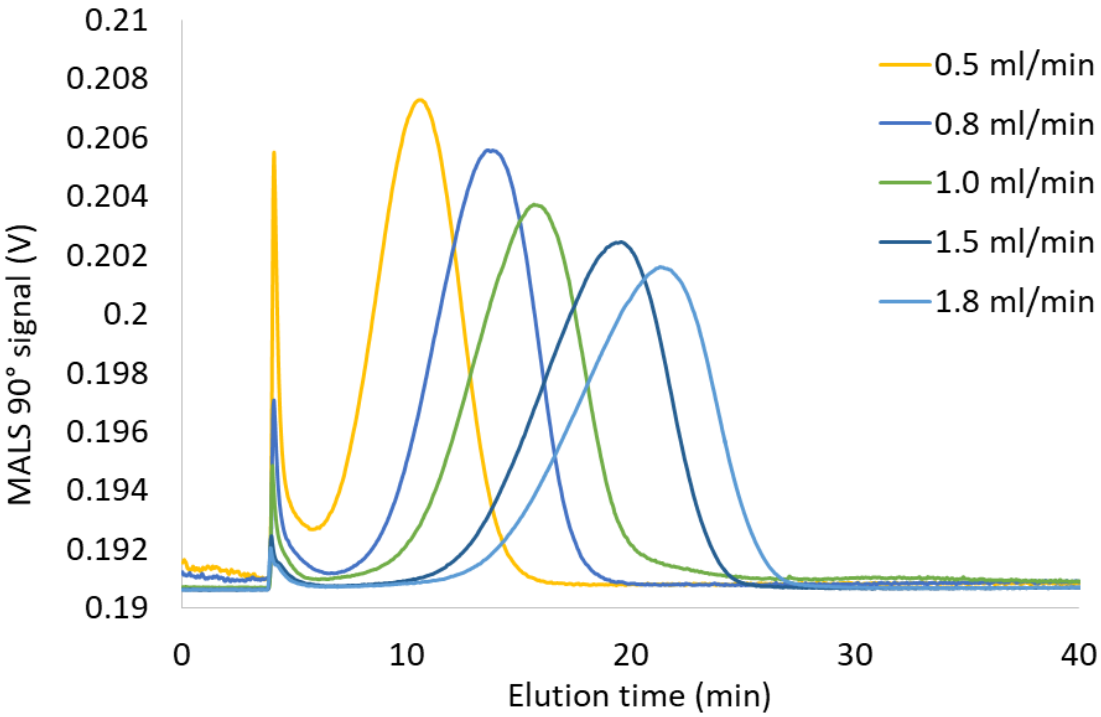

Figure 3.5. Effect of changing the crossflow on the separation behaviour of PNIPAM65 in $NaNO_3$.

As the objective of this work was to obtain a versatile single method to separate nanogel samples with a wide range of sizes we wanted to choose a single crossflow for all samples. We therefore also determined the recovery during separation of samples. Typically, recovery can be obtained from UV–Vis absorbance, differential refractometer, fluorescence, or ICP–MS, where changes of analyte mass can be detected.[33] We used an inline UV–Vis detector to quantify the recovery, the calculated results are shown in Table 3.3.

Table 3.3. The calculated recovery for 3 samples PNIPAM65, PNIPAM160, PNIPAM310 (replicated 3 times) based on area of peak obtained from UV-Vis detector with different initial crossflow values.

	Recovery (%)		
Crossflow (mL/min)	PNIPAM65	PNIPAM160	PNIPAM310
0.5	98 ± 2	99 ± 1	70 ± 5
0.8	98 ± 2	99 ± 1	70 ± 5
1	98 ± 2	98 ± 1	70 ± 5
1.5	98 ± 2	98 ± 1	65 ± 5
1.8	98 ± 2	97 ± 1	63 ± 5
2	98 ± 2	97± 1	60 ± 5

The recovery for smaller nanogels (diameter <160 nm) showed good recovery R>98% for all tested cross-flows. However, for the nanogels with higher diameter (>160 nm) the recovery decrease with higher cross-flows. This finding was due to the separation force being too strong for larger nanogels which likely led to adsorption of the nanogels onto the membrane and lower recovery R<65%. An initial crossflow of 1 mL/min displayed high recovery for all samples and displayed effective separation for all samples, as seen in the comparison of the fractograms for the largest and smallest nanogels in Figure 3.6.. Additionally, an increase in R_g with elution time was observed for each of the samples which indicates effective separation in normal mode.[33]

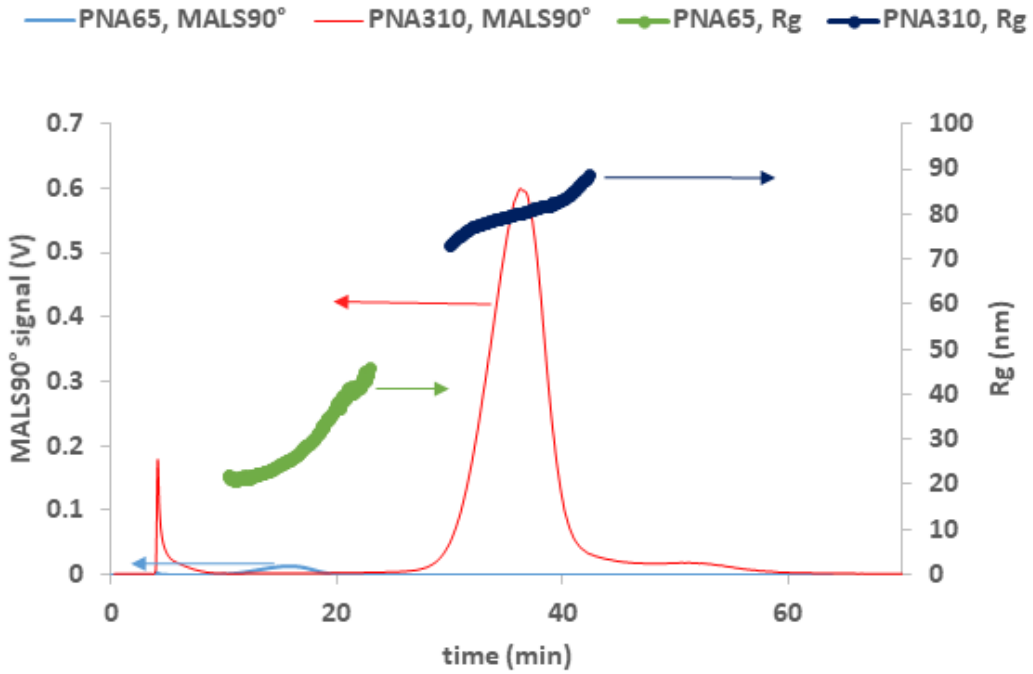

Figure 3.6. A crossflow of 1 ml/min led to effective fractionation with normal mode separation occurring for all samples.

3.3.4. Relationship between particle size and internal structure

Comparison of the fractograms for the four differently sized nanogel samples combined with the data obtained from MALS and DLS analysis (**Figure 3.7.**) provided insight into the structural differences between the samples. The signal obtained for 90° light scattering detector gives an indication of particle concentration. The online MALS and DLS detectors allow the measurements for both the R_g and $R_{h,}$ of the nanogels exiting the AF4 separation channel. The R_g values was calculated based on sphere fit. The elution time for different nanogels can be seen to increase with increasing mean diameter; 16 min (PNIPAM65), 19 min (PNIPAM100), 26 min (PNIPAM160) and 37 min (PNIPAM310). This increase of the nanogels size with the elution time indicated that the cross flow solvent and the method used was optimal to achieve a satisfactory separation of the nanogels. Each nanogel sample also showed an increase in the R_h with increasing elution time. AF4 separates based on the diffusion coefficients of the particles and therefore particles with a larger R_h are

closer to the membrane and experience a reduced flow rate along the channel. Therefore the larger the R_h and longer the elution time.[15] Some inconsistency was observed in the values for R_h obtained at either end of the size distribution, which was due to the reduced signal-to-noise at lower concentrations. That said, the width of the particle size distributions were relatively narrow for all the samples except PNIPAM310, with the difference between the smallest and largest particles in a population being <20 nm. For PNIPAM310, the smallest particles eluting at 30 minutes were ~90 nm but this quickly increased to ~120 nm at an elution time of 35 minutes. It is interesting to compare the widths of the distributions found by fractionation to the polydispersity index values obtained by batch DLS, the latter measurement indicated that the two smallest nanogel samples (PNIPAM65 and PNIPAM100) had the highest polydispersity index values (0.13 and 0.14) compared to the larger nanogels (PNIPAM160, PNIPAM310, at 0.02 and 0.01, respectively). This overestimation on the polydispersity index values by batch DLS was likely due to the weaker light scattering from the smaller particles, this might allowing any signal from dust contamination to contribute a larger component of the data of the overall sample. The R_g values for all samples also increased with increasing elution time. For populations of nanoparticles with consistent internal structure this was expected; for a population of nanoparticles with consistent internal structure, i.e. a constant shape factor, the R_h and R_g should increase at the same time. However, for a number of the nanogel samples this was not the case. For PNIPAM65, the R_h displayed a constant gradient with elution time, but the R_g increases faster than expected, with the values for $R_g > R_h$ from elution times of ~18 minutes. This indicates that the internal structure of the nanogels was within the single population of nanogel particles changing with increasing size. A plot of the shape factors for all samples can be seen in SI Figure 3.10. Such differences in the internal structure of the particles in the distribution might result from differences in the formation of the nanogels during the dispersion polymerisation.

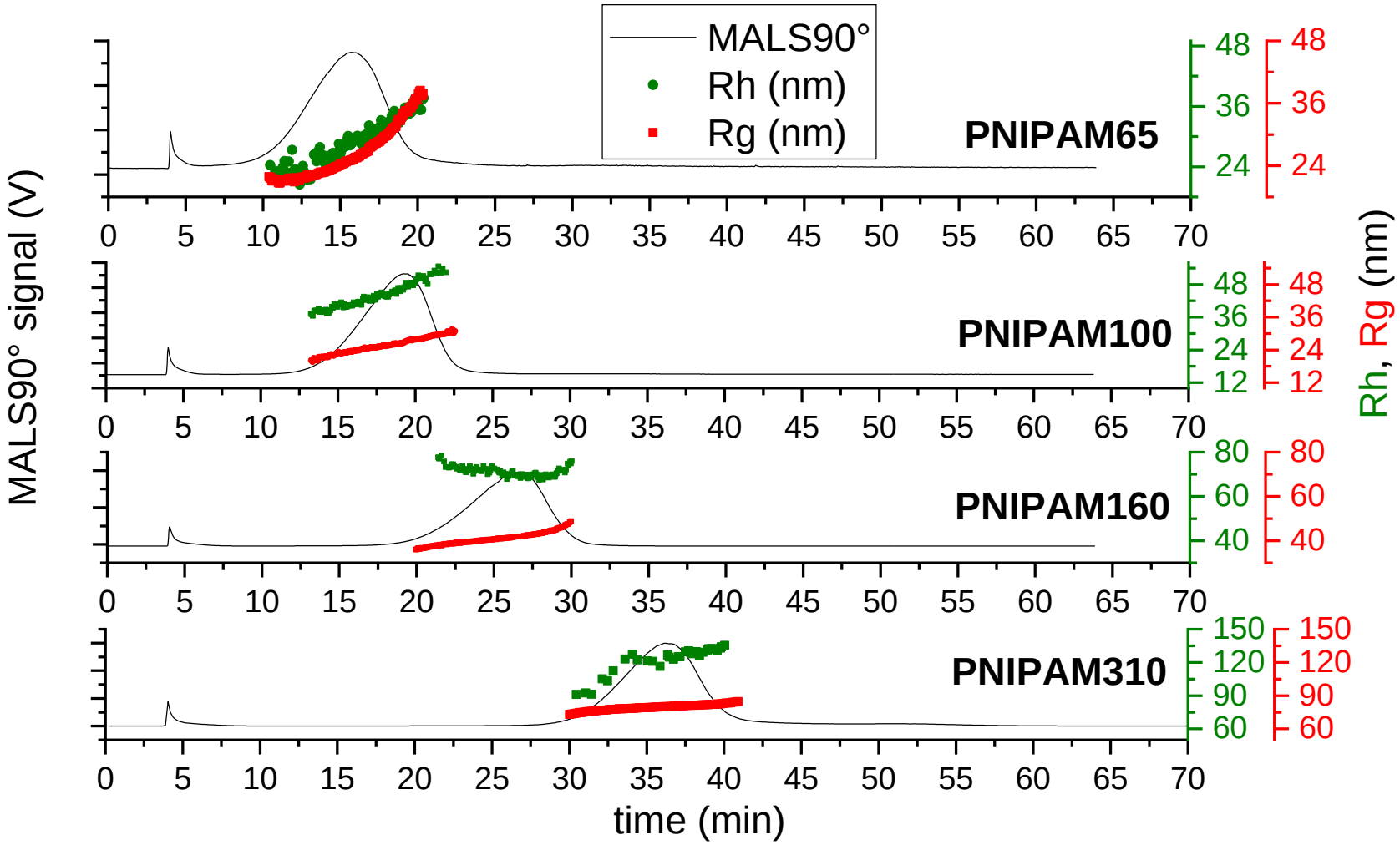

Figure 3.7. AF4-MALS-DLS analysis of nanogels. Fractograms showing the light 90◦ scattering detector signal (black line, left hand scale), radius of gyration (red dotted line, right hand scale) and hydrodynamic radius (green dotted line, right hand scale) obtained from AF4-MALS-DLS measurements for PNIPAM65, PNIPAM100, PNIPAM160, PNIPAM310 and PNIPAM400 for cross-flow 1 mL/min.

The values for the modes of the distributions can be considered to give an indication of the properties of the majority of the particles (Table 3.4) in the distribution. The R_h values for the mode of the distribution generally agreed closely with the R_h obtained by the batch DLS measurement. The exception to this agreement was the difference between the online and batch values for the R_h for PNIPAM310, this difference might be due to an underestimation of the R_h in the flow measurement. It has previously been reported that the detector flow rate leads to a translational component in the measurement cell that may be recorded as Brownian motion by the DLS. For larger nanoparticles the translational component of particle movement increases relative to the diffusional component of particle movement.[43] This potentially leads to the underestimation of R_h in larger samples. The comparison of the shape factors for the differently sized nanogel samples reveal values ranging from 0.58-0.73 which are in agreement with literature values.[27,28,44] The smallest nanogel possessed the largest shape factor with a value of 0.73 which is similar to that of a hard sphere with a constant internal polymer density (0.78), therefore indicating a close to homogeneous internal crosslinking density. The larger nanogels provided lower values for the shape factor, ranging between 0.58-0.66. These values are typical for swollen nanogel with a denser inner core compared to the outer shell.[44] All the nanogels were made at the same monomer composition however, the larger nanogels were obtained by using a lower concentration of the surfactant SDS in the dispersion polymerization. It has previously been shown that using larger amounts of SDS during the dispersion polymerization route used for nanogels creates smaller more homogeneous partices,[30] while using less SDS generates larger particles with a more heterogeneous structure which contains a dense gel particle core.[29] Therefore, this AF4 separation method provides a clear insight into the internal structure of the nanogels.

Table 3.4. The mode values of R_g, R_h and ρ for nanogels obtained from AF4-MALS-DLS for fractionation with 1 mL/min cross-flow.

Sample	R_g [nm]	R_h [nm]	R_h [nm] batch*	$\boldsymbol{\rho}$
PNIPAM65	25 ± 0.1	35 ± 1.0	31 ± 0.6	0.73
PNIPAM100	26 ± 0.1	43 ± 0.3	43 ± 0.4	0.61
PNIPAM160	42 ± 0.1	73 ± 1.0	75 ± 0.6	0.58
PNIPAM310	80 ± 0.5	137 ± 0.3	180 ± 2.0	0.59

R_h [nm] batch* have been measured by DLS using 1 mg/mL concentration of nanogels, at 28 °C in 0.1 M $NaNO_3$.

3.4. Conclusion

This study has demonstrated the value of AF4 coupled online with MALS and DLS for analysing nanogel samples from 65-310 nm in diameter. The diameters of particles and information on the internal structure of the nanogels can be easily obtained by using a single AF4-MALS-DLS fractionation method. In the research, we have successfully fractionated PNIPAM nanogels obtaining radius of gyration, hydrodynamic radius and shape factors for all five samples. The chosen mobile phase 0.1 M $NaNO_3$ and method showed good reproducibility and high resolution of sizes for AF4-MALS-DLS measurements. The fractionation of the samples revealed that the internal structure of some of the samples varied within the distribution. Such information cannot be obtained through the use of bulk analysis methods such as SAXS. Determination of the mode values of R_g/R_h for the distribution of the nanogels showed that diameters higher than 100 nm had values ~0.61 indicating that the particles showed more like core-shell structures. The analysis of the smallest nanogel (65 nm) gave R_g/R_h values 0.78 indicating more homogenous structures. The measurements showed differences in internal structure of nanogels depending on the synthesis conditions which also controlled the hydrodynamic diameter. This work will be of importance to researchers working with aqueous nanogels/microgels by providing a versatile method for obtaining a clear insight into the internal structures of nanogels within differently sized populations of particles.

3.5. References

1 J. K. Oh, R. Drumright, D. J. Siegwart and K. Matyjaszewski, *Prog. Polym. Sci.*, 2008, **33**, 448–477.

2 J. B. Thorne, G. J. Vine and M. J. Snowden, *Colloid Polym. Sci.*, 2011, **289**, 625–646.

3 A. E. Ekkelenkamp, M. R. Elzes, J. F. J. Engbersen and J. M. J. Paulusse, *J. Mater. Chem. B*, 2017, 210–235.

4 N. M. B. Smeets and T. Hoare, *J. Polym. Sci. Part A Polym. Chem.*, 2013, **51**, 3027–3043.

5 A. R. Town, M. Giardiello, R. Gurjar, M. Siccardi, M. E. Briggs, R. Akhtar and T. O. McDonald, *Nanoscale*, 2017, **9**, 6302–6314.

6 A. R. Town, J. Taylor, K. Dawson, E. Niezabitowska, N. M. Elbaz, A. Corker, E. Garcia-Tuñón and T. O. McDonald, *J. Mater. Chem. B*, 2019, **7**, 373–383.

7 M. Stieger, W. Richtering, J. S. Pedersen and P. Lindner, *J. Chem. Phys.*, 2004, **120**, 6197–6206.

8 A. Town, E. Niezabitowska, J. Kavanagh, M. Barrow, V. R. Kearns, E. García-Tuñón and T. O. McDonald, *J. Phys. Chem. B*, 2019, 123, 6303-6313.

9 F. A. Messaud, R. D. Sanderson, J. R. Runyon, T. Otte, H. Pasch and S. K. R. Williams, *Prog. Polym. Sci.*, 2009, **34**, 351–368.

10 G. Yohannes, M. Jussila, K. Hartonen and M. L. Riekkola, *J. Chromatogr. A*, 2011, **1218**, 4104–4116.

11 C. Weber, J. Simon, V. Mailänder, S. Morsbach and K. Landfester, *Acta Biomater.*, 2018, **76**, 217–224.

12 C. Contado, *Anal. Bioanal. Chem.*, 2017, **409**, 2501–2518.

13 P. Iavicoli, P. Urbán, A. Bella, M. G. Ryadnov, F. Rossi and L. Calzolai, *J. Chromatogr. A*, 2015, **1422**, 260–269.

14 A. Zattoni, D. C. Rambaldi, P. Reschiglian, M. Melucci, S. Krol, A. M. C. Garcia, A. Sanz-Medel, D. Roessner and C. Johann, *J. Chromatogr. A*, 2009, **1216**, 9106–9112.

15 M. Wagner, S. Holzschuh, A. Traeger, A. Fahr and U. S. Schubert, *Anal. Chem.*, 2014, **86**, 5201–5210.

16 H. Pasch, A. C. Makan, H. Chirowodza, N. Ngaza and W. Hiller, *Anal. Bioanal. Chem.*, 2014, **406**, 1585–1596.

17 S. K. Ratanathanawongs Williams and D. Lee, *J. Sep. Sci.*, 2006, **29**, 1720–1732.

18 M. H. Smith, A. B. South, J. C. Gaulding, L. A. Lyon, G. A. Medeiros, G. A. Bataglion, D. A. C. Ferreira, H. C. B. De Oliveira, M. N. Eberlin, B. A. D. Neto, T. Chemistry, U. De Brasilia and T. Mass, *Anal. Chem.*, 2010, **82**, 523–530.

19 J. C. Gaulding, M. H. Smith, J. S. Hyatt, A. Fernandez-Nieves and L. A. Lyon, *Macromolecules*, 2012, **45**, 39–45.

20 J. C. Gaulding, A. B. South and L. A. Lyon, *Colloid Polym. Sci.*, 2013, **291**, 99–107.

21 S. Boye, F. Ennen, L. Scharfenberg, D. Appelhans, L. Nilsson and A. Lederer, *Macromolecules*, 2015, **48**, 4607–4619.

22 C. Fuentes, J. Castillo, J. Vila and L. Nilsson, *Anal. Bioanal. Chem.*, 2018, **410**, 3757–3767.

23 V. Vezočnik, K. Rebolj, S. Sitar, K. Ota, M. Tušek-Žnidarič, J. Štrus, K. Sepčić, D. Pahovnik, P. Maček and E. Žagar, *J. Chromatogr. A*, 2015, **1418**, 185–191.

24 B. Walter, *Adv. Polym. Sci.*, 1983, **48**, 1–124.

25 A. K. Brewer and A. M. Striegel, *Anal. Bioanal. Chem.*, 2009, **393**, 295–302.

26 A. K. Brewer and A. M. Striegel, *Analyst*, 2011, **136**, 515–519.

27 H. Senff and W. Richtering, *Colloid Polym. Sci.*, 2000, **278**, 830–840.

28 I. Varga, T. Gilányi, R. Mészáros, G. Filipcsei and M. Zrínyi, *J. Phys. Chem. B*, 2001, **105**, 9071–9076.

29 L. Arleth, X. Xia, R. P. Hjelm, J. Wu and H. U. Zhibinc, *J. Polym. Sci. Part B Polym. Phys.*, 2005, **43**, 849–860.

30 M. Andersson and S. L. Maunu, *J. Polym. Sci. Part B Polym. Phys.*, 2006, **44**, 3305–3314.

31 R. Acciaro, T. Gilanyi and I. Varga, *Langmuir*, 2011, **27**, 7917–7925.

32 K. Rebolj, D. Pahovnik and E. Žagar, *Anal. Chem.*, 2012, **84**, 7374–7383.

33 J. Gigault, J. M. Pettibone, C. Schmitt and V. A. Hackley, *Anal. Chim. Acta*, 2014, **809**, 9–24.

34 W. McPhee, K. C. Tam and R. Pelton, *J. Colloid Interface Sci.*, 1993, 156, 24–30.

35 M. Muratalin, P. F. Luckham, A. Esimova, S. Aidarova, B. Mutaliyeva, G. Madybekova, A. Sharipova and A. Issayeva, *Colloids Surfaces A Physicochem. Eng. Asp.*, 2017, **532**, 8–17.

36 A. R. Town, J. Taylor, K. Dawson, E. Niezabitowska, N. M. Elbaz, A. Corker, E. Garcia-Tuñón and T. O. McDonald, *J. Mater. Chem. B*, , DOI:10.1039/C8TB01597J.

37 A. Shimoda, S. ichi Sawada, A. Kano, A. Maruyama, A. Moquin, F. M. Winnik and K. Akiyoshi, *Colloids Surfaces B Biointerfaces*, 2012, **99**, 38–44.

38 J. S. Hong, S. M. Stavis, S. H. Depaoli Lacerda, L. E. Locascio, S. R. Raghavan and M. Gaitan, *Langmuir*, 2010, **26**, 11581–11588.

39 S. Hupfeld, D. Ausbacher and M. Brandl, *J. Sep. Sci.*, 2009, **32**, 1465–1470.

40 M. Rasmusson, A. Routh and B. Vincent, *Langmuir*, 2004, **20**, 3536–3542.

41 J. Omar, A. Boix, G. Kerckhove and C. von Holst, *Food Addit. Contam. - Part A Chem. Anal. Control. Expo. Risk Assess.*, 2016, **33**, 1775–1784.

42 M. Y. Hwang, S. G. Kim, H. S. Lee and S. J. Muller, *Soft Matter*, 2018, **14**, 216–227.

43 S. Sitar, V. Vezočnik, P. Maček, K. Kogej, D. Pahovnik and E. Žagar, *Anal. Chem.*, 2017, acs.analchem.7b03251.

44 G. R. Deen and J. S. Pedersen, *Cogent Chem.*, 2015, **1**, 1–15.

45 K. G. Wahlund, *J. Chromatogr. A*, 2013, **1287**, 97–112.

46 S. K. R. Williams, J. R. Runyon and A. A. Ashames, *Anal. Chem.*, 2011, **83**, 634–642.

47 M. E. Schimpf, K. Caldwell and J. C. Giddings, *Field-Flow Fractionation Handbook*, John Wiley & Sons, Inc., 2000.

48 S. Podzimek, Light Scattering, Size Exclusion Chromatography and Asymmetric Flow Field Flow Fractionation: Powerful Tools for the Characterization of Polymers, Proteins and Nanoparticles, John Wiley & Sons, Inc., 2011, 353–354.

Supporting Information

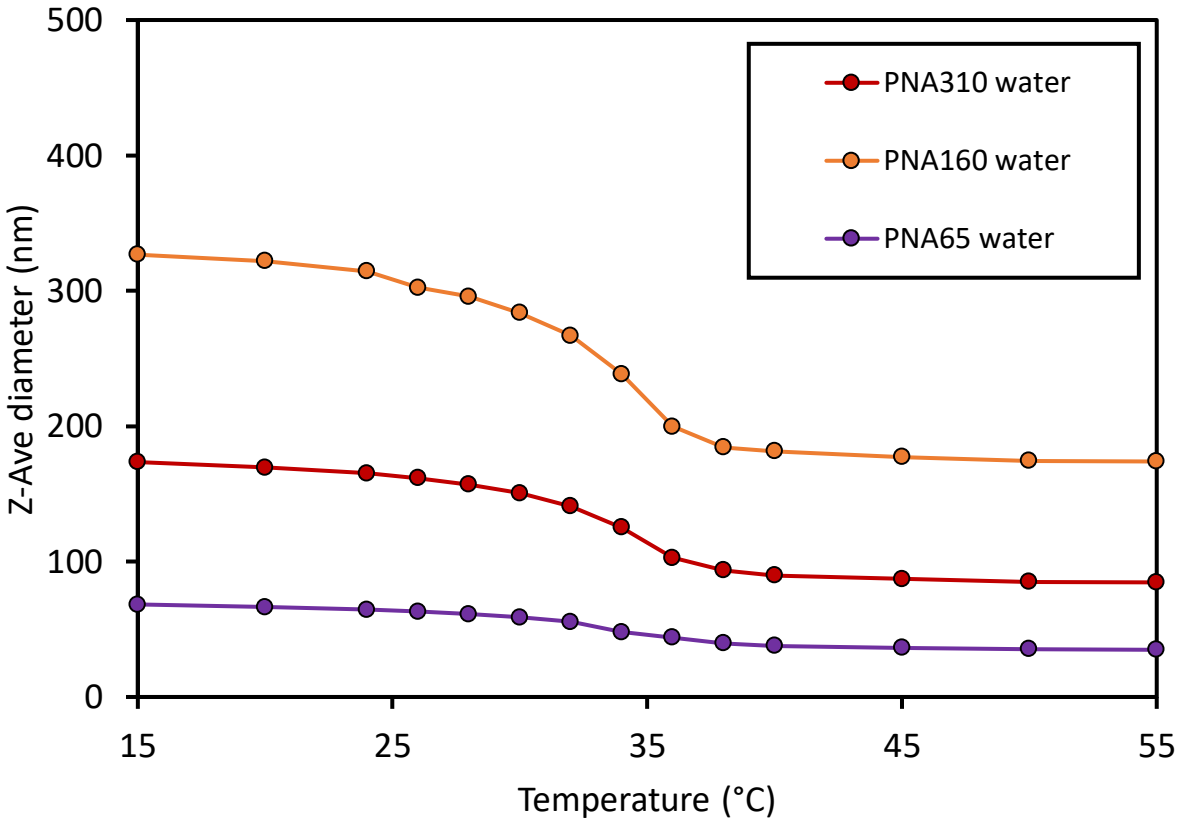

Figure 3.8. The thermoresponsive behaviour of the PNIPAM nanogels in water as characterised by dynamic light scattering. The particles undergo a deswelling transition at the volume phase transition temperature of 34 °C. This behaviour is exemplified by PNA65, PNA160 and PNA 310.

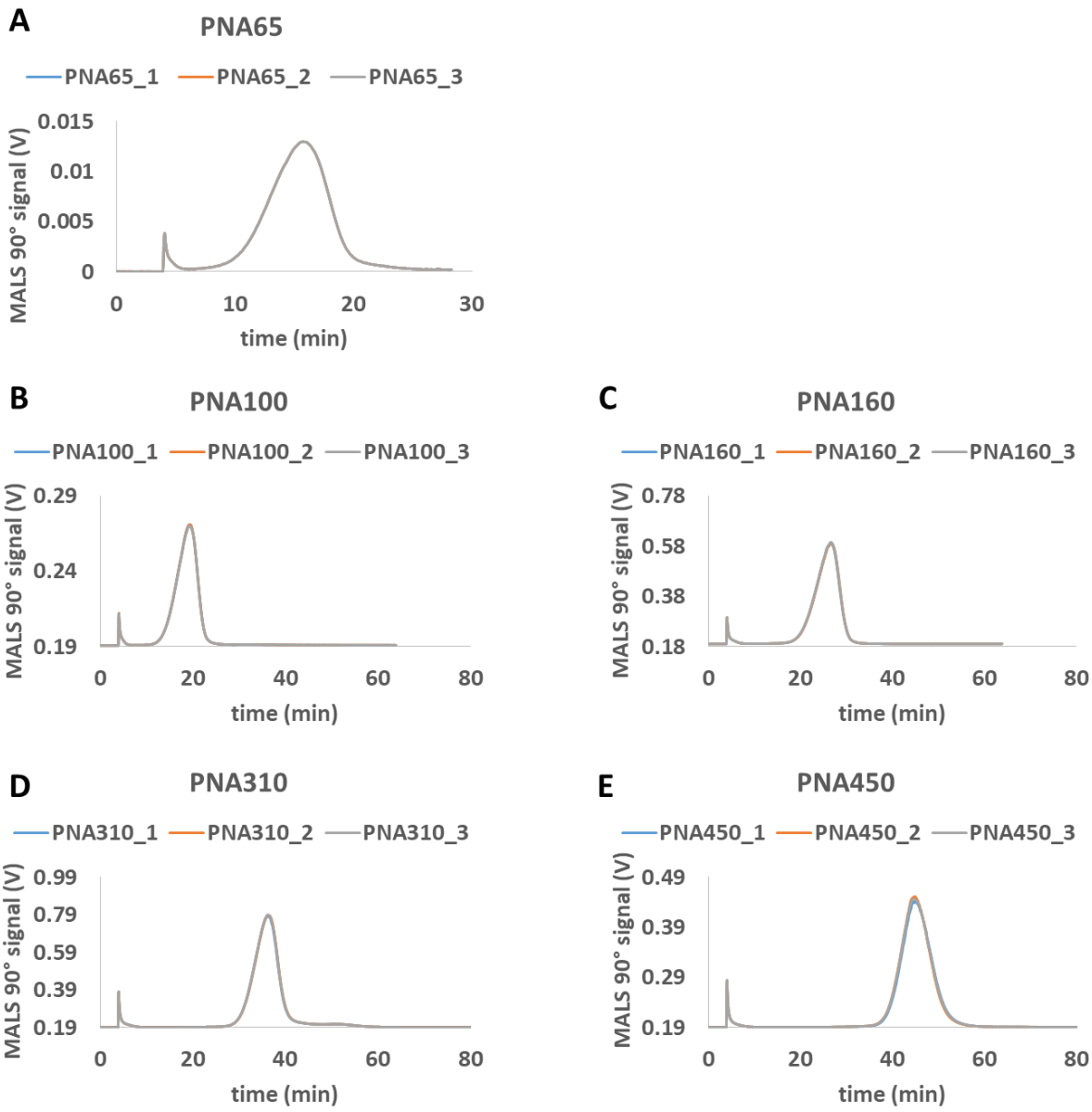

Figure 3.9. The reproducibility data for three repeat measurements of the different nanogel samples. A) PNIPAM65, B) PNIPAM100 C) PNIPAM160 D) PNIPAM310 E) PNIPAM450 using cross-flow 1 mL/min.

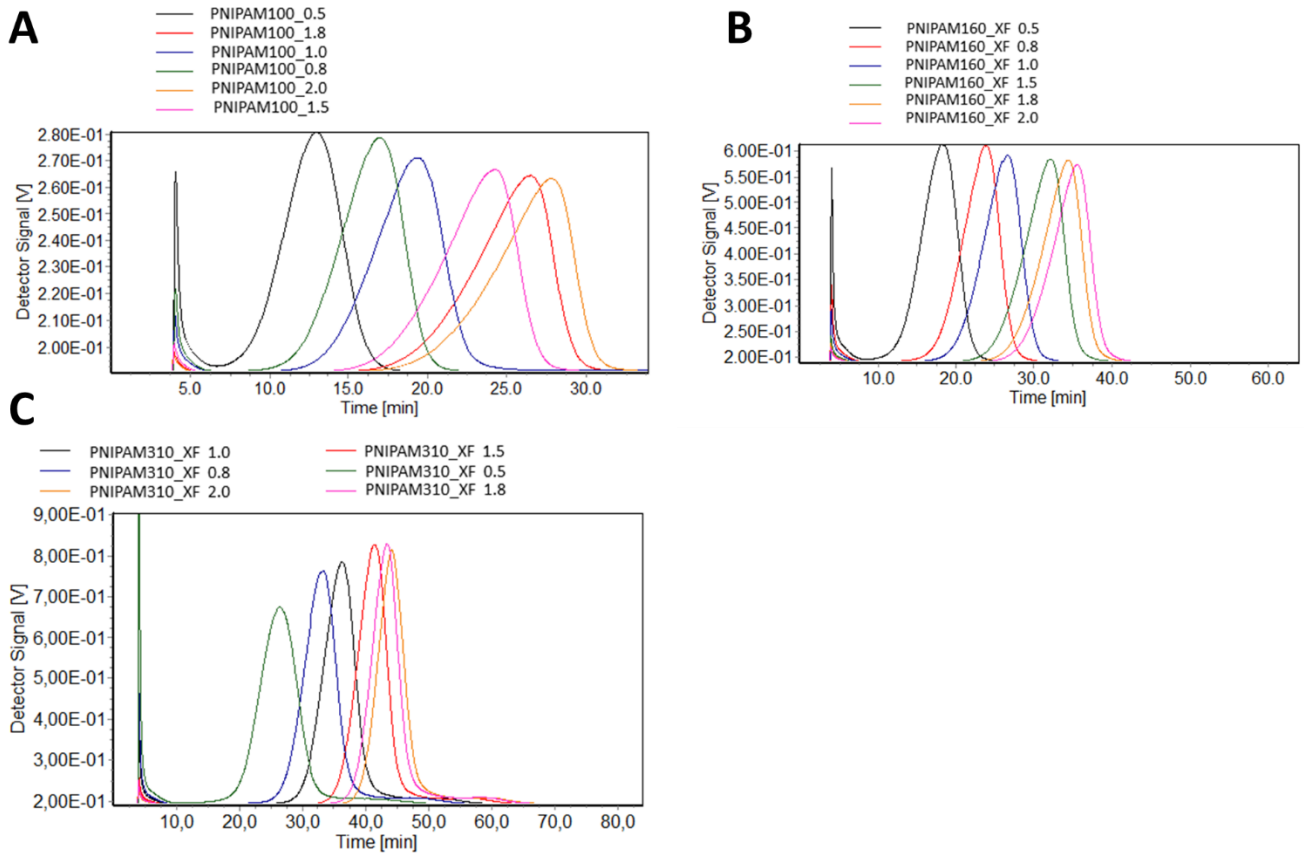

Figure 3.10. The effect of varying the crossflow on the elution time for the PNIPAM100, PNIPAM160 and PNIPAM310 in 0.1 M $NaNO_3$.

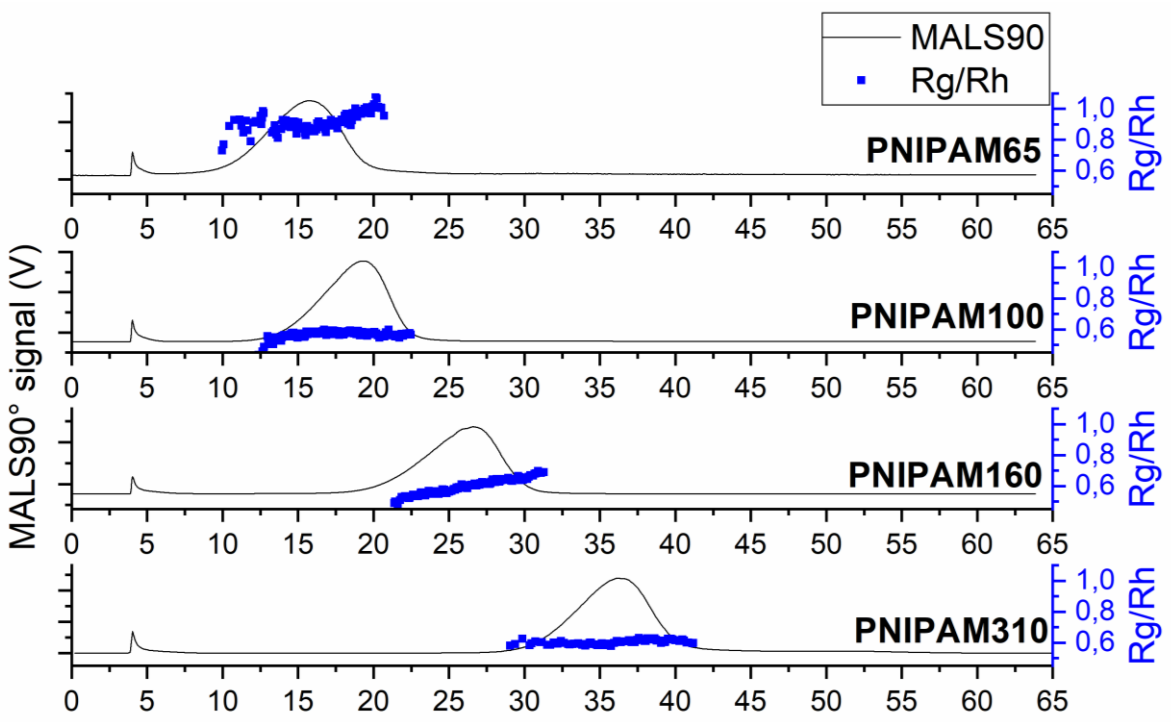

Figure 3.11. AF4-MALS-DLS analysis of nanogels. Fractograms showing the light 90° scattering detector signal (black line, left hand scale) and shape factor (blue dotted line, right hand scale) obtained from AF4-MALS-DLS measurements for PNIPAM65, PNIPAM100, PNIPAM160 and PNIPAM310.

Chapter 4

The synthesis and characterisation of degradable poly(N-isopropylacrylamide) nanogels by RAFT polymerisation

I would like to thank: Dr Emma L. Owen, Marissa Marissa Morales Moctezuma and Dr Seb Spain from University of Sheffield for providing 2-(hydroxyethylthiocarbonothioylthio)-2-methylpropanoic acid chain transfer agent

4.1. Introduction

PNIPAM nanogels have well-characterised thermoresponsive behaviour where the particles deswell when heated above their volume phase transition temperature (VPTT).[1] Additionally, dual-stimuli responsive behaviour of the nanogels has also been demonstrated by combining temperature stimuli with either ionic strength[2] or pH[3,4] causing aggregation to form a gel matrix. This dual-responsive behaviour has previously been exploited as per the formation of *in situ* forming implants (ISFI).[2,5,6] These PNIPAM nanogels underwent aggregation when stimulated by body temperature and physiological ionic strength, leading to the formation of a solid implant. Ideally, these ISFI drug delivery systems should be degradable so that they do not accumulate in the body otherwise they are required to be removed after the drug release is complete, which can lead to patient non-compliance due to the physically invasive removal procedure. In order for removal to occur through renal excretion, the cross-linked nanogels need to degrade into low molecular weight polymers (<40 kDa)[7] or smaller nanogels (< 20 nm).[8] The nanogel network can be degraded by either cleavage of the polymer backbone or the crosslinker. The carbon-carbon backbone of PNIPAM is extremely resistant to degradation, and previous studies have tried to increase the degradability of the polymer backbone by insertion of a either a degradable main-chain group or polymer blocks.[9] However, as more commonly shown, the use of a degradable crosslinker is preferable. There have been a range of different crosslinkers reported which can degrade in response to various conditions and be easily incorporated into the nanogel structure during synthesis. For example, ketal crosslinked nanogels, which degrade in response to a low pH,[10] hydrolytically degraded glycolate ester based biodegradable crosslinkers[11] and many others.[12–14] One biodegradable crosslinker that can be incorporated into a PNIPAM network is N,N'-bis(acryloyl)cystamine (BAC), which contains a biodegradable disulphide bond.[15–18] In the body, this disulphide bond can be reduced by glutathione (GSH). In this process, GSH is oxidised to form the dimer glutathione disulphide, cleaving a disulphide bond into two thiols.[19] Dithiothreitol (DTT) is often used alternatively to GSH in order to study *in vitro* reduction of disulphide bonds,[17,18] with

reduction of the disulphide bond achieved *via* a thiol-disulphide exchange reaction forming a six membered ring in DTT (see Figure 4.1).[20]

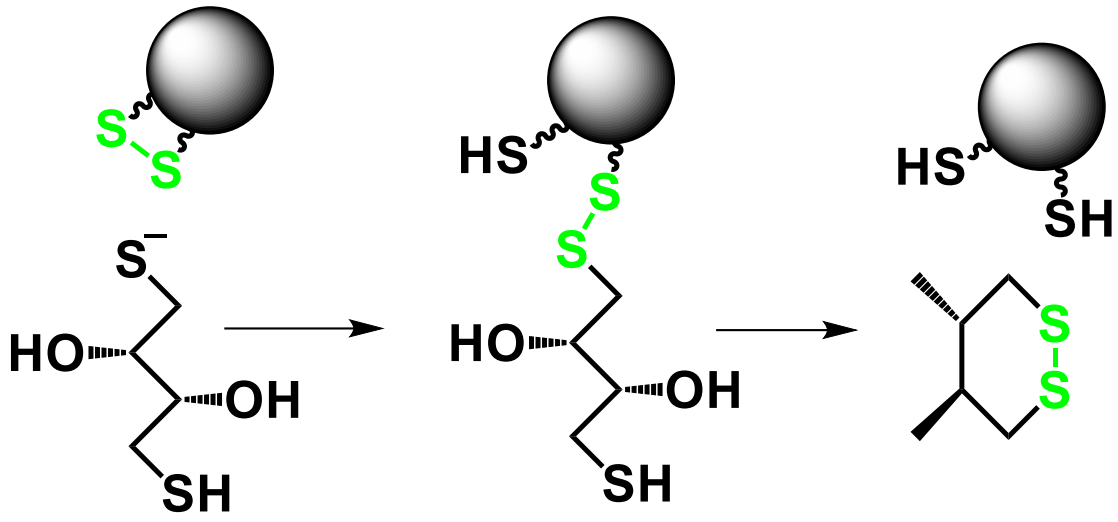

Figure 4.1 Disulphide exchange reaction between nanogel disulphide and dithiothreitol (DTT).[21]

Controlled radical polymerisations such as reversible addition–fragmentation chain-transfer (RAFT) afford significant control over polymer molecular weight (M_w) and the polydispersity (PdI).[22,23] By utilising a well-controlled polymerisation of PNIPAM nanogels, would allow the linear polymer chains regained after degradation of the nanogel network to be well-defined and below 40 kDa to allow for successful removal *via* renal excretion.[7] This criteria is necessary for the synthesis of degradable materials which can then be used as ISFIs.[2,6,16,17,24,25] The aim of this chapter is to produce degradable PNIPAM nanogels by RAFT polymerisation with well-defined length of polymer chains, that might be used as ISFIs. Nanogels were synthesised in the presence of two chain transfer agents (CTA); poly(N-hydroxyethyl acrylamide) macro CTA and poly(ethylene glycol) methyl ether 2-(dodecylthiocarbonothioylthio)-2-methylpropionate. The polymerisation was conducted in the presence of a degradable BAC crosslinker to form crosslinked PNIPAM nanogels. Different ratios of NIPAM:BAC are used to study the influence of crosslinking density on the hydrodynamic diameter (H_d) of the synthesised nanogels, as characterised by dynamic light scattering (DLS). The nanogels were further characterised using nuclear

magnetic resonance (NMR) and AF4. The degradation studies were conducted in the presence of DTT and studied by AF4-MALS and DLS. The polymer structure synthesised using the poly(N-hydroxyethyl acrylamide) as macro CTA which is crosslinked using BAC to form the nanogels discussed in this chapter, (Figure 4.2).

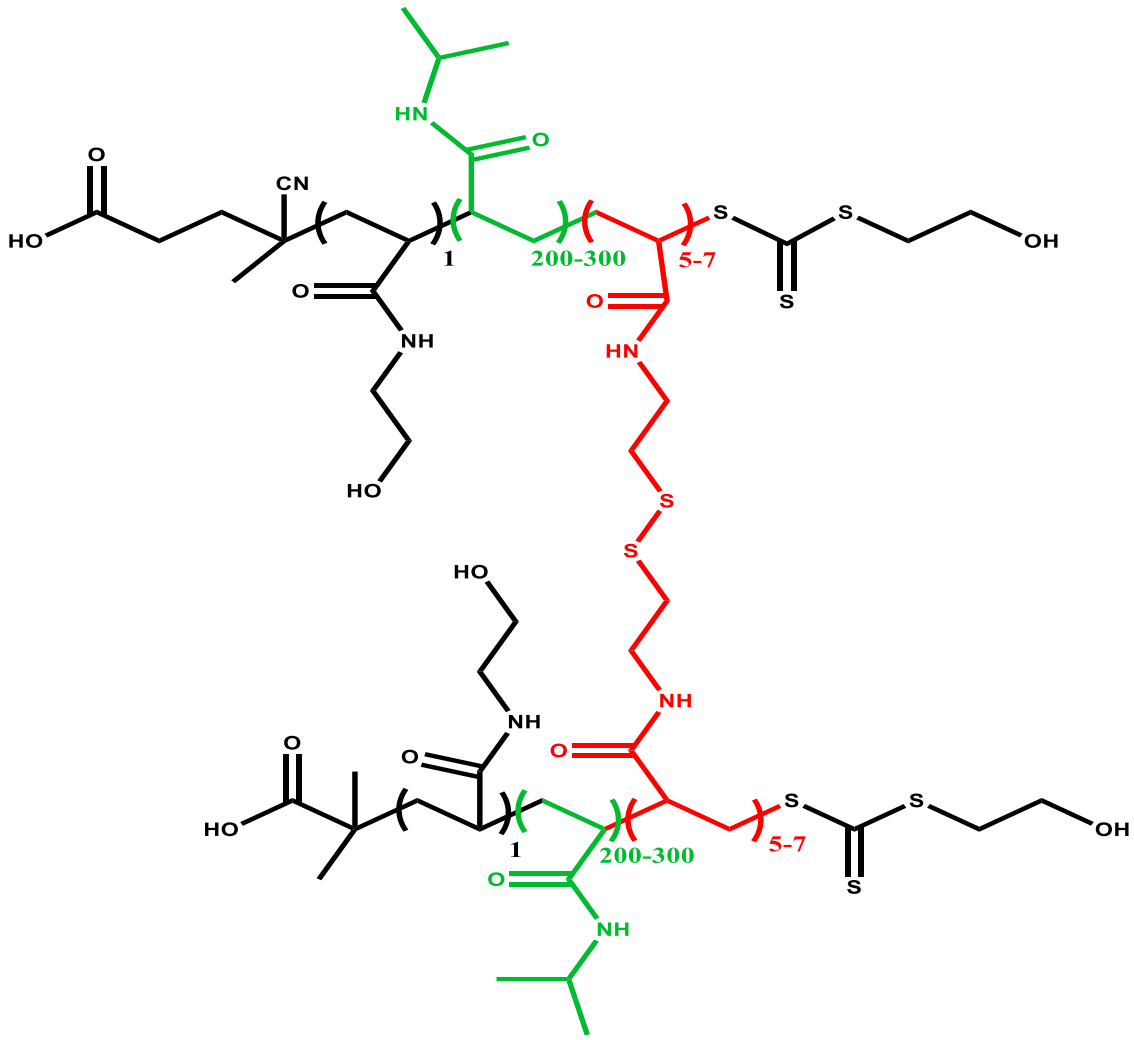

Figure 4.2. The structure of PNIPAM synthesised by RAFT polymerisation in the present of poly(N-hydroxyethyl acrylamide) as RAFT agent.

4.2. Experimental

4.2.1. Materials

N-isopropylacrylamide (NIPAM, ≥ 99%), N,N'-bis(acryloyl)cystamine (BAC, 98% HPLC), 4,4'-azobis(4-cyanovaleric acid), poly(ethylene glycol) methyl ether 2-(dodecylthiocarbonothioylthio)-2-methylpropionate (average M_n = 1100 g mol^{-1}; PEG CTA), dithiothreitol (DTT), sodium hydroxide (NaOH), sodium chloride (NaCl, ≥ 99.5%), sodium nitrate ($NaNO_3$, ≥ 99%), sodium dodecyl sulphate (SDS, ≥ 99%) were purchased from Sigma-Aldrich Company Ltd, Gillingham (Dorset) UK, a subsidiary of Merck KGaA, Darmstadt, Germany. Poly(N-hydroxyethyl acrylamide) macro chain transfer agent (HEMP CTA, M_n = 7140 g/mol) was kindly provided from the University of Sheffield. Phosphate buffered saline tablets (PBS) were purchased from Fischer Scientific. Milli-Q water obtained from a water purification system had a resistivity of > 18 MΩ cm^{-1} (PURELAB option R, Veolia). Spectra/por 2 (MWCO = 12-14 kDa) and spectra/por 3 (MWCO = 3.5 kDa) dialysis tubing was purchased from Spectrum Europe B.V., Breda, The Netherlands. Corning bottle top vacuum filter system with cellulose acetate membrane (pore size 0.22 μm) was purchased from Sigma-Aldrich Company Ltd, Gillingham (Dorset) UK, a subsidiary of Merck KGaA, Darmstadt, Germany.

4.2.2. Synthesis of 2-(hydroxyethylthiocarbonothioylthio)-2-methylpropanoic acid chain transfer agent

The 2-(hydroxyethylthiocarbonothioylthio)-2-methylpropanoic acid chain transfer agent was kindly provided by University of Sheffield. The synthesis was as follows: 2-mercaptoethanol (6.1 mL, 87.54 mmol) and potassium phosphate tribasic (19.16 g, 87.54 mmol) were dissolved and stirred in acetone (150 mL). After 30 mins, carbon disulphide (11 mL, 0.17 mol) was added and the mixture was left to stir for another 30 min. 2-bromoisobutyric acid (14.92 g, 87.54 mmol) was finally added and the mixture was left to react at ambient temperature. After 18 h, the mixture was purged

with N_2 for 2 h. The mixture was filtered and the acetone was removed under *in vacuo*. The product was acidified by adding a 1M solution of hydrochloric acid (2x 100 mL) and the organic phase was extracted with DCM (2 x 100 mL). The organic phase was then washed with a saline solution (100 mL). All the organic phases were collected and dried using (Na_2SO_4). DCM was then remove *in vacuo*. Finally, the crude product was recrystallised using a mixture of hot hexane and ethyl acetate (7:3 v/v ratio) to give a bright yellow solid as product (17.2 g, 86%); m.p. 62-64 °C; ^{1}H NMR (400.2 MHz; $CDCl_3$, 25 °C), δ_H (ppm): 3.86 (m, 2H, C<u>H</u>$_2$OH), 3.53 (t, 2H, C<u>H</u>$_2$SC), 1.73 (s, 6H, SC(C<u>H</u>$_3$)$_2$). ^{13}C (100.25 MHz; $CDCl_3$, 25 °C), δ_C: 25.19 (C(S)SC(CH_3)$_2$), 39.31 (CH_2SC(S)S), 60.48 (CH_2OH), 177.50 (C(O)OH), 220.60 (SC(S)S).

4.2.3. Synthesis of poly(N-hydroxyethyl acrylamide) (HEMP CTA) macro chain transfer agent

The poly(N-hydroxyethyl acrylamide) (HEMP CTA) macro chain transfer agent was kindly provided by University of Sheffield. The synthesis was as follows; azobisisobutyronitrile (0.0079 g, 0.04 mmol), 2-(hydroxyethylthiocarbonothioylthio)-2-methylpropanoic acid (3.09 g, 26.1 mmol) and N-hydroxyethyl acrylamide (0.1047 g, 0.43 mmol) were dissolved and stirred in ethanol (9.33 g). The mixture was stirred (400 rpm) and purged with N_2 for 30 min. The solution was then heated to 70 °C. The reaction was maintained under a N_2 atmosphere for 1.5 hours at 70 °C before being cooled to room temperature. The product was precipitated 3 times in ethyl ether to remove unreacted monomer and then freeze dried. ^{1}H NMR (500 MHz; D_2O 25 °C), δ_H (ppm): 4.7 (m, 2H, CH_2OH), 3.8 (m, 2H, CH_2SC), 3.58 (s, 6H, SC(CH_3)$_2$), 3.51 (m, 2H*60, CH2NH), 3.3 (t, 2H, CH2CH2), 2.68 (m, 2H*60, CH_2CH), 1.5 (s, 6H, CH_3C).

4.2.4. Synthesis of degradable PNIPAM by RAFT polymerisation

The PNIPAM nanogels were synthesised by RAFT dispersion polymerisation. The total solid content was kept at around 5 wt %. The nanogels were synthesised by reacting monomer NIPAM to form varying degrees of polymerisation (DP = 200, 250, 300) and the ratio between BAC crosslinker and macromolecular transfer agent were also varied. The composition used in the synthesis of each nanogel can be found in Table 4.1 and Table 4.2. The NIPAM monomer, BAC crosslinker, SDS surfactant, HEMP CTA or PEG CTA were dissolved in distilled water in 25 mL vials with a stirrer bar and rubber septum. This was then sealed and nitrogen was bubbled through the aqueous solution for 30 min whilst stirring (400 rpm) to remove dissolved oxygen. The solution was then heated to 70 °C. Separately, ACVA initiator was dissolved in distilled water and degassed with N_2 for 30 min before being transferred to the flask containing the monomers. The reaction was maintained under a N_2 atmosphere for 19 hours at 70 °C before being cooled to room temperature. To remove unreacted impurities, the nanogel suspension was dialyzed for 5 days using regenerated cellulose dialysis tubing (12-14 kDa MWCO), (Spectrum Labs), replacing the distilled water every 12 hours. The synthesised PNIPAM nanogels were analysed by DLS, AF4 and tested in degradation studies.

Table 4.1. The composition used in nanogels synthesis using HEMP CTA as RAFT agent.

Sample	NIPAM (mg)	[SDS] (mg/mL)	BAC (mg)	ACVA (mg)	HEMP CTA (mg)	Water (ml)
HEMP200:7	200	0.5	16.1	0.88	2.1	4.162
HEMP250:7	200	0.5	12.8	0.66	1.7	4.089
HEMP300:7	200	0.5	10.7	0.55	1.4	4.041
HEMP200:5	200	0.5	11.5	0.82	2.1	4.075
HEMP250:5	200	0.5	9.2	0.66	1.7	4.020
HEMP300:5	200	0.5	7.7	0.55	1.4	3.983
HEMP200:3	200	0.5	6.9	0.82	2.1	3.987
HEMP250:3	200	0.5	5.5	0.66	1.7	3.949
HEMP300:3	200	0.5	5.5	0.55	1.4	3.925

Table 4.2. The composition used in nanogels synthesis using PEG CTA as RAFT agent.

Sample	NIPAM (mg)	[SDS] (mg/mL)	BAC (mg)	ACVA (mg)	PEG CTA (mg)	Water (ml)
PEG250:7	200	0.5	12.8	0.66	7.7	4.205
PEG250:5	200	0.5	9.2	0.66	7.7	4.135
PEG250:3	200	0.5	5.5	0.66	7.7	4.065

4.2.5. Characterisation of PNIPAM nanogels by DLS

Characterisation of the nanogels was carried out using DLS. DLS was performed using a Malvern Zetasizer Nano ZS (running Malvern Zetasizer software V7.12) with 633 nm He-Ne laser and the detector positioned at 173 °. Dialysed samples were diluted to 1 mg/mL. The Z-average diameter was recorded in the range 15-55 °C using a thermal equilibration time of 600 seconds in 1 cm path length disposable polystyrene cuvettes. Measurements were repeated in triplicate to give a mean Z-average diameter and polydispersity index (PdI). Measurements were repeated in triplicate to give a mean hydrodynamic diameter and polydispersity index (PdI). Zeta potential measurements were performed using DTS1070 folded capillary cells (Malvern, UK). The pH of the sample was measured before performing zeta potential measurements, and both samples fell in the range pH 7 ± 0.5. DTS1070 folded capillary cells were flushed with ethanol and water prior to usage. The zeta potential measurement was made with a minimum of 10 and maximum of 40 runs, and the voltage applied was automatically selected by the software. The Smoluchowski approximation where f(Ka) = 1.5 was used, and dispersions contained 10 mM NaCl and were measured at 25 °C.

4.2.6. Characterisation of PNIPAM nanogels by AF4

Asymmetric flow field flow fractionation (AF4) experiments were performed on an MT2000 with RI and UV-Vis detectors from Postnova Analytics, Landsberg, Germany. Multi angle light scattering detector (MALS) PN3621 from Postnova Analytics with 21 angle detection (from 7° to 164 °) operating at 532 nm power wavelength were coupled online to AF4. Autosampler (PN5300) was purchased from Postnova Analytics. A UV-Vis detector was used to monitor wavelengths of 250 and 300 nm. The hydrodynamic radius of the samples was obtained by DLS using a Malvern Zetasizer Nano ZS (Malvern Instruments, Malvern, UK) running Malvern Zetasizer software V7.12 with 633 nm He–Ne laser and the detector positioned at 173°, coupled online to the MT2000. A 350 µm spacer and 10 kDa regenerative cellulose (RC) membrane were installed in the separation channel. The conditions used for the separations was based on a method existing in the literature,[18,26] where, the eluent was 0.1 M $NaNO_3$. Type I distilled water was obtained from a water purification system with a resistivity of > 18 MΩ cm^{-1} (PURELAB option R, Veolia). The eluents were filtered using a bottle top vacuum filter system with cellulose acetate membrane with pore size 0.22 µm. 20 µL of sample (1 mg/mL) was injected *via* the use of an autosampler. The samples were injected three times to check reproducibility. A blank sample was measured between sample injections to clean the system. The conditions used for the separations was as follows; the injection/focussing time was 3 minutes using a cross flow from 2 to 0.5 mL/min. The chosen cross flow rate was kept for the first 0.2 min (t_0-$t_{0.2}$) in a constant manner, and thereafter, the cross flow was decreased in a power manner (exponent 0.2) from its initial value to 0.1 mL/min over a period of 40 min. Following the complete reduction in cross flow, the tip-flow 0.1 mL/min continued for an additional 40 min. Hydrodynamic radius was calculated from translational diffusion coefficient according to Einstein-Stokes equation. Radius of gyration was measured on the MALS and calculated based on a spherical fit.

4.2.7. Nanogel degradation studies

Nanogels were degraded as a 1 mg/ml pH 10 aqueous dispersion using 10 mM DTT, or 150 mM when immediate degradation was required. DLS was used to measure the mean count rate of a degraded and non-degraded sample at the same attenuator value and measurement position. Count rate was measured in kilo counts per second, which provides a measure of the fluctuation in scattered light intensity over time.[27] The count rate is a function of particle size, concentration and the difference in particle to medium refractive index.[28] The attenuator value was fixed at a value found to be suitable for the dispersion at the start of the degradation, and the measurement position of the laser was fixed at 4.65 mm (centre of the cuvette). Leber *et al*. and Chen *et al.* [10,11] previously showed that the count rate of a nanogel sample decreases as the nanogel degrades, assuming that a decrease in count rate over time was related to a change in particle to medium refractive index due to particle degradation. Polymers may be lost from the particle and replaced by solvent which can lead to a change in count rate.

For DLS measurements, the percentage of nanogels remaining were calculated by dividing the derived count rate for samples before and after addition of DTT (concentration of nanogels 1 mg/mL) and then multiplying it by 100 %. The results from the AF4 were calculated similarly, by analysing the area under the curve for MALS90 ° for all samples before and after addition of DTT were divided by each other and multiplied by 100 %.

4.3. Results

4.3.1. Degradable nanogels synthesis and size characterisation

To synthesise nanogels consisting of polymers with well-defined primary chain length and the ability to aggregate at about 37 ˚C at physiological ionic strength, a series of PNIPAM nanogels were synthesised by RAFT polymerisation with BAC as a degradable crosslinker (see Table 4.3). Two different RAFT agents were initially used for the nanogel synthesis, these were 2-(hydroxyethylthiocarbonothioylthio)-2-methylpropanoic acid (HEMP, M_n=7,128 g/mol; see Figure 4.3A) and poly(ethylene

glycol) methyl ether 2-(dodecylthiocarbonothioylthio)-2-methylpropionate (M_n=1,100 g/mol; see Figure 4.3B). These two RAFT agents were chosen due to their solubility in water, the solvent for the dispersion polymerisation. In order to assess the effect of using a macro CTA, the CTAs were used in the RAFT polymerisation process. The full composition for PNIPAM nanogels made with macro HEMP CTA can be found in Table 4.4. The name of each sample indicates the ratio of monomer and crosslinker to the CTA. For example, HEMP200:7 consists of 200 moles of monomer and 7 moles of crosslinker for each mole of CTA. The different ratios of BAC and NIPAM was used to investigate the influence of these variables on size, polydispersity and the degradability of the nanogels. The molar ratios between initiator, HEMP CTA and SDS was kept constant. A secondary PEG based CTA (Figure 4B) was also used in the synthesis of degradable PNIPAM nanogels, where the full nanogel ratios are highlighted in Tables 4.2 and 4.4. It was expected that the length of the primary chains would be controlled by the molar ratio of the monomer to the CTA.[29] The chain ends in the nanogel would be either the R or Z group of the CTA as shown in Chapter 1, Figure 1.10 or the initiator fragment as schematically presented in Figure 4.4. The reaction scheme is presented in Scheme 4.1.

Table 4.3. The molar ratio of chemicals used for the preparation of PNIPAM nanogels with the presence of HEMP CTA.

Sample	NIPAM	[SDS]	BAC	ACVA	HEMP CTA
HEMP200:7	200	1	7	0.33	1
HEMP250:7	250	1	7	0.33	1
HEMP300:7	300	1	7	0.33	1
HEMP200:5	200	1	5	0.33	1
HEMP250:5	250	1	5	0.33	1
HEMP300:5	300	1	5	0.33	1
HEMP200:3	200	1	3	0.33	1
HEMP250:3	250	1	3	0.33	1
HEMP300:3	300	1	3	0.33	1

Table 4.4. The molar ratio of chemicals used for the preparation of PNIPAM nanogels with the presence of PEG CTA.

Sample	NIPAM	[SDS]	BAC	ACVA	PEG CTA
PEG250:7	250	1	7	0.33	1
PEG250:5	250	1	5	0.33	1
PEG250:3	250	1	3	0.33	1

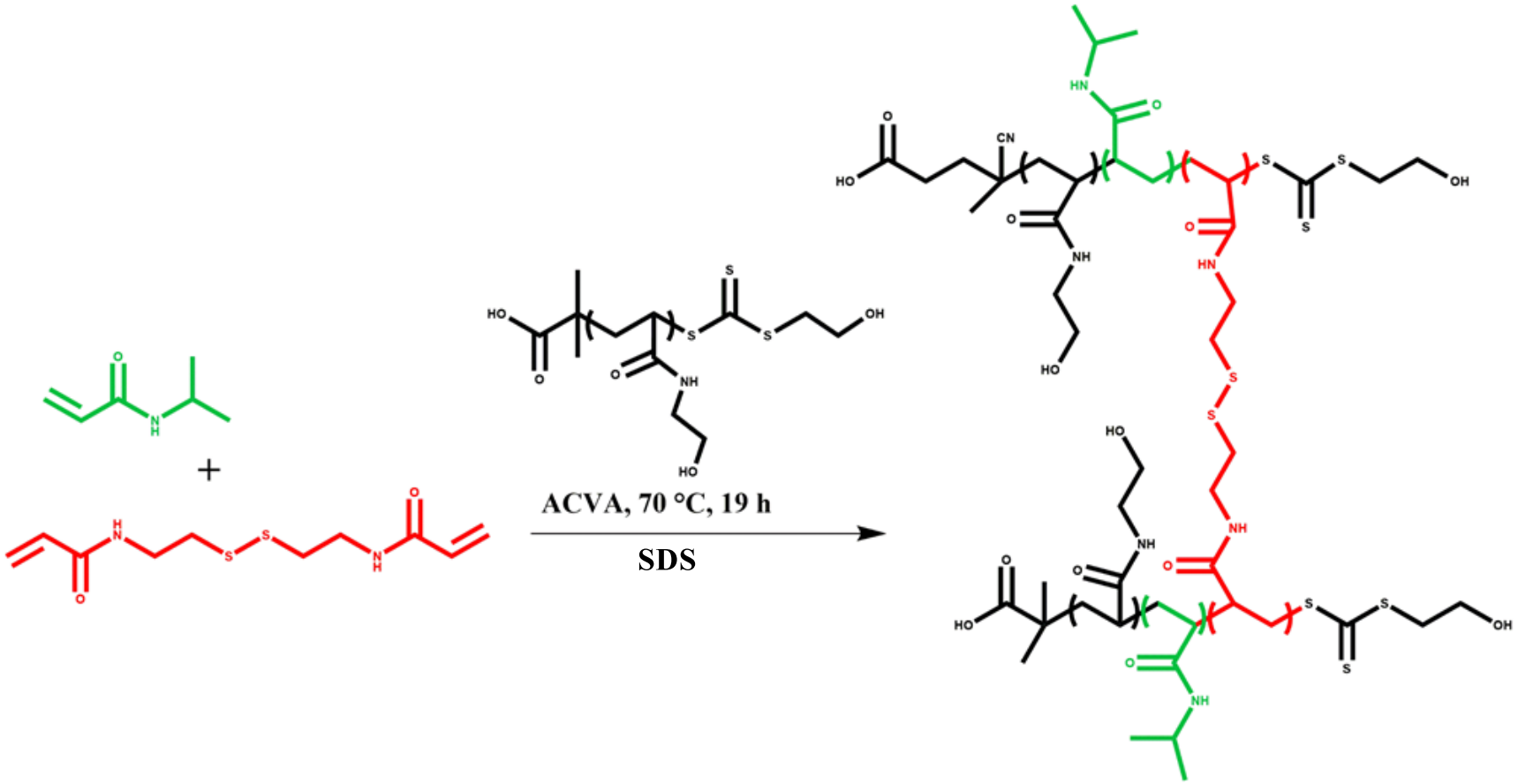

Scheme 4.1. Generalised RAFT polymerisation of NIPAM (green) in the presence of BAC as crosslinker (red), ACVA as initiator and HEMP CTA as RAFT agent (black).

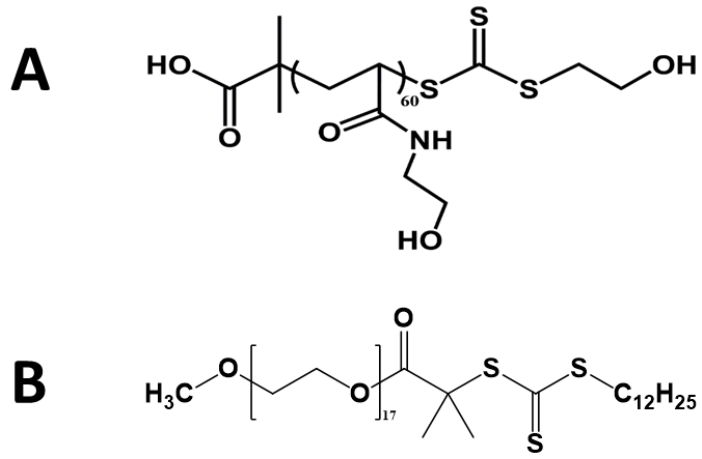

Figure 4.3. The structure of A) HEMP RAFT agent B) PEG RAFT agent.

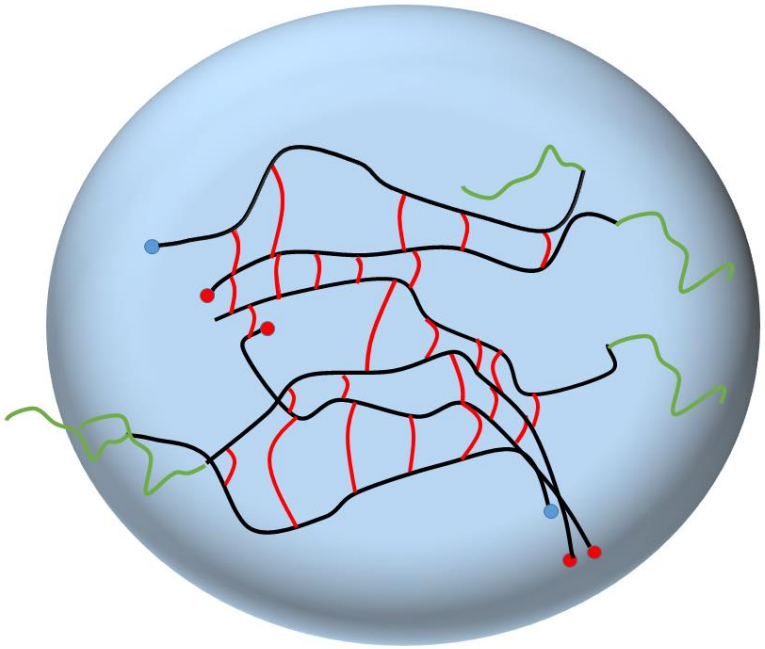

Figure 4.4. Cartoon representation of HEMP200:5. The comparative lengths of the polymer chains represent their comparative degrees of polymerisation. Black lines indicates PNIPAM repeating units, red lines represents BAC crosslinker, green lines shows HEMP CTA, red dots – ACVA and blue dots – RAFT end groups.

The samples were characterised by DLS as discussed in Section 4.2.7, and the data is presented in Table 4.5. When RAFT polymerisations were conducted in the presence of a PEG CTA, at a monomer:crosslinker ratio of 250:3, no formation of nanogels were apparent. As the molar concentration of BAC was increased (≥ 5), samples contained large insoluble aggregates, which were unable to be accurately characterised *via* DLS. This could possibly be due to the fact that the RAFT agent was not compatible with monomer or poor reactivity of RAFT agent.[30]

RAFT polymerisations conducted with HEMP CTA and crosslinker ratio of BAC > 3, produced nanogels with a hydrodynamic diameter (H_D) in the range of 318 - 457 nm and PdI ≤ 0.15. The low PdI and high derived count rate (>11000 kcps) suggest a single population of nanogels with good monodispersity. The samples were turbid in appearance caused by light scattering of particles, indicating successful synthesis. Samples prepared with the lower molar ratio of BAC (samples HEMP200:3-HEMP300:3), showed much lower derived count rates (< 140 kcps) with high PdIs (from 0.48 to 0.8; see Table 4.5). This is in comparison to literature values, where the typical PdI for PNIPAM nanogels has been shown to be less than 0.15.[2,31–33] HEMP200:3-HEMP300:3 nanogels were also visually transparent. It is likely due to the lower concentration of crosslinker in the nanogel synthesis, may have resulted in branched or linear polymers chains, rather than the fully crosslinked networks that make up nanogels. ^{1}H NMR was used to analyse the structure of a PNIPAM nanogel synthesised in the presence of HEMP CTA, the spectrum for the nanogel was rather complex with many overlapping peaks. It was challenging to gather conclusive information from solution NMR on nanogels as they are crosslinked and some of the chains may not be mobile enough to show up on the NMR (see SI, Figure 4.18).

Table 4.5. DLS analysis of PNIPAM nanogels synthesised with varying ratios of monomer:crosslinker in an aqueous solution (1 mg/mL). The black colour of font indicates successfully synthesised nanogels and red font represents obtained linear polymer chains or branched polymers.

Sample	HEMP200:7	HEMP250:7	HEMP300:7	HEMP200:5	HEMP250:5	HEMP300:5	HEMP200:3	HEMP250:3	HEMP300:3	PEG250:3
D (nm)	437 ± 2	369 ± 11	361 ± 3	457 ± 12	352 ± 2	318 ± 4	427 ± 51	415 ± 116	1213 ± 870	182 ± 2
PdI	0.142 ± 0.014	0.093 ± 0.046	0.065 ± 0.011	0.088 ± 0.092	0.156 ± 0.047	0.108 ± 0.092	0.474 ± 0.058	0.490 ± 0.062	0.800 ± 0.199	0.249 ± 0.018
Der. Count Rate (kcps)	17171 ± 1053	19177 ± 208	27926 ± 1189	11647 ±500	30078 ± 510	43323 ± 1251	99 ± 12	174 ± 8	136 ± 27	1370 ±5

The H_D values of successfully synthesised nanogels were found to slightly decrease when higher ratios of monomer to crosslinker were used (BAC ≥ 5), which would be expected to result in longer primary PNIPAM chains. This may be due to the influence of the CTA on the colloidal stability during the dispersion polymerisation, the hydrophilic CTA might be disrupting the aggregation of the primary nucleated chains resulting in less dense crosslinking and larger nanogel particles. However, the influence of the ratio of crosslinker to monomer did not show a significant impact, which may be due to the fact that the changes in the molar ratio of crosslinker were not large enough to see an effect.

In next part of this chapter, the six samples that had successfully formed nanogels (HEMP200:7, HEMP250:7, HEMP300:7, HEMP0200:5, HEMP250:5, HEMP300:5) were taken forward for further analysis. These samples had three different degrees of polymerisations (DPs) and two different crosslinker contents and the effect of these variables on the temperature responsive behaviour and degradation behaviour were assessed via DLS and AF4.

4.3.2. Dynamic light scattering measurements to investigate temperature responsive behaviour

The temperature responsive behaviour of the nanogels was analysed by using gradual heating within the Malvern Zetasizer and measuring the change in mean diameter. When the nanogels were heated in water they all showed characteristic deswelling at the volume phase transition temperature (VPTT) (Figure 4.5) and remained colloidally stable as first shown by Pelton et *al*.,[34] where the VPTT was determined as the halfway point in the slope.[35] The VPTT for all the PNIPAM-RAFT nanogels was around 34 ˚C, which agrees with literature findings.[2] Typical values of VPTT for PNIPAM nanogels has been previously shown as around 34 ˚C,[36] with some dependence on crosslinker structure as well as crosslinking density.[37,38] Below the VPTT the nanogels exist as hydrophilic particles with the network swollen by water molecules, due to favourable hydrogen bonding between the amide units and water.[39] These solvated polymer chains are also able to provide steric stabilisation of the particles. Above the VPTT the polymer–polymer hydrogen bonding becomes more favourable and the particles de-swell as they expel solvent, decreasing the diameter of the particle. In the deswollen form the potential for steric stabilisation from the PNIPAM chains is lost and typically, electrostatic

repulsion between particles provides colloidal stability.[40] In the case of the samples in this work, the electrostatic stabilisation is caused by the presence of SDS salt in the system during the polymerisation. This SDS is then removed during the dialysis purification step and therefore the colloidal stability comes from the polymer chains and initiator fragments that make up the nanogels. These nanogels therefore contain a small number of ACVA initiator fragments which provide carboxylic chain ends. The pK_a of these groups is 3.85[41] which indicates partial dissociation into its ions in a natural aqueous solution which would provide some surface charge to the nanogels.[42] Additionally, the nanogels also contain the poly(N-hydroxyethyl acrylamide) macro CTA which could act as a steric stabiliser, these two factors must provide the electrostatic stabilisation above the VPTT. However, they appear to have limited impact on the temperature responsive behaviour compared to PNIPAM nanogels prepared by free radical dispersion polymerisation. The polydispersity index was found to be stable with increasing temperature over time, indicating good colloidal stability (see SI, Figure 4.13).

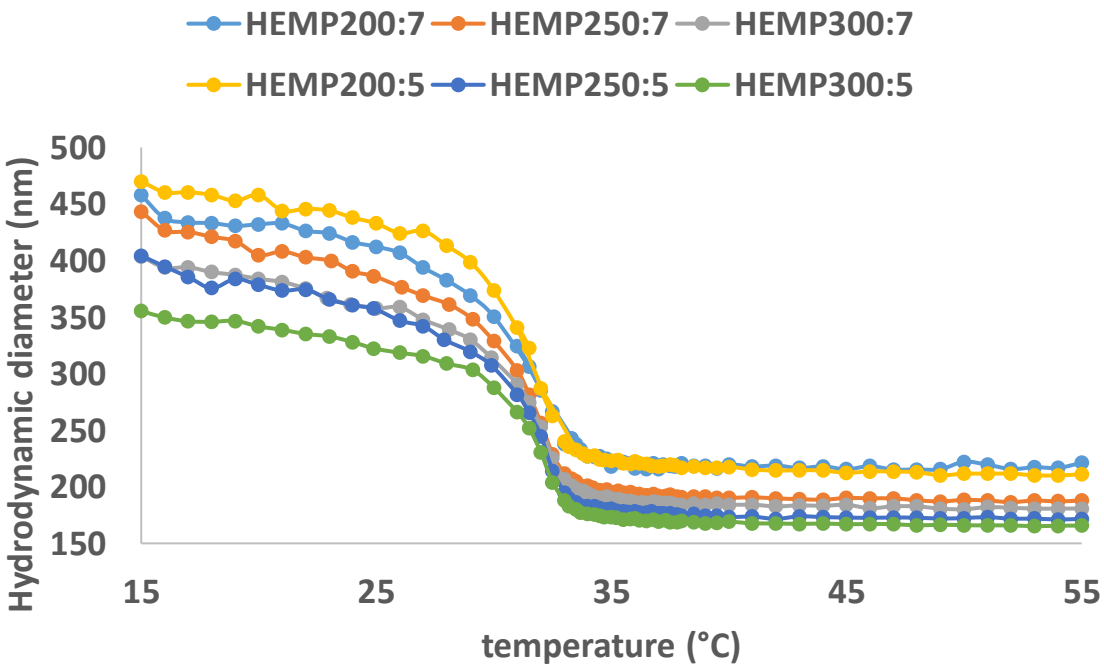

Figure 4.5. Graph showing the change in H_D (nm) versus temperature for PNIPAM nanogels with varying monomer: crosslinker ratios, in aqueous solution (concentration 1 mg/mL).

The swelling ratios of the nanogels in aqueous solution were calculated from DLS measurements of hydrodynamic diameters, where the nanogels showed similar swelling ratios (1.9-2.0). Verga *et al*. showed that for PNIPAM nanogels, swelling ratio is related to crosslinking density.[40] However, the experimental data showed that such changes to crosslinking density did not cause an observable different in our samples. It may be due to the range of crosslinking densities in the samples not being not sufficient enough to have a significant impact on the swelling ratios.

Table 4.6 Swelling ratio for PNIPAM nanogels in water

Sample	HEMP200:7	HEMP250:7	HEMP300:7	HEMP200:5	HEMP250:5	HEMP300:5
Swelling ratio[a]	1.9	2.0	2.0	2.0	2.0	2.0

[a] Swelling ratio calculated from DLS measurement of hydrodynamic diameter (H_d) using 1 mg/mL aqueous dispersion, swelling ratio = H_d (25°C) / H_d (55°C)

The temperature responsive behaviour of the nanogels was then assessed when dispersed in PBS which was conducted by heating the samples in 1 °C intervals to determine the temperature at which the particles aggregated. This aggregation temperature was indicated by a dramatic rise in hydrodynamic diameter and PdI (see Figure 4.6). The aggregation temperature was 28 °C for almost all nanogels, except HEMP300:5. Sample HEMP300:5 underwent aggregation at 27 °C. It is not fully understood why this sample had a different aggregation temperature in comparison to the other nanogels tested. There was a clear difference in the VPTT between the samples analysed in aqueous dispersions and the aggregation behaviour in PBS. It is known that the VPTT can be decreased by introduction of hydrophobic group into the polymer chains.[43] In PBS and above the VPTT, the increased concentration of ions means that the charges that provided electrostatic stabilisation in aqueous conditions were screened and therefore flocculation occurs.[44] The presence of salt also decreased the VPTT of PNIPAM nanogels due to the increased ionic strength of the solvent making it a worse solvent for the nanogels as suggested by earlier research.[33] Town *et al*. showed that VPTT of PNIPAM nanogels in PBS was 31 °C for samples prepared by dispersion polymerisation using potassium persulphate as initiator and N,N-methylenebis(acrylamide) as crosslinker where the ratio between monomer and

crosslinker was 10:1.[33] In the RAFT nanogels discussed in this work a macro CTA was used during synthesis, which can act as steric stabiliser and the more hydrophobic crosslinker (BAC) means that a direct comparison in the VPTT behaviour cannot be made in comparison to previous studies. However, generally the VPTT of nanogels can be reduced through the incorporation of a greater number of hydrophobic components. This reduction in the VPTT might suggest that the CTA and initiator used in this work were less polar in character compared to the end groups obtained using potassium persulphate as the initiator. The aggregation behaviour of the RAFT nanogels was consistent with the aggregation behaviour of PNIPAM nanogels made by free radical polymerisation, showing that the macro CTA did not considerably alter the colloidal stability of the final particles, allowing aggregation in PBS to occur.

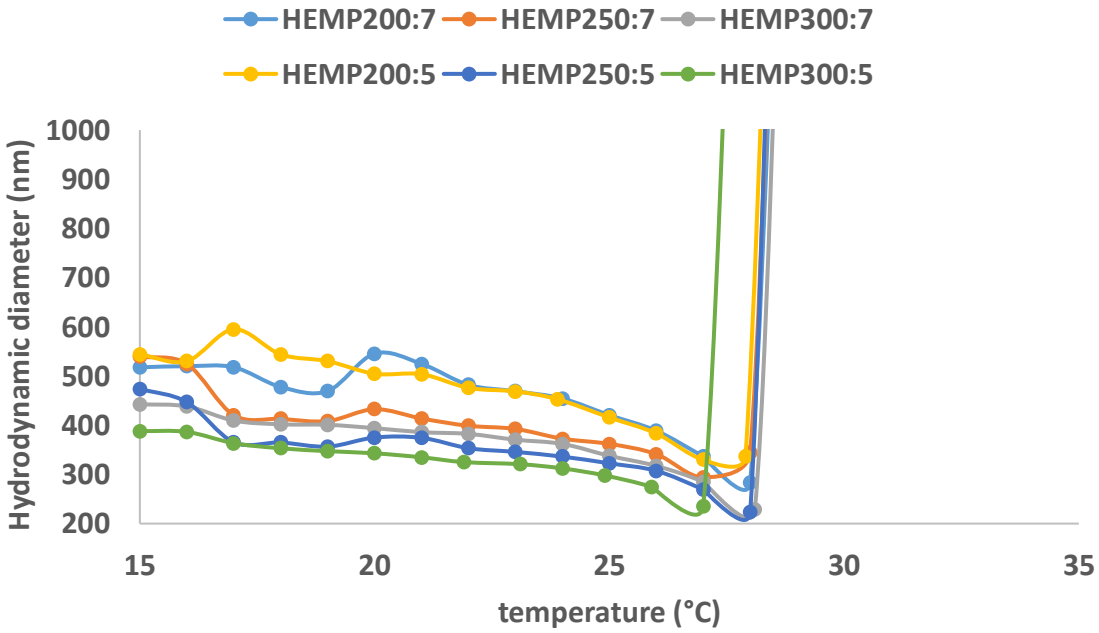

Figure 4.6. Change in hydrodynamic diameter (nm) versus temperature for PNIPAM nanogels with varying monomer:crosslinker ratios in PBS (1 mg/mL).

Zeta potential measurements were carried out to investigate the colloidal stability of the nanogels. The zeta potential showed values between -1.9 and -2.3 mV for all samples (see SI Table 4.9). For particles to have good electrostatic stabilisation zeta potential values should be over ± 30 mV.[45] Therefore, as expected, stability of the colloids must have been provided

by steric stabilisation.[46] The nanogels had both the solvated PNIPAM chains and the non-temperature responsive macro CTA offering steric repulsion.

4.3.2. Degradation studies by dynamic light scattering

In order to investigate the degradation process for RAFT-PNIPAM nanogels over time, DTT was used at different concentrations (10 and 150 mM) while under constant basic pH conditions (pH 10). The conditions were kept at pH 10 as the reducing power of DTT is limited by the reactivity of negatively charged thiolate S^- form. The thiols of DTT have pK_a of 9.2 and 10.1 which means that pH > 9 should be used to maintain DTT in the active thiolate form.[20] The nanogels were degraded at room temperature over 72 h. The example of HEMP300:7 nanogels before and after degradation is shown in Figure 4.7. In the picture, the changes in turbidity and colour from white (left hand side) to a less turbid sample with a blue tint (right hand side) are visible and it can be attributed to Tyndall scattering effect. The samples contain the same concentration of nanogel (1 mg/mL). The change of turbidity may be caused by degradation of nanogels into smaller particles and potentially soluble polymer chains.

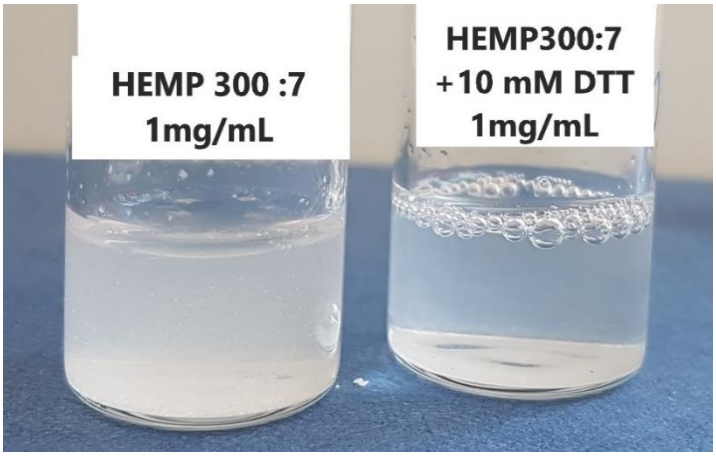

Figure 4.7. HEMP300:7 before and after degradation (72 h) in the presence of 10 mM DTT at pH 10.

The degradation process was monitored by DLS, observing the changes in diameter and the derived count rate of samples. The changes in hydrodynamic diameter (%) for samples before and after addition of DTT over 72 h are shown in Figure 4.8. It was found that the majority of

samples increased in diameter with increased concentration of DTT added to the samples. This can be explained by the effects from crosslink scission of the nanogels; the nanogels swell as the disulphide bonds forming the crosslinker are broken. The higher concentration of DTT resulted in larger nanogel, potentially caused by more crosslink scission. Previous work has showed that the maximum size to which a nanogel can swell is constrained by the density of crosslinking present.[47,48] It is possible that within the samples there are heterogeneity in structure (i.e. crosslinking density) of the particles and therefore some of the nanogels are dissolving while others are swelling. Therefore it was important to quantify changes in the light scattering intensity by measuring the derived count rate.

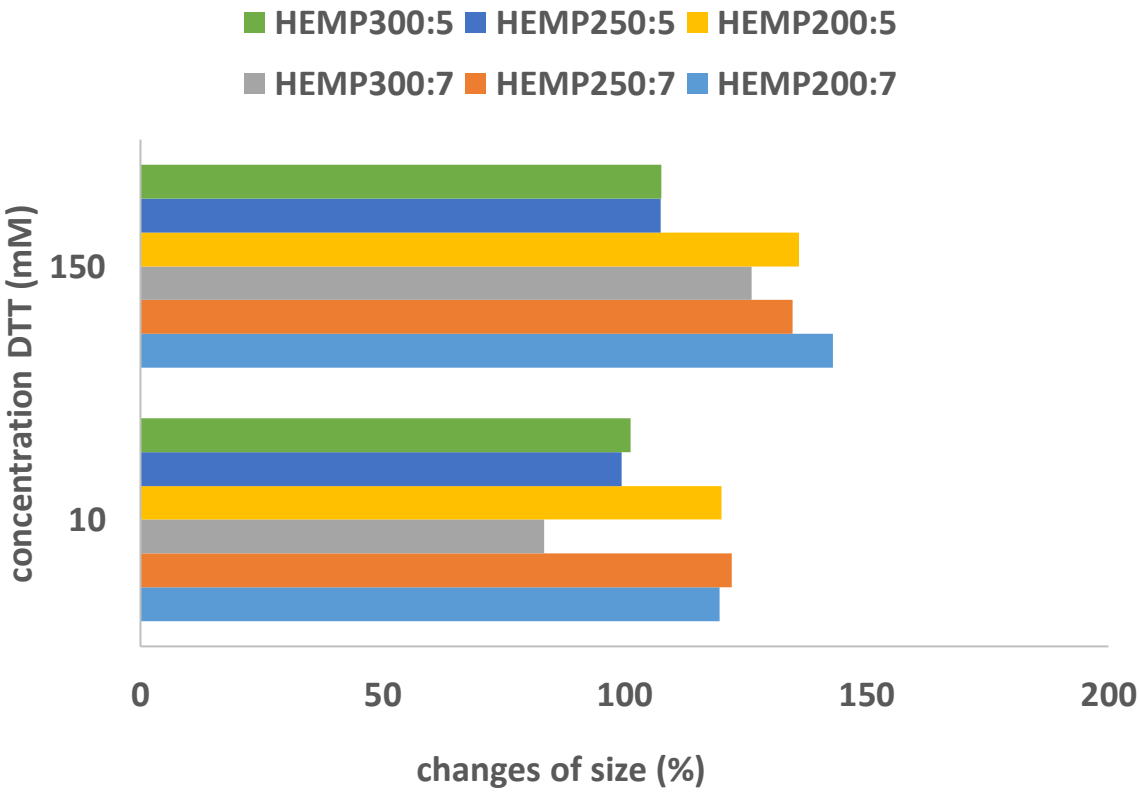

Figure 4.8. Changes in size (%) versus concentration of DTT for RAFT-PNIPAM nanogels, with varying monomer:crosslinker ratios after 72h.

Changes in the derived count rate provide information about the degradation of the nanogels. A reduction in count rate would indicate that the particles are reducing in size, reducing in concentration, or the difference in refractive index between the particles and the continuous phase is reducing. Of course, it is possible that these variables may also be changing

simultaneously. It may be expected that partial scission of the crosslinked network would result in swelling which would increase the mean diameter of the particles but also reduce the difference in refractive index between the particles and the continuous phase. This might lead to a slight increase in the derived count rate. It was found that the derived count rate of samples generally increased after addition of 10 mM DTT after 72h (see Figure 4.9). This may indicate that 10 mM DTT was not sufficient to allow full degradation of the crosslinked network in the nanogels. The nanogel samples that had shown an increase in diameter also had the most dramatic increases in derived count rate, this indicates that the majority of the nanogel particles are swelling. The nanogels may be still able to form a stable polymer network, even in the case for absence of crosslinking agents. The PNIPAM probably formed a stable polymer network by interchain self-cross-linking through chain transfer reaction, both during and after polymerisation. [49,50]

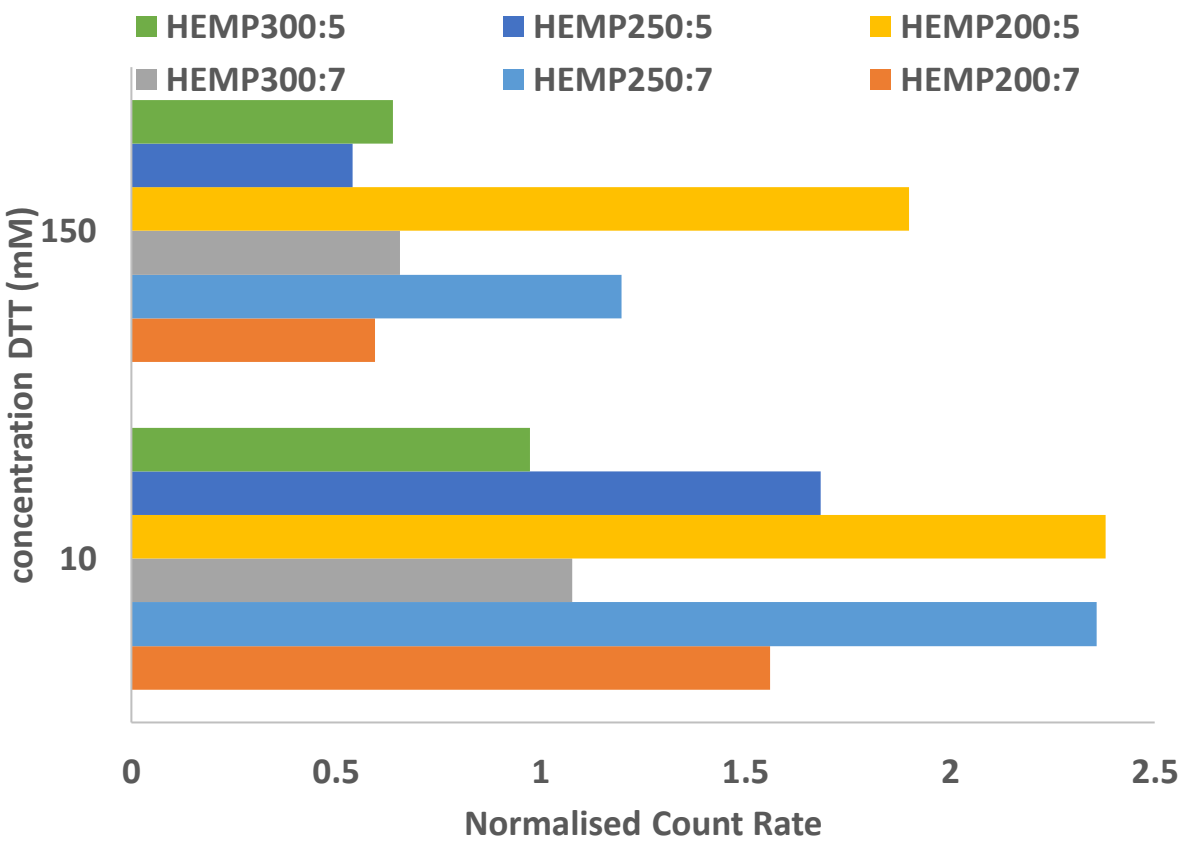

Figure 4.9. Changes in derived count rate versus concentration of DTT for RAFT-PNIPAM nanogels after 72h.

The addition of 150 mM DTT showed a decrease in count rate for most of the samples analysed. However, in two samples analysed, increased scattering was observed (see Figure 4.9, HEMP200:5, HEMP250:7). The normalised count rate showed values 1.9 for HEMP200:5 and 1.19 for HEMP250:7. This could indicate that DTT might have changed the refractive index or that the nanogels changed structure, thus resulting in an increase in the refractive index of the nanogels. Werner *et al.* showed that refractive index can be changed during a coil to globule transition.[51] A second possibility may be that the larger swollen particles resulted in more intense scattering and that this signal obscures the weak scattering from the soluble polymer chains. Another possibility as previously mentioned, is that self-crosslinking through chain transfer reaction could have occurred during polymerisation of PNIPAM, resulting in some non-degradable crosslinks and therefore complete degradation could not occur. The analysis of the samples by DLS meant that the presence of some non-degradable nanogels within a sample would potentially mask the degradation of other nanogels due to the relationship between size and scattering intensity in DLS analysis.

Previously in the literature, the degradation studies of nanogels have also been carried out using AF4.[18,31] The AF4 coupled with MALS and DLS detectors were shown to produce more accurate results compared with DLS batch measurements (see Chapter 3 'The separation behaviour of non-spherical nanoparticles in asymmetric flow field flow fractionation'). In the next part of these studies, the degradation of nanogels was tested using AF4 measurements to obtain information about radius of gyration, hydrodynamic radius, shape factor and the attempt to quantify the amount of degradation of the nanogels in the sample.

4.3.3. AF4 measurements

The AF4 separation conditions were chosen based on measurements and data from a previous chapter (Chapter 3 Insights into the Internal Structures of Nanogels Using a Versatile Asymmetric-Flow Field-Flow Fractionation Method). The hydrodynamic diameter versus temperature in 0.1 M $NaNO_3$ as mobile phase was firstly measured to make sure that the aggregation process does not appear in the AF4 system (see SI, Figure 4.14). The data showed that temperature of aggregation for nanogels was 31.5 °C in 0.1 M $NaNO_3$. Therefore, 28°C

was chosen as the set temperature throughout these experiments, to avoid the onset of aggregation. Sample measurements were performed at least in triplicate and showed good reproducibility. The fractograms display time of elution for particles versus the signal obtained for 90° light scattering detection, the online MALS and DLS detectors allow the measurements for both R_g and R_h of the nanogels exiting the AF4 separation channel. Nanogel samples were analysed both before and after the degradation process caused by the addition of 10 mM DTT or 150 mM DTT. The increase of the nanogel R_h with the elution time indicated that the cross flow (1 mL/min), eluent and the method used was optimal to achieve a satisfactory separation of the particles. Figure 4.10 shows an example of AF4-MALS-DLS fractograms obtained for sample HEMP200:5, HEMP250:5 and HEMP300:5. These samples were chosen to illustrate three types of behaviour found during the DLS analysis; i.e. swelling, and indication of either higher or lower degradation. Unfortunately, the amount of R_h data obtained for samples after degradation was very limited due to the weak scattering which is the reason why R_h is not presented on the graph. The non-degraded (i.e. before addition of DTT) sample HEMP200:5 showed two peaks after 40 min of elution and 55 min from MALS90º signal, which indicated two populations of nanogels. The R_g increased with elution time, which indicate normal elution according to AF4 theory. The addition of 10 mM DTT to HEMP200:5, showed increased and shifted signal to 50 min of elution for MALS90º, which may be explained by swelling behaviour. An extra small peak was also visible on MALS90º after 30 min of elution, which may be attributed to small amount of swelled crosslinked soluble polymers or smaller nanogels. The R_g values increased compared with R_g data obtained before addition of DTT, which could also indicate swelling behaviour. The addition of 150 mM DTT, shifted the modes of the signals of MALS90 º to longer elution times (45 min and 58 min) and the signal intensities also decreased compared to the non-degraded sample, indicating degradation and swelling of the nanogels. The R_g values slightly decreased compared with R_g obtained for sample before addition of DTT. HEMP250:5 showed main peak of MALS90 º after 40 min of elution with smaller shoulder compared with sample HEMP200:5 after 50 min of elution. The non-degraded HEMP250:5 sample showed elution of nanogels after 40 and 45 min for MALS90º. The second population of nanogels was smaller compared with HEMP200:5 which may indicate better control of the polymerisation process. The addition of 10 mM DTT shifted the peaks to 45 and 55 min of elution, indicating swelling behaviour. The addition 150 mM DTT, decreased the area under curve compared with undegraded nanogels for MALS90º

signal. This may indicate the degradation of nanogels in the presence of 150 mM DTT. The non-degraded sample HEMP300:5 showed two peaks at 30 min and 50 min of elution obtained by AF4-MALS-DLS measurements. The second smaller peak may indicate some aggregation of particles due to the fact that R_g is higher (R_g ~ 300 nm) compared with first peak (R_g ~ 100 nm) or a population of particles with different structure. When the nanogels had been treated with DTT, the intensity obtained from MALS90° decreased with higher concentrations of added DTT. The concentration of nanogels in the samples prior to DTT treatment was the same (1 mg/mL) which means that the nanogels were degraded in the presence of DTT; scission of crosslinks reduced the scattering of the samples as the nanogels dissolved. The second peak on AF4 fractogram disappeared with increasing concentration of DTT, indicating that a small residue of nanogels left after at ~40 minutes elution time. This loss of the second peak might indicate that the second peak represents different structure of particles containing fewer non-degradable crosslinks. The R_g slightly increased also after addition of DTT which can be explained by the slight swelling behaviour of nanogels due to the breaking of the sulphur bonds in crosslinker. The polymer chains have more space and their conformation is more elongated as shown by an increase in the radius of gyration. To understand more about internal structure and the shape of the nanogels, the shape factor was calculated from R_g and R_h at the modes for the populations as determined from the AF4 measurements. Shape factor after degradation was not calculated because as previously mentioned the amount of obtained R_h was not sufficient and it may cause some discrepancies in calculations. The results are shown in Table 4.7.

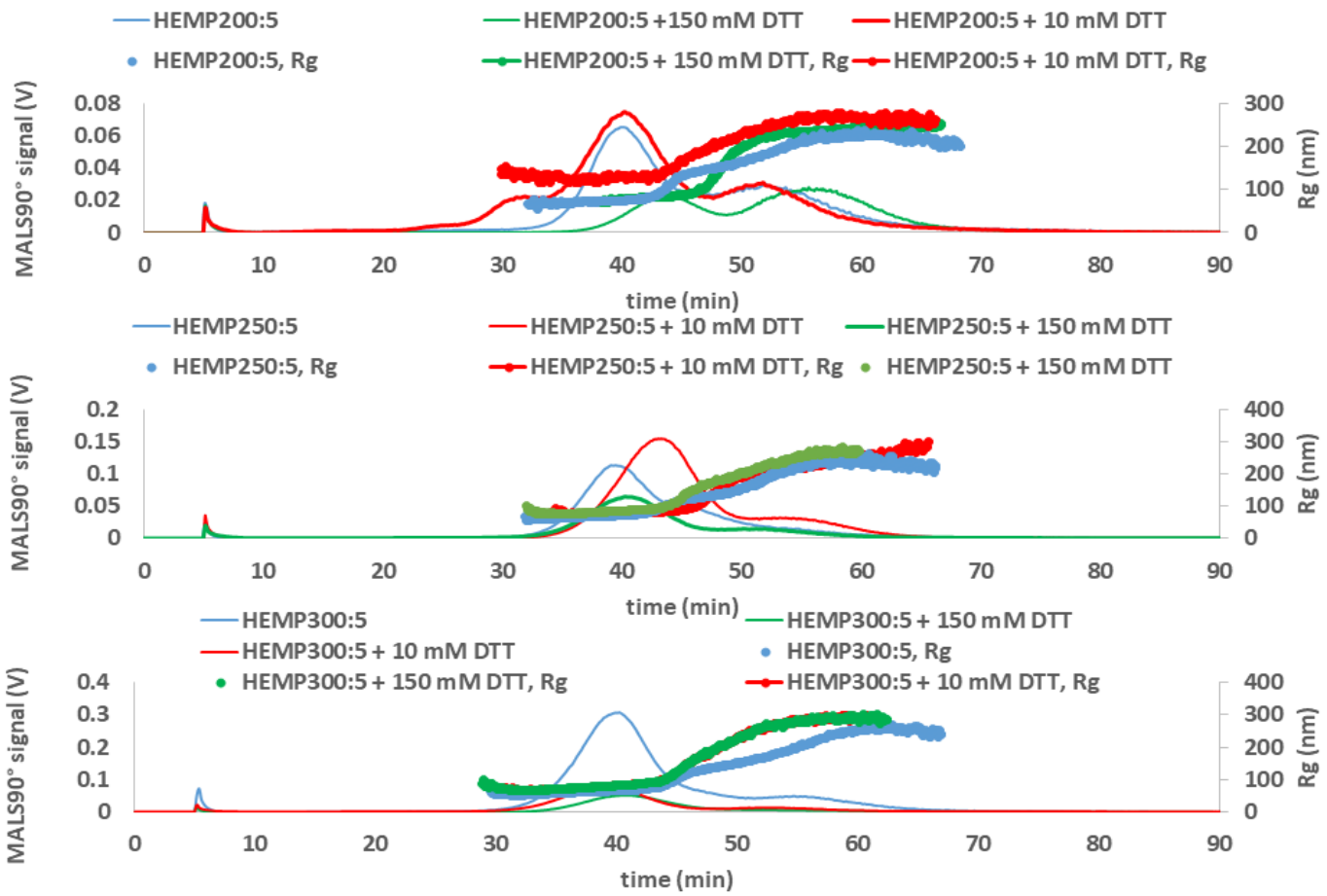

Figure 4.10. AF4-MALS-DLS analysis of HEMP300:5 nanogel. Fractograms showing the 90 ◦ light scattering detector signal (blue, red, green solid line; left hand scale) and radius of gyration (blue, red and green dotted line, right hand scale) obtained from AF4-MALS-DLS measurements. The sample was measured before (blue lines) and after degradation with the presence of 10 mM DTT (red line) and 150 mM DTT (green line).

Table 4.7. The mode values of hydrodynamic radius, radius of gyration and PdI obtained from AF4-MALS-DLS measurement for PNIPAM nanogels before degradation. Shape factor is calculated only for the first population.

Sample	R_g/ nm	R_h/ nm	Shape factor
HEMP200:5	77 & 184	226	0.34
HEMP250:5	70 & 124	179	0.39
HEMP300:5	65 & 186	170	0.38

Table 4.7 showed mode values for R_g, R_h and shape factor. The mode R_g was taken from first and second peak. The R_h did not show second peak on DLS measurements, so the R_h value represents first peak. The example of fractogram, showing lack of R_h is presented in Figure 4.11.

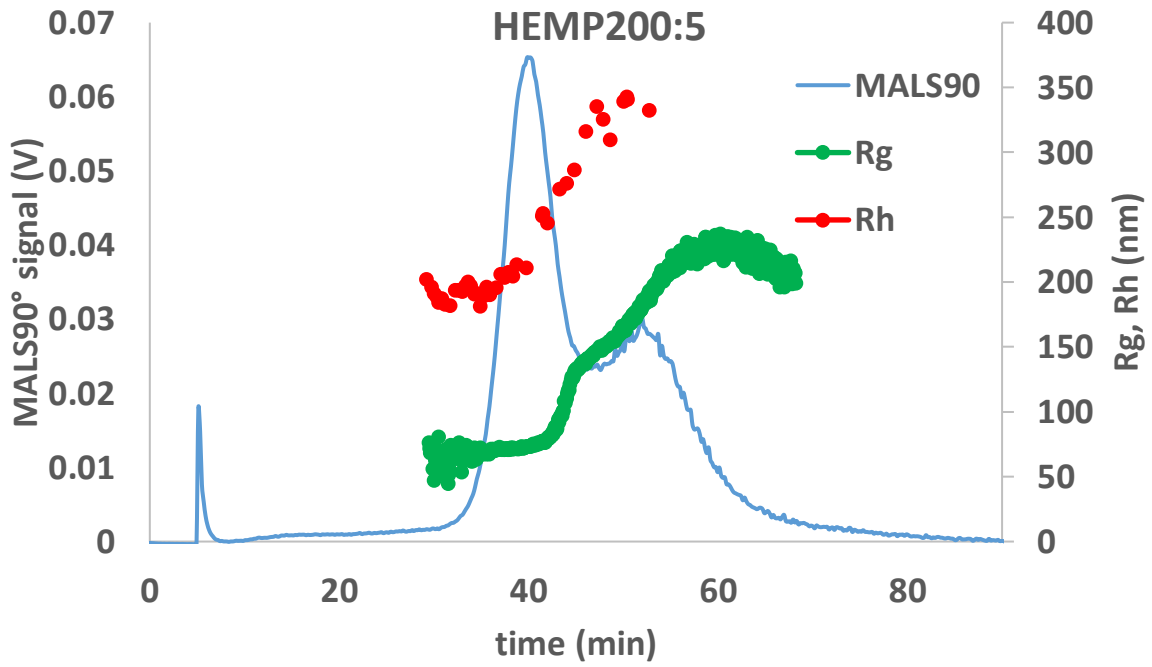

Figure 4.11. AF4-MALS-DLS analysis of HEMP200:5 nanogel. Fractograms showing the light 90◦ scattering detector signal (blue solid line; left hand scale) and radius of gyration (green dotted line, right hand scale) and hydrodynamic radius (red dotted line, right hand scale) obtained from AF4-MALS-DLS measurements.

The lack of R_h data for the second peaks was likely due to the low concentration of these species and the lower sensitivity of the DLS instrument compared to the MALS. The R_h data obtained in flowing mode was really similar compared with batch DLS. The nanogels R_h

obtained from AF4-DLS measurements was only a few nm higher compared with batch results. The AF4-MALS-DLS measurements showed that the nanogels have core-shell structure due to shape factor ≤ 0.65. In literature, typical values for core-shell particles are <0.65.[52] The really low value of shape factor can indicate really dense core and less dense shell. Generally, hydrodynamic radius obtained after fractionation matches with batch DLS measurements which also was shown in previous chapters.

4.3.4. Comparison of degradation data from DLS and AF4

The data obtained from the degradation process from batch DLS measurements was compared with AF4 data. All data is presented in Table 4.8. The DLS data showed that derived count rates had not reduced for degradation process in the presence of 10 mM DTT but the AF4 results indicate degradation for samples HEMP250:5 and HEMP300:5. Interestingly, the trend between the samples is the same in both techniques. This difference between DLS and AF4 results could be caused by changing the size of particles or refractive index during the swelling and degradation process. In that case, data obtained from AF4-MALS-DLS studies will be discussed. The AF4 measurements showed that the nanogel with lowest amounts of crosslinker relative to the PNIPAM primary chains (HEMP300:5) was the most degradable sample obtained from the synthesis. At the highest concentration of DTT, the amount of remaining nanogels was 15% for HEMP300:5. Lower concentrations of DTT showed less degradation of nanogels; the amount of remaining nanogels was smaller for samples treated with 10 mM compared with 150 mM DTT. The influence of the ratio of NIPAM to BAC can also be noticed. The nanogels with higher amounts of NIPAM compared with BAC showed higher degradation. This can possibly be attributed to the better ability of DTT to penetrate through the polymer network. The nanogels with a higher ratio of NIPAM to BAC would likely have longer primary chains and should have larger spaces between the crosslink chains which might assist degradation of the disulphide bonds. The higher molar content of BAC showed a higher tendency to swell rather than degrade. Previous work by Gaulding *et al*. showed also that PNIPAM nanogels synthesised by precipitation polymerisation and crosslinked with BAC were not fully degradable unless low temperature redox polymerisation was employed.[18] The studies showed the ability for the PNIPAM RAFT nanogels to degrade. The most degradable

sample showed a high affinity for degradation, with only 15 % of the nanogels remaning. However, the data also showed that some self-crosslinking may have also been occurring due to the swelling behaviour of sample after addition of DTT.

Table 4.8. Summary of finding for PNIPAM-RAFT nanogels.

Sample	HEMP200:5	HEMP250:5	HEMP300:5
Degradation studies DLS			
Derived Count Rate before DTT (kcps)	9528 ± 467	26718 ± 1291	36619 ± 1868
Derived Count Rate 10 mM DTT (kcps)	22681 ± 841	44979 ± 3208	35666 ± 686
% of left after degradation, 72h, 10 mM DTT	238%	168%	97%
Derived Count Rate, 150 mM DTT (kcps)	18095 ± 153	14441 ± 326	23386 ± 895
% of left after degradation, 72h, 150 mM DTT	189%	54%	63%
Degradation studies AF4			
% left after degradation, 10 mM DTT	126 %	56 %	26%
% left after degradation, 150 mM DTT	113 %	60 %	15 %

4.4.Conclusion

PNIPAM nanogels were successfully synthesised by RAFT polymerisation. The nanogels were synthesised with varying amounts of monomer and crosslinker. The HEMP CTA showed better ability to create nanogels compared with PEG CTA. The hydrodynamic diameters for synthesised samples were between 318 and 457 nm with narrow PdI values (< 0.15). The swelling ratio was similar for all samples ~ 2.0, indicating that the changes in crosslinking densities were not large enough to shown any influence. The synthesised nanogels showed a characteristic deswelling at 33 °C. The aggregation temperature for all samples in the presence of PBS was around 28 °C, showing potential for the use of these nanogels as *in situ* forming implants and delivery vehicles for poorly water-soluble drug. The AF4 measurements showed that nanogels have a core-shell structure due to the value of the shape factor being ≤ 0.65 for all samples. The degradation studies were conducted in the presence of 10 mM and 150 mM DTT. AF4-MALS-DLS measurements showed good degradation of PNIPAM nanogels. The most degradable sample (HEMP300:5) was shown to contain only 15 % nanogel after the degradation process. Generally, the samples degraded better in the presence of 150 mM DTT, showing that excess of DTT allows for faster degradation. This work has shown that the degradation process could be monitored over time using AF4 to measure particle hydrodynamic radius, radius of gyration and shape factor. DLS degradation studies showed that the derived count rates for samples cannot be directly compared before and after degradation, probably because of changes of refractive index. RAFT polymerisation showed potential to control the size of nanogels and degradation behaviour. The RAFT polymerisation in aqueous media is still developing and it requires deeper understanding. The limitation which was presented is associated with the choice of RAFT agent and initiator. Unfortunately, there is currently not a lot of commercially available water soluble RAFT agents.

4.5. References

1 J. Du, X. Li, H. Zhao, Y. Zhou, L. Wang, S. Tian and Y. Wang, *Int. J. Pharm.*, 2015, **495**, 738–749.

2 A. R. Town, M. Giardiello, R. Gurjar, M. Siccardi, M. E. Briggs, R. Akhtar and T. O. McDonald, *Nanoscale*, 2017, **9**, 6302–6314.

3 W. Xiong, X. Gao, Y. Zhao, H. Xu and X. Yang, *Colloids Surfaces B Biointerfaces*, 2011, **84**, 103–110.

4 M. R and A. BD, *J. Nanomed. Nanotechnol.*, 2016, 7, 2.

5 Y. Cao, C. Zhang, W. Shen, Z. Cheng, L. (Lucy) Yu and Q. Ping, *J. Control. Release*, 2007, **120**, 186–194.

6 A. R. Town, J. Taylor, K. Dawson, E. Niezabitowska, N. M. Elbaz, A. Corker, E. Garcia-tun and T. O. Mcdonald, , *J. Mater. Chem. B***,** 2019,**7**, 373-383.

7 M. Patenaude and T. Hoare, *ACS Macro Lett.*, 2012, **1**, 409–413.

8 G. Dougherty, *Digit. Image Process. Med. Appl.*, 2018, 381–394.

9 V. Delplace and J. Nicolas, *Nat. Chem.*, 2015, **7**, 771–784.

10 N. Leber, L. Kaps, M. Aslam, J. Schupp, A. Brose, D. Schäffel, K. Fischer, M. Diken, D. Strand, K. Koynov, A. Tuettenberg, L. Nuhn, R. Zentel and D. Schuppan, *J. Control. Release*, 2017, **248**, 10–23.

11 Y. Chen, M. J. van Steenbergen, D. Li, J. B. van de Dikkenberg, T. Lammers, C. F. van Nostrum, J. M. Metselaar and W. E. Hennink, *Macromol. Biosci.*, 2016, 1122–1137.

12 G. Aguirre, J. Ramos and J. Forcada, *Soft Matter*, 2013, **9**, 261–270.

13 L. Nuhn, N. Vanparijs, A. De Beuckelaer, L. Lybaert, G. Verstraete, K. Deswarte, S. Lienenklaus, N. M. Shukla, A. C. D. Salyer, B. N. Lambrecht, J. Grooten, S. A. David, S. De Koker and B. G. De Geest, *Proc. Natl. Acad. Sci.*, 2016, **113**, 8098–8103.

14 P. D. Thornton, S. M. R. Billah and N. R. Cameron, Macromol. Rapid Commun. 2013, 34, 257−262.

15 H. Yang, Q. Wang, S. Huang, A. Xiao, F. Li, L. Gan and X. Yang, *ACS Appl. Mater. Interfaces*, 2016, **8**, 7729–7738.

16 X. Zhang, S. Lü, C. Gao, C. Chen, X. Zhang and M. Liu, *Nanoscale*, 2013, **5**, 6498–506.

17 Y. Zhan, M. Gonçalves, P. Yi, D. Capelo, Y. Zhang, J. Rodrigues, C. Liu, H. Tomás, Y. Li and P. He, *J. Mater. Chem. B*, 2015, **3**, 4221–4230.

18 J. C. Gaulding, M. H. Smith, J. S. Hyatt, A. Fernandez-Nieves and L. A. Lyon, *Macromolecules*, 2012, **45**, 39–45.

19 B. Gyarmati, Á. Némethy and A. Szilágyi, *Eur. Polym. J.*, 2013, **49**, 1268–1286.

20 W. W. Cleland, *Biochemistry*, 1964, **3**, 480–482.

21 A. Town, Dual-Stimuli Responsive Nanogels for Injectable Drug Delivery Implants, PhD Thesis, University of Liverpool, 2018.

22 S. Perrier, *Macromolecules*, 2017, **50**, 7433–7447.

23 G. Moad, E. Rizzardo and S. H. Thang, *Polymer (Guildf).*, 2008, **49**, 1079–1131.

24 L. A. Lyon, *Macromolecules*, 2012, **45**, 39–45.

25 Z. Gu, A. A. Aimetti, Q. Wang, T. T. Dang, Y. L. Zhang, O. Veiseh, H. Cheng, R. S. Langer and D. G. Anderson, *ACS Nano*, 2013, **7**, 4194–4201.

26 S. Hupfeld, D. Ausbacher and M. Brandl, *J. Sep. Sci.*, 2009, **32**, 1465–1470.

27 J. Smeraldi, R. Ganesh, J. Safarik and D. Rosso, *J. Environ. Monit.*, 2012, **14**, 79–84.

28 V. V. Vysotskii, O. Y. Uryupina, A. V. Gusel'nikova and V. I. Roldugin, *Colloid J.*, 2009, **71**, 739–744.

29 S. W. Prescott, *Macromolecules*, 2003, **36**, 9608–9621.

30 https://www.sigmaaldrich.com/technical-documents/articles/materials-science/polymer-science/raft-polymerization.html#process.

31 M. H. Smith, A. B. South, J. C. Gaulding and L. A. Lyon, *Anal. Chem.*, 2010, **82**, 523–530.

32 W. H. Blackburn and L. A. Lyon, *Colloid Polym. Sci.*, 2008, **286**, 563–569.

33 A. R. Town, J. Taylor, K. Dawson, E. Niezabitowska, N. M. Elbaz, A. Corker, E. Garcia-Tuñón and T. O. McDonald, J. Mater. Chem. B, 2019, 7, 373-383.

34 W. McPhee, K. C. Tam and R. Pelton, *J. Colloid Interface Sci.*, 1993, 156, 24–30.

35 S. Bandyopadhyay, A. Sharma, M. A. Ashfaq Alvi, R. Raju and W. R. Glomm, *RSC Adv.*, 2017, **7**, 53192–53202.

36 M. Rasmusson and B. Vincent, *React. Funct. Polym.*, 2004, **58**, 203–211.

37 C. Obeso-Vera, J. M. Cornejo-Bravo, A. Serrano-Medina and A. Licea-Claverie, *Polym. Bull.*, 2013, **70**, 653–664.

38 K. Kratz, A. Lapp, W. Eimer and T. Hellweg, *Colloids Surfaces A Physicochem. Eng. Asp.*, 2002, **197**, 55–67.

39 M. Das, H. Zhang and E. Kumacheva, *Annu. Rev. Mater. Res.*, 2006, **36**, 117–142.

40 B. Nystrom, N. Al-Manasir, K. Z. Zhu, A. L. Kjoniksen, K. D. Knudsen and G. Karlsson, *J. Phys. Chem. B*, 2009, **113**, 11115–11123.

41 https://www.chemicalbook.com/productmsdsdetailcb9344530_en.htm.

42 https://www.thoughtco.com/definition-of-weak-acid-604687.

43 T. Y. Wu, A. B. Zrimsek, S. V. Bykov, R. S. Jakubek and S. A. Asher, *J. Phys. Chem. B*, 2018, **122**, 3008–3014.

44 M. Rasmusson, A. Routh and B. Vincent, *Langmuir*, 2004, **20**, 3536–3542.

45 S. Honary and F. Zahir, *Trop. J. Pharm. Res.*, 2013, **12**, 255–264.

46 T. F. Tadros, 1991, 683–696.

47 X. Wu, R. H. Pelton, a. E. Hamielec, D. R. Woods and W. McPhee, *Colloid Polym. Sci.*, 1994, **272**, 467–477.

48 S. Nayak and L. Andrew Lyon, *Angew. Chemie - Int. Ed.*, 2005, **44**, 7686–7708.

49 J. Gao and B. J. Frisken, *Langmuir*, 2003, **19**, 5212–5216.

50 X. Hu, Z. Tong and L. A. Lyon, *Langmuir*, 2011, **27**, 4142–4148.

51 P. Werner, M. Münzberg, R. Hass and O. Reich, *Anal. Bioanal. Chem.*, 2017, **409**, 807–819.

52 G. R. Deen, T. Alsted, W. Richtering and J. S. Pedersen, *Phys. Chem. Chem. Phys.*, 2011, **13**, 3108–3114.

4.6. Supporting Information

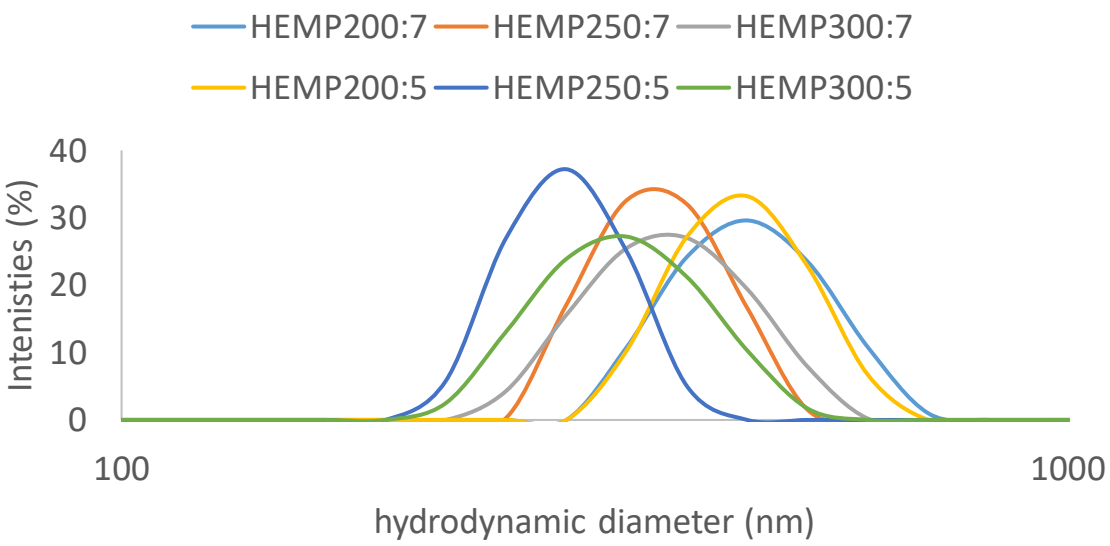

Figure 4.12. DLS size distribution by intensity at 25 °C for each nanogel as a 1 mg ml-1 aqueous dispersion

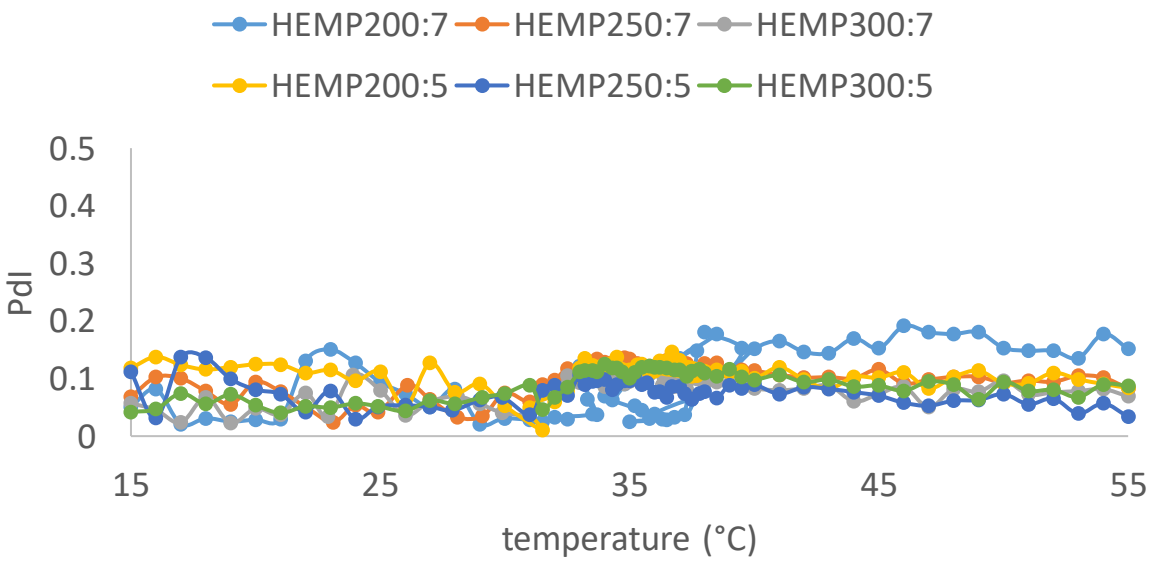

Figure 4.13. The graph shows changes of polydispersity (PdI) versus temperature for PNIPAM nanogels in water.

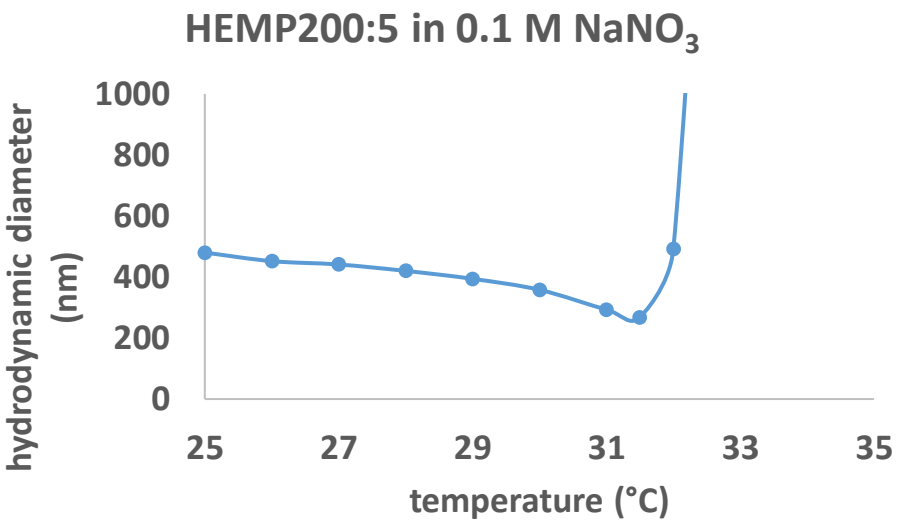

Figure 4.14. The graph shows the hydrodynamic diameter vs temperature for HEMP200:5 in 0.1 M $NaNO_3$.

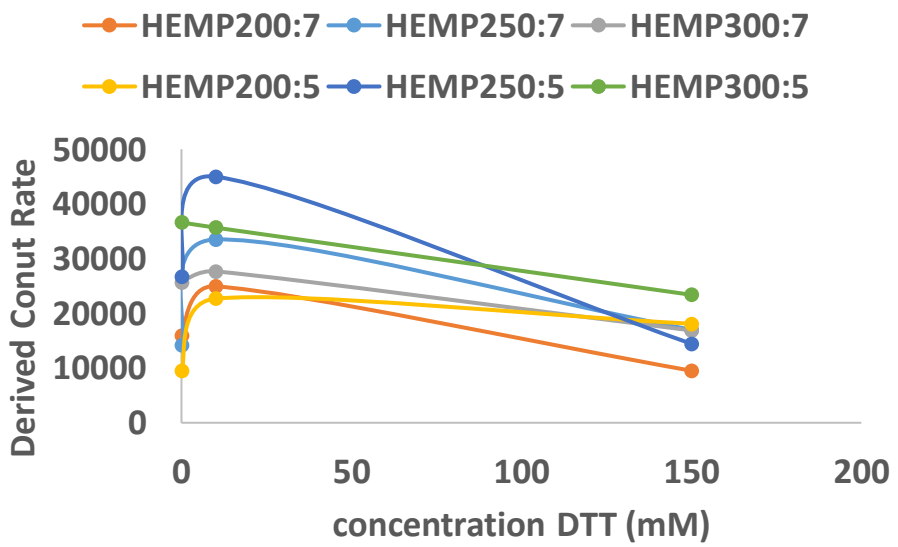

Figure 4.15. The graph shows concentration of DTT (mM) vs derived count rate (kcps) for all six samples.

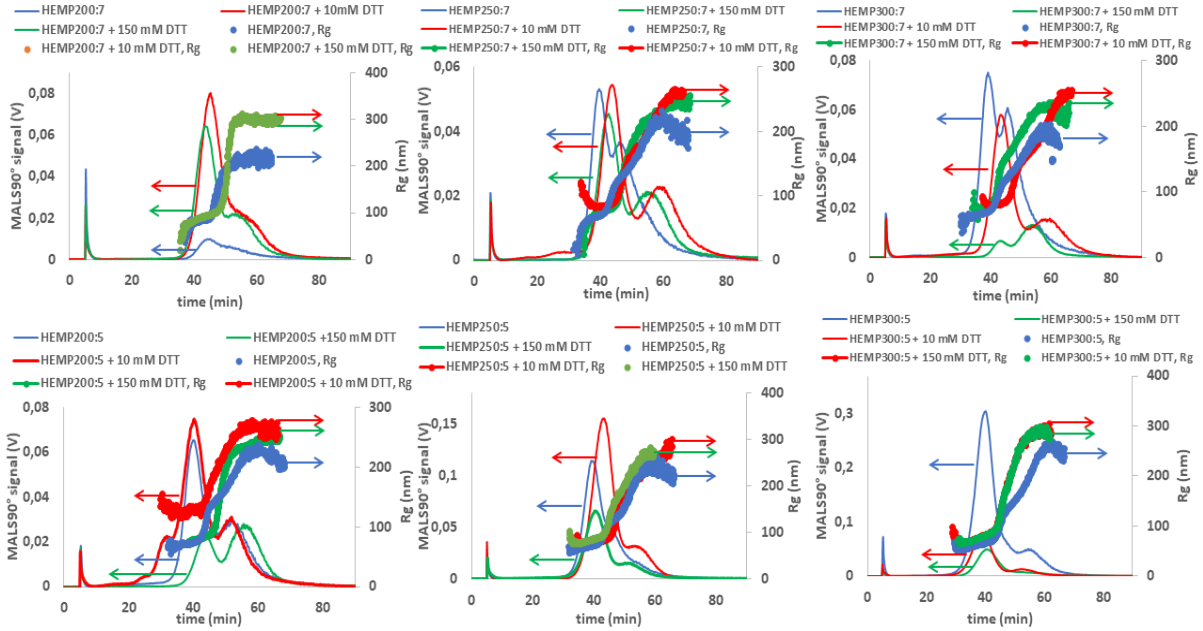

Figure 4.16. AF4-MALS-DLS analysis of nanogels. Fractograms showing the light 90◦ scattering detector signal (blue, red, green solid line; left hand scale) and radius of gyration (blue, red and green dotted line, right hand scale) obtained from AF4-MALS-DLS measurements. The samples have been measured before (blue lines) and after degradation with the presence of 10 mM DTT (red line) and 150 mM DTT (green line).

Table 4.9. Table shows zeta potential, hydrodynamic diameter and polydispersity index (PdI) in 10 mM NaCl for PNIPAM nanogels.

Sample	HEMP200:7	HEMP250:7	HEMP300:7	HEMP200:5	HEMP250:5	HEMP300:5
Zeta potential (mV)	-2.25 ± 0.38	-1.95 ± 0.11	-1.97 ± 0.83	-1.91 ± 0.29	-1.94 ± 0.87	-2.27 ± 0.42
Hydrodynamic diameter (nm) in 10 mM NaCl	475 ± 16	386 ± 19	354 ± 7	462 ± 19	351 ± 20	327 ± 5
PdI	0.203 ± 0.036	0.162 ± 0.040	0.158 ± 0.039	0.219 ± 0.027	0.198 ± 0.021	0.127 ± 0.019

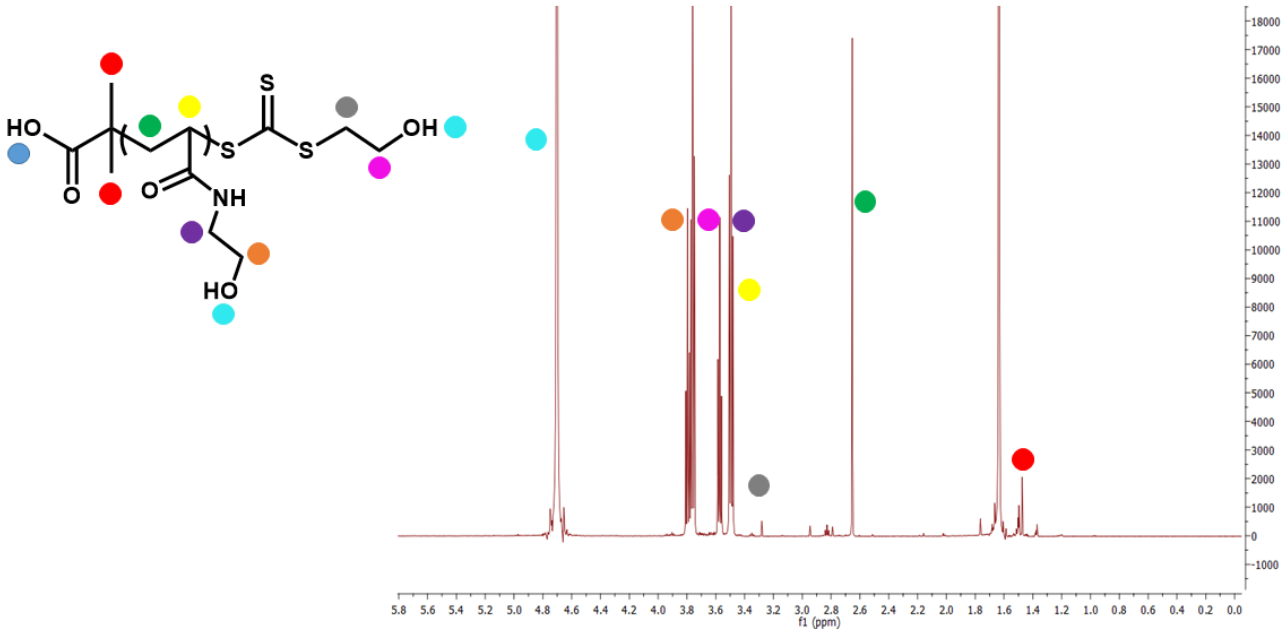

Figure 4.17. ^{1}HNMR (500 MHz) of HEMP CTA in D_2O.

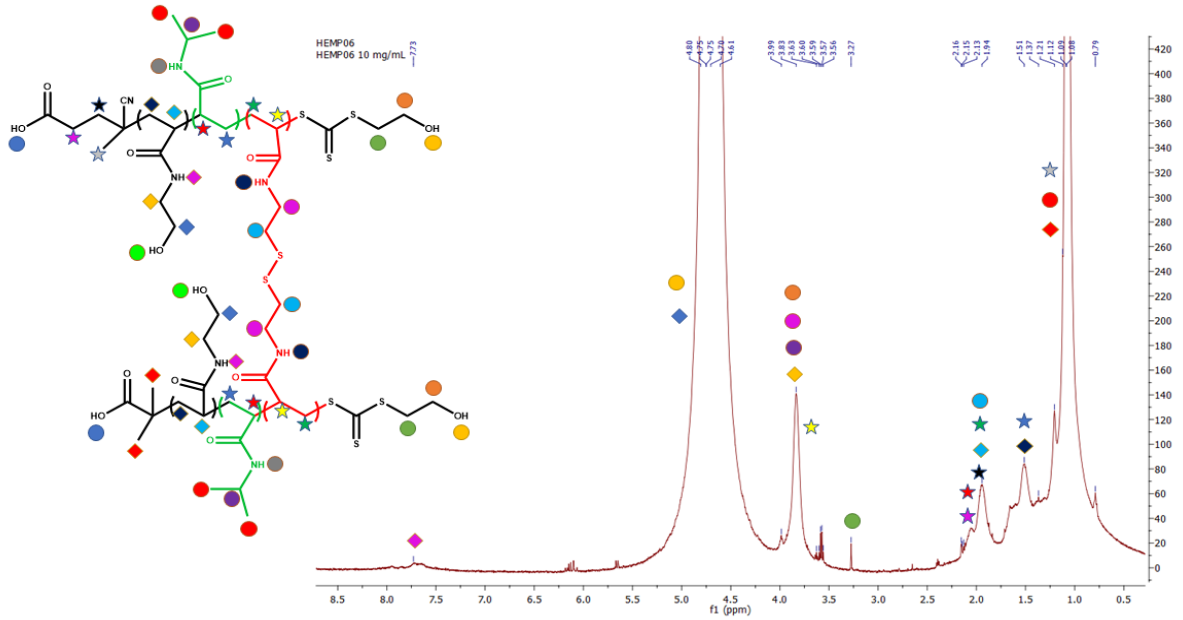

Figure 4.18. The ^{1}HNMR spectra ((500 MHz) of HEMP300:5.

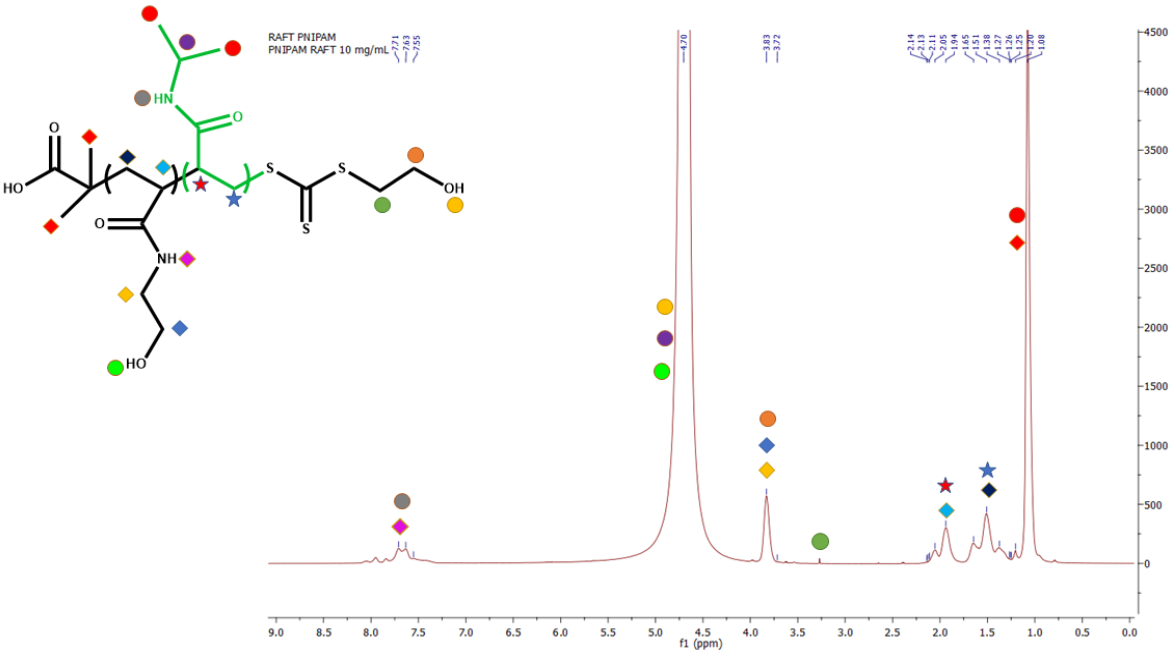

Figure 4.19. The ^{1}H NMR (500 MHz) spectra of polymer made of NIPAM and HEMP as CTA in D_2O.

Chapter 5

The separation behaviour of non-spherical nanoparticles in asymmetric flow field flow fractionation

I would like to thank: Dr Tiago Entradas for providing gold nanorods and Dr Gareth Morris for providing silver nanoplates and silver nanoprisms.

5.1. Introduction

The shape of micro/nanoparticles is known to be important in applications for drug delivery. For example, elongated or non-spherical particles have shown potential benefits for use in drug delivery systems.[1] Ellipsoidal particles showed better adhesion to aortae when tested *in vivo* compared to spherical micro and nanoparticles.[2] In another example, non-spherical particles have been shown to load more hydrophobic drug than spherical ones.[3] The characterisation of non-spherical particles typically utilises electron microscopy which allows the shape and aspect ratio (defined as ratio between major axis and minor axis for ellipsoidal particles)[4] of the sample to be determined. However, this technique is time-consuming, may be influenced by drying effects and is limited to a relatively small number of particles that may not be representative of the complete sample.[5,6] Analysis approaches based on the bulk sample can address these issues.[7] However, there are few effective bulk methods for providing information about the shape of non-spherical particles as many bulk characterisation techniques assume spherical particles. AF4 is a promising tool in the field of analytical chemistry and it is based on hydrodynamic principles and interaction of particles with a cross flow and parallel (tip) flow of carrier liquid.[8] The samples are injected into the flat channel containing permeable membrane and filled with eluent. Particles can be separated by combination of two flows (i.e. cross-flow and tip flow) of eluent due to the differences in diffusion coefficients, then analysed by range of detectors. Coupling AF4 with different detectors such as MALS and DLS can give information about size and shape of particles.[9–11] A MALS detector can provide the radius of gyration (R_g) while a DLS instrument determines the hydrodynamic radius (R_h). It has been shown that R_g/R_h, defined as shape factor, can give information about shape of particles and internal structure.[12,13] Gigault *et al.* used this approach to measure the length of carbon nanotubes by AF4.[14] The calculation of length and diameter of carbon nanotubes was based on correlation between R_g and R_h.[14] The results showed that longer carbon nanotubes have higher values for shape factor. The shape of nanoparticles has also been shown to influence the separation behaviour, with different separation behaviour found for gold

nanorods compared with spherical nanoparticles.[15] It has been proposed that non-spherical gold nanorods with larger aspect ratios were located higher in the channel and therefore elute faster.[15] In other work, theoretical experiments were conducted to understand accurate mechanism of fractionation for elongated particles.[16–20] These studies showed that separation of anisotropic particles cannot be obtained by 'normal' mode. Therefore, a steric-entropic mode was proposed as it considers the transition between normal and steric mode. Due to this combination of factors it was predicted that elongated particles would have lower retention times than a sphere of the same mass. However, experimental confirmation of this theory was challenging due to a difficulties of finding suitable well-characterised uniform non-spherical particles.[20] Therefore, the steric-entropic theory is still being developed.[18,21] Up to date, there is small amount of articles focused on AF4 analysis of particles with different shapes and shape factors. [14,22,23]

This chapter is focussed on the analysis of a range of nanoparticles made of different materials with different sizes and shapes. The particles were fractionated by AF4-MALS-DLS, with the aim of better understanding the relationship between particle size, shape and separation behaviour. The samples analysed were gold nanoparticles, gold nanorods, silver nanoparticles and silver nanoprisms. Batch DLS measurement were conducted to characterise hydrodynamic radius of particles. The development of a sufficient method for separation of the differently sized samples by AF4 was studied to understand a retention behaviour for particles with different shapes. The particles were also characterised by scanning electron microscope (SEM) and scanning transmission electron microscopy (STEM) to characterise morphology and structure. This data was used also to compare with the shape factors obtained by AF4-MALS-DLS measurements. We believe that it is first time that silver nanoprisms and silver nanoplates have been studied by AF4-MALS-DLS.

5.2. Experimental

5.2.1. Materials

Gold nanoparticles stabilised in citrate buffer solution were purchased from Sigma Aldrich with a mean hydrodynamic diameter of 58-66 nm and core size 50 nm. Silver nanoparticles stabilised in sodium citrate were purchased from Sigma Aldrich with particles size 60 nm from TEM, according to provider. Gold nanorods, silver nanoplates, silver prisms were kindly provided from Surface Science Research Centre, University of Liverpool. Gold nanorods were synthesised by methods already existing in literature.[24] The method for preparation of silver nanoplates and silver nanoprisms was also adopted from the literature.[25] Typical synthesis for gold nanorods, silver nanoplates and silver nanoprisms are discussed below.

5.2.2. Synthesis of gold nanorods_A

The synthesis of gold nanorods_A were adapted from methods previously detailed in literature.[26] In a typical procedure, for synthesis of seed solution, 0.250 mL of an aqueous 0.01 M solution of $HAuCl_4,3H_2O$ was added to 7.5 mL of a 0.10 M cetyltrimethylammonium bromide (CTAB) solution in a glass vial. The solutions were gently mixed, appearing bright brown-yellow in colour. Then, 0.600 mL of an aqueous 0.01 M ice-cold $NaBH_4$ solution was added all at once, followed by rapid inversion mixing for 5 min. Then the vial was kept in a water bath maintained at 25 °C for future use. This seed solution was used for up to 2 h after its preparation. Next, 4.75 mL of 0.10 M CTAB, 0.200 mL of 0.01 M $HAuCl_4,3H_2O$, and 0.030 mL of 0.01 M $AgNO_3$ solutions were added in that order to a vial, followed by gentle mixing. Then 0.032 mL of 0.10 M L-ascorbic acid (AA) was added to it. Finally, 0.010 mL of seed solution was added, and the reaction mixture was gently mixed for 10 s and left undisturbed for at least 3 h. To the nanorods stock solution 0.1 ml of a PSS stock (10 mg PSS in 1 ml 0.01 M NaCl) and 0.05 ml of 0.01 M NaCl solution was added with gentle vortexing,

and maintained at 4 °C with stirring for 24 h. The sample was then centrifuged and the supernatant with unbound PSS was discarded.

5.2.3. Synthesis of gold nanorods_B

The synthesis of gold nanorods_B with smaller particle sizes have previously been published in literature. [24] Gold nanorods seed and growth solutions were prepared from the 0.1 M CTAB. For the seed solution, after adding 25 mM $HAuCl_4$ (10 µL) to warm 0.1 M CTAB (990 µL) in a 2 mL microcentrifuge tube, the seed $HAuCl_4$–CTAB mixture was vortexed. 600 µL of ice-cold NaBH4 were added to the seed $HAuCl_4$ – CTAB mixture and vortexed again. The resulting light brown solution was kept at room temperature. For the growth solution, 25 mM $HAuCl_4$ (200 µL) was added to 10 mL of 0.1 M CTAB in each of six 15 mL centrifuge tubes, the growth $HAuCl_4$–CTAB mixture was vortexed until the colour of the solution turned clear orange. Addition of 300 µL of 4 mM $AgNO_3$ followed by 150 µL of 80 mM ascorbic acid to the growth $HAuCl_4$–CTAB mixture turned the solution colourless after gentle mixing. Once both the seed and growth solutions were prepared, 12 µL of the seed solution was added to each tube of growth solution and kept at 33 °C. Within 15 minutes, the colour of the solution mixture changed from clear to dark brown, indicating nanorod formation. The solution mixture was left in the water bath for next 1 hour, to finalise the formation of the rods. Afterwards, the six vials of mixed seed and growth solutions were centrifuged in the 15 mL centrifuge tubes, at 8,000 revolutions per minute (rpm) for 20 minutes. Once centrifugation was complete, the supernatant was carefully removed leaving behind pellets of nanorods. The pellets were resuspended in 1 mL of water, and centrifuged again at 7000 rpm for 15 minutes. This time, the pellets containing larger material, including large impurities and nanorods, were discarded. The supernatant was retained as it contained the desired size of GNRs.

5.2.4. Synthesis of silver nanoplates and silver nanoprisms

All solutions for synthesis were prepared fresh, straight before synthesis. Solution containing distilled water (1.965 mL), 100 µL of trisodium citrate (75 mM), 9.3 µL of $AgNO_3$ (10 mM), and 12.8 µL of H_2O_2 (0.6%) was prepared in 14 mL vial equipped with a stir bar. In next step, 9.6 µL of $NaBH_4$ (100 mM) was added rapidly during vigorous stirring. After 5 min, 200 µL of L-ascorbic acid (5 mM) was added, followed by dropwise addition of 150 µL of $AgNO_3$ (10 mM) for silver nanoplates and 50 µL of $AgNO_3$ for silver nanoprisms.

5.2.5. Characterisation

AF4 experiments were performed on an MT2000 with RI and UV-Vis detectors from Postnova Analytics, Landsberg/Germany. MALS detector PN3621 from Postnova Analytics, Landsberg, Germany with 21 angles (from 7 ° to 164 °) detector operating at 532 nm power wavelength were coupled online to AF4. Autosampler (PN5300) was provided from Postnova Analytics, Landsberg/Germany. The hydrodynamic radius of the samples were obtained *via* DLS using a Malvern Zetasizer Nano ZS (running Malvern Zetasizer software V7.12) (Malvern Instruments, Malvern, UK) with 633 nm He–Ne laser and the detector positioned at 173 °, coupled online to the MT2000. A 350 µm spacer and 10 kDa regenerated cellulose membrane were installed in the separation channel. The conditions used for the separations were based on a method existing in the literature. Briefly, the mobile phase was Milli-Q H_2O for gold particles and 0.05 % NaCl + 0.05 % NovaChem was used for fractionation of silver particles. Type I distilled water was obtained from a water purification system had a resistivity of > 18 MΩ cm^{-1} (PURELAB option R, Veolia). The solutions were filtered using Corning bottle top vacuum filter system with cellulose acetate membrane with pore size 0.22 µm. The injected volume was 20 µL of sample by autosampler. The samples were injected three times to obtain good reproducibility.

Blank samples were measured between injections of new sample to make sure that system was clean. The UV-Vis detector measured two wavelengths 520 and 700 nm for silver and gold samples. The conditions used for the separations was as follows; the injection/focussing time was 3 min using a cross flow 0.5 mL min^{-1}. The cross flow rate was kept for the first 4 min (t_0-t_4) in constant manner, and thereafter, the cross flow was decreased in a linear manner (exponent 1.0) from its initial value to 0.1 over a period of 30 min. Following the complete reduction in cross flow, the tip-flow 0.1 mL min^{-1} continued for an additional 10 min. The z-average diameter and count rate were measured by an inline Malvern Zetasizer ZS DLS at 3 second intervals. DLS calculates the z-average size of particles using the Stokes-Einstein equation.

Characterisation of the bulk (unfractionated) samples was carried out using DLS using a Malvern Zetasizer Nano ZS (running Malvern Zetasizer software V7.12) with 633 nm He-Ne laser and the detector positioned at 173°. The Z-average diameter was recorded using a 1 cm path length disposable polystyrene cuvettes. Measurements were repeated in triplicate to give a mean Z-average diameter and polydispersity index (PdI). Zeta potential measurements were performed using DTS1070 folded capillary cells (Malvern, UK). The capillary cells were flushed with ethanol and water prior to usage. The zeta potential measurement was made with a minimum of 10 and maximum of 40 runs, and the voltage applied was automatically selected by the software. The Smoluchowski approximation where f(Ka) = 1.5 was used, and dispersions contained 10 mM NaCl and were measured at 25 °C.

A Hitachi S-4800 cold Field emission (FE-SEM) scanning electron microscope (SEM) was used to image gold and silver particles. The samples to be analysed were put into a silicon wafer stuck onto an aluminium stub using PELCO Conductive Silver Paint (Agar Scientific, Essex, UK) and left to evaporate overnight. The prepared samples were coated with gold for 2.5 minutes at 20 mA using an EMITECH K550X Sputter Coater.

The annular dark-field (AD) and bright-field (BF) scanning transmission electron (STEM) images were obtained with aberration-corrected Field Emission transmission

electron microscope JEOL 2100F operated at 200 kV. The samples were dispersed, sonicated and drop-casted onto a 400 mesh copper grid with a Lacey carbon film.

Spectrophotometric absorbance measurements between 300 and 750 nm were made using a Nanodrop™ 2000 c spectrophotometer (Thermo Fisher Scientific). Samples were vortexed immediately prior to measurement in order to avoid artefacts from sedimentation of agglomerates. The absorbance of samples was measured directly in a 1 cm path length polystyrene cuvette. Water was used as the background measurement.

5.3. Results

The results section is divided into two subsections. In the first section, the results of the physical characterisation of gold samples are presented. The three gold samples were analysed: gold nanoparticles (gold NPs) and two different sizes of gold nanorods (gold nanorods_A and gold nanorods_B). In the second section, three different types of silver nanoparticles (silver nanoparticles (silver NPs), silver nanoplates and silver nanoprisms) were characterised and the results discussed.

5.3.1. Gold particles

The gold samples with different shapes were characterised by DLS batch and SEM to obtain information about samples before AF4 analysis. The commercially sourced gold NPs are supplied stabilised in citrate buffer and their specified hydrodynamic diameter was 58-66 nm with a core size of 47-53 nm. Unfortunately, provider did not mentioned how core size was measured, but it would be expected that it was determined by electron microscopy. Our DLS measurements (Figure 5.1) showed a similar diameter (70 nm) compared with information provided by the supplier. The difference in the hydrodynamic diameter compared to the core was likely due to the coating by citrate around the nanoparticles which increases the hydrodynamic diameter.[27] The zeta potential for gold nanoparticles was -26 mV, indicating colloidal stabilisation through electrostatic repulsion. Gold nanorods_A and gold nanorods_B were also measured by DLS, showing mean hydrodynamic diameters of 192 nm and

10 nm and zeta potentials of -8.2 mV and -55.5 mV respectively. The DLS traces are presented in Figure 5.1, showing bimodal distributions for both samples of gold nanorods and monomodal distribution for gold nanoparticles. The measurements of PdI have shown high values for nanorods i.e. 0.505 and 0.495. Gold nanorods showed high PdI potentially due to different potential diffusion behaviour of rods.[28] It is important to note that the hydrodynamic diameter as determined by DLS of a non-spherical particle is the equivalent diameter of a sphere that has the same translational diffusion speed. In this case, it is extremely important to compare DLS hydrodynamic diameters with sizes obtained from SEM images. Lie *et al.* tried previously to measure hydrodynamic diameter of gold nanorods by DLS. However, they showed that hydrodynamic diameter cannot be deducted from DLS due to the fact that Stokes-Einstein equation is based on the diffusion coefficient for spherical particles. [29]

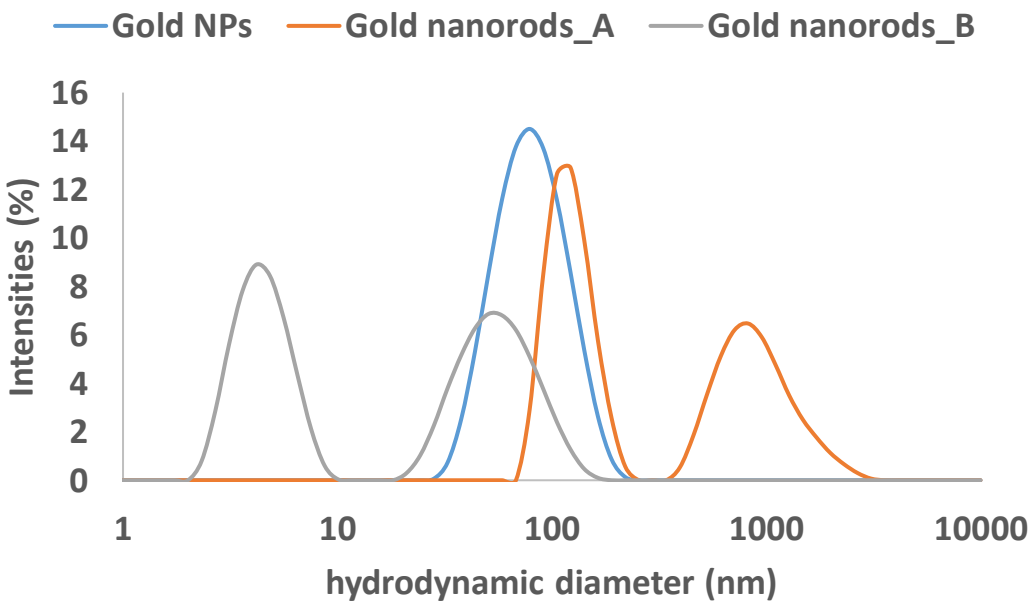

Figure 5.1. DLS analysis of gold NPs, gold nanorods_A and gold nanorods_B.

The morphology of gold samples was then analysed by SEM and is shown in Figure 5.2. The SEM images showed spherical morphology for gold NPs and ellipsoidal structures for gold nanorods. The diameters of particles obtained from SEM was measured using ImageJ (Table 5.1). The diameter of gold NPs and gold nanorods_A

obtained from DLS was higher compared with SEM values. This was likely due to the solvation sphere of citrate stabiliser. Gold nanorods_B showed higher diameter from DLS data compared with SEM length and width. As it was mentioned before, the value provided by DLS is a measure of the hydrodynamic diameter, a value that is not necessarily directly related to either the length or width of the nanoparticle. Gold nanorods_A appeared as aggregates when dried so this sample is hard accurately to characterise by SEM. However, ellipsoidal shape of individual particles was clearly visible on the surface of aggregates.

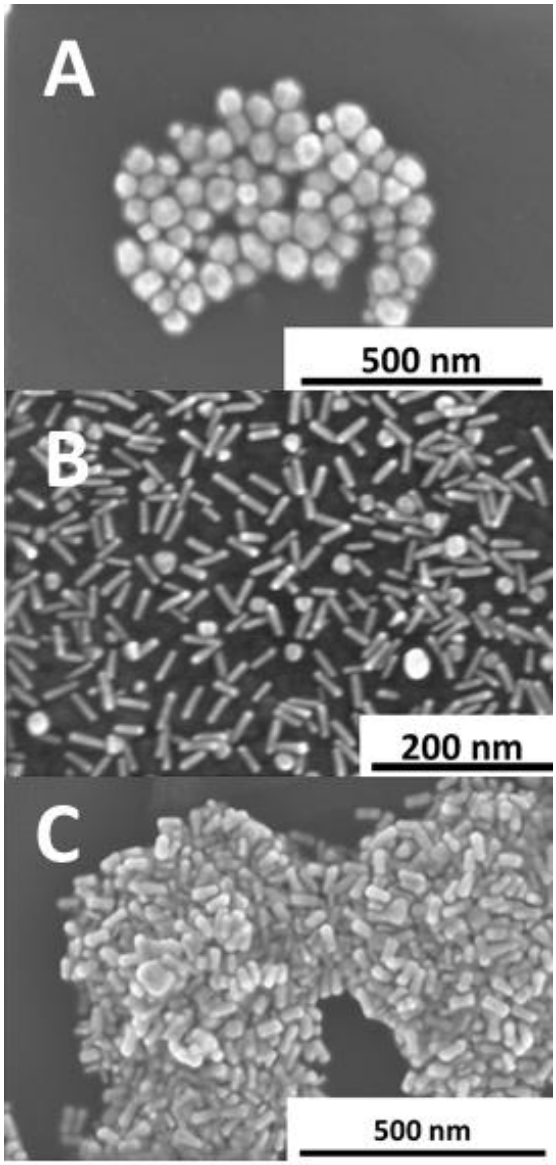

Figure 5.2. SEM characterisation of the gold nanomaterials, A) gold nanoparticles, B) gold nanorods_A, and C) gold nanorods_B.

Due to the issues with detection of single particles on SEM, gold nanorods_A were analysed by scanning transmission electron (STEM) microscopy. The resulting image is shown in Figure 5.3. The STEM images showed non-spherical morphology of particles with the presence of some more spherical particles for gold nanorods_A.

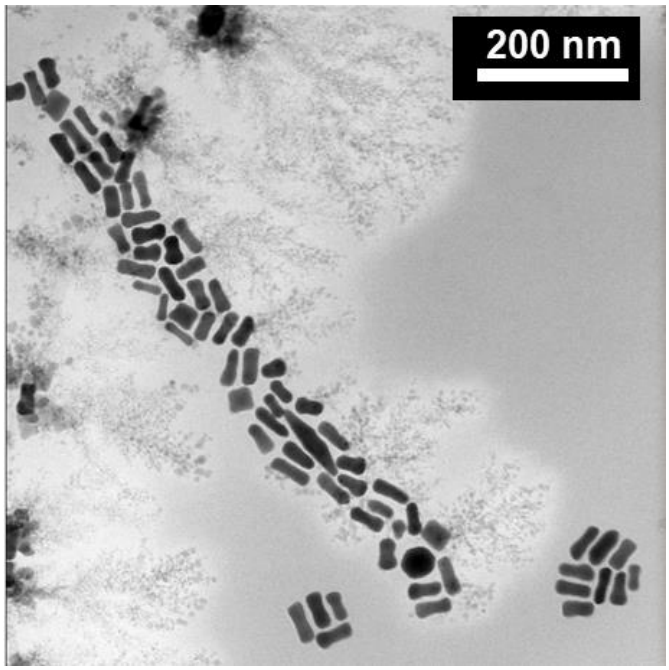

Figure 5.3. Bright-field (BF) scanning transmission electron (STEM) image of gold nanorods_A.

SEM images showed that gold nanorods_B have two population of particles i.e. ellipsoidal nanorods and particles with a slightly more spherical morphology. It agrees with bimodal distribution obtained by DLS measurements. The aspect ratio was also measured from the images for non-spherical particles. Gold nanorods_A showed a mean aspect ratio of 2.4 and non-spherical particles with smaller hydrodynamic diameter had aspect ratio of 3.3. The data for samples is summarised in Table 5.1.

Table 5.1. DLS and SEM characterisation of gold NPs, gold nanorods_A and gold nanorods_B.

Samples	R_h / nm	PdI	Zeta Potential / mV	Size from SEM (average) / nm	Aspect ratio
Gold NPs	35 ± 0.3	0.187± 0.005	-26 ± 0.3	60 ± 14	1
Gold nanorods_A	96 ± 11	0.505 ± 0.080	-8 ± 2.3	47.5 ± 11 (length) 20.1 ± 3 (width)	2.4 ± 0.5
Gold nanorods_B	10 ± 0.01	0.495 ± 0.01	-55 ± 0.4	33 ± 5 (length) 10 ± 2 (width)	3.3 ± 3

The three of gold nanoparticle samples were then fractionated and characterised by AF4-MALS-DLS. Each sample was measured at least in triplicate and showed good reproducibility. Figure 5.4 shows the results obtained from AF4-MALS-DLS measurements for the three gold samples. The fractograms plot the time of elution for particles against the signal obtained for 90° light scattering detector. The online MALS and DLS detectors allow the measurements R_g and the R_h of the particles exiting the AF4 separation channel. R_g was calculated based on sphere fit for gold nanoparticles and random coil for gold nanorods due to the most appropriate fit. In the following section the AF4-MALS-DLS data will be compared with SEM and DLS findings. In the subsequent sections, the separation behaviour and then shape factor of the samples will be discussed.

The fractogram for gold NPs showed the presence of void peak at 5 min, followed by main peak centred at 12 min with slight shoulder at 17 min elution time (see Figure 5.4). The second smaller shoulder indicates gold NPs with a slightly larger size. This observation agreed with SEM findings as the gold NPs showed a polydisperse population of particles (see Figure 5.2A). The values of R_g and R_h increased with elution time, with the mode of the MALS90° showing values for R_g of 19 nm and R_h

32 nm. The mode hydrodynamic value obtained from AF4 measurements showed good comparison with size values obtained from SEM images (mean radius was 30 nm from the SEM images). The differences between mean size obtained from SEM and R_h at the mode of the distribution was only around 2 nm. The separation of gold nanorods_A showed population of two particles – after 9 min and 11 min of elution. The MALS90° signal also showed void peak around 7 min of elution. The R_g values increased in the first peak and then dropped dramatically and then increased again in the beginning of second peak, an indication of two population of particles. The mode R_g value obtained for first population was 117 nm and 132 nm for second population of particles. The mode R_h obtained from flow measurements for first peak was 19 nm and 86 nm for the second population of particles. Two populations of particles agrees also with SEM analysis because the samples appear to contain two populations: one non-spherical population and a second less common population of more spherical particles (see Figure 5.3). These flow measurements showed better comparison of R_h values with size obtained from SEM values (52 nm - length and 25 nm – width), than DLS batch measurements (R_h = 96 nm). The previously published theoretical research has suggested that elongated particles can be oriented in different positions in separation channel.[16,30] The issue which was reported before, showed that contribution of rotational diffusion should be taken into account for anisotropic particles.[31,32] The rotational diffusion coefficient can be defined from following equation:

$$D = \frac{k_B T}{3\eta\pi L} F_D$$

Where D is diffusion coefficient, η is the viscosity of the solvent, k_B the Boltzmann constant, T the temperature of the sample and L is the major axis of particles. F_D is a geometrical coefficient depending on the shape of particles.[33] For spherical particles F_D = 1. Currently, the calculations within the DLS software does not take into account F_D and improving of measurements for non-spherical particles is still in progress.[34,35]

AF4-MALS-DLS measurements for gold nanorods_B showed one peak after 5 min of elution with a small shoulder at higher elution times (7 min of elution), indicating population of particles with increasing size or the presence of a small amount of

aggregates. The R_g showed an initial decrease with elution time, followed by an increase for shoulder of the peak. The mode value of R_g was 16 nm. R_h showed increase with elution time and mean value was 12 nm. The size of gold nanorods_B was smaller compared with gold nanorods_A as determined by electron microscopy, the AF4 measurements agrees with those results. R_h obtained from online AF4 measurements showed that gold nanorods_B are smaller compared with gold nanorods_A.

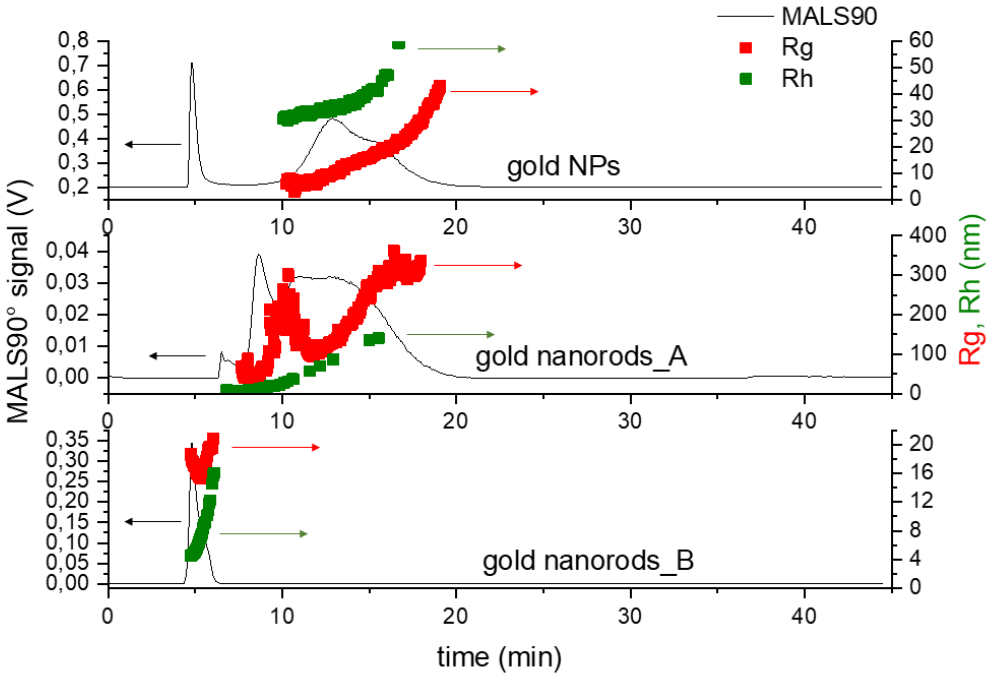

Figure 5.4. AF4-MALS-DLS analysis of gold particles. Fractograms showing the light scattering 90° detector signal (black line, left hand scale), radius of gyration (red dotted line, right hand scale) and hydrodynamic radius (green dotted line, right hand scale) obtained from AF4-MALS-DLS measurements for gold nanoparticles, gold nanorods_A, gold nanorods_B for a cross-flow of 0.5 mL/min.

Comparison of the R_h values for the samples with the calculated hydrodynamic radius (R_h calc) based on AF4 theory may provide an insight into the different separation behaviour of the three different samples. The R_h calc has therefore been plotted on the same graph. Where, R_h calc was calculated using following equation:

$$R_{h\ calc} = \frac{t_R k_B T}{\pi\, \eta\, \omega^2 (\frac{F_x}{F_c})}$$

Where $R_{h\ calc}$ is theoretical hydrodynamic radius, t_R is retention time, k_B is Boltzmann constant, T is absolute temperature, η is dynamic viscosity of solvent, ω is channel thickness, F_x/ F_c is the ratio of cross-flow rate F_x to channel flow F_c.

This equation for the R_h calc can only be accurately applied for a separation method that uses a constant cross-flow throughout fractionation.[8] The method used in this work uses a cross-flow that changes with elution time. Therefore, the R_h calc for all the gold samples did not match with the data obtained from flowing mode, the R_h calc underestimated the values for R_h compared with measured R_h. However, the value for R_h calc can assist in the comparison of the separation behaviour of the samples with different shapes. As seen for the spherical sample, gold NPs, the R_h calc consistently underestimates the measured R_h by 40 % for all the particles in the population. However, for both the gold nanorod samples elute much earlier than would be expected for a spherical sample.[15,36] Additionally, for both non-spherical samples the discrepancy between the calculated and measured values increased with increasing R_h. This may indicate that larger non-spherical nanomaterials may reside higher in the AF4 channel than expected for a spherical particle and thus experience faster flow rates resulting in earlier elution times.

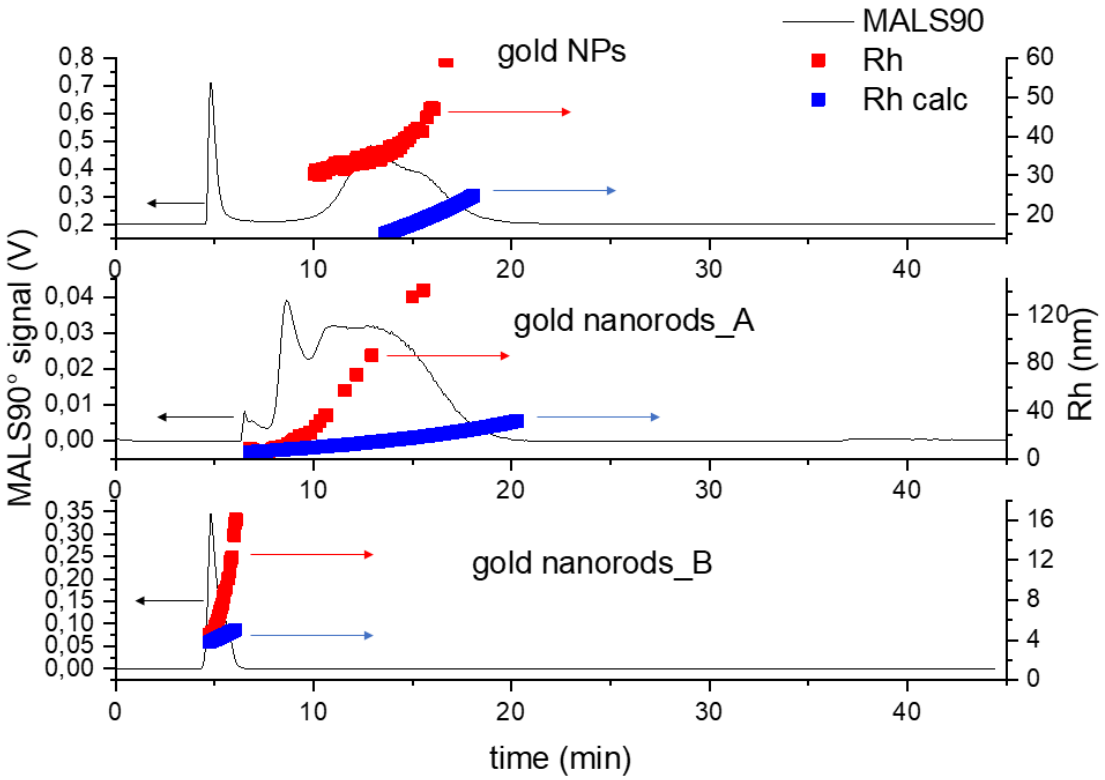

Figure 5.5. AF4-MALS-DLS analysis of gold particles. Fractograms showing the light 90◦ scattering detector signal (black line, left hand scale), hydrodynamic radius (red dotted line, right hand scale) and hydrodynamic radius calculated (blue dotted line, right hand scale).

The online data obtained from MALS and DLS allows for determination of the shape and internal structure of particles by calculating the shape factor (ratio of the R_g/R_h). The fractograms and the calculated shape factors (blue dotted line) are shown in Figure 5.6.

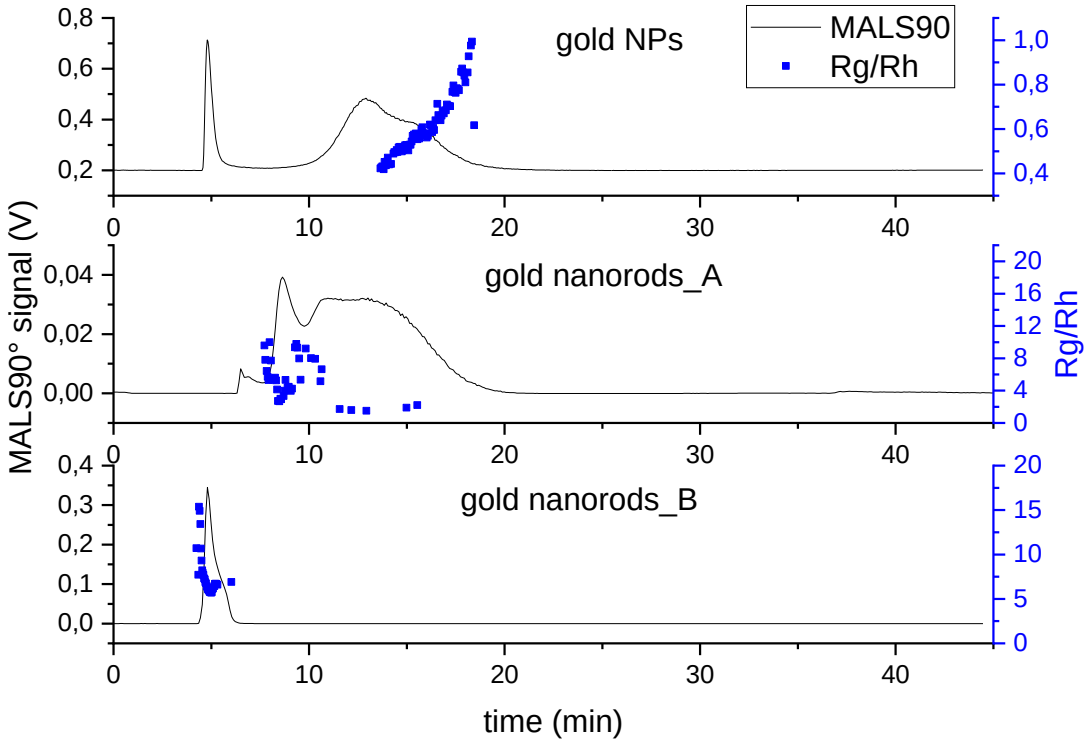

Figure 5.6. Fractograms showing the light 90 ◦ scattering detector signal (black line, left hand scale) and shape factor (blue dotted line, right hand obtained from AF4-MALS-DLS measurements for gold nanoparticles, gold nanorods_A, gold nanorods_B for cross flow 0.5 mL/min.

The shape factors for gold NPs increased from ~0.4 to ~1.0 which indicates that the there is some differences in the shape/structure of particles in the population, with the smallest nanoparticles possessing the lower shape factors. The expected shape factor for a hard sphere is 0.77 and therefore these measurements indicate that there are differences in the morphologies of the particles in this sample. Smaller nanoparticles would be expected to have the same corona thickness as larger particles and therefore for a smaller NP this would represent a large contribution to the total particle size,[37] this might give lower shape factor values. The schematic representation of difference in corona contribution for gold particles is presented in Figure 5.7. While the gold NPs can be seen to have a generally spherical shape in the SEM images (Figure 5.2A), it is apparent that they possess an angular/irregular surface and some particles displayed a more rod-like shape. These morphologies

might explain the shape factor values approaching ~1 found for the larger particles in the distribution.

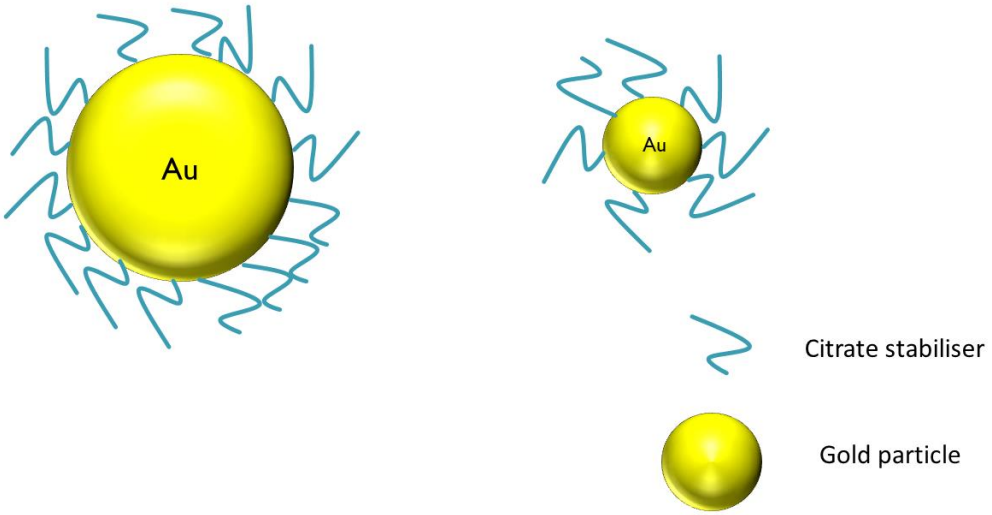

Figure 5.7. Cartoon representation of differences in corona contribution for gold particles. Blue line represents citrate stabiliser and gold spheres represents gold nanoparticles.

For gold nanorods_A, the ratio R_g/R_h decreased along with elution time for the first population of particles, followed by increasing and then decreasing again after ~12 mins. The first peak showed values of shape factor from ~ 12 to ~ 4. The second peak for gold nanorods_A showed a decrease in shape factor from ~ 10 to ~ 1.5. It may indicate that first peak was representative of more elongated gold particles and larger particles in the second peak presented more spherical structures. The SEM image suggested that there are some particles in the sample which are longer and some which are shorter gold nanorods (see Figure 5.3). The mean aspect ratio obtained from SEM was 2.4 for gold nanorods_A, which is quite different compared with values obtained from AF4. However, the value of aspect ratio obtained from SEM measurements was done in dry form, which can decrease the value compared with shape factor obtained from AF4 technique. The aspect ratio and shape factor cannot be directly compared. The difference can come from citrate coating and solvation shell. For gold nanorods_B, ratio R_g/R_h decreased from 17 until ~ 5. Similar trend than for gold nanorods_A was visible, where shape factor was decreasing with elution time. The mean shape factor obtained from AF4 measurements was 1.4.

It was slightly lower compared with SEM value for aspect ratio of 3.3. It can be explained by the fact that MALS detector is able to detect R_g >8 nm, which can decrease the mean shape factor. [38]

Table 5.2. The mode results of R_g, R_h and R_g/R_h for gold NPs, gold nanorods_A, gold nanorods_B obtained from AF4-MALS-DLS.

	Flow measurements			Theoretical (Calculated)
Sample	R_g/ nm	R_h/ nm	R_g/R_h	Rg /nm
Gold NPs	19	32	0.65	23
Gold Nanorods_A	132 117	19 ± 0.6 80 ± 0.6	6.95 1.46	15
Gold nanorods_B	16	12 ± 2.0	1.33	9.5

The shape factors values, R_g and R_h for the mode population (centre of the peak) obtained from AF4-MALS-DLS measurements for gold nanoparticles and gold nanorods are presented in Table 5.2. The spherical gold nanoparticles showed the mode value for shape factor 0.65, gold nanorods_A 6.95 and 1.46 and gold nanorods_B 1.33. In the literature general values of shape factors for hard sphere is 0.775, random coil ~ 1.5 and rigid rod >2.0.[39] The shape factor for core shell particles was shown previously as <0.7.[40] The experimental data matched with theoretical values for shape factor for gold NPs as nanoparticles showed the shape factor <0.7 which can be explained by thick solvation shell made of citrate stabiliser. However, the shape factor of gold nanorods showed different values compared with aspect ratio obtained from SEM images. It should be kept in mind that those two values cannot be directly compared to one another. Aspect ratio as previously mentioned is defined as ratio between length and width of particles. While, shape factor is

determined as ratio of radius of R_g and R_h. Detailed equations for calculation of R_g and R_h particles with different shapes are given in SI section.

The theoretical R_g was calculated for all gold samples based on diameter and length obtained from SEM images, where the values analysed are as follows: gold NPs 23 nm, gold nanorods_A 15 nm and gold nanorods_B 9.5 nm. The theoretical R_g values for gold NPs and gold nanorods_B matched relatively closely with the results obtained for mode values from AF4 measurements, showing a difference about 6 nm. Gold nanorods_A showed a bigger difference, as R_g obtained from AF4-MALS measurements was 117 and 132 and theoretical value was 15 nm. This larger R_g can be attributed to formation of aggregates of gold nanorods_A. As previously showed, zeta potential of gold nanorods_A was -8 mV which can explain the fact that particles are not very colloidal stable over time. The sample of gold nanorods_A was found to have stability issues, as aggregates were noted with increasing storage time, the sample could be redispersed by sonication. Therefore, it is likely that the sample might show a propensity to aggregate during AF4 analysis perhaps during the focussing step.

5.3.2. Silver particles

The three different morphology of silver particles, silver nanoparticles, silver nanorods and silver nanoprisms, were characterised by DLS batch and electron microscopy to obtain information about size, zeta potential and morphology, this data is shown in Table 5.3. DLS measurements showed a monomodal distribution and low PdI for silver nanoparticles (see Figure 5.8). The DLS distributions for silver nanoprisms and silver nanoplates showed bimodal distributions of particles. The zeta potential of all samples was ≤ -13 mV which appeared to be sufficient to provide colloidal stability over the course of this work. The silver nanoprisms and silver nanoplates had high PdI (> 0.6) compared with the spherical particles. However, as previously mentioned for the gold nanorods, DLS obtains information of the hydrodynamic diameter for a non-spherical particle as the diameter of a sphere

which has the same translational diffusion speed as the particle according to Stokes-Einstein equation. It may also indicate that particles have tendency to agglomerate. Another consideration is that the LSPR for silver nanoprism and nanoplates is around wavelength of laser (633 nm). In that case, particles can absorb light from DLS and this can lead to errors in the measurements.[41]

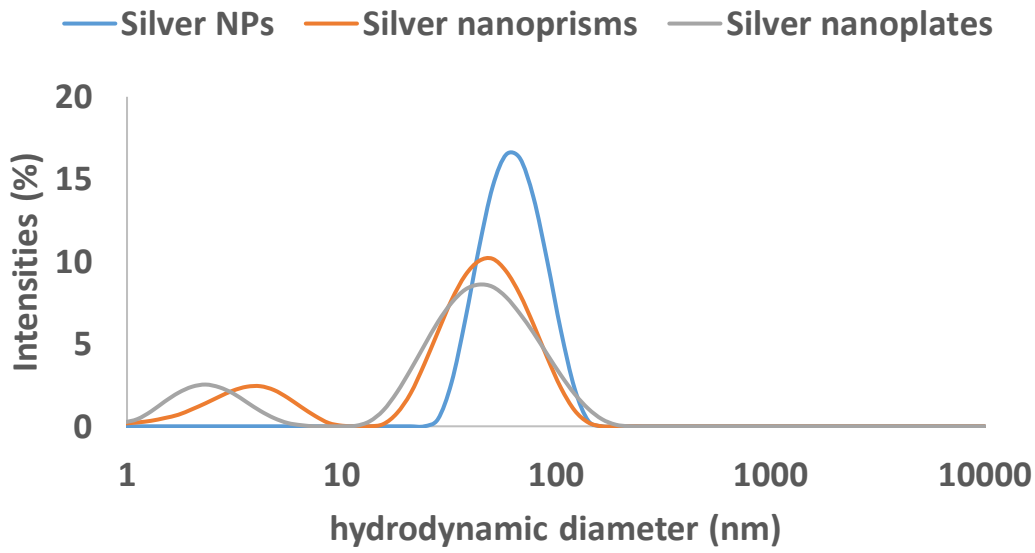

Figure 5.8. DLS analysis of silver NPs (blue line), silver nanoprisms (orange solid line) and silver nanoplates (grey solid line).

The SEM images showed spherical morphology with narrow distribution for the silver nanoparticles. The hydrodynamic radius (R_h = 28 nm) agreed with the size obtained from SEM images (48 nm – diameter; see Figure 5.9A). The DLS showed a slight difference, with the diameter values analysed around 8 nm larger compared with SEM images, which can be attributed to solvation shell of citrate stabiliser in the aqueous media. The SEM analysis of the silver nanoprisms showed a mixture of triangle structures and spheres (see Figure 5.9B). The mean diameter obtained from DLS measurements was smaller compared with the diameters obtained *via* SEM. However, SEM images showed that the sample was a mixture of two different morphologies which was indicated by high PdI (~ 0.6) which would not be resolved as separate populations by DLS. The analysis of the silver nanoplates sample by SEM did not reveal individual nanoplates, it appeared that the particles had assembled through their large flat faces into larger structures, sometimes greater than 200 nm

(see Figure 5.9C). The individual plates were approximately 32 nm in thickness and 12 nm width. The hydrodynamic diameter and PdI from DLS suggested the nanoplates sample was not as aggregated when dispersed as it appeared when dry. The morphology of all of the silver particles are shown in Figure 5.9.

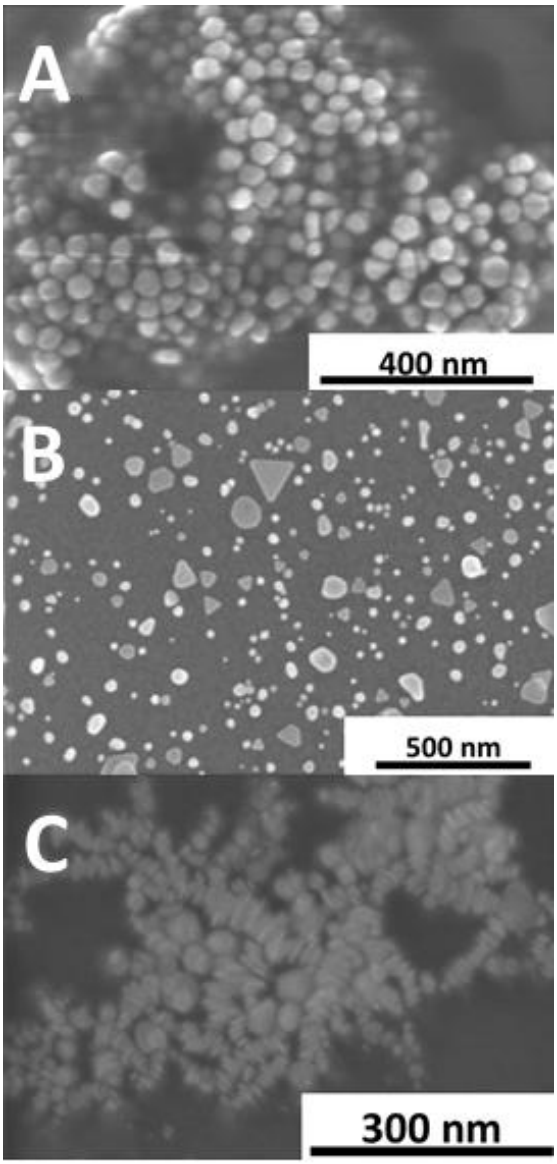

Figure 5.9. SEM imaging of A) Silver NPs, B) Silver nanoprisms and C) silver nanoplates

Due to the issues with imaging of single particles on SEM, silver nanoplates were also analysed by scanning transmission electron (STEM) microscopy. The obtained image is shown in Figure 5.10. The analysis of sample silver nanoplates showed the mixture of different shapes for particles like rods (~ 9.6 nm), triangles (~ 30 nm), hexagons (~ 9.7 nm) and some potentially spherical nanoparticles (~ 5.2 nm). This observed polydispersity agreed with DLS analysis, as the measured PdI was high (>0.6) for silver nanoplates.

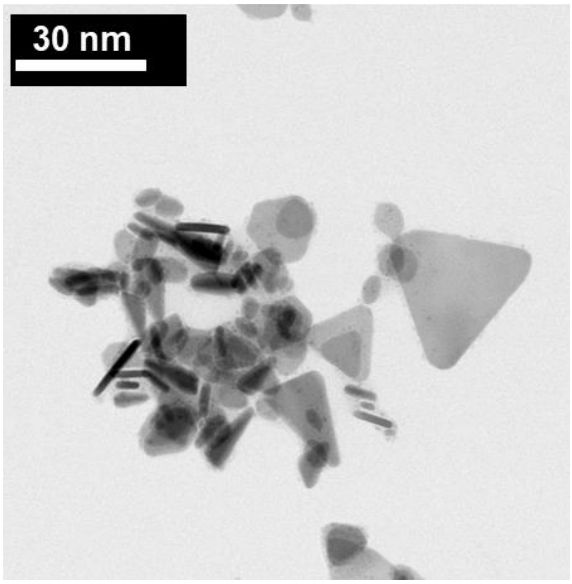

Figure 5.10. Bright-field (BF) scanning transmission electron (STEM) image of silver nanoplates.

Table 5.3. DLS and SEM characterisation of silver NPs, silver nanoprisms and silver nanoplates.

Sample	R_h/ nm	PdI	Zeta Potential / mV	Size from SEM / nm
Silver NPs	28 ± 0.7	0.161 ± 0.010	-13 ± 0.9	48 ± 6
Silver nanoprisms	11 ± 0.06	0.618 ± 0.004	-17 ± 3.2	64 ± 8 (length of edge of triangles) 55 ± 10 (spheres)
Silver nanoplates	10 ± 0.01	0.680 ± 0.002	-40 ± 1.3	32 ± 4 (length) 12 ± 3 (width)

In the next step, the three samples of silver nanoparticles were characterised by AF4-MALS-DLS measurements. Figure 5.11 shows the fractograms obtained from AF4-MALS-DLS measurements for three samples. The fractograms displays elution time for particles versus the signal obtained for 90° light scattering detector, R_g and R_h data. The R_g was calculated based on sphere fit for silver nanoparticles and random coil for silver nanoplates and nanorods. The fractogram for silver nanoparticles (Figure 5.11) showed the void peak at 6 min, followed by the presence of a main peak centred at 8 min. It is also worth mentioning that R_g was calculated only after 10 min, this can be caused by a limitation of detector as MALS can only measure $R_g > 8$ nm.[38] The mean R_h was around 20 nm which it matched with size obtained from SEM analysis (R_h = 24 nm). The SEM images showed one population of spherical silver nanoparticles, which it agrees with AF4 findings. Silver nanoprisms showed two broad populations with the first peak eluted at 20 min with mode R_g value 11 nm and second one 28 min with mean R_g value 13 nm for R_g and MALS90°. Interestingly, the R_h value showed little increase over the complete sample, this is unexpected as AF4

separates based on R_h and therefore larger particles should be eluted at longer elution times. This behaviour suggests that the shape of the nanoprisms is influencing the separation; the particles with a with a flat plate-like shape may be located closer to the membrane than expected purely for their R_h value, thus eluting at a later time. This AF4 data for the nanoprisms agrees with SEM images (see Figure 5.9B) as silver nanoprisms showed mixture of triangular and more like sphere particles. The main peak for silver nanoplates is presented at 10 min of elution. As previously mentioned, morphology of single silver nanoplates was detected by STEM, showing of mixture of triangular and hexagonal particles. The AF4 measurements showed single peak obtained from MALS90°, centred after 10 min of elution, preceded by void peak. The mode value of R_g was 28 nm and R_h was 22 nm.

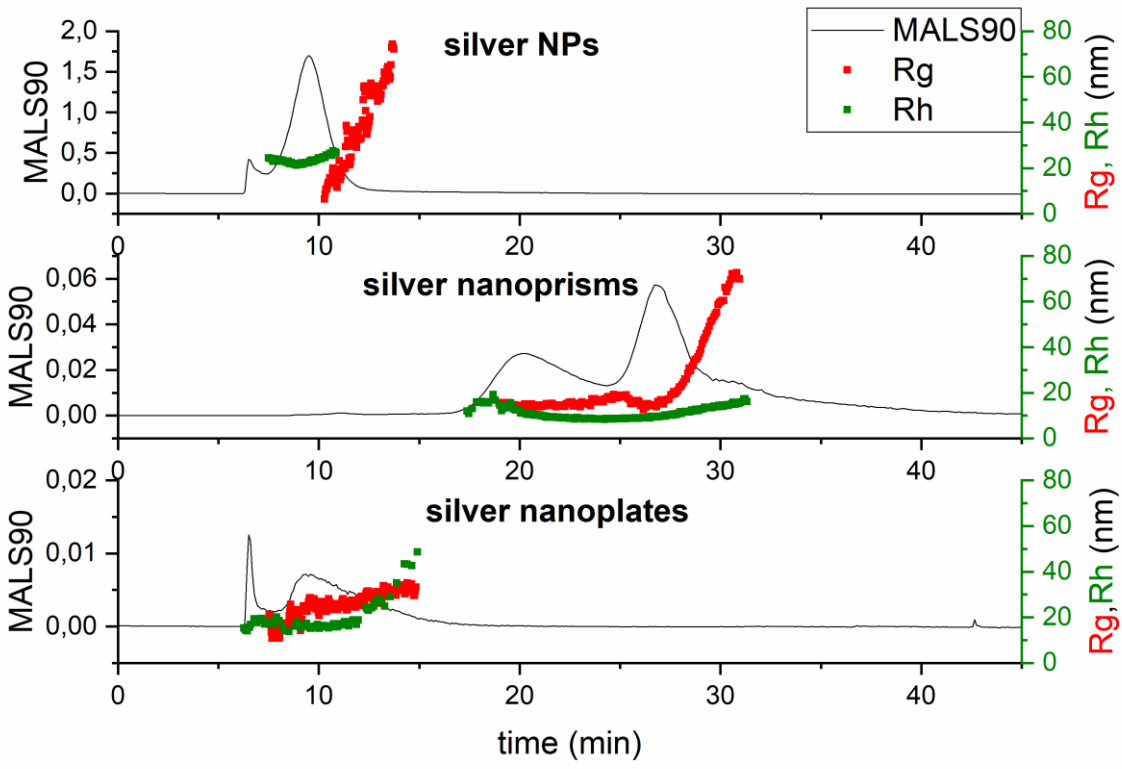

Figure 5.11. AF4-MALS-DLS analysis of silver particles. Fractograms showing the light 90◦ scattering detector signal (black line, left hand scale), radius of gyration (red dotted line, right hand scale) and hydrodynamic radius (green dotted line, right hand scale) obtained from AF4-MALS-DLS measurements for silver nanoparticles, silver nanoprisms, silver nanoplates for cross-flow 0.5 mL/min.

The fractograms (Figure 5.12), obtained from MALS90° for silver particles were plotted against the obtained data for R_h and R_h calc. As for the gold nanoparticles, the R_h calc for silver particles does not match with the data obtained from flowing mode. The R_h calc for silver NPs was an underestimation compared with R_h values obtained during flow measurements. As seen for the spherical gold NPs before, R_h calc is also underestimated for silver NPs about 40%. For the silver nanoprisms the R_h calc was much higher that the measured R_h. The SEM images suggest that these particles are relatively flat compared with the spherical particles and the gold nanorods. Silver nanoplates appear to have a more 3-D morphology, as gold nanorods, which could possibly be why the silver nanoplates were placed higher in the channel compared with silver nanoprisms. It can also be clearly seen that the silver nanoprisms elute much later compared with silver nanoparticles. It can therefore be explained that the shape, dimension and 3-D structure is critical for AF4 measurements and it can play a crucial role in the separation of particles. Potentially the shape of the nanoprisms results in them being pushed closer to the membrane by the cross flow than would happen for spherical particles, this would mean that they experience a slower flow towards the detector and elute at a later time.

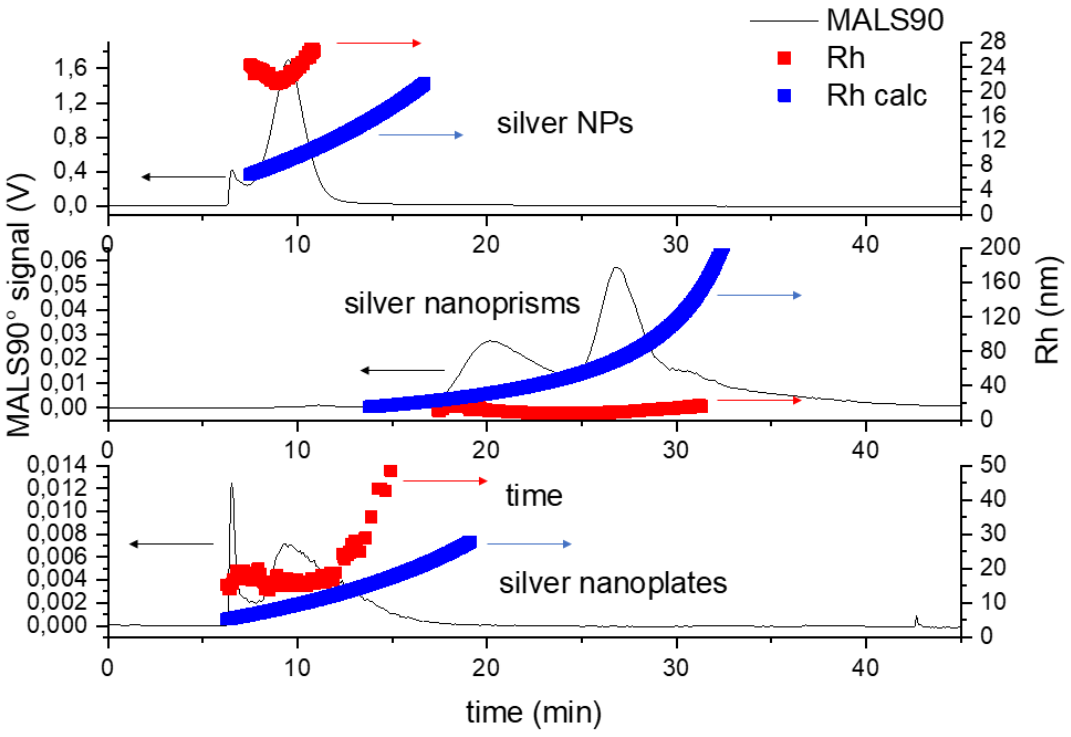

Figure 5.12. Fractograms showing the light 90◦ scattering detector signal (black line, left hand scale), hydrodynamic radius (red dotted line, right hand scale) and hydrodynamic radius calculated (blue dotted line, right hand scale) for silver particles.

The fractograms with shape factors determined from the experimentally measured R_g and R_h values is shown in Figure 5.13. The shape factor for silver NPs was in range of 0.4-0.8 indicating that some particles appear to have a core-shell type structure. The shell can be associated with citrate buffer which it acts also as a stabiliser. The shape factors for silver nanoparticles and silver nanoprisms increase with the elution time from separation channel. In case of silver nanoprisms, there are two population of shapes. The first population (elution time between 18 and 25 min) was more closely related to spheres (R_g/R_h ~ 0.8) and second type of particles (elution time between 25 and 32 min) was more elongated (R_g/R_h values increased from 0.85 until 4.0) which agrees with the SEM findings, where images showed two populations of particles more spherical and more triangular particles. For silver nanoplates, the shape factor increased with elution time and it showed values between 0.7 until 2.0. Shape factor values for silver nanoplates are smaller compared with silver

nanoprisms. This can be explained by the fact that silver nanoparticles are smaller and more spherical in shape. According to STEM analysis, morphology of particles is the mixture of triangles and hexagons.

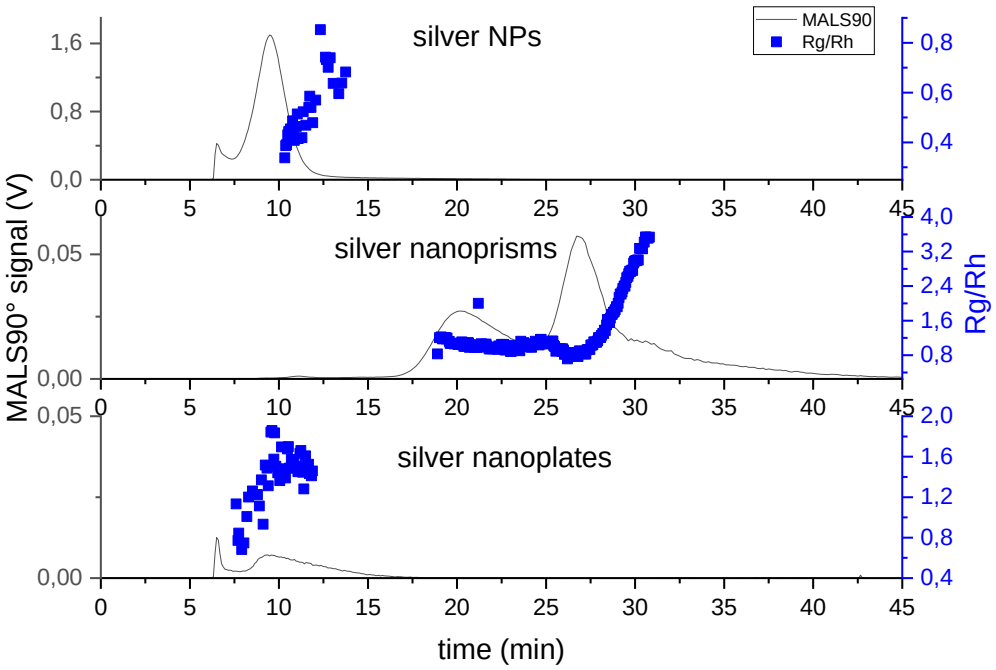

Figure 5.13. Fractograms showing the light 90◦ scattering detector signal (black line, left hand scale) and shape factor (blue dotted line, right hand obtained from AF4-MALS-DLS measurements for silver nanoparticles, silver nanoprisms, silver nanoplates for cross flow 0.5 mL/min.

Table 5.4 provides average results for mode R_g, R_h and shape factors for all silver samples. Theoretical R_g was calculated for silver nanoparticles using equation (2) and it was 18.6 nm. The theoretical value of R_g was exactly as obtained from AF4 measurements, proving the concept of successful separation of particles. Unfortunately, the theoretical R_g could not be calculated for silver nanoprisms and silver nanoplates due to high varieties in shapes of particles.

Table 5.4. The results of Rg, Rh and Rg/Rh for silver nanoparticles, silver nanoplates, silver nanoprisms obtained from AF4-MALS-DLS.

	Flow measurements		
Sample	R_g/ nm	R_h/ nm	R_g/R_h
silver NPs	18.6	23.6	0.79
silver nanoprisms	10.6 13.0	9.5 11.2	1.11 1.16
silver nanoplates	28.5	22.3	1.27

In case of silver nanoprisms, there are two population of particles with similar values of shapes factor i.e. 1.11 and 1.16. It could be possible that first peak represents spherical particles and second one is representation of triangles. The assumption is based on the values of shape factors and size obtained from SEM, as spherical particles showed slightly smaller size compared with the triangular particles. For silver nanoplates, the shape factor was 1.27. According to STEM analysis, silver nanoplates have more varieties of shapes than the silver nanoprisms, which can increase shape factor. The AF4 analysis along with SEM images, showed that the silver nanoplates are smaller than silver nanoprisms.

5.4. Conclusion

The gold and silver particles with different morphology were characterised by range of techniques like DLS, zeta potential measurement, SEM, STEM, UV-Vis spectroscopy and AF4-MALS-DLS. The particles showed different shapes, morphology, hydrodynamic diameters and shape factors. The size obtained from DLS was usually slightly higher compare with SEM images due to solvate shell and non-spherical shapes of particles. AF4 measurements showed successful separation of particles with different shapes and the data matches with morphology obtained from SEM images. Gold and silver nanoparticles with spherical shapes showed that size

increases with elution time according to the AF4 theory. AF4 separation was able to fractionate different populations of particles in the samples of gold nanorods_A and silver nanoprisms, showing great potential in the nanotechnology area. The capability of AF4 to be coupled to MALS and DLS detectors is a really important measurement to obtain information shape and structure of nanomaterials. Before nanoparticles can be used for biomedical applications, size, size distribution, shape and other factors must be precisely known due to their influences within the body. Using AF4, it can be possible to overcome the inaccuracies that arise using batch DLS measurements. The data showed that AF4 analysis can be used for high-resolution characterisation of range of sizes and shapes of particles. However, alone it should not be used as an alternative to obtain morphology from SEM or STEM images.

5.5. References

1 A. Albanese, P. S. Tang and W. C. W. Chan, *Annu. Rev. Biomed. Eng.*, 2012, **14**, 1–16.

2 K. Namdee, A. J. Thompson, A. Golinski, S. Mocherla, D. Bouis and O. Eniola-Adefeso, *Atherosclerosis*, 2014, **237**, 279–286.

3 S. Cai, K. Vijayan, D. Cheng, E. M. Lima and D. E. Discher, *Pharm. Res.*, 2007, **24**, 2099–2109.

4 G. M. Lee and S. J. Park Dr, *Process optimization in component manufacturing*, 2013.

5 A. Bootz, V. Vogel, D. Schubert and J. Kreuter, *Eur. J. Pharm. Biopharm.*, 2004, **57**, 369–375.

6 J. B. Hall and S. E. Mcneil, *Nanomedicine*, 2007, **2**, 789–803.

7 J. A. Gallego-Urrea, J. Hammes, G. Cornelis and M. Hassellöv, *J. Nanoparticle Res.*, 2014, 16, 2383.

8 M. E. Schimpf, K. Caldwell and J. C. Giddings, *Field-Flow Fractionation Handbook*, John Wiley & Sons, Inc., 2000.

9 H. Hagendorfer, R. Kaegi, J. Traber, S. F. L. Mertens, R. Scherrers, C. Ludwig and A. Ulrich, *Anal. Chim. Acta*, 2011, **706**, 367–378.

10 S. Sitar, V. Vezočnik, P. Maček, K. Kogej, D. Pahovnik and E. Žagar, *Anal. Chem.*, 2017, acs.analchem.7b03251.

11 S. Boye, F. Ennen, L. Scharfenberg, D. Appelhans, L. Nilsson and A. Lederer,

Macromolecules, 2015, **48**, 4607–4619.

12 P. Jurney, R. Agarwal, V. Singh, D. Choi, K. Roy, S. V. Sreenivasan and L. Shi, *J. Control. Release*, 2017, **245**, 170–176.

13 B. Plazzotta, J. S. Diget, K. Zhu, B. Nyström and J. S. Pedersen, *J. Polym. Sci. Part B Polym. Phys.*, 2016, **54**, 1913–1917.

14 J. Gigault, I. Le Hécho, S. Dubascoux, M. Potin-Gautier and G. Lespes, *J. Chromatogr. A*, 2010, **1217**, 7891–7897.

15 J. Gigault, T. J. Cho, R. I. MacCuspie and V. A. Hackley, *Anal. Bioanal. Chem.*, 2013, **405**, 1191–1202.

16 S. Monjezi, M. Schneier, J. Choi, S. Lee and J. Park, *J. Chromatogr. A*, 2019, **1587**, 189–196.

17 F. R. Phelan and B. J. Bauer, *Chem. Eng. Sci.*, 2009, **64**, 1747–1758.

18 M. Alfi and J. Park, *J. Sep. Sci.*, 2014, **37**, 876–883.

19 J. Park and A. Mittal, *Chromatography*, 2015, **2**, 472–487.

20 R. Beckett and J. Giddings, *J. Colloid Interface Sci.*, 1997, **186**, 53–9.

21 S. Monjezi, J. D. Jones, A. K. Nelson and J. Park, *Nanomaterials*, 2018, **8**, 130.

22 R. Mathaes, G. Winter, J. Engert and A. Besheer, *Int. J. Pharm.*, 2013, **453**, 620–629.

23 E. Niezabitowska, J. Smith, M. R. Prestly, R. Akhtar, F. W. Von Aulock, Y. Lavallée, H. Ali-Boucetta and T. O. Mcdonald, *RSC Adv.*, 2018, **8**, 16444–16454.

24 M. J. Cheng, N. N. Bal, P. Prabakaran, R. Kumar, T. J. Webster, S. Sridhar and E. E. Ebong, *Int. J. Nanomedicine*, 2019, **14**, 319–333.

25 J. Haber and K. Sokolov, *Langmuir*, 2017, **33**, 10525–10530.

26 T. K. Sau and C. J. Murphy, *Langmuir*, 2004, **20**, 6414–6420.

27 T. Zheng, S. Bott and Q. Huo, *ACS Appl. Mater. Interfaces*, 2016, **8**, 21585–21594.

28 M. A. C. Potenza, Krpetić, T. Sanvito, Q. Cai, M. Monopoli, J. M. De Araújo, C. Cella, L. Boselli, V. Castagnola, P. Milani and K. A. Dawson, *Nanoscale*, 2017, **9**, 2778–2784.

29 H. Liu, N. Pierre-Pierre and Q. Huo, *Gold Bull.*, 2012, **45**, 187–195.

30 S. Monjezi, G. K. Patterson, A. K. Nelson and J. Park, *Chem. Eng. Sci.*, 2018, **189**, 394–400.

31 T. Liu and Z. Xiao, *Macromol. Chem. Phys.*, 2012, **213**, 1697–1705.

32 B. N. Khlebtsov and N. G. Khlebtsov, *Colloid J.*, 2011, **73**, 118–127.

33 P. Arenas-Guerrero, Á. V. Delgado, K. J. Donovan, K. Scott, T. Bellini, F. Mantegazza and M. L. Jiménez, *Sci. Rep.*, 2018, **8**, 1–10.

34 D. Bossert, J. Natterodt, D. A. Urban, C. Weder, A. Petri-Fink and S. Balog, *J. Phys. Chem. B*, 2017, **121**, 7999–8007.

35 A. D. Levin, E. A. Shmytkova and B. N. Khlebtsov, *J. Phys. Chem. C*, 2017, acs.jpcc.6b10226.

36 H. El Hadri, J. Gigault, J. Tan and V. A. Hackley, *Anal. Bioanal. Chem.*, 2018, **410**, 6977–6984.

37 G. R. Deen, T. Alsted, W. Richtering and J. S. Pedersen, *Phys. Chem. Chem. Phys.*, 2011, **13**, 3108–3114.

38 P. Clarke and B. Sabagh, Seminar – Light Scattering The Postnova Characterization Platform, Posnova 2019.

39 J. Lohrke, A. Briel and K. Mäder, *Nanomedicine*, 2008, **3**, 437–452.

40 G. R. Deen, T. Alsted, W. Richtering and J. S. Pedersen, *Phys. Chem. Chem. Phys.*, 2011, **13**, 3108–3114.

41 D. Geißler, C. Gollwitzer, A. Sikora, C. Minelli, M. Krumrey and U. Resch-Genger, *Anal. Methods*, 2015, **7**, 9785–9790.

Supporting information

For ellipsoidal/ rod like particles R_g can be calculated from following equation:

$$R_g^2 = \frac{L^2}{12} \text{ (1)}$$

Where L is the mean square end to end distance of rod length radius.

Compact sphere and spherical particles can be calculated from following equation:

$$R_g^2 = \frac{3D^2}{20} = \frac{3}{5}a^2 \text{ (2)}$$

Where D and a are the mean square end to end distance of sphere diameter and radius, respectively.

Hydrodynamic radius obtained from DLS measurements, the values are based on SLS theory:

$$R_h = \frac{kT}{6\pi\eta D} \text{ (3)}$$

T is the temperature, kB is the Boltzmann constant, η is the dynamic viscosity of the solvent, and D is the diffusion coefficient.

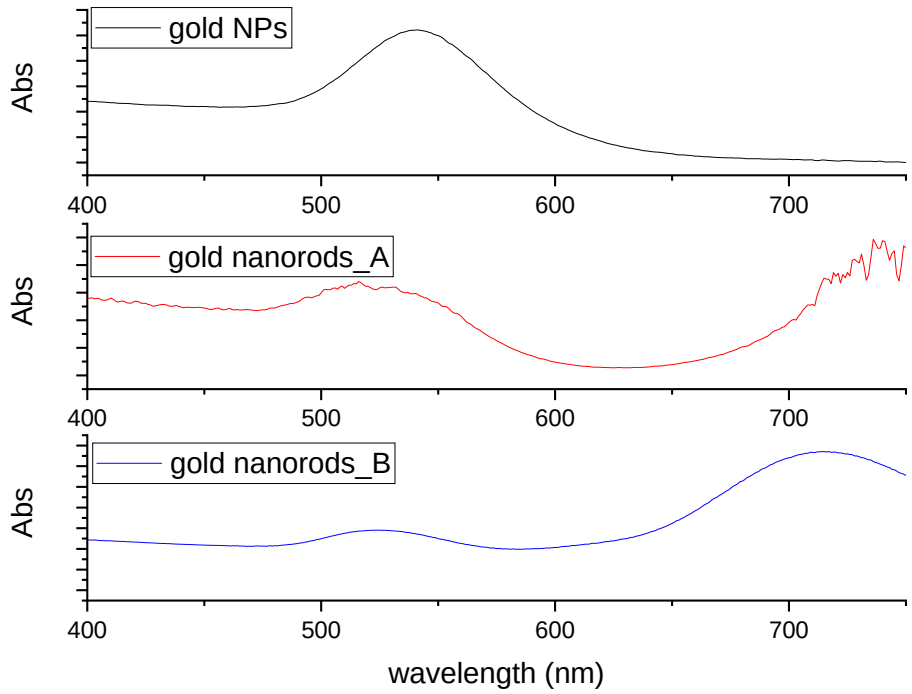

Figure 5.14. The UV-VIS absorbance spectrum for gold NPs, gold nanorods_A and gold nanorods_B.

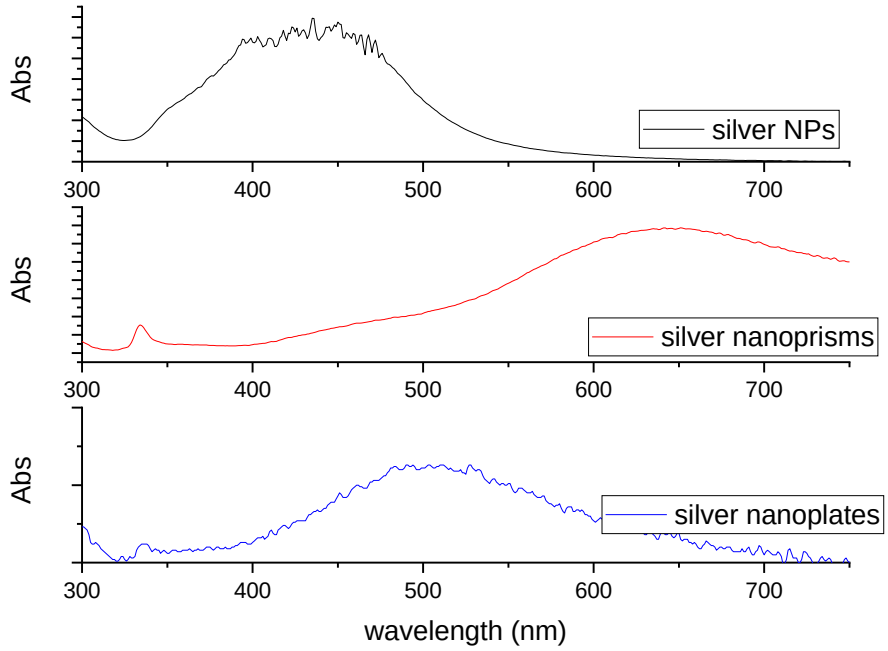

Figure 5.15. The absorbance spectrum for silver nanoparticles, silver nanoprisms and silver nanoplates.

Chapter 6

Conclusions and Future Work

6.1. Conclusions

The focus of this thesis was to synthesise range of novel nanomaterials with range of shapes and morphologies and then to use asymmetric flow field flow fractionation (AF4) to obtain a detailed understanding of the structure of these materials. AF4 is relatively a new technique and therefore this thesis investigates the development of new methods to effectively fractionate and characterise the materials. These new methods allow about the measurement of R_g and R_h which allow the shape factor and internal structure of nanoparticles to be determined. This analysis provided considerable insight into the size distribution over batch DLS alone. It also offered information on how shape and morphology change within a size distribution that would not be possible by other techniques such as SAXS. The work presented in this thesis looked at three different types of materials: non-spherical nanocomposites made of multiwalled carbon nanotubes (CNTs) and polycaprolactone (PCL), poly(N-isopropylacrylamide) (PNIPAM) nanogels and metallic nanoparticles with differing sizes and shapes. The conclusions for each of the results chapter can be found below.

6.1.1. Chapter 2

In Chapter 2, nanocomposites made of CNTS and PCL were prepared by a facile oil-in water emulsion solvent evaporation method. Up to now, the surface modification of CNTs was done in a few steps reactions.[1–8] This simple, one pot method produced rod-like, non-spherical PCL-CNTs nanocomposites. SEM analysis of the nanocomposites indicated the non-spherical shape while AFM analysis revealed that the incorporation of the CNTs in the nanocomposites did not increase the modulus of the particles, including the successful surface coverage of the CNTs with PCL. Asymmetric flow field flow fractionation measurements showed good separation of particles and indicated that the shape of the particles appeared to influence separation behaviour, something that would be further investigated in chapter 5. The loading of docetaxel (DCX) in PCL, CNTs and the PCL-CNTs nanocomposites was determined by HPLC and showed high entrapment efficiencies (CNT = 95%, PCL= 81% and PCL-CNT = 89%). Moreover, faster release of DCX from PCL-CNTs was observed

with about 90% of the drug released from the nanocarriers after approximately 100 h. This finding suggests that this synthesis approach might be used to attempt to tune the drug release behaviour. Overall, this research provides a simple synthesis of non-spherical CNTs nanocomposites. The simplicity of this method means that it has potential to be used in the future for different non-spherical nanomaterials with alternative polymers for the coating, potentially allowing other novel nanocomposites to be prepared. PCL-CNTs nanocomposites showed potential to be used as anticancer drug delivery systems due to high entrapment efficiencies and relatively slow profile release of DCX.

The AF4 measurements allowed for successful analysis of the different shapes and morphologies of the synthesised nanoparticles. This was a motivation to continue the development of AF4 methods for analysis of different materials like PNIPAM nanogels.

6.1.3. Chapter 3

In Chapter 3, a versatile asymmetric flow field flow fractionation method was developed to provide detailed characterisation of PNIPAM nanogels with different sizes from 65- 310 nm. In the literature, there are only a few examples where nanogels were characterised by AF4 technique.[9–12] The diameters of particles and information on the internal structure of the nanogels can be easily obtained by using a single AF4-MALS-DLS fractionation method. Four PNIPAM nanogel samples from 65-310 nm in diameter were successfully fractionated, obtaining radius of gyration (R_g), hydrodynamic radius (R_h) and shape factors (ρ) for all four samples. The chosen mobile phase (0.1 M $NaNO_3$) and method showed good reproducibility and high resolution of sizes for AF4-MALS-DLS measurements. The fractionation of the samples revealed that the internal structure of some of the samples varied within the distribution. Determination of the mode values of R_g/R_h for the distribution of the nanogels showed that diameters higher than 100 nm had values ~0.61 indicating that the particles had more core-like shell structures. The analysis of the smallest nanogel (65 nm) gave R_g/R_h values of 0.78 indicating more homogenous structures. The

measurements showed differences in internal structure of nanogels depending on the synthesis conditions which also controlled the hydrodynamic diameter. The AF4 analysis showed advantage over commonly used techniques like DLS and SAXS. The range of different sizes, R_g and R_h can be easily obtained by AF4, where SAXS and DLS provide only mean value in the sample. This work will enable other researchers to utilise this AF4 method to provide considerable insight into the size distribution and internal structure of their nanogels, additionally this method will serve as an excellent starting point for the analysis of other soft polymer samples in the size range ~50-400 nms. The development of this AF4 method was then applied in the in next chapter, to characterise PNIPAM nanogels synthesised by different type of polymerisation (Reversible addition−fragmentation chain-transfer polymerization - RAFT) with the presence of degradable crosslinker.

6.1.4. Chapter 4

Chapter 4 focussed on the synthesis of degradable PNIPAM nanogels by RAFT polymerisation. The use of RAFT polymerisation offers the potential to obtain greater control of the internal structure of PNIPAM nanogels compared to free radical polymerisation. The nanogels were synthesised with varying amounts of monomer and crosslinker. The poly(N-hydroxyethyl acrylamide) (HEMP CTA) macro chain transfer agent (HEMP CTA) showed better ability to create nanogels compared with poly(ethylene glycol) methyl ether 2-(dodecylthiocarbonothioylthio)-2-methylpropionate macro chain transfer agent (PEG CTA). The hydrodynamic diameters for synthesised samples were between 318 and 457 nm with narrow PdI values (< 0.15). The swelling ratio was similar for all samples ~2.0, indicating that the changes in crosslinking densities were not large enough to have any influence. The synthesised nanogels showed a characteristic deswelling at 33 °C. The aggregation temperature for all samples in the presence of PBS was around 28 °C, showing potential for the use of these nanogels as *in situ* forming implants (ISFIs) and delivery vehicles of poorly water-soluble drug.[13,14] The AF4 measurements showed that nanogels have a core-shell structures due to the value of the shape factor (≤ 0.65) for

all samples. Degradation studies were conducted in the presence of 10 mM and 150 mM DTT. AF4-MALS-DLS measurements showed good degradation of PNIPAM nanogels. The most easily degradable sample was shown to contain only 15 % nanogel after the degradation process. This work has shown that the degradation process could be monitored over time using AF4 to measure particle hydrodynamic radius, radius of gyration and shape factor. RAFT polymerisation showed potential to control the size of nanogels and degradation behaviour. The RAFT synthesis can also control the length of polymer chains which can be also analysed by GPC. The ability to control the length of polymer chains can be advantageous, enabling well-characterised nanogels to be synthesised and further used as degradable ISFIs. The research again showed that the information about internal structure can be obtained by AF4 technique.

6.1.5. Chapter 5

Given the insight that AF4 had provided for the samples tested in earlier chapters, in Chapter 5, the technique was applied to analyse metallic nanoparticles (gold and silver). Here, the work focussed on insights into shape and separation behaviour that can be obtained for non-spherical metallic particles. Up to now, in the literature there is only a few examples where non spherical particles were fractionated and analysed by AF4 technique.[15–17] The AF4 measurements were also supported by a range of techniques including DLS, zeta potential measurement, SEM, STEM, UV-Vis spectroscopy and AF4-MALS-DLS. The particles showed different shapes, morphology, hydrodynamic diameters and shape factors. The size obtained from DLS was usually slightly higher compared with SEM images due to solvate shell and non-spherical shapes of particles. AF4 measurements showed successful separation of particles with different shapes and the data matches with morphology obtained from SEM images. Gold and silver nanoparticles with spherical shapes showed that size increases with elution time according to the AF4 theory. AF4 separation was able to fractionate different populations of particles in the samples of gold nanorods and silver nanoprisms, showing great potential in the nanotechnology area. The capability

of AF4 to be coupled to MALS and DLS detectors is a really important technique to allow for information on shape and structure of nanomaterials to be obtained. Before nanoparticles can be used for biomedical applications, size, size distribution, shape and other factors must be precisely known due to their influences within the body. Using AF4, it can be possible to overcome the inaccuracies that arise using batch DLS measurements.

6.2. Future work

There are several areas where the research and development conducted could be expanded upon further. In Chapter 2, biological studies could be studied to check toxicity *in vitro* and *in vivo* studies, as this would allow a better understanding of the impact of the shape on the biological behaviour. The surface modification of PCL-CNTs nanocomposites may be studied to prepare more hydrophilic particles and thus potentially more compatible with biological cells. Another opportunity would be to use a responsive hydrophilic polymer such as PNIPAM for modification of CNTs to check influence on synthesis method along with properties of nanocomposites. X-Ray Photoelectron Spectroscopy could be also used to give more evidence of surface modification of CNTs. In Chapter 3, PNIPAM nanogels with higher diameters (>310 nm) could be synthesised and analysed by AF4 to check internal structure of nanogels. SAXS analysis could be conducted to compare R_g obtained from flowing mode in AF4 and static SAXS analysis to see if there will be any differences in $R_{g,}$ caused by fractionation and interaction with eluent and membrane. Nanogels made of another polymer like for example poly(acrylic acid) could be fractionated by AF4 method to check if the obtained condition will be appropriate for analysis following materials. The research in Chapter 4 indicated that the CTA might influence their swelling behaviour and therefore the synthesis of PNIPAM nanogels with other CTAs soluble in water could be carried out in order to get a better understanding of this behaviour. An alternative degradable crosslinker may be also used to produce degradable nanogels for example (2-i-propyl-2-oxo-1,3,2-dioxaphospholane-co-2-(2-

oxo-1,3,2-dioxaphosphoroyloxyethyl methacrylate) which is hydrolytically and nonenzymatically degradable.[18] A different initiator for example potassium persulphate (KPS) could also be used to test the role of the initiator fragments on the colloidal stability of formed nanogels. KPS may provide more charge at the surface PNIPAM nanogels which could potentially provide better colloidal stability. The degradable products after addition of DTT could be analysed by GPC to check the M_n of polymer chains. In Chapter 5, the influence of shape of the separation behaviour might be better understood by the use of mathematical models to calculate theoretical R_h with a changing crossflow which could then be compared with R_h data obtained online.

6.3. References

1 Y. P. Sun, K. F. Fu, Y. Lin and W. J. Huang, *Acc. Chem. Res.*, 2002, **35**, 1096–1104.

2 H. Kong, C. Gao and D. Yan, *J. Am. Chem. Soc.*, 2004, **126**, 412–413.

3 H. Zeng, C. Gao and D. Yan, *Adv. Funct. Mater.*, 2006, **16**, 812–818.

4 L. Meng, C. Fu and Q. Lu, *Prog. Nat. Sci.*, 2009, **19**, 801–810.

5 Z. Liu, X. Sun, N. Nakayama-Ratchford and H. Dai, *ACS Nano*, 2007, **1**, 50–56.

6 X. Zhang, L. Meng, Q. Lu, Z. Fei and P. J. Dyson, *Biomaterials*, 2009, **30**, 6041–6047.

7 H. Ali-Boucetta, K. T. Al-Jamal, D. McCarthy, M. Prato, A. Bianco and K. Kostarelos, *Chem. Commun.*, 2008, 459–461.

8 S. Mallakpour and S. Soltanian, *RSC Adv.*, 2016, **6**, 109916–109935.

9 A. Shimoda, S. ichi Sawada, A. Kano, A. Maruyama, A. Moquin, F. M. Winnik and K. Akiyoshi, *Colloids Surfaces B Biointerfaces*, 2012, **99**, 38–44.

10 J. C. Gaulding, A. B. South and L. A. Lyon, *Colloid Polym. Sci.*, 2013, **291**, 99–107.

11 M. H. Smith, A. B. South, J. C. Gaulding and L. A. Lyon, *Anal. Chem.*, 2010, **82**, 523–530.

12 J. C. Gaulding, M. H. Smith, J. S. Hyatt, A. Fernandez-Nieves and L. A. Lyon,

Macromolecules, 2012, **45**, 39–45.

13 A. R. Town, M. Giardiello, R. Gurjar, M. Siccardi, M. E. Briggs, R. Akhtar and T. O. McDonald, *Nanoscale*, 2017, **9**, 6302–6314.

14 A. R. Town, J. Taylor, K. Dawson, E. Niezabitowska, N. M. Elbaz, A. Corker, E. Garcia-tun and T. O. Mcdonald, J. Mater. Chem. B, 2019, 7, 373--383.

15 R. Mathaes, G. Winter, J. Engert and A. Besheer, *Int. J. Pharm.*, 2013, **453**, 620–629.

16 J. Gigault, I. Le Hécho, S. Dubascoux, M. Potin-Gautier and G. Lespes, *J. Chromatogr. A*, 2010, **1217**, 7891–7897.

17 J. Gigault, T. J. Cho, R. I. MacCuspie and V. A. Hackley, *Anal. Bioanal. Chem.*, 2013, **405**, 1191–1202.

18 Y. Iwasaki, C. Nakagawa, M. Ohtomi, K. Ishihara and K. Akiyoshi, *Biomacromolecules*, 2004, **5**, 1110–1115.